

**STUDY OF UNSTEADY HYDRODYNAMIC EFFECTS IN THE SHIP
STERN AREA UNDER SHALLOW WATER CONDITIONS**

UNTERSUCHUNG DER INSTATIONÄREN HYDRODYNAMISCHEN EFFEKTE IM
HECKBEREICH EINES SCHIFFES IM FLACHWASSER

Dissertation
zur
Erlangung des akademischen Grades
Doktor-Ingenieur (Dr.-Ing.)
der Fakultät für Maschinenbau und Schiffstechnik
der Universität Rostock

vorgelegt von	Ivan Shevchuk
	geboren am 16 März 1988
	in Leningrad
aus	Rostock

Rostock
2016

Date of submission: 9 September 2016

Reviewers:

Prof. Dr.-Ing. habil. Nikolai Kornev, Universität Rostock, Lehrstuhl für Modellierung und Simulation

Prof. Dr.-Ing. Bettar Ould el Moctar, Universität Duisburg-Essen, Institut für Schiffstechnik und Transportsysteme

Date of defense: 21 November 2016

Acknowledgements

My sincere gratitude is expressed to:

- My scientific advisor, Prof. Dr. Nikolai Kornev, for giving me the chance for becoming a Ph.D. student at Rostock University. Without his guidance and support in scientific issues this study would be impossible.
- My family, who believed in me and constantly supported me, despite the distance between us.
- Prof. Dr. Bettar el Moctar for a thorough review of my thesis, which helped me to improve the manuscript.
- Dr. Hannes Kröger for fruitful and enlightening discussions on turbulence, marine propellers and computational methods, as well as for his help with open-source software issues.
- Mr. Benjamin Friedhoff from DST for providing the validation data for M1926 model.
- All my former and present colleagues at the Chair of Modeling and Simulation and the Chair of Ship Design of the University of Rostock for sharing their knowledge in the field of CFD and ship hydrodynamics.

Additionally, I would like to thank all the persons, who helped me in any way during my Ph.D. study at Rostock University.

Rostock, 08.12.2016

This page intentionally left blank

Contents

List of Figures	ix
List of Tables	xiii
Nomenclature	xv
Acronyms	1
1. Introduction	3
1.1. Motivation	3
1.2. Sources of vibration excitation	3
1.3. Shallow water effects on the ship	4
1.4. Application of CFD to unsteady wake calculation	6
1.5. Objectives of the study	7
1.6. Thesis outline	7
I. Theoretical background	9
2. Mathematical model	11
2.1. Dynamics of incompressible Newtonian fluids	11
2.1.1. Continuum hypothesis	11
2.1.2. Mass conservation	11
2.1.3. Momentum equation	13
2.1.4. Boundary and initial conditions	14
2.1.5. Well-posedness of the problem	15
2.1.6. Pressure equation	15
2.2. Turbulence and its modeling	15
2.2.1. Laminar and turbulent flows	15
2.2.2. Reynolds averaged Navier-Stokes equations	16
2.2.3. Reynolds Stress Transport Equations	17
2.2.4. Turbulent viscosity and gradient diffusion assumptions	18
2.2.5. Turbulence kinetic energy equation	19
2.2.6. Equation for the isotropic dissipation rate	19
2.2.7. The $k - \epsilon$ turbulence model	20
2.2.8. The $k - \omega$ turbulence model	21
2.2.9. The $k - \omega$ SST turbulence model	21
2.2.10. Applicability of RANSE turbulence models	23
2.2.11. Large-Eddy Simulation	23
2.2.12. Filtering	24
2.2.13. Subgrid scale stress modeling	25
2.2.14. Applicability of LES	28
2.3. Overview of hybrid turbulence models	28
2.3.1. Blending of RANS and LES	29
2.3.2. LeMoS hybrid model (LH)	31
2.3.3. DES family methods	32
2.3.4. Partially Averaged Navier-Stokes Equations (PANS)	38
2.3.5. Hybrid-Filtered Navier-Stokes (HFNS)	39

2.4.	Generation of turbulent inflow conditions	40
2.4.1.	Description of the synthetic turbulence generator	43
2.5.	Free surface formulation	44
2.6.	Dynamics of a ship with two degrees of freedom	46
3.	Numerical method	49
3.1.	Finite volume method	49
3.1.1.	Approximation of the convection term	50
3.1.2.	Approximation of the diffusion term	52
3.1.3.	Temporal discretization	53
3.2.	Solution algorithms for the incompressible Navier-Stokes equations	54
3.2.1.	Discrete pressure equation	55
3.2.2.	Pressure-velocity coupling algorithms	56
3.3.	Solution algorithm for the viscous incompressible free-surface flows	57
3.3.1.	Mesh deformation algorithm for shallow water	58
3.3.2.	Details of trim and sinkage computation method	59
II.	Applications	61
4.	Validation	63
4.1.	Canonical flows	63
4.1.1.	Channel flow	63
4.1.2.	Asymmetric plane diffuser flow	64
4.2.	Ship flows	69
4.2.1.	Prediction of the wake of an inland ship in a restricted shallow channel . .	69
4.2.2.	Prediction of squat effect in a restricted shallow channel	78
5.	Nominal wake analysis	81
5.1.	Geometry of the studied hull form	81
5.2.	Choice of simulation conditions	82
5.3.	Description of the program of computations	83
5.4.	Preliminary computations using LH model	83
5.4.1.	Single-phase simulations setup	83
5.4.2.	Two-phase simulations setup	84
5.4.3.	Results and discussion	85
5.5.	Preliminary computations using LH model with account for squat effect	88
5.6.	Conclusions of the preliminary study	90
5.7.	Grid convergence study	90
5.7.1.	Conditions	90
5.7.2.	Numerical setup	91
5.7.3.	Analysis of the results	92
5.7.4.	Conclusions on the grid convergence study	96
5.8.	Final computations of the nominal wake	97
5.8.1.	Conditions and setup	97
5.8.2.	Analysis of the results. Straight course	98
5.8.3.	Analysis of the results. Drift angle $\beta = 10^\circ$	100
5.8.4.	Concluding remarks for Chapter 5	103
6.	Prediction of thrust oscillations on rotating propellers	107
6.1.	Geometry and conditions	107

6.2. Numerical setup	108
6.3. Results and discussion	109
6.4. Motion at straight course	109
6.4.1. Thrust fluctuations	109
6.4.2. Pressure pulses on the hull	110
6.4.3. Rough estimation of cavitation inception	111
6.5. Motion with drift angle	112
6.5.1. Thrust fluctuations	112
6.5.2. Pressure pulses on the hull	114
6.5.3. Rough estimation of cavitation inception	114
7. Conclusions and outlook	117
Bibliography	123

This page intentionally left blank

List of Figures

1.1. Sketch of the flow geometry at the stern of a river cruise vessel	6
2.1. Arbitrary volume V with the boundary S , filled with fluid	12
2.2. Random signal $y = f(x)$, filtered using top-hat filter with different filter widths h	24
2.3. Schematic explanation of recycling approach for the case of plane asymmetric diffuser flow	41
2.4. Schematic explanation of recycling approach for the case of plane asymmetric diffuser flow	41
2.5. Ship coordinate system for squat computations	46
3.1. Sketch of a two-dimensional computational stencil in FVM	49
3.2. Face interpolation: (a) - central and neighbor cells and a face, on which the value in terms of ϕ_P and ϕ_{N_i} should be obtained, (b) - sketch of linear interpolation. P - center of the cell, for which the equation is discretized. N_i - center of one of the neighboring cells. The vectors $\overline{f_i N_i}$ and $\overline{P N_i}$ are used for the calculation of the weight w	51
3.3. Upwind face interpolation: a piecewise-constant interpolation from the cell center, from which the flow is incoming	51
3.4. Sketch of the vectors, used for over-relaxed non-orthogonality correction approach	52
3.5. Mesh motion algorithm: (a) - sketch of the vectors used in formula (3.46), (b) - bounding boxes used for λ prescription in computational domain	58
3.6. Example of application of presented algorithm: (a) - undeformed mesh, (b) - mesh with rotated body, (c) - distribution of λ . One can see that the cells in the vicinity of the body preserve their form	59
4.1. Channel flow test case: (a) - geometry of the case, (b) - comparison of the computed velocity profile with the correlation and the results of Gritskevich [48] (Orig) for $Re_\tau = 395$	63
4.2. Comparison of the computed velocity profile (SSTIDDES-OF) with the correlation and the results of Gritskevich [48] (SSTIDDES-Orig) for: (a) $Re_\tau = 2400$ and (b) $Re_\tau = 18000$	64
4.3. Geometry of the diffuser test case	65
4.4. Fragment of the computational mesh (coarse)	65
4.5. Diffuser test case: (a) sketch of domain boundaries, (b) application of turbulence generator	66
4.6. Comparison of velocity and Reynolds stress profiles along z-axis between different approaches on the fine mesh	67
4.7. Comparison of velocity and Reynolds stress profiles along x-axis between different refinement levels for combination DSM + recycling	68
4.8. Comparison of velocity and Reynolds stress profiles along z-axis between different refinement levels for combination SSTIDDES + synthetic turbulence	68
4.9. Plots of skin friction coefficient (upper wall) predicted by different approaches on the fine mesh	69
4.10. Sketch of computational domain boundaries for the single-phase simulation of the flow around M1926 model	70
4.11. Bow and stern geometry of M1926 model. The plane where the velocity field was measured in shown at $x = 0.48$ at the stern.	70

4.12. Vortical structures ($\lambda_2 = -20$) in the stern of M1926 predicted using SSTIDDES + synthetic turbulence generator. One can see, where the turbulent structures are added to the flow.	71
4.13. Comparison of the wake obtained on the coarse grid using different methods: (a) - experiment, (b) - RANS, (c) - LH, (d) - SSTIDDES	72
4.14. Comparison of the wake obtained on the medium grid using different methods: (a) - experiment, (b) - RANS, (c) - LH, (d) - SSTIDDES	73
4.15. Comparison of the solutions obtained on different grids, sampled on the line $x = 0.48$ m, $z = -0.23$ m (left) and on the circle corresponding to $r/R = 0.7$ in the propeller plane (right)	74
4.16. Comparison of the wake obtained on the fine grid using different methods: (a) - experiment, (b) - RANS, (c) - LH, (d) - SSTIDDES	75
4.17. Comparison of the wake obtained using SLH (right) and original LH (left) formulation on different grids: (a),(b) - coarse mesh, (c),(d) - medium mesh (e),(f) - fine mesh	76
4.18. Comparison of the solutions obtained using LH, SLH and SSTIDDES on different meshes. Wake was sampled on the line $x = 0.48$ m, $z = -0.23$ m (left) and on the circle corresponding to $r/R = 0.7$ in the propeller plane (right)	77
4.19. Standard deviation of velocity field at six points along the line $x = 0.48$ m, $z = -0.25$ m	78
4.20. (a) - full scale channel section, (b) - PPM55 model geometry	79
4.21. Plots of the measured and computed values of squat at aft (left) and fore (right) perpendiculars	80
5.1. Generic hull form: (a) - the view of the stern geometry , (b) - body plan	81
5.2. Top, side and front views over the generic hull form	81
5.3. Shallow water influence diagram (taken from [9]). In the region above the dashed line the effects on the wavemaking wake and wave resistance are present. The region above the solid line corresponds to the influence on the viscous wake and frictional resistance. The points show the regimes, considered in the presented work	82
5.4. Sketch of the computational domain for single-phase simulations. Motion at straight course	84
5.5. Points in the propeller plane, at which the velocity fluctuations were recorded. Fluctuations in P1 (3.065 1.23 -1.375) and P2 (3.065 3.53 -1.375) were used for comparative analysis in preliminary computations	85
5.6. Average f (left) and k_{res}/k_{tot} (right) in the propeller plane. Propeller disks are shown with black circles	85
5.7. Comparison of the vortical structures ($\lambda_2 = -15$) predicted by URANS and hybrid model in a single phase formulation: (a) - 1PH61, hybrid, (b) - 1PH61, URANS, (c) - 1PH62, hybrid, (d) - 1PH62, URANS. View to the stern area from below ship	86
5.8. Comparison of the vortical structures ($\lambda_2 = -15$) obtained from two-phase simulations with the hybrid model for different regimes: (a) - 2PH61, (b) - 2PH62, (c) - 2PH41, (d) - 2PH42. View of the stern area from below	86
5.9. Time history of longitudinal velocity at two points in propeller disks. (a) - 1PH61, (b) - 2PH61, (c) - 2PH41, (d) - 1PH62, (e) - 2PH62, (f) - 2PH42	87
5.10. Stern wave pattern for different cases: (a) - 2PH61, (b) - 2PH62 , (c) - 2PH41, (d) - 2PH42	87
5.12. Schematic explanation of the free surface influence on the wake unsteadiness, revealed in the preliminary study: left - flow geometry in single-phase simulation, right - the case of critical Fn_h , stern wave causes the change of flow geometry . .	88

5.13. Comparison of the vortical structures ($\lambda_2 = -15$) predicted by LH model in a two-phase simulation with squat (upper row) and without squat (lower row): (a) - 2PH41S, (b) - 2PH42S, (c) - 2PH62S, (d) - 2PH41, (e) - 2PH42, (f) - 2PH62 . . .	89
5.14. Y-Slice of the mesh structure at the stern (coarse mesh)	91
5.15. Top view of the mesh structure (coarse mesh)	91
5.16. Comparison of $\langle u_x \rangle$, k_{tot} profiles between the different meshes for SSTIDDES, LH and RANS $k - \omega$ SST models along the line $x = 3.065$, $z = -1.375$ (a,b,d,e,g,h) ; convergence of the relative standard deviation in the propeller plane (c,f)	93
5.17. Sampling lines for comparison of solutions and probe points for collection of u_x statistic (P1U, P1R, P1L, P1D, P2U, P2R, P2L, P2D)	94
5.18. Comparison of the solutions produced by different models on the fine mesh	94
5.19. Contour plots of the time-averaged longitudinal velocity field $\langle u_x \rangle$ in the propeller plane, predicted by RANS (a), SSTIDDES (b), and LH (c) on the fine mesh . . .	94
5.20. Sampling lines for comparison of solutions and probe points for collections of u_x statistic (1U, 1R, 1L, 1D), (2U, 2R, 2L, 2D)	94
5.21. Contour plots of the longitudinal velocity field in the propeller plane, predicted by RANS (a), SSTIDDES (b), and LH (c) on the medium mesh with $y^+ \leq 1$. . .	96
5.22. Profiles of k_{res}/k_{tot} ratio along three lines in propeller plane	96
5.23. Sketch of the computational domain for the computations with the drift angle . .	97
5.24. Nominal wake w in the propeller plane at $r/R=0.7$ for first (a) and second (b) propeller disks	99
5.25. Plots of the resolved Reynolds stresses $\langle u_x^2 \rangle$ (left) and wake (right). Figures correspond to the following cases: a, b - FB1-0; c, d - FB2-0; e, f - FB3-0	100
5.26. Comparison of empirical distribution functions of velocity fluctuations built at points (a) - P1U; (b) - P1R; (c) - P2L for different depths for $\beta = 0^\circ$	101
5.27. Comparison of empirical distribution functions of velocity fluctuations built at points (a) - P1U, (b) - P1R, (c) - P2L for different depths for $\beta = 10^\circ$	101
5.28. Nominal wake w in the propeller plane at $r/R=0.7$ for first (a) and second (b) propeller disks	102
5.29. Plots of the resolved Reynolds stresses $\langle u_x^2 \rangle$ (left) and wake (right). Figures correspond to the following cases: a, b - FB1-10; c, d - FB2-10; e, f - FB3-10 . . .	102
5.30. Streamlines built from the averaged velocity fields for the case with $\beta = 0^\circ$ (left) and with $\beta = 10^\circ$ (right). Figures a, c, e correspond to FB1-0, FB2-0, FB3-0, b, d, f - to FB1-10, FB2-10, FB3-10	104
6.1. Geometry of the pods and shafting of the azimuth thrusters, designed by the author (propeller blades are not shown)	107
6.2. Geometry of the front (left) and rear (right) propellers, installed on the thrusters	108
6.3. Generic hull form with thrusters on the port side	108
6.4. Comparison of empirical distribution functions of total (front + rear propeller) thrust fluctuations between different depths for $\beta = 0^\circ$: (a) - first thruster, (b) - second thruster	110
6.5. Power spectral density of the thrust fluctuations on the front (left) and rear (right) propellers of the thruster near the skeg at $h/T = 1.25$	110
6.6. Comparison of empirical distribution functions of pressure pulses above front propellers between different depths for $\beta = 0^\circ$, (a) - first thruster, (b) - second thruster	111
6.7. Comparison of the regions on the front propeller of the near-skeg thruster, where cavitation inception can occur	111
6.8. Comparison of empirical distribution functions of pressure pulses above rear propellers between different depths for $\beta = 0^\circ$, (a) - first thruster, (b) - second thruster	112

6.9. Comparison of empirical distribution functions of total (front + rear propeller) thrust fluctuations between different depths for $\beta = 10^\circ$: left - first thruster, right - second thruster	112
6.10. Comparison of empirical distribution functions of total (front + rear propeller) thrust fluctuations between $\beta = 0^\circ$ and $\beta = 10^\circ$ for $h/T=1.25$: left - first thruster, right - second thruster	113
6.11. Comparison of empirical distribution functions of total (front + rear propeller) thrust fluctuations between $\beta = 0^\circ$ and $\beta = 10^\circ$ for $h/T=1.5$: left - first thruster, right - second thruster	113
6.12. Resolved Reynolds stress $\langle u_x'^2 \rangle$ in the plane of the front propellers for $\beta = 10^\circ$; left - without propellers, right - with propellers	113
6.13. Comparison of empirical distribution functions of pressure pulses above front propellers between different depths for $\beta = 10^\circ$: left - first thruster, right - second thruster	114
6.14. Comparison of empirical distribution functions of pressure pulses above rear propellers between different depths for $\beta = 10^\circ$: left - first thruster, right - second thruster	114
6.15. Comparison of empirical distribution functions of pressure pulses above front propellers between $\beta = 0^\circ$ and $\beta = 10^\circ$: left - first thruster, right - second thruster. $h/T=1.25$	115
6.16. Comparison of empirical distribution functions of pressure pulses above front propellers between $\beta = 0^\circ$ and $\beta = 10^\circ$: left - first thruster, right - second thruster. $h/T=1.5$	115
6.17. Comparison of the regions on the front propeller of the near-skeg thruster, where cavitation inception can occur	115
6.18. Comparison of empirical distribution functions of pressure pulses above front propellers between $\beta = 0^\circ$ and $\beta = 10^\circ$: left - first thruster, right - second thruster. $h/T=2.0$	116
6.19. Vortical structures in the wake of a river cruise ship during the motion with $\beta = 10^\circ$: (a) - without thrusters (b) - with thrusters, $h/T = 1.25$. Isosurfaces $\lambda_2 = -10$ [60]	116

List of Tables

2.1. Commonly used LES filters [13]. Gaussian filter is written for the isotropic case $\Delta_x = \Delta_y = \Delta_z = \Delta$	24
4.1. Characteristics of the computational meshes	66
4.2. Boundary conditions imposed on the unknowns	66
4.3. Conditions considered in the M1926 model simulations	69
4.4. Boundary conditions imposed on the unknowns for M1926 validation case	71
4.5. Conditions considered in validation of squat prediction	79
4.6. Boundary conditions imposed on the unknowns in squat computations	79
4.7. Comparison of the experimental values of squat at fore and aft perpendiculars with computed ones	80
5.1. Summary of the computed preliminary cases. FS - free surface	83
5.2. Boundary conditions for the single-phase simulations	84
5.4. Summary of the computed cases with squat	88
5.5. Values of trim angle, sinkage and standard deviation of longitudinal velocity for the considered cases	90
5.6. List of the considered conditions with corresponding labels	97
5.7. Boundary conditions for nominal wake computations with the drift angle	98
5.8. Relative standard deviation of velocity σ_u in eight points in the propeller plane. For the point designations see Figure 5.17. The sketch of the probe points is added for the ease of understanding	100
5.9. Relative standard deviation of velocity σ_u in eight points in the propeller plane. For the point designations see Figure 5.17. The sketch of the probe points is added for the ease of understanding	103
6.1. List of considered conditions for the computations with rotating propellers	107
6.2. Statistics of the total thrust oscillations on the first and second pods for the motion at straight course	109
6.3. Statistics of the total thrust oscillations on the first and second thruster for $\beta = 10^\circ$	112

This page intentionally left blank

Nomenclature

α	Indicator function of VOF algorithm (volume fraction)	[-]
\mathcal{T}	Stress tensor	[Pa]
Ω	Vorticity tensor	[s ⁻¹]
S	Rate-of-strain tensor	[s ⁻¹]
Δ	Characteristic cell size	[m]
$\Delta_x, \Delta_y, \Delta_z$	Cell sizes in x, y, z directions (for hexahedral cells)	[m]
Δ_{\max}	Maximum edge of the hexahedral cell $\max(\Delta_x, \Delta_y, \Delta_z)$	[m]
$\nabla \cdot (..)$	Divergence operator	
ϵ	Turbulence dissipation rate	[m ² s ⁻³]
ϵ_s	Isotropic (pseudo) turbulence dissipation rate	[m ² s ⁻³]
η	Kolmogorov lengthscale	[m]
$\nabla(..)$	Gradient (nabla) operator	
κ	Wavenumber	[rad m ⁻¹]
μ	Dynamic viscosity	[kg m ⁻¹ s ⁻¹]
μ_t	Turbulent dynamic viscosity	[kg m ⁻¹ s ⁻¹]
ν	Kinematic viscosity	[m ² s ⁻¹]
ν_h	Hybrid kinematic viscosity (mix of turbulent viscosity and subgrid viscosity)	[m ² s ⁻¹]
ν_t	Turbulent kinematic viscosity	[m ² s ⁻¹]
ν_{SGS}	Subgrid kinematic viscosity	[m ² s ⁻¹]
Ω	Magnitude of vorticity tensor $\sqrt{2\Omega_{ij} : \Omega_{ij}}$	[s ⁻¹]
ω	Specific turbulence dissipation rate	[m ² s ⁻³]
ρ	Density	[kg m ⁻³]
$\sigma_k, \sigma_\epsilon$	Prandtl-Schmidt numbers for k and ϵ	[-]
τ_{ij}^h	Hybrid stress tensor (mix of Reynolds stresses and residual stresses)	[m ² s ⁻²]
τ_{ij}^{SGS}	Residual-stress tensor	[m ² s ⁻²]
\mathbf{g}	Gravitational acceleration vector ($00 - g_z$)	[m s ⁻²]
\mathbf{u}	Velocity vector with components u_x, u_y, u_z	[m s ⁻¹]
C_s	Smagorinsky constant	[-]

C_{DES}	DES model constant	[-]
f	Blending function of hybrid RANS/LES methods	[-]
f_d	DES shielding function	[-]
F_z	Force along z axis	[N]
Fn	Froude number	[-]
Fn_h	depth Froude number	[-]
k	Turbulence kinetic energy	$[m^2 s^{-2}]$
k_{sgs}	Residual kinetic energy	$[m^2 s^{-2}]$
Kn	Knudsen number	[-]
M_y	Moment about y axis	[N m]
Ma	Mach number	[-]
p	Pressure (dynamic or kinematic, depending on the context)	[Pa] or $[m^2 s^{-2}]$
r_d	Argument of the DES shielding function	[-]
Re	Reynolds number	[-]
S	Magnitude of the strain rate tensor $\sqrt{2S_{ij} : S_{ij}}$	$[s^{-1}]$
t	Time	[s]
y_w	Wall distance (used in DES family methods)	[m]
δ_{ij}	Kronecker delta	
$\tau_{ij}^t, \tau_{ij}^{RANS}$	Reynolds stress tensor	$[m^2 s^{-2}]$

Acronyms

ARSM	Algebraic Reynolds Stress Model
DDES	Delayed Detached-Eddy Simulation
DES	Detached-Eddy Simulation
DNS	Direct Numerical Simulation
EARSM	Explicit Algebraic Reynolds Stress Model
FSM	Flow Simulation Methodology
GIS	Grid Induced Separation
HFNS	Hybrid-Filtered Navier-Stokes
IC	Initial Conditions
IDDES	Improved Delayed Detached-Eddy Simulation
LES	Large-Eddy Simulation
LLM	Log-Layer Mismatch
MSD	Modeled Stress Depletion
RANS	Reynolds Averaged Navier-Stokes
RSTM	Reynolds Stress Transport Modeling
SBES	Stress-Blended Eddy Simulation
SDES	Shielded Detached-Eddy Simulation
URANSE	Unsteady Reynolds Averaged Navier-Stokes Equations
VOF	Volume-of-Fluid
WMLES	Wall-Modelled LES

This page intentionally left blank

Chapter 1

Introduction

1.1 Motivation

In recent years river cruises through Europe have become very popular. Despite the relatively high prices these leisure activities attract people by the combination of a high comfort level and rich sightseeing experience. In an eight to fourteen day period one can visit a great number of tourist attractions (e.g. European capital cities) without considerable stress, while having constant access to luxurious cabins.

Thus, the passenger comfort is a very important feature of such journeys. However, the fact that the vessels often operate under shallow water conditions may impair the habitability of the ship and decrease the attractiveness of the cruises. The reason for this is that the ship motion in fairways with depth restriction often leads to rise of strong vibration at the stern. Absence of vibration is one of the most important criteria for evaluation of passenger (e.g. cruise) vessels. Based on the resulting level of vibration and noise the ship comfort class is determined by classification societies (see, for example [6, 133]). Usually, the shipyard bears the responsibility for ensuring the vibration limits, agreed with the ship owner. If the limits are exceeded additional technical measures must be implemented to suppress the excessive hull oscillations and noise, which results in additional costs. In order to avoid this scenario, the mechanisms, leading to the rise of stern vibration under shallow water conditions should be understood. This way the recommendations for the design phase can be provided, which would allow for avoiding the excessive vibration levels.

Much work has been done for understanding the ship vibration exciters and developing the measures for its suppression [156, 133]. At the same time, the discussion of the shallow water influence on hydrodynamic vibration sources can be found literally in a few works [119, 164, 165]. This indicates that further research on this topic should be conducted in order to clarify the mechanism, by which the depth restriction affects the hull oscillations.

In order to approach this problem in a more detailed manner, the usual sources of vibration excitation should be discussed.

1.2 Sources of vibration excitation

By the origin the exciters of ship vibration can be split into two groups: mechanical and hydrodynamical ones [65, 6]. The former group consists of working mechanisms: main and auxiliary engines, shaft machinery, gearboxes, etc. Main engine is usually considered to have a major contribution here [133]. Obviously, the working conditions of the mentioned devices are not influenced by the change of the water depth. Therefore the cause of the above mentioned problem should be searched for in the second group of vibration sources.

The main reason of the hydrodynamically excited vibration is the propeller, which can in multiple ways affect the hull structure. Firstly, the forces and moments, produced by the propeller may considerably fluctuate in time because of the wake nonuniformity and instationarity. This effect is due to the change of the angle of attack of a propeller blade in circumferential direction and in time. These periodic forces are transmitted through the shafting to the ship structure. Secondly, the propeller blades rotating in water create pressure pulses on the hull and by these means cause the oscillations of the hull surface. The pressure pulses consist of three different parts: lift part (due to propeller blade lifting force), displacement part (depending on blade thickness) and cavitation part. For the latter mechanism the cavitation sheets are most

important, not the cavitation bubbles [156]. If the irregularities in the inflow velocity field are present the cavities can collapse in a repeating fashion. In this case the contribution of cavitation to the pressure pulses may be much higher, than that of lift and displacement contributions [156, 19]. Usually, if the propeller is cavitating the pressure pulses play the major role for vibration excitation [133]. If this is not the case, the thrust fluctuations are dominant.

Generally speaking, study of the reasons for vibration should involve both hydromechanical and structural analysis. Not only the excitation is important here, but also the structural response. As it is known, the strongest hull oscillations occur when the frequency of the excitation source coincides with one of the hull natural frequencies. However, in this particular situation, when the vibration occurs only in confined waters, it is to expect, that the changes in flow picture are a key issue. From this standpoint it makes sense to analyze the hydrodynamical part of the problem separately and clarify, which mechanisms are responsible for the observed phenomenon. In particular, how the change of the wake parameters due to the bottom proximity influences the propeller forces oscillations. Therefore the structural analysis is left out of the scope of the present research. Thus, the focus of the work is placed on the study of the unsteady ship wake and propeller thrust oscillations under shallow water conditions.

Despite the potential importance, modeling of cavitation is left out of the scope of the present work. Accounting for the cavitation in conjunction with unsteady wake fluctuations would require application of extremely complicated numerical model. Since the wake parameters are the determining factors for whether or not the cavitation occurs, the present research can become a basis for the future work, in which the cavitation will be thoroughly analyzed. Thus, in the framework of the present research only a rough estimation of cavitation inception was undertaken.

1.3 Shallow water effects on the ship

Ship behavior under shallow water conditions is a classical problem considered in ship theory and it has been studied by marine engineers for a long time. Influence of depth restriction on the ship is a complex matter, including a lot of various phenomena [150]. The studies dealing with shallow water effects are mostly devoted to the following aspects:

1. **Influence of depth restriction on the wave pattern and resulting change in wave resistance.** The wave generation by a moving ship in shallow water is considerably more intense than for the deep water case. The determining parameter of the influence of water depth on the wave pattern is the depth Froude number $Fn_h = \frac{U}{\sqrt{gh}}$. For small Fn_h the wave pattern is almost the same as for unrestricted water, but as the mentioned parameter grows, the transversal waves at the same propagation speed become longer and the width of the Kelvin wedge increases [77]. At the so-called (trans)critical regime $Fn_h \approx 1$ strong transverse crests at the bow and stern are observed [61, 9]. The diverging waves at the same time are to a much less extent affected by the water depth. Because of the described changes in the wave pattern the wave resistance considerably increases with increasing Fn_h till the latter reaches unity. In supercritical regimes ($Fn_h > 1$) only diverging waves are present and the wave-making resistance decreases again. Here one should mention the works of Jiang [61], Chen [22], Soomere [138].
2. **Viscous resistance in confined waters.** Both the frictional and the viscous pressure resistance can be noticeably affected by the bottom proximity. Depth restriction leads to acceleration of the fluid under the ship and results into the increase of wall-normal velocity gradient at the ship hull and subsequent growth of skin friction. Viscous pressure resistance is affected by the change of pressure distribution on the ship hull, caused by shallow water effects (e.g. wave making). The research efforts were mainly aimed at deriving the rescaling

laws for shallow water viscous resistance from model to full scale. The usual assumption of ship hydrodynamics that the wave pattern has insignificant influence on the viscous resistance and the consequent breakdown into independent resistance parts are not quite correct in shallow water. The change of pressure distribution due to the intensified wave generation may be noticeable and may lead to considerable boundary layer separations. This phenomenon causes a dramatic change in viscous pressure resistance. Under certain conditions ($Fr_h \approx 1$) the latter may become equal and even higher than the frictional resistance [155]. Due to these peculiarities it is difficult to develop a reliable method to extrapolate the resistance forces from the model to the full scale under shallow water conditions. For further details reader is referred to the work of Raven [118] and references therein.

3. **Squat prediction.** One of the most important effects of shallow water is the dramatic increase of dynamic trim and sinkage compared to deep water. The reason for this is the Ventouri effect, which decreases the pressure under the ship hull and on this account produces the suction force, which pulls the vessel toward the fairway bottom. This effect is of a high significance because of the risk of the grounding in case of excessive squat. For this reason prediction of squat is a very important task. A number of methods was proposed for solution of this problem: analytic and empirical formulas, slender body methods, potential flow methods and CFD. The latter approach is at the moment the most accurate one, but at the same time the most time-consuming (see [46], [132] and references therein). Experience shows, that in extreme shallow water CFD seems to be the only alternative [131].
4. **Maneuvering behavior in shallow water.** Presence of the bottom increases the derivatives of forces (except for C_y^Ω) and moments, acting on the ship. The added masses (m_{11}, m_{22}, m_{66}) of the hull also become larger. Due to these changes the turning circle radius increases and the ship becomes sluggish [53]. Because of the described effects the shallow water influence on the ship motion must be accounted for in assessment of ship maneuverability [29]. Latest achievements in this field of research are regularly presented at the International Conference on Ship Maneuvering in Shallow and Confined Water (MASH-CON).

Despite the fact, that the topic of shallow water is generally studied quite well, there is a lack of literature discussing the influence of the depth on the wake nonuniformity or instationarity or the mechanism of ship vibration under such conditions. Unfortunately, only a few works can be mentioned here.

Reed and Basset [119] described the results of a series of full-scale trials conducted on the cargo ships operating on Great Lakes under shallow water conditions. They showed that very strong pressure pulses on the hull can occur in such circumstances which lead to severe hull oscillations. The reasons for the observed effect were attributed to the unsteadiness of the wake and the sheet cavitation resulting from it. However, the detailed analysis of the wake parameters was not presented because of the complexity of the velocity field measurements in full scale.

Zibell and Müller [164] presented the results of a research project devoted to development of ships and propulsion systems for extremely shallow water conditions. Even though the research project was not directly aimed at the hull vibration assessment, the pressure pulses on the hull and vibration amplitudes were measured for two full scale ships moving at $h/T = 1.1$. For both ships very high fluctuations (20-35 kPa) of pressure on the hull were observed. As previously, this effect was attributed to sheet cavitation, arising because of high propeller loading coefficient and the influence of shallow water on the wake fraction distribution. Authors concluded, that due to severe pressure fluctuations special structural measures should be implemented in order to avoid stern vibration in shallow water.

Zong and Lam [165] analyzed the change of added masses of the ship hull in shallow water using the method of matched asymptotic expansions and BEM. They showed that the change of added masses of a hull caused by the proximity of the bottom can considerably change the hull natural frequencies. The conclusion was drawn, that this effect should be accounted for in the ship design phase.

The effect which has not been widely discussed in literature so far is the increase of the adverse pressure gradient along the hull in the stern under shallow water conditions and its influence on the wake parameters. Restriction of depth makes the flow geometry at the stern of the river cruise vessel similar to that of a diffuser flow (see Figure 1.1). Under these conditions the flow can separate from the hull surface. The discussed trend can be noticed in the results, presented by Raven [118]. Even though other types of ships were considered there, the analysis of the wake field clearly shows that depth restriction may lead to separations. Effect was more pronounced for model scale, but significant changes can be observed also for real scale.

The presence of recirculation zone in this case would lead to appearance of irregularities of the wake fraction and resulting severe thrust oscillations. Additional contribution may come for the generation of unsteady vortices, transported to the propeller.

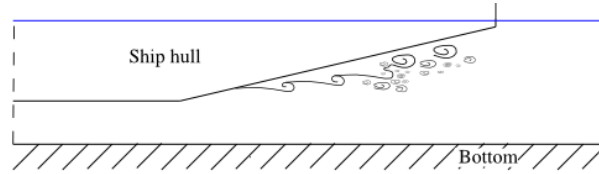


Figure 1.1: Sketch of the flow geometry at the stern of a river cruise vessel

1.4 Application of CFD to unsteady wake calculation

The study of the described phenomena will be conducted by means of CFD simulations. Even though the latter can suffer from a number of inaccuracies, (stemming from modeling errors, approximation errors etc.), they are nowadays widely accepted as a research tool, because of relatively low cost and simplicity, compared to model scale experiments or full scale trials. However, the quality of the computational results should be constantly assessed. For this purpose a number of validation studies of the numerical models will be performed (see Chapter 4).

The most applications of CFD to ship hydrodynamics are restricted to RANS-based analysis. The scale-resolving simulations, like LES or hybrid RANS/LES are not widely used because of higher computational demands. In cases, where strong separations do not occur (e.g. ships with low block coefficients) RANS may be a perfect choice. However, as the results of the recent workshop on CFD in ship hydrodynamics (2015) indicate, increase of the block coefficient may impair the accuracy of model predictions. The reason is most likely, that RANS models may in some cases poorly predict the momentum transport after separation [141]. RANS is also known to smear out the flow features in time and space (for more details see Chapter 2). Due to the described issues the hybrid RANS/LES models are chosen as the main research tool in the present work.

Calculations of the unsteady ship wake using scale resolving methods have been described in a significant number of research papers in the last years [16, 14, 162, 70, 108, 38]. Yet, only a few works to date have addressed the influence of wake instationarity on the pressure or thrust fluctuations.

In the recent series of works Abbas (see for example [2]) studied the unsteady loadings on the propeller of a KVLCC tanker at different maneuvering conditions in model scale using hybrid URANS/LES method of Kornev et al. [70]. The results were in a fair agreement with the engineering methods for estimation of forces and moments fluctuations on the propellers.

It was shown that a significant contribution to thrust oscillations is due to large-scale flow instabilities. One of the most important conclusions of the work was that URANS was not capable of reproducing the correct statistics of propeller forces and moments variations.

Liefvendahl and Bensow [84] conducted the analysis of thrust and pressure fluctuations for the model of a chemical tanker using LES with wall functions. In their paper the authors noted the importance of capturing of the wake instationarity for the successful prediction of alternating thrust - in all simulations the signal of thrust contained non-periodic components, attributed to unsteady effects in the velocity field. Good agreement with experimental data for thrust fluctuations was attained. In the presented results one can notice a considerable dependence of the thrust variations on the upstream flow separation. The major contribution to the observed pressure oscillations was that from propeller blade rotation and was mostly periodic.

1.5 Objectives of the study

The main objective of the present research is the assessment of the influence of shallow water conditions on the hydrodynamic exciters of ship hull vibration¹ using hybrid RANS/LES methods. A river cruise vessel is selected for consideration. In order to achieve the claimed goal following steps will be taken:

1. Overview of the existing hybrid RANS/LES methods for turbulence modeling and selection of the most appropriate ones for the current research
2. Validation of the selected methods for canonical and ship flows
3. Analysis of the influence of different factors on the characteristics of the nominal wake of a river cruise vessel under shallow water conditions
4. Assessment of thrust fluctuations and pressure pulses and their sensitivity to motion conditions

1.6 Thesis outline

The present work consists of seven chapters and is organized as follows:

- Chapter 2 describes the mathematical model, used in the present work. Since the turbulence modeling is one of the major aspects of the successful flow simulations, an overview of the existing turbulence modeling methods is given.
- Chapter 3 presents the numerical method, employed in the further CFD simulations.
- Chapter 4 contains the validation data of the computational methods for canonical and ship flows.
- Chapter 5 presents the results of the simulation of the nominal wake of a river cruiser under different operating conditions.
- In Chapter 6 the geometrically resolved rotating propellers are added to the numerical model. Influence of motion conditions on the thrust fluctuations and pressure pulses on the hull is analyzed.
- Finally, in Chapter 7 the results of the study are summarized and the possible directions for the future work are proposed.

¹Unsteady fluctuations of propeller forces and pressure pulses on the hull

This page intentionally left blank

Part I.

Theoretical background

Chapter 2

Mathematical model

2.1 Dynamics of incompressible Newtonian fluids

In the presented study the mathematical model of incompressible Newtonian fluid is used. Its description consists of the continuum hypothesis, the law of mass conservation and the law of momentum conservation, which are shortly described below.

2.1.1 Continuum hypothesis

The mass of a fluid or a gas is concentrated in the nuclei of atoms, of which the molecules consist and therefore is distributed nonuniformly over the volume occupied by the material. The same situation is observed also for other properties of the fluid such as velocity. However, since the fluid dynamics is concerned with the macroscopic fluid behavior, it turns out that in this case the microscopic structure of the material can be neglected. The reason for this is that the length and time scales of the molecular motion are orders of magnitude smaller than these of the fluid flow.

In kinetic theory of gases the dimensionless Knudsen number is introduced

$$Kn \equiv \frac{\lambda}{l}, \quad (2.1)$$

where l is the characteristic geometric length scale of the flow and λ is a molecule mean free path. Kn characterizes, to what extent the molecular structure and interactions are relevant for the considered problem. If $Kn \ll 1$, the fluid can be considered as a continuous matter and its macroscopic properties at a point \mathbf{x}, t are thought of as the molecular properties averaged over the volume l^{*3} , $\lambda \ll l^* \ll l$, with \mathbf{x} being the center of that volume. This way one can meaningfully talk about the “velocity at a point”, even though when considering the microscopic structure this makes no sense.

Kn for the ship hydrodynamics applications can be roughly estimated as follows. For water λ equals $2.5 \cdot 10^{-10} m$. The flow scale l should be taken equal to Kolmogorov scale

$$\eta = l_0 \cdot Re^{-3/4},$$

where Re is the Reynolds number and l_0 is the size of the largest eddies.

If one takes typical for ship flows $Re = 5 \cdot 10^8$ and l_0 , say, 1 m, one can obtain the $Kn \approx 10^{-3}$. This satisfies the discussed above constraint.

Thus in fluid mechanics the mathematical description of the moving fluid is normally done using the *continuous* functions, describing the distribution of the velocity $\mathbf{u} = \mathbf{u}(x, y, z, t)$ and any two of the thermodynamic quantities in space and time. For example, pressure $p = p(x, y, z, t)$ and density $\rho = \rho(x, y, z, t)$ [76]. Standard operations of calculus can be applied to these functions because of continuity of the latter. The continuum hypothesis is in further details discussed in [114],[10],[21].

2.1.2 Mass conservation

Let us consider a fixed subregion of a three-dimensional space, V which is filled with fluid (see Fig. 2.1). The amount of mass, which is enclosed in this volume can be represented as $\int_V \rho dV$ and its rate of change can be expressed as $\frac{\partial}{\partial t} \int_V \rho dV$. On the other hand, the amount of fluid,

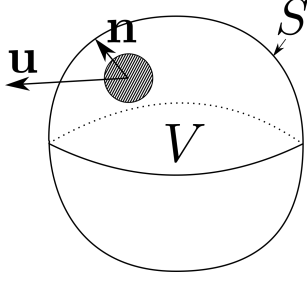


Figure 2.1: Arbitrary volume V with the boundary S , filled with fluid

leaving V through its boundary S per unit time reads $\int_S \rho \mathbf{u} \cdot \mathbf{n} dS$, where \mathbf{n} is an outward pointing normal to S . According to the principle of mass conservation, the mass is neither created nor destroyed. Expressing this statement using the integrals above, one obtains its mathematical representation:

$$\frac{\partial}{\partial t} \int_V \rho dV = - \int_S \rho \mathbf{u} \cdot \mathbf{n} dS, \quad (2.2)$$

also known as the integral form of mass conservation law. The surface integral on the right-hand side can be transformed into a volume integral by application of the Gauss' theorem:

$$\int_S \rho \mathbf{u} \cdot \mathbf{n} dS = \int_V \nabla \cdot (\rho \mathbf{u}) dV$$

This way one obtains:

$$\frac{\partial}{\partial t} \int_V \rho dV = - \int_V \nabla \cdot (\rho \mathbf{u}) dV,$$

which straightforwardly leads to:

$$\int_V \left[\frac{\partial \rho}{\partial t} + \nabla \cdot (\rho \mathbf{u}) \right] dV = 0.$$

Since the mass conservation must hold for any V , the integrand should be equal to zero, i.e.

$$\frac{\partial \rho}{\partial t} + \nabla \cdot (\rho \mathbf{u}) = 0, \quad (2.3)$$

The relation (2.3) is the differential form of the mass conservation law, also known as continuity equation. Expanding the second term on the left-hand side of (2.3), one obtains:

$$\frac{\partial \rho}{\partial t} + \mathbf{u} \cdot \nabla \rho + \rho (\nabla \cdot \mathbf{u}) = 0. \quad (2.4)$$

The first two terms in (2.4) represent the material derivative of density $\frac{D\rho}{Dt}$.

Hypothesis of incompressibility Incompressible flow is a flow, in which the material derivative of density equals zero. Application of this condition to (2.4) leads to the following equation:

$$\nabla \cdot \mathbf{u} = 0, \quad (2.5)$$

which is the continuity equation for the case of incompressible flow [23]. In tensor notation it reads:

$$\frac{\partial u_i}{\partial x_i} = 0. \quad (2.6)$$

Strictly speaking, incompressible flows do not exist. However, for some particular applications the fluid flow can be modeled to be incompressible without any considerable loss of accuracy.

Whether or not this assumption is applicable to the case of interest can be quantified by dimensionless Mach number

$$Ma \equiv \frac{U}{c},$$

where U is a characteristic speed, c - speed of sound in the considered medium. The fluid may be treated as incompressible if $Ma \ll 1$ (usually, a threshold value is 0.3) [23],[112]. Taking the maximum speed that will be considered in the present work, 6 ms^{-1} , and the speed of sound in water at 20° C , 1490 ms^{-1} , one can obtain $Ma = 0.004$, and therefore continuity equation in form (2.5) will be considered in further derivations.

It should be noted, that one should distinguish between the incompressible flow, where $\frac{\partial \rho}{\partial t} + \mathbf{u} \cdot \nabla \rho = 0$ and constant density flow, where $\rho = \text{constant}$. A constant density flow is always incompressible, but not vice versa.

2.1.3 Momentum equation

Let us again consider the same region V , filled with fluid. According to the second Newton's law, the rate of change of momentum of the portion of the fluid equals the force acting on it. As it is known [23] there are two types of forces, which can act on a volume in some medium: surface forces (normal and shear stresses, surface tension) and body forces (gravity, electromagnetic forces, inertia). The former are the forces, which act only on a boundary of the volume, whereas the latter exert a force on each fluid particle inside the volume. Let \mathcal{T} be the stress tensor in the considered medium and \mathbf{f} be the body force applied to it. Then the integral balance of momentum, following from the second Newton's law reads:

$$\frac{d}{dt} \int_V \rho \mathbf{u} dV = \int_S \mathcal{T} \cdot \mathbf{n} dS + \int_V \rho \mathbf{f} dV \quad (2.7)$$

According to the transport theorem [23] the integral on the left-hand side of the equation above can be rewritten as $\int_V \rho \frac{D\mathbf{u}}{Dt} dV$, giving:

$$\int_V \rho \left[\frac{\partial \mathbf{u}}{\partial t} + (\mathbf{u} \cdot \nabla) \mathbf{u} \right] dV = \int_S \mathcal{T} \cdot \mathbf{n} dS + \int_V \rho \mathbf{f} dV \quad (2.8)$$

Applying the Gauss theorem to the surface integral on the right-hand side of (2.8) one can obtain:

$$\int_V \rho \left[\frac{\partial \mathbf{u}}{\partial t} + (\mathbf{u} \cdot \nabla) \mathbf{u} \right] dV = \int_V [\nabla \cdot \mathcal{T} + \mathbf{f}] dV \quad (2.9)$$

Since the conservation of the linear momentum should be satisfied for any volume, the integrands on the left- and right-hand sides should be equal, giving:

$$\rho \frac{\partial \mathbf{u}}{\partial t} + \rho (\mathbf{u} \cdot \nabla) \mathbf{u} = \nabla \cdot \mathcal{T} + \rho \mathbf{f} \quad (2.10)$$

For Newtonian fluids tensor \mathcal{T} has the following form:

$$\mathcal{T} = - \left[p + \frac{2}{3} \mu (\nabla \cdot \mathbf{u}) \right] \mathbf{I} + \mu (\nabla \mathbf{u} + \nabla \mathbf{u}^T),$$

where \mathbf{I} is the identity matrix and μ is the dynamic viscosity of the fluid considered. After the application of the incompressibility constraint (2.5) this reduces to:

$$\mathcal{T} = -p \mathbf{I} + \mu (\nabla \mathbf{u} + \nabla \mathbf{u}^T), \quad (2.11)$$

Taking (2.11) into account one can write $\nabla \cdot \mathcal{T}$ as follows:

$$\nabla \cdot \mathcal{T} = -\nabla p + \nabla \cdot (\mu \nabla \mathbf{u}). \quad (2.12)$$

Insertion of (2.12) into (2.8) gives the momentum equation for the incompressible Newtonian fluid [23, 76]:

$$\rho \frac{\partial \mathbf{u}}{\partial t} + \rho(\mathbf{u} \cdot \nabla) \mathbf{u} = -\nabla p + \nabla \cdot (\mu \nabla \mathbf{u}) + \rho \mathbf{f}. \quad (2.13)$$

In the framework of the numerical solution using finite volume method the equation above is usually used in the following form: (see e.g. [36]):

$$\frac{\partial \rho \mathbf{u}}{\partial t} + \nabla \cdot (\rho \mathbf{u} \mathbf{u}) = -\nabla p + \nabla \cdot (\mu \nabla \mathbf{u}) + \rho \mathbf{f}. \quad (2.14)$$

Using the continuity equation one can show, that these two forms are equivalent.

Eq. (2.13) can be divided by ρ in order to obtain:

$$\frac{\partial \mathbf{u}}{\partial t} + (\mathbf{u} \cdot \nabla) \mathbf{u} = -\frac{\nabla p}{\rho} + \nabla \cdot (\nu \nabla \mathbf{u}) + \mathbf{f}, \quad (2.15)$$

where ν is the kinematic viscosity of the fluid, $\nu = \mu/\rho$. Eq. (2.15) is written for a vector field \mathbf{u} and represents 3 scalar equations (one for each of the velocity components). These equations are called Navier-Stokes equations for viscous incompressible fluids.

For further manipulations it is worth rewriting (2.13) in tensor notation for a Cartesian coordinate system:

$$\frac{\partial u_i}{\partial t} + \frac{\partial u_i u_j}{\partial x_j} = -\frac{1}{\rho} \frac{\partial p}{\partial x_i} + \frac{\partial}{\partial x_j} \left[\nu \left(\frac{\partial u_i}{\partial x_j} + \frac{\partial u_j}{\partial x_i} \right) \right] + f_i \quad (2.16)$$

The system, consisting of equations (2.6),(2.16) describes the motion of incompressible viscous fluids. It consists of four equations with four unknowns: p, u_x, u_y, u_z .

2.1.4 Boundary and initial conditions

In order to obtain a determined solution of (2.6), (2.16) one has to specify boundary and initial conditions for the unknowns.

Let us consider a part of the boundary S and discuss the conditions for \mathbf{u} . If the value of the velocity on S is known (e.g. inflow) the Dirichlet boundary condition is imposed:

1. On the walls the fluid velocity coincides with the wall velocity (no slip and no penetration condition): $\mathbf{u}|_S = \mathbf{u}_{wall}$. For fixed walls this gives $\mathbf{u}|_S = 0$.
2. For the inflow boundary the condition is $\mathbf{u}|_S = \mathbf{u}_s(\mathbf{x}, t)$, where \mathbf{u}_s is the velocity of the incoming fluid.

On the truncation boundaries (e.g. outflow), a Neumann condition for velocity $\frac{\partial \mathbf{u}}{\partial n}|_S = 0$ is usually set. For the outflow this condition is satisfactory only if the flow is not changing rapidly in time, otherwise the convective boundary condition is preferred (e.g. in LES) [36]:

$$\left(\frac{\partial \mathbf{u}}{\partial t} + U \frac{\partial \mathbf{u}}{\partial n} \right) \Big|_S = 0 \quad (2.17)$$

Here U is a constant outflow velocity, independent of the location, chosen in such a way, that the overall conservation is not violated.

It should be noted, that even though the system (2.6),(2.16) contains also pressure as the unknown quantity, boundary conditions for the pressure are not imposed [115]. The reason for this is that pressure in an incompressible flow is a Lagrange multiplier, which should guarantee the mass conservation. Simply put, the pressure should be found in such a way, that its gradient, substituted into the momentum equation would force the solution of (2.16) to be solenoidal [115,

36, 121].

The initial condition for the velocity field simply specifies the distribution of the velocity at $t = 0$: $\mathbf{u}|_{t=0} = \mathbf{u}_0(\mathbf{x})$. The function \mathbf{u}_0 is assumed to be solenoidal ($\nabla \cdot \mathbf{u}_0 = 0$). Additionally, the initial and boundary conditions, set for the incompressible Navier-Stokes system, must satisfy the compatibility constraint $\mathbf{n} \cdot \mathbf{u}_s(\mathbf{x}, 0) = \mathbf{n} \cdot \mathbf{u}_0(\mathbf{x})$ [115].

2.1.5 Well-posedness of the problem

Additional remarks should be given regarding the well-posedness of the system (2.6), (2.16). According to the definition, a PDE problem is said to be well-posed if [31]:

1. a solution to the problem exists
2. the solution is unique
3. the solution depends continuously on data given in the problem.

The existence and uniqueness of the classical solution [31] to (2.6), (2.16) has been so far proven only for a certain time interval ($t < \infty$) and only for the smooth IBVP. In this case the solution is proven to be continuously dependent on the problem data [75]. However, regarding the infinite time and general three-dimensional case, no results regarding the existence of the classical solution have been obtained. The proof of existence and smoothness of solution to (2.6), (2.16) for all $t \geq 0$ is one of the Millennium Prize problems, stated by the Clay Mathematics Institute in 2000 [35]. Concerning the weak solution [31] Hopf showed, that there exists at least one such solution defined for all $t \geq 0$, which has a finite energetic norm [163]. But strictly speaking the well-posedness of the formulated IBVP still remains an open question.

2.1.6 Pressure equation

One can notice that even though the pressure gradient is present in the momentum equation, no equation for obtaining p is given explicitly in the system (2.6), (2.16). And therefore the way of determining the pressure is not quite clear. This fact triggered the attempts to reformulate the system and derive the equation for the pressure. Taking the divergence of (2.16) and substituting it into (2.6), one can obtain the Poisson equation for pressure (PPE):

$$\Delta p = -\rho \frac{\partial u_i}{\partial x_j} \frac{\partial u_j}{\partial x_i} \quad (2.18)$$

Given a velocity field that satisfies the continuity equation one can find the pressure by solving (2.18) with the boundary condition $\frac{\partial p}{\partial n} = \mu \frac{\partial^2 \mathbf{u}}{\partial n^2}$. Therefore, pressure gradient turns out to be dependent only on the current velocity field irrespective of the flow history [114].

2.2 Turbulence and its modeling

2.2.1 Laminar and turbulent flows

It is known, that there are two qualitatively different regimes of a fluid flow: laminar, in which the fluid particles move along the ordered parallel trajectories, and turbulent, in which there exists a chaotic distribution of vorticity and the fluid motion is essentially irregular. Flows become turbulent at high Reynolds numbers:

$$Re = \frac{UL}{\nu}, \quad (2.19)$$

where U, L are characteristic velocity and length of the considered problem respectively and ν is the kinematic viscosity.

Since turbulence occurs in the vast majority of flows in nature and in engineering applications, it is considered a very important physical phenomenon. Therefore the mathematical

description and simulation of turbulence are of a high practical and theoretical relevance.

A characteristic property of a turbulent flow are the chaotic fluctuations of velocity and its practical unpredictability for the infinite interval of time. The described above mathematical model (Navier-Stokes equations) in theory can describe the motion of viscous incompressible fluids in any regimes, may it be laminar or turbulent, because no specific assumptions related to the flow regimes were done. There are, however, multiple reasons, why this equation cannot be directly used for practical purposes. These reasons are related to the properties of the Navier-Stokes equations.

As can be seen, the system (2.6), (2.16) contains a nonlinear convective term $\frac{\partial u_i u_j}{\partial x_j}$. Lorenz showed, that even a simplest deterministic system of ordinary differential equations under particular conditions can show a chaotic behavior in sense that the solution of such system can be strongly dependent on the initial conditions. As a consequence even a smallest perturbation of the IC can cause a considerable change of the resulting solution starting from some time instant [88]. Thus it turns out that even though the system of equations is deterministic, its solution may be unpredictable. This phenomenon is called the deterministic chaos [130]. Turbulent flows show analogous behavior because of the nonlinearity of the convection term. For this reason it is senseless to consider the pressure and velocity fields (as well as other properties) in a turbulent flow as deterministic quantities. And in practice usually these are considered as random fields and are treated statistically. On the contrary to the instantaneous velocity $\mathbf{u}(\mathbf{x}, t)$, the time-averaged velocity values $\bar{\mathbf{u}}(\mathbf{x})$ are stable, which means that the minute change in IC will lead to a small deviation of the outcome [27].

Because of the convective term the analytic solutions of the Navier-Stokes equations cannot in general be obtained using available mathematical tools (there are, however solutions for some special cases). Therefore one has to rely on numerical methods (i.e. CFD) for obtaining the solution for a given IBVP. Turbulence is a multi-scale phenomenon [125] and in order to make a reliable simulation of a turbulent flow using the eqs. (2.6), (2.16) “as is” all scales of fluid motion should be resolved. This simulation approach is called Direct Numerical Simulation (DNS) and is not widely applied nowadays due to the fact, that the size of the smallest scales of motion is dependent on Re , so that the computational cost scales with Re^3 [114]. In order to make (2.6), (2.16) applicable for flow at high Re , additional manipulations (averaging, filtering) should be performed. The sense of these operations is the separation of different scales of motion one from another, so as to account for the influence of these scales on the flow differently [125].

2.2.2 Reynolds averaged Navier-Stokes equations

The most widely used method for solving the above listed problems is the Reynolds averaging. In 1895 Reynolds proposed to apply the time averaging operation to Navier-Stokes equations in order to derive the evolution equation for the time-averaged flow properties instead of their instantaneous counterparts.

The flow properties (pressure, velocity, etc.) are decomposed into the fluctuating and the mean components. For a general property ϕ in a turbulent flow the Reynolds decomposition reads:

$$\phi(\mathbf{x}, t) = \bar{\phi}(\mathbf{x}, t) + \phi'(\mathbf{x}, t) \quad (2.20)$$

The averaging operation over time period T is introduced as follows:

$$\bar{\phi}(\mathbf{x}, t) = \frac{1}{T} \int_t^{t+T} \phi(\mathbf{x}, t^*) dt^*, \quad (2.21)$$

where T is assumed to be at least an order of magnitude larger than the characteristic time scale of turbulent fluctuations in the considered flow T_1 and at the same time smaller than that of the large scale unsteadiness T_2 . It is straightforward to prove, that this operation obeys the

following rules [161]:

$$\overline{\phi(\mathbf{x})} = \overline{\phi}(\mathbf{x}) \quad (2.22)$$

$$\overline{\phi'(\mathbf{x}, t)} = 0 \quad (2.23)$$

$$\overline{\phi_1 + \phi_2} = \overline{\phi_1} + \overline{\phi_2} \quad (2.24)$$

$$\overline{\frac{\partial \phi}{\partial x}} = \frac{\partial \overline{\phi}}{\partial x} \quad (2.25)$$

$$\overline{\frac{\partial \phi}{\partial t}} = \frac{\partial \overline{\phi}}{\partial t} \quad (2.26)$$

After substituting (2.20) into the momentum and continuity equations and applying the averaging operation, one obtains the Unsteady Reynolds Averaged Navier-Stokes Equations (URANSE), accompanied by the time-averaged continuity constraint:

$$\frac{\partial \overline{u_i}}{\partial t} + \overline{u_j} \frac{\partial \overline{u_i}}{\partial x_j} + \frac{1}{\rho} \frac{\partial \overline{p}}{\partial x_i} = \frac{\partial}{\partial x_j} \left[\nu \left(\frac{\partial \overline{u_i}}{\partial x_j} + \frac{\partial \overline{u_j}}{\partial x_i} \right) - \overline{u'_i u'_j} \right] + \overline{f_i} \quad (2.27)$$

$$\frac{\partial \overline{u_i}}{\partial x_i} = 0 \quad (2.28)$$

Sometimes (2.27) are also referred to as Reynolds equations. For the case when period of averaging tends to infinity, the time derivative in the momentum equation vanishes and the method is referred to as RANS. It can be noticed that after the manipulations, made with the momentum equations, additional unknown terms $\tau_{ij}^t = \overline{u'_i u'_j}$ appeared on the right hand side of (2.27) as a result of averaging of the convection term. These terms form the so-called Reynolds' stress tensor ¹:

$$\tau_{ij}^t = \begin{pmatrix} \overline{u'_x u'_x} & \overline{u'_x u'_y} & \overline{u'_x u'_z} \\ \overline{u'_y u'_x} & \overline{u'_y u'_y} & \overline{u'_y u'_z} \\ \overline{u'_z u'_x} & \overline{u'_z u'_y} & \overline{u'_z u'_z} \end{pmatrix}, \quad (2.29)$$

representing the correlations between the fluctuations of different velocity components. Since the tensor is symmetric, only six unknowns were added after averaging. However, no additional equations were obtained, hence the problem has become underdetermined. Therefore one has to append the system with extra equations so as to attain the determined solution. The ways of closure of the constructed system will be discussed in the following subsections.

2.2.3 Reynolds Stress Transport Equations

In attempt to derive the equations for the recently obtained unknowns τ_{ij}^t additional statistical moments of (2.16) are taken into consideration. If one defines the Navier-Stokes operator as

$$N(u_i) \equiv \frac{\partial u_i}{\partial t} + u_j \frac{\partial u_i}{\partial x_j} + \frac{1}{\rho} \frac{\partial p}{\partial x_i} - \nu \frac{\partial^2 u_i}{\partial x_i^2}, \quad (2.30)$$

(2.16) can be rewritten as $N(u_i) = 0$. For the derivation of (U)RANSE $\overline{N(u_i)}$ was analyzed. Now so as to produce additional relations for τ_{ij}^t , the following second moment will be derived:

$$\overline{u'_i N(u_j) + u'_j N(u_i)} = 0,$$

¹Strictly speaking the Reynolds stresses are $\rho \tau_{ij}^t$, only then they have the dimensions of stress (Pa). But it is conventional to refer to τ_{ij}^t as the Reynolds stresses [114].

which after some manipulations gives [161]:

$$\frac{\partial \tau_{ij}^t}{\partial t} + \bar{u}_k \frac{\partial \tau_{ij}^t}{\partial x_k} = -\tau_{ik}^t \frac{\partial \bar{u}_j}{\partial x_k} - \tau_{jk}^t \frac{\partial \bar{u}_i}{\partial x_k} - \epsilon_{ij} + \Pi_{ij} - \frac{\partial}{\partial x_k} \left[\nu \frac{\partial \tau_{ij}^t}{\partial x_k} + C_{ijk} \right], \quad (2.31)$$

where

$$\Pi_{ij} = \frac{1}{\rho} p' \left(\frac{\partial u'_i}{\partial x_j} + \frac{\partial u'_j}{\partial x_i} \right) \quad (2.32)$$

$$\epsilon_{ij} = 2\nu \frac{\partial u'_i}{\partial x_k} \frac{\partial u'_j}{\partial x_k} \quad (2.33)$$

$$C_{ijk} = \overline{u'_i u'_j u'_k} + \frac{1}{\rho} (\overline{p' u'_i \delta_{jk}} + \overline{p' u'_j \delta_{ik}}) \quad (2.34)$$

This way additional six equations are derived, but along with them twenty two new unknowns are produced: $\overline{u'_i u'_j u'_k}$, $2\nu \frac{\partial u'_i}{\partial x_k} \frac{\partial u'_j}{\partial x_k}$, $p' \left(\frac{\partial u'_i}{\partial x_j} + \frac{\partial u'_j}{\partial x_i} \right)$, $(\overline{p' u'_i \delta_{jk}} + \overline{p' u'_j \delta_{ik}})$ [161]. One can consider the moments of higher order, but this would produce further unknown quantities, so that after the manipulations performed the system will still remain underdetermined. This way an infinite system of differential equations can be constructed (Friedmann-Keller chain), which is the complete analytic description of the problem of turbulence. Unfortunately, it turns out that any finite subsystem of this system is not closed [105, 154]. Hence it is theoretically impossible to construct a practically applicable analytic closure. This fact led to the involvement of empiricism into the (U)RANSE turbulence modeling methods.

Using empirical data and various simplifications different authors propose different approximations for the unknown correlations in (2.31). Examples of the closures can be found in [78, 145, 91]. After complementing the system with these relations it becomes determined, so that the Reynolds stresses τ_{ij}^t can be obtained from the solution of (2.31) and then can be used in (2.27) (the coupling is done in an iterative manner). This class of closure models is called RSTM. Among all the RANSE models this approach is the most accurate as well as the most time-consuming.

Under the weak equilibrium assumption [50], differential equations (2.31) can be reduced to a system of nonlinear algebraic equations giving an ARSM. The solution of the latter should be found by iterative techniques. Unluckily, the iterative process sometimes converges to the nonphysical roots and therefore a lot of attempts have been made to obtain an explicit solution. Methods, which are based on the explicit solutions of the simplified system (2.31) are called EARSM.

It should be mentioned that the use of empiricism makes the accuracy of (U)RANSE predictions case-dependent which is the main drawback of the approach.

2.2.4 Turbulent viscosity and gradient diffusion assumptions

The most popular and widely applied RANS turbulence models are based on the Boussinesq approximation. Within this class of models it is assumed that the Reynolds stress tensor can be expressed in terms of turbulent eddy viscosity ν_t and the averaged strain rate tensor $\bar{S}_{ij} = (\frac{\partial \bar{u}_i}{\partial x_j} + \frac{\partial \bar{u}_j}{\partial x_i})/2 = (\nabla \bar{\mathbf{u}} + (\nabla \bar{\mathbf{u}})^T)/2$:

$$-\tau_{ij}^t = 2\nu_t \bar{S}_{ij} - \frac{2}{3} k \delta_{ij} \quad (2.35)$$

Here k is the turbulence kinetic energy which will be defined later and μ_t is obtained from the turbulence models of different level of complexity (algebraic, differential). The methods of determining ν_t will be presented in the next sections. The assumption (2.35), called turbulent viscosity assumption has a lot of limitations. Pope [114] clearly demonstrates some situations,

when this relation fails to reproduce τ_{ij}^t properly. For instance one of the necessary conditions of applicability of (2.35) is the production to dissipation equilibrium ($\mathcal{P}/\epsilon \approx 1$). By using (2.35) the Reynolds equation can be written as follows:

$$\frac{\partial \bar{u}_i}{\partial t} + \bar{u}_j \frac{\partial \bar{u}_i}{\partial x_j} + \frac{1}{\rho} \frac{\partial \bar{p}^*}{\partial x_i} = \frac{\partial}{\partial x_j} \left[(\nu + \nu_t) \left(\frac{\partial \bar{u}_i}{\partial x_j} + \frac{\partial \bar{u}_j}{\partial x_i} \right) \right] + \bar{f}_i \quad (2.36)$$

The term $-\frac{2}{3}k\delta_{ij}$ is absorbed into the the modified pressure $\bar{p}^* = \bar{p} + \frac{2}{3}k\delta_{ij}$. Analogous to turbulent viscosity assumption, gradient diffusion hypothesis allows to represent the turbulent transport of quantity ϕ in terms of turbulent eddy viscosity, turbulent Prandtl-Schmidt number σ_ϕ and the gradient of the averaged scalar field ϕ :

$$\overline{u'_j \phi} = -\frac{\nu_t}{\sigma_\phi} \frac{\partial \bar{\phi}}{\partial x_j}$$

2.2.5 Turbulence kinetic energy equation

The turbulence kinetic energy (TKE) is defined as:

$$k \equiv \frac{1}{2} \overline{u'_i u'_i} = \frac{1}{2} (\overline{u'^2_x} + \overline{u'^2_y} + \overline{u'^2_z}). \quad (2.37)$$

TKE represents the mean kinetic energy of the fluctuating motion per unit mass. It is possible to derive a transport equation for k by the contraction of (2.31). Summing up the equations for $i = j$ and multiplying by 1/2 one obtains:

$$\frac{\partial k}{\partial t} + \bar{u}_j \frac{\partial k}{\partial x_j} = \mathcal{P}_k - \epsilon_s + \frac{\partial}{\partial x_j} \mathcal{D}_k, \quad (2.38)$$

where

$$\mathcal{D}_k = -\frac{1}{2} \overline{u'_i u'_i u'_j} - \frac{1}{\rho} \delta_{jk} \overline{p' u'_j} + \nu \frac{\partial k}{\partial x_j},$$

$$\mathcal{P}_k = -\overline{u'_i u'_j} \frac{\partial \bar{u}_i}{\partial x_j},$$

$$\epsilon_s = \nu \frac{\partial u'_i}{\partial x_j} \frac{\partial u'_i}{\partial x_j}.$$

\mathcal{D}_k represents the diffusion of turbulence energy, consisting of molecular diffusion ($\nu \frac{\partial k}{\partial x_j}$), turbulent transport ($-\frac{1}{2} \overline{u'_i u'_i u'_j}$) and pressure diffusion ($-\frac{1}{\rho} \overline{p' u'_j}$). \mathcal{P}_k is the production of turbulence energy, reflecting the transition of energy from the mean flow to the fluctuating motion. Finally, ϵ_s is called an isotropic or pseudo dissipation rate of turbulence energy, it is the rate at which the energy of velocity fluctuations is transformed into internal energy of the fluid. Pseudo-dissipation rate is distinct from the true dissipation rate ϵ :

$$\epsilon = \epsilon_s + \nu \frac{\partial^2 \overline{u'_i u'_j}}{\partial x_i \partial x_j}$$

However, the second term on the r.h.s is usually very small [114] and therefore can be neglected, so that in the following the pseudodissipation is used instead of true dissipation.

2.2.6 Equation for the isotropic dissipation rate

Isotropic turbulence dissipation rate is defined as:

$$\epsilon_s \equiv \nu \frac{\partial u'_i}{\partial x_j} \frac{\partial u'_i}{\partial x_j}. \quad (2.39)$$

Equation for ϵ_s can be obtained by taking the moment $2\nu \overline{\frac{\partial u'_i}{\partial x_j} \frac{\partial}{\partial x_j} N(u_i)}$ of Navier-Stokes equations, which yields [161, 144]:

$$\frac{\partial \epsilon_s}{\partial t} + \bar{u}_j \frac{\partial \epsilon_s}{\partial x_j} = \frac{\partial}{\partial x_j} \mathcal{D}_\epsilon + \mathcal{P}_\epsilon - \epsilon_\epsilon, \quad (2.40)$$

where

$$\mathcal{D}_\epsilon = \nu \frac{\partial \epsilon_s}{\partial x_j} - \nu \overline{u'_j \frac{\partial u'_i}{\partial x_k} \frac{\partial u'_i}{\partial x_k}} - 2 \frac{\nu}{\rho} \overline{\delta_{ij} \frac{\partial u'_j}{\partial x_k} \frac{\partial p'}{\partial x_k}}$$

represents the diffusion of dissipation, consisting of molecular diffusion, diffusion due to turbulent mixing and diffusion due to pressure fluctuations,

$$\mathcal{P}_\epsilon = -2\nu \overline{u'_j \frac{\partial u'_i}{\partial x_k} \frac{\partial^2 \bar{u}_i}{\partial x_j \partial x_k}} - 2\nu \left(\overline{\frac{\partial u'_i}{\partial x_k} \frac{\partial u'_j}{\partial x_k} \frac{\partial \bar{u}_i}{\partial x_j}} + \overline{\frac{\partial u'_i}{\partial x_j} \frac{\partial u'_i}{\partial x_k} \frac{\partial \bar{u}_j}{\partial x_k}} \right) - 2\nu \overline{\frac{\partial u'_i}{\partial x_j} \frac{\partial u'_j}{\partial x_k} \frac{\partial \bar{u}_i}{\partial x_k}}$$

is the generation of the dissipation, where the first and second term express the generation due to turbulent mixing in the average motion and the last one - in the fluctuating motion. Finally,

$$\epsilon_\epsilon = 2\nu^2 \overline{\frac{\partial^2 u'_i}{\partial x_j \partial x_k} \frac{\partial^2 u'_i}{\partial x_j \partial x_k}} \quad (2.41)$$

is called the destruction of the dissipation.

2.2.7 The $k - \epsilon$ turbulence model

The equations (2.38),(2.40) contain unknown terms, which due to the closure problem of turbulence cannot be found analytically and therefore should be modeled. Different ways of modeling of the correlations result in different versions of the transport equations for k and ϵ . In this work only the “standard” $k - \epsilon$ model of Launder [79] will be described:

- using the Boussinesq approximation production term is transformed as follows:

$$\begin{aligned} \mathcal{P}_k &= -\tau_{ij}^t \frac{\partial \bar{u}_i}{\partial x_j} \stackrel{(2.35)}{=} (2\nu_t \bar{S}_{ij} - \frac{2}{3} k \delta_{ij}) \frac{\partial \bar{u}_i}{\partial x_j} \stackrel{(2.6)}{=} \\ &= 2\nu_t \bar{S}_{ij} (\bar{S}_{ij} + \bar{\Omega}_{ij}) \stackrel{\bar{S}_{ij} \bar{\Omega}_{ij}=0}{=} 2\nu_t \bar{S}_{ij} \bar{S}_{ij} \end{aligned} \quad (2.42)$$

In the further derivations only the short designation \mathcal{P}_k will be used.

- for the first term in \mathcal{D}_k the gradient diffusion assumption is utilized, whereas the second one is usually neglected [144]. This gives:

$$\mathcal{D}_k = \left(\nu + \frac{\nu_t}{\sigma_k} \right) \frac{\partial k}{\partial x_j},$$

- the turbulent Prandtl-Schmidt number is taken to be $\sigma_k = 1$.

For (2.40) the following simplifications are made:

- analogous to \mathcal{D}_k in the equation (2.38), \mathcal{D}_ϵ is modeled using the gradient transport hypothesis:

$$\mathcal{D}_\epsilon = \left(\nu + \frac{\nu_t}{\sigma_\epsilon} \right) \frac{\partial \epsilon}{\partial x_j}$$

with $\sigma_\epsilon = 1.3$

- for the production term the following approximation is used

$$\mathcal{P}_\epsilon = C_{\epsilon 1} \frac{\epsilon}{k} \mathcal{P}_k$$

- the destruction of dissipation reads:

$$\epsilon_\epsilon = C_{\epsilon 2} \frac{\epsilon^2}{k}$$

The detailed reasoning of the manipulations undertaken with (2.38),(2.40) can be found, for example, in the review article of Speziale [144]. After all the transformations done with original k and ϵ equations one obtains:

$$\frac{\partial k}{\partial t} + \bar{u}_j \frac{\partial k}{\partial x_j} = \frac{\partial}{\partial x_j} \left[\left(\nu + \frac{\nu_t}{\sigma_k} \right) \frac{\partial k}{\partial x_j} \right] + \mathcal{P}_k - \epsilon_s \quad (2.43)$$

$$\frac{\partial \epsilon_s}{\partial t} + \bar{u}_j \frac{\partial \epsilon_s}{\partial x_j} = \frac{\partial}{\partial x_j} \left[\left(\nu + \frac{\nu_t}{\sigma_\epsilon} \right) \frac{\partial \epsilon_s}{\partial x_j} \right] + C_{\epsilon 1} \frac{\epsilon_s}{k} \mathcal{P}_k - C_{\epsilon 2} \frac{\epsilon_s^2}{k} \quad (2.44)$$

$$\nu_t = C_\mu \frac{k^2}{\epsilon_s} \quad (2.45)$$

The values of the closure coefficients are the following: $\sigma_k = 1$, $\sigma_\epsilon = 1.3$, $C_{\epsilon 1} = 1.44$, $C_{\epsilon 2} = 1.92$, $C_\mu = 0.09$. These numbers were obtained by the fine-tuning of the model predictions for the turbulent boundary layer and the decay of isotropic turbulence [144]. The model performance for specific flows can be tuned by adjusting the model constants $C_{\epsilon 1}$, $C_{\epsilon 2}$ [114].

A very important issue associated with the standard $k - \epsilon$ model is that it cannot be integrated to a wall without the application of additional damping or wall functions. The reason for this is that ϵ_s is non-zero at the wall, whereas k is zero, which yields $\frac{\epsilon}{k} \rightarrow \infty$ near the wall.

2.2.8 The $k - \omega$ turbulence model

The other choice of scale-determining variables was proposed independently by Kolmogorov (1942) and Saffman (1970). Instead of using the transport equation for the dissipation rate ϵ , they proposed to use the equation for the specific dissipation rate ω . Many versions of the closure were created but only the most popular of them will be discussed in the present work - the one proposed by Wilcox [160].

The model equations read:

$$\frac{\partial k}{\partial t} + \bar{u}_j \frac{\partial k}{\partial x_j} = \frac{\partial}{\partial x_j} \left[\left(\nu + \frac{\nu_t}{\sigma_k} \right) \frac{\partial k}{\partial x_j} \right] + \mathcal{P}_k - \beta^* \omega k \quad (2.46)$$

$$\frac{\partial \omega}{\partial t} + \bar{u}_j \frac{\partial \omega}{\partial x_j} = \frac{\partial}{\partial x_j} \left[\left(\nu + \frac{\nu_t}{\sigma_\omega} \right) \frac{\partial \omega}{\partial x_j} \right] + \gamma_1 \frac{\omega}{k} \mathcal{P}_k - \beta_1 \omega^2 \quad (2.47)$$

$$\nu_t = \frac{k}{\omega}, \quad (2.48)$$

where the closure coefficients are: $\sigma_k = 2.0$, $\sigma_\omega = 2.0$, $\gamma_1 = 5/9$, $\beta_1 = 3/40$, $\beta^* = 9/100$. In his paper Wilcox [160] argues, that the proposed model is more accurate for the flows with adverse pressure gradient, than the $k - \epsilon$ model of Launder. In addition, the system (2.46),(2.47) can be integrated through the viscous sublayer without introduction of wall damping or use of wall functions.

Among the drawbacks of the model of Wilcox is the sensitivity of the solution to the freestream values of ω and poor performance for the free shear flows.

2.2.9 The $k - \omega$ SST turbulence model

After the analysis of the performance of $k - \epsilon$ model of Launder and $k - \omega$ model of Wilcox and their advantages and disadvantages Menter [96] noted, that the $k - \epsilon$ model is favorable in the wake regions and free shear layers and does not possess the strong sensitivity to the freestream values, whereas the $k - \omega$ model shows better performance in the logarithmic and viscous parts of the boundary layer. Due to this fact, Menter proposed to blend the two closures in order to use

each of them in the region, where it shows the best accuracy. The blended model is constructed in the following way (the version SST2003 in NASA classification is presented [99]).

The Wilcox's model is used with a slight reformulation of production term in ω -equation:

$$\frac{\partial k}{\partial t} + \bar{u}_j \frac{\partial k}{\partial x_j} = \frac{\partial}{\partial x_j} \left[(\nu + \sigma_{k1} \nu_t) \frac{\partial k}{\partial x_j} \right] + \mathcal{P}_k - \beta^* \omega k \quad (2.49)$$

$$\frac{\partial \omega}{\partial t} + \bar{u}_j \frac{\partial \omega}{\partial x_j} = \frac{\partial}{\partial x_j} \left[(\nu + \sigma_{\omega 1} \nu_t) \frac{\partial \omega}{\partial x_j} \right] + \frac{\gamma_1}{\nu_t} \mathcal{P}_k - \beta_1 \omega^2 \quad (2.50)$$

The governing equation system of $k - \epsilon$ model (2.143),(2.144) is rewritten for $k - \omega$ variables by substituting the formula $\epsilon = \beta^* \omega k$ into the ϵ -equation [114], which gives:

$$\frac{\partial k}{\partial t} + \bar{u}_j \frac{\partial k}{\partial x_j} = \frac{\partial}{\partial x_j} \left[(\nu + \sigma_{k2} \nu_t) \frac{\partial k}{\partial x_j} \right] + \mathcal{P}_k - \beta^* \omega k \quad (2.51)$$

$$\frac{\partial \omega}{\partial t} + \bar{u}_j \frac{\partial \omega}{\partial x_j} = \frac{\partial}{\partial x_j} \left[(\nu + \sigma_{\omega 2} \nu_t) \frac{\partial \omega}{\partial x_j} \right] + \frac{\gamma_2}{\nu_t} \mathcal{P}_k - \beta_2 \omega^2 + 2\sigma_{\omega 2} \frac{1}{\omega} \frac{\partial k}{\partial x_j} \frac{\partial \omega}{\partial x_j} \quad (2.52)$$

Subsequently a blending function F_1 is introduced. The equations (2.49),(2.50) are multiplied by F_1 and (2.51),(2.52) by $1 - F_1$ and after that the k -equations and the ω -equations of both systems are summed up, resulting in:

$$\frac{\partial k}{\partial t} + \bar{u}_j \frac{\partial k}{\partial x_j} = \frac{\partial}{\partial x_j} \left[(\nu + \sigma_k \nu_t) \frac{\partial k}{\partial x_j} \right] + \mathcal{P}_k - \beta^* \omega k \quad (2.53)$$

$$\frac{\partial \omega}{\partial t} + \bar{u}_j \frac{\partial \omega}{\partial x_j} = \frac{\partial}{\partial x_j} \left[(\nu + \sigma_\omega \nu_t) \frac{\partial \omega}{\partial x_j} \right] + \frac{\gamma}{\nu_t} \mathcal{P}_k - \beta_2 \omega^2 + 2(1 - F_1) \sigma_{\omega 2} \frac{1}{\omega} \frac{\partial k}{\partial x_j} \frac{\partial \omega}{\partial x_j}, \quad (2.54)$$

where the constants (σ_k, \dots) represent a blending between those of Wilcox model (index "1") and standard $k - \epsilon$ (index "2") in the form:

$$C = C_1 F_1 + C_2 (1 - F_1).$$

The constants of the first set are:

$$\begin{aligned} \sigma_{k1} &= 0.85, \quad \sigma_{\omega 1} = 0.5, \quad \beta_1 = 0.0750 \\ \beta^* &= 0.09, \quad \kappa = 0.41, \quad \gamma_1 = \beta_1 / \beta^* - \sigma_{\omega 1} \kappa^2 / \sqrt{\beta^*} \end{aligned} \quad (2.55)$$

and of the second one:

$$\begin{aligned} \sigma_{k2} &= 1.0, \quad \sigma_{\omega 2} = 0.856, \quad \beta_2 = 0.0828 \\ \beta^* &= 0.09, \quad \kappa = 0.41, \quad \gamma_2 = \beta_2 / \beta^* - \sigma_{\omega 2} \kappa^2 / \sqrt{\beta^*} \end{aligned} \quad (2.56)$$

The turbulent viscosity is calculated as:

$$\nu_t = \frac{a_1 k}{\max(a_1 \omega; S F_2)}, \quad (2.57)$$

where S is the magnitude of the strain-rate tensor and $a_1 = 0.3$. This formula guarantees, that in the adverse pressure gradient boundary layers the Reynolds stress τ_{xy}^t will be proportional to the turbulent kinetic energy $\tau_{xy}^t = a_1 k$ (Bradshaw's assumption). Such definition of ν_t helps in avoiding the overprediction of τ_{xy}^t for the mentioned regions of the flow [96]. The blending functions F_1 and F_2 are defined as follows:

$$F_1 = \tanh(arg_1^4), \quad (2.58)$$

$$arg_1 = \min \left[\max \left(\frac{\sqrt{k}}{0.09 \omega y}; \frac{500 \nu}{y^2 \omega} \right); \frac{4 \sigma_{\omega 2} k}{C D_{k\omega} y^2} \right], \quad (2.59)$$

$$F_2 = \tanh(arg_2^2), \quad (2.60)$$

$$arg_2 = \max \left(\frac{2\sqrt{k}}{0.09\omega y}, \frac{500\nu}{y^2\omega} \right), \quad (2.61)$$

where y is the distance from the wall and $CD_{k\omega}$ is:

$$CD_{k\omega} = \max \left(2\rho\sigma_{\omega 2} \frac{1}{\omega} \frac{\partial k}{\partial x_j} \frac{\partial \omega}{\partial x_j}, 10^{-10} \right). \quad (2.62)$$

The functions are designed such that close to the wall the application of Wilcox's model is guaranteed and away from the wall - the application of $k - \epsilon$ model. Additionally, a so called production limiter is added to the model in order to avoid the nonphysical growth of the eddy-viscosity due to jumps in the strain-rate tensor [97], so that \mathcal{P}_k in (2.53),(2.54) is replaced by

$$\tilde{\mathcal{P}}_k = \min(\mathcal{P}_k, 10 \cdot \beta^* k \omega). \quad (2.63)$$

It should be mentioned, that at the moment the $k - \omega$ SST model is one of the standard RANSE closure models used for the industrial applications and it is represented in the vast majority of CFD software packages because of its good performance for the adverse pressure gradient flows.

2.2.10 Applicability of RANSE turbulence models

The main drawback of all RANSE turbulence models is the dependence on the empirical data and theoretical assumptions which are not generally valid. The calibration of model constants is done based on the experimental data available for the flows in question. This means, that one has to first validate the model for some particular application before relying on it, since the assumptions done may not be applicable under considered conditions. This drawback stems from closure problem of turbulence and cannot be avoided. Therefore, even the most complex RSTM model suffer from the same problem.

The second problem of RANSE models is the prediction of considerably unsteady flows. In Section 2.2.2 it was assumed that the averaging period T is larger than the time period of turbulent fluctuations and at the same time shorter than the time period of the large-scale unsteadiness. Put another way it is assumed that there is a "spectral gap" between the turbulent fluctuations and large-scale instabilities and no interaction between them [125]. When the flow unsteadiness is implied by the boundary conditions this assumption holds. However, when the flow instabilities come from inside of the flow (e.g. boundary layer separations), neglect of the interaction between the resolved and modeled scales can introduce errors in the results.

According to Spalart [141], RANS models can be used to predict the growth and separation of the boundary layers with acceptable accuracy, whereas the correct modeling of the momentum transport after the flow separation is a much more challenging problem. RSTM models are the best what RANS approach can provide, but even they cannot give the desired accuracy for a wide range of separated flows.

A good alternative to URANS for the prediction of momentum transport after separation is the LES.

2.2.11 Large-Eddy Simulation

On the contrary to (U)RANSE method, which models the influence of turbulent motions on the mean flow, the LES is intended to resolve a major portion of turbulent energy ($\geq 80\%$) and to model only the rest [114]. Since the macroscopic parameters of the flow are mostly dependent on the large-scale energy-containing structures, LES generally provides more realistic results compared to RANS and needs less tuneup. LES allows for gaining a deeper insight into the flow structure, including the information about the unsteady coherent structures, turbulence spectrum, unsteady fluctuations of forces and moments (see, for example [157]).

The concept of LES will be briefly explained in the following subsections.

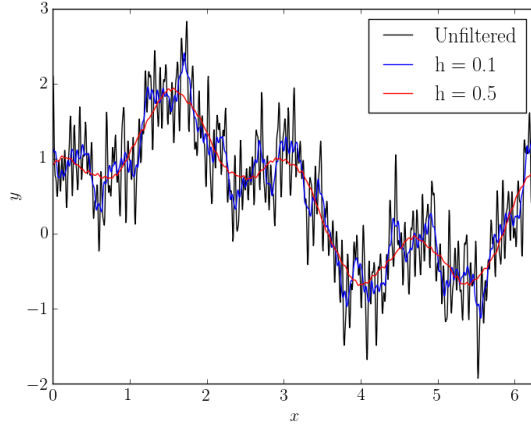


Figure 2.2: Random signal $y = f(x)$, filtered using top-hat filter with different filter widths h

2.2.12 Filtering

The separation of the scales, which are to be resolved on the mesh from those which are to be modeled is done by the application of low-pass filtering operation to the momentum and continuity equations (2.6),(2.16). The filtering operation is defined as:

$$\tilde{\phi}(\mathbf{x}, t) = \int_V G(\mathbf{r}, \mathbf{x}) \phi(\mathbf{x} - \mathbf{r}, t) d\mathbf{r}, \quad (2.64)$$

where $G(\mathbf{r}, \mathbf{x})$ is a filter function, V is the flow domain. The operation presented above is a convolution of the field ϕ with the filter, which effects in (roughly speaking) the removal of the length scales which are smaller than the filter width from the input signal. An example of filter application to a random harmonic function is shown in Figure 2.2. The function G has to be defined such, that

$$\int_V G(\mathbf{r}, \mathbf{x}) d\mathbf{r} = 1 \quad (2.65)$$

and should be independent of \mathbf{x} .

The most widely used filtering kernels are: top-hat (has compact support in real space), Gaussian and sharp cutoff (has compact support in wave number space) [114], [125], their description is given in Table 2.1. Compared to the earlier introduced Reynolds averaging operation,

Table 2.1: Commonly used LES filters [13]. Gaussian filter is written for the isotropic case $\Delta_x = \Delta_y = \Delta_z = \Delta$.

Name	Filter function	Transfer function
Top-hat	$G(\mathbf{r}) = \prod_{i=1}^3 \frac{1}{\Delta_i} H(\frac{1}{2}\Delta_i - r_i)$	$\hat{G}(\boldsymbol{\kappa}) = \prod_{i=1}^3 \frac{\sin(\frac{\kappa_i \Delta_i}{2})}{(\frac{\kappa_i \Delta_i}{2})}$
Gaussian	$G(\mathbf{r}) = (\frac{6}{\pi})^{3/2} \frac{1}{\Delta^3} e^{-\frac{6 \mathbf{r} ^2}{\Delta^2}}$	$\hat{G}(\boldsymbol{\kappa}) = e^{-\frac{\Delta^2 \boldsymbol{\kappa} ^2}{24}}$
Sharp spectral	$G(\mathbf{r}) = \prod_{i=1}^3 \frac{\sin(\frac{2\pi r_i}{\Delta_i})}{\pi r_i}$	$\hat{G}(\boldsymbol{\kappa}) = \prod_{i=1}^3 H(\frac{\pi}{\Delta_i} - \kappa_i)$

which can be also seen as a scale separation, the filtering operation has important differences:

1. Generally $\tilde{\tilde{\phi}} \neq \tilde{\phi}$. The exception is a sharp cutoff filter
2. Differentiation and filtering do not commute on arbitrary meshes: $\tilde{\frac{\partial \phi}{\partial x}} \neq \frac{\partial \tilde{\phi}}{\partial x}$ (except for

uniform meshes)

3. Time differentiation does not commute with filtering on the moving meshes [114].

The inaccuracies, which are produced because of the non-commutativity of the filtering with differentiation are of order $O(\Delta^2)$, where Δ is the characteristic cell size [42]. Thus, if the order of accuracy of the computational code is second, this error can be neglected.

The most widely used in practice is the top-hat filter. For the hexahedral cells it turns into the averaging over the computational cell:

$$\tilde{\phi}(\mathbf{x}, t) = \frac{1}{\Delta_1 \Delta_2 \Delta_3} \int_{x_3-\Delta_3/2}^{x_3+\Delta_3/2} \int_{x_2-\Delta_2/2}^{x_2+\Delta_2/2} \int_{x_1-\Delta_1/2}^{x_1+\Delta_1/2} \phi(\mathbf{x}', t) dx'_1 dx'_2 dx'_3$$

When solving the equations using numerical techniques (e.g. FVM), it is not necessary to apply the filtering explicitly, because the discretization by construction filters out the length scales which are less than the local cell size. The requirement of resolving the bulk of TKE (which guaranties the reliability of the result) is therefore satisfied by choosing the appropriate cell size. Usually, it is desired that Δ lies in the inertial interval [114].

The next task after introduction of scale separation operator is its application to the Navier-Stokes and continuity equations. Assuming the commutative properties of filtering with respect to differentiation, filtering of (2.6), (2.16) is quite straightforward, except for the convective term, which is treated as follows:

$$\begin{aligned} \widetilde{\frac{\partial u_i u_j}{\partial x_j}} &= \frac{\partial \widetilde{u_i u_j}}{\partial x_j} = \frac{\partial}{\partial x_j} (\widetilde{u_i u_j} + \widetilde{u_i} \widetilde{u_j} - \widetilde{u_i u_j}) = \frac{\partial \widetilde{u_i u_j}}{\partial x_j} + \frac{\partial}{\partial x_j} (\widetilde{u_i u_j} - \widetilde{u_i} \widetilde{u_j}) \stackrel{(2.6)}{=} \\ &\quad \widetilde{u_j} \frac{\partial \widetilde{u_i}}{\partial x_j} + \frac{\partial}{\partial x_j} \tau_{ij}^{SGS}. \end{aligned}$$

After these manipulations one obtains:

$$\frac{\partial \widetilde{u_i}}{\partial t} + \widetilde{u_j} \frac{\partial \widetilde{u_i}}{\partial x_j} + \frac{1}{\rho} \frac{\partial \widetilde{p}}{\partial x_i} = \frac{\partial}{\partial x_j} \left[\nu \left(\frac{\partial \widetilde{u_i}}{\partial x_j} + \frac{\partial \widetilde{u_j}}{\partial x_i} \right) - \tau_{ij}^{SGS} \right] + \widetilde{f_i} \quad (2.66)$$

$$\frac{\partial \widetilde{u_i}}{\partial x_i} = 0 \quad (2.67)$$

The term $\tau_{ij}^{SGS} = \widetilde{u_i u_j} - \widetilde{u_i} \widetilde{u_j}$ which appeared in (2.66) after filtering is called the residual (or subgrid) stress tensor and is analogous to the Reynolds tensor [114]. The obtained system of equations is not closed and in order to make it determined a model for the residual stresses should be employed. This is the topic of the next subsection.

2.2.13 Subgrid scale stress modeling

On the contrary to RANS closures the LES models are usually much simpler and contain less (or no) empirical data. It is assumed that the subgrid scales lie in the inertial interval, therefore, according to Kolmogorov's hypotheses, the turbulent flow at these scales becomes statistically isotropic [114] and possesses a universal structure, which allows to avoid the involvement of empiricism in the description of influence of these scales on the large-scale (filtered) flow.

Along with the residual-stress tensor τ_{ij}^{SGS} the residual kinetic energy is defined:

$$k_{sgs} = \frac{1}{2} \tau_{kk}^{SGS}, \quad (2.68)$$

being the trace of τ_{ij}^{SGS} . The anisotropic residual-stress tensor is introduced as follows:

$$\tau_{ij}^{sgs} = \tau_{ij}^{SGS} - \frac{2}{3} k_{sgs} \delta_{ij}, \quad (2.69)$$

Smagorinsky model

Smagorinsky (1963) proposed the most simple SGS model, which is based on the earlier introduced eddy viscosity assumption. The anisotropic residual stress tensor is represented as follows:

$$\tau_{ij}^{sgs} = -2\nu_{sgs}\tilde{S}_{ij}. \quad (2.70)$$

Analogous to the Prandtl's mixing length model, the subgrid viscosity is modeled as:

$$\nu_{sgs} = l_s^2 \tilde{S}, \quad (2.71)$$

where $\tilde{S} = \sqrt{2\tilde{S}_{ij}\tilde{S}_{ij}}$ is the magnitude of the filtered strain-rate tensor and l_s is the Smagorinsky length scale, which is represented in terms of the filter width and a called the Smagorinsky constant C_s :

$$l_s = C_s \Delta. \quad (2.72)$$

It is possible to estimate the value of the constant based on the analysis of energy transfer in the inertial interval. As it is known in this interval the equilibrium assumption holds, which means, that the mean production of energy $\overline{\mathcal{P}_{sgs}}$ equals its dissipation ϵ . Using the Smagorinsky model these quantities can be represented in the following way:

$$\epsilon = \overline{\mathcal{P}_{sgs}} = \overline{\nu_{sgs}\tilde{S}^2} = l_s^2 \overline{\tilde{S}^3}. \quad (2.73)$$

Based on the Kolmogorov spectrum an estimation for $\overline{\tilde{S}^2}$ can be done:

$$\overline{\tilde{S}^2} \approx 7C\epsilon^{2/3}\Delta^{-4/3}, \quad (2.74)$$

where $C = 1.5$ is a Kolmogorov constant. Finding ϵ from (2.74) and substituting it into (2.73) one gets:

$$l_s = \frac{\Delta}{(7C)^{3/4}} \left(\frac{\overline{\tilde{S}^2}^{3/2}}{\overline{\tilde{S}^3}} \right). \quad (2.75)$$

Lilly [86] used the approximation $\overline{\tilde{S}^3} \approx \overline{\tilde{S}^2}^{3/2}$ to obtain the approximate value of the Smagorinsky constant:

$$C_s = \frac{l_s}{\Delta} = \frac{1}{(7C)^{3/4}} \approx 0.17. \quad (2.76)$$

van Driest damping

The Smagorinsky model has been derived for the case, when the filter width Δ lies in the inertial subrange, in which the turbulence production and dissipation are in equilibrium. However, in the vicinity of the wall this assumption does not hold and therefore the Smagorinsky model erroneously produces non-zero subgrid-scale stresses. In order to avoid this Moin and Kim [104] applied the damping function of van Driest to l_s :

$$l_s = C_s \Delta (1 - e^{y^+/A^+}), \quad (2.77)$$

this way reducing ν_{sgs} at the wall. In (2.77) y^+ is the dimensionless wall distance and $A^+ = 25$. Moreover, in order to obtain the agreement with the experimental data, the value of the Smagorinsky constant had to be reduced to $C_s = 0.1$.

Dynamic Smagorinsky model

A serious drawback of the original Smagorinsky model is the dependence of the coefficient C_s on the particular flow regime. In the turbulent flow its value usually lies in the range 0.1–0.2,

whereas in the laminar flow it should be equal to zero. Moreover, the proper value of Smagorinsky constant is dependent on the discretization schemes used for underlying PDE. Because of this lack of generality, Germano [41] proposed a procedure for dynamical determination of C_s .

In order to derive an equation for C_s one has to first define a so-called test filter which has the same filtering kernel as previously introduced grid filter, but its width $\widehat{\Delta}$ is twice larger than Δ . Filtering operation using the test filter will be further designated as $\widehat{\cdot}$. The subtest stresses which are based on the double-filtering (grid filter + test filter) are defined as:

$$T_{ij} = \widehat{u_i u_j} - \widehat{u_i} \widehat{u_j}. \quad (2.78)$$

Subtraction of the test-filtered subgrid scale stress $\widehat{\tau_{ij}^{SGS}}$ from T_{ij} yields the Germano identity:

$$\mathcal{L}_{ij} \equiv T_{ij} - \widehat{\tau_{ij}^{SGS}} = \widehat{u_i u_j} - \widehat{u_i} \widehat{u_j} \quad (2.79)$$

For the deviatoric parts of both stress tensors in (2.79) the original Smagorinsky model can be applied, giving:

$$\begin{aligned} \widehat{\tau_{ij}^{SGS}} - \frac{1}{3} \widehat{\tau_{kk}^{SGS}} \delta_{ij} &= -2(C_s \Delta)^2 \widehat{\widetilde{\mathcal{S}}_{ij}} \\ T_{ij} - \frac{1}{3} T_{kk} \delta_{ij} &= -2(C_s \widehat{\Delta})^2 \widehat{\widetilde{\mathcal{S}}_{ij}}. \end{aligned}$$

Using these representations the deviatoric part of \mathcal{L}_{ij} can be represented as follows:

$$\mathcal{L}_{ij} - \frac{1}{3} \mathcal{L}_{kk} \delta_{ij} = 2C \mathcal{M}_{ij}, \quad (2.80)$$

where $C = (C_s)^2$ and

$$\mathcal{M}_{ij} = \Delta^2 \widehat{\widetilde{\mathcal{S}}_{ij}} - \widehat{\Delta}^2 \widehat{\widetilde{\mathcal{S}}_{ij}} \quad (2.81)$$

Matrix equation (2.80) consists of five independent equations in one unknown: C , therefore one cannot satisfy all the equations. In order to convert (2.80) to a single scalar equation Germano proposed to contract (2.80) by multiplying it with $\widetilde{\mathcal{S}}_{ij}$, which yields

$$C = \frac{\mathcal{L}_{ij} \widetilde{\mathcal{S}}_{ij}}{2 \mathcal{M}_{ij} \widetilde{\mathcal{S}}_{ij}}. \quad (2.82)$$

Unfortunately, this formula, being applied to the calculations of the channel flow [41] caused numerical instabilities for the cases, where the denominator was small or was equal to zero. In order to overcome this, Lilly [85] proposed to find the solution for (2.80) in least squares sense, i.e. minimizing the square of the error Q :

$$Q = (\mathcal{L}_{ij} - \frac{1}{3} \mathcal{L}_{kk} \delta_{ij} - 2C \mathcal{M}_{ij})^2. \quad (2.83)$$

The extrema of Q lies where $\frac{\partial Q}{\partial C} = 0$. From this condition one can find:

$$C = \frac{1}{2} \frac{\mathcal{L}_{ij} \mathcal{M}_{ij}}{\mathcal{M}_{ij}^2}. \quad (2.84)$$

In order to get sure, that the found extrema represent the minimum of Q one has to analyze $\frac{\partial^2 Q}{\partial C^2}$:

$$\frac{\partial^2 Q}{\partial C^2} = 8 \mathcal{M}_{ij} \mathcal{M}_{ij} > 0. \quad (2.85)$$

So the second derivative is always positive, identifying the minimum of Q .

The variety of different LES models is at the time very wide, a good review of them can be found in the monograph of Sagaut [124].

2.2.14 Applicability of LES

Being less costly than DNS, for wall flows at high Re LES still requires very fine resolution of the mesh. The reason for this is the described above constraint of resolving the bulk of turbulent energy. Near the wall the energy containing vortical structures are very small and their size decreases depending on Re . Therefore, the higher Re is considered in the application, the higher number of cells is required to resolve the dynamics of energy-containing vortices.

For example, for the channel flow the number of computational nodes, needed to conduct a reliable LES scales with $Re^{1.76}$ [114], which obviously imposes a severe limitation on the range of applicability of LES. Due to this restriction in practice pure LES models are used mostly for low and moderate Re flows. For high Reynolds number flows nowadays different kinds of hybrid RANS/LES approaches are applied.

2.3 Overview of hybrid turbulence models

Hybrid turbulence modeling is a relatively new technique, which nowadays gains more and more popularity. The tasks, set for CFD in present time have become very complicated. For typically high Reynolds numbers, considered in ship hydrodynamics not only the steady parameters (e.g. resistance or mean propeller thrust and torque) of the studied objects are now requested, but also the considerably unsteady or distributed characteristics, like peaks of the thrust or moment produced by the propeller operating in an unsteady ship wake. The former task can nowadays be easily solved by application of RANS closure models. Experience shows, that even the isotropic RANS models, based on Boussinesq assumption can provide satisfactory results for resistance prediction for ships with moderate block coefficients [30, 63], propeller open-water tests [83], ship maneuvering [103], prediction of ship motion in waves [102] etc. At the same time, for the wakes behind ships with high block coefficients and for the prediction of unsteady thrust and torque oscillations, some kind of hybrid modeling should be utilized [2].

As it was previously described, the application of LES can considerably reduce the computational cost of the flow predictions compared to DNS, since the dissipative scales and the part of the vortices in inertial interval should no more be resolved. However for wall bounded flows at high Re application of LES still remains impractical. At the same time its ability to capture the time evolution the large-scale anisotropic structures is very attractive for flows with strong separations.

On the contrary, the RANS turbulence models can predict the growth and separation of the boundary layer relatively well with a relatively low computational cost, but even the best RANS models - RSTM cannot always function reliably for prediction of the momentum transport after the separation [141].

This led the turbulence researchers to the idea of hybridization of the RANS and LES approaches, where the two methods are applied in different regions of the flow: RANS is used in the vicinity of the wall, where the resolution of energy containing vortices using LES would require enormous number of computational nodes, whereas LES is used farther from the wall, where the large-scale instabilities in the flow occur.

A number of attempts has been done to classify the existing hybrid models [37, 125]. In this work the classification proposed by Fröhlich and von Terzi [37] will be adopted. Following their classification, one can distinguish two main branches of RANS/LES approaches: the first one is called the unified (global) modeling, in which the single velocity and pressure field is used in both RANS and LES regions and segregated (zonal) approach, which divides the computational domain explicitly into RANS and LES subregions and the coupling between the regions is done by posing the boundary conditions at the border. The unified models gained more popularity because they generally need less user input, which is a very attractive advantage for industrial applications. Therefore in the present work the description of hybrid approaches will be restricted

to unified models.

2.3.1 Blending of RANS and LES

Probably the simplest strategy of RANS/LES hybridization is the following. Looking at the momentum equations of URANS and LES (2.27),(2.66) one can notice, that they have an identical structure which makes it possible to rewrite both equations in the following form:

$$\frac{\partial \bar{u}_i}{\partial t} + \bar{u}_j \frac{\partial \bar{u}_i}{\partial x_j} + \frac{1}{\rho} \frac{\partial \bar{p}}{\partial x_i} = \frac{\partial}{\partial x_j} \left[\nu \left(\frac{\partial \bar{u}_i}{\partial x_j} + \frac{\partial \bar{u}_j}{\partial x_i} \right) - \tau_{ij}^h \right] + \bar{f}_i. \quad (2.86)$$

For LES the overline operation would mean the filtering and the hybrid turbulent stresses would be the sugrid-scale stresses $\tau_{ij}^h = \tau_{ij}^{SGS}(\Delta, \tilde{u}_i, C)$, whereas for URANS the overline would mean the time averaging and the turbulent stresses are the Reynolds stresses $\tau_{ij}^h = \tau_{ij}^{RANS} = \tau_{ij}^t(\bar{u}_i, k, \epsilon, C)$. This similarity is of course, purely structural, but from the point of view of the computational method, it allows to easily blend the two approaches by changing the τ_{ij}^h according to the region of the flow. The equation (2.86) is accompanied by the continuity constraint:

$$\frac{\partial \bar{u}_i}{\partial x_i} = 0. \quad (2.87)$$

In the following description of hybrid methods, the variables with the overline $\overline{(\cdot)}$ should be understood as “hybrid” quantities. For example, \bar{p} and \bar{u} are the pressure and velocity which are obtained as the result of a simulation with the hybrid RANS/LES stresses. The description of the theoretical issue of interpretation of these quantities can be found in [37, 125]. Usually, the concept of effective filter is adopted.

Weighted sum of RANS and LES

Given a blending function $f(\mathbf{x}, t) \in [0, 1]$ which is 1 in the RANS region, 0 in the LES region the blended (hybrid) stress τ_{ij}^h can be represented as a weighted sum of the RANS and LES stresses.

$$\tau_{ij}^h = f \tau_{ij}^{RANS} + (1 - f) \tau_{ij}^{SGS} \quad (2.88)$$

Solution of the momentum equation with the substituted hybrid stress provides a velocity field which is continuous over the whole computational domain. Later it will be shown that the choice of f is the main challenge in the construction of a unified hybrid method.

If the blending function is a step function, so that the region, where $0 < f < 1$ is thin, the hybridization strategy is called RANS/LES interfacing. If $f = f(\mathbf{x})$, then the interface is called “hard”, and if it changes in time depending on the solution, (i.e. $f = f(\mathbf{x}, t)$) then the interface is “soft” [37],[125]. The examples of the models, based on these approaches will be discussed later.

Blending of the RANS and LES models, which both use the eddy viscosity assumption (e.g. $k - \omega$ SST model with Smagorinsky model) is done through the viscosity instead of the stress itself:

$$\begin{aligned} \tau_{ij}^h &= -2 (f \nu_t \bar{S}_{ij} + (1 - f) \nu_{sgs} \bar{S}_{ij}) = -2 (f \nu_t + (1 - f) \nu_{sgs}) \bar{S}_{ij} \\ &= -2 \nu_h \bar{S}_{ij} \end{aligned} \quad (2.89)$$

If zero-equation RANS and LES models are used, it is possible to just blend the viscosities using (2.89) (see e.g. [110]), whereas for the RANS and LES closures based on the transport equations, additional modifications of these are performed.

The approach proposed in [32] is a typical example of the hybrid method described in this section. As a basis, the $k - \omega$ SST model is used, but, instead of using the RANS $k - \epsilon$ model far from the wall, the one-equation SGS model based on the transport equation for k_{sgs} is used.

The hybrid viscosity for this model reads:

$$\nu_h = f \frac{k}{\omega} + (1 - f) C_s \sqrt{k} \Delta, \quad (2.90)$$

where $C_s = 0.01$, Δ is the filter width defined as the cube root from the cell volume and the blending function f is:

$$f = \tanh \left(\left[\frac{1}{\omega} \max \left\{ \frac{500\nu}{y^2}; \frac{\sqrt{k}}{C_\mu y} \right\} \right]^4 \right) \quad (2.91)$$

In the k and ω equations the dissipation rate is blended with the same blending function:

$$\epsilon = f \beta^* k \omega + (1 - f) C_s \frac{k^{3/2}}{\Delta} \quad (2.92)$$

FSM

Speziale [146] proposed to damp the RANS model based on the local mesh resolution. In this approach the stresses estimated by the underlying turbulence closure are multiplied by the damping function f_Δ :

$$\tau_{ij}^h = f_\Delta \tau_{ij}^t \quad (2.93)$$

The function f_Δ depends on the mesh resolution Δ and the Kolmogorov scale $\eta \approx (\frac{\nu^3}{\epsilon})^{1/4}$ and reads:

$$f_\Delta \left(\frac{\Delta}{\eta} \right) = \left(1 - e^{-\beta \frac{\Delta}{\eta}} \right)^n \quad (2.94)$$

The constants $\beta = 0.001$, $n = 1$ were chosen on a phenomenological basis. As a RANS closure the ARSM of Gatzki and Speziale [39] was utilized [34].

This approach bridges a gap between RANS and LES and in fact is able to work in any regime, ranging from DNS to RANS, depending on the mesh resolution, which was shown by Fasel [34]. Because of the generality of the approach it was given a name Flow Simulation Methodology (FSM). In [34, 148] FSM was applied for the simulation of the flow around the bluff bodies and produced considerably better results compared to URANS.

Dynamic Hybrid RANS/LES (DHRL)

Bhushan and Walters [15] proposed to determine the blending function f of arbitrary RANS and LES models, based on a dynamic procedure. The velocity field \mathbf{u} was decomposed into Reynolds averaged ($\bar{\mathbf{u}}$), resolved fluctuating (\mathbf{u}') and unresolved fluctuating (\mathbf{u}'') components:

$$u_i = \bar{u}_i + u'_i + u''_i, \quad (2.95)$$

where $\bar{u}_i + u'_i = \hat{u}_i$ is the resolved velocity. The hybrid stress is represented, as previously in the form:

$$\tau_{ij}^h = f \tau_{ij}^{RANS} + (1 - f) \tau_{ij}^{SGS} \quad (2.96)$$

and the function f is found using the following procedure:

$$1 - f = \frac{\langle u''_i u''_j \rangle \langle S_{ij} \rangle}{\tau_{ij}^{RANS} \langle S_{ij} \rangle - \langle \tau_{ij}^{SGS} \rangle \langle S_{ij} \rangle}, \quad (2.97)$$

where the operator $\langle (\cdot) \rangle$ represents the explicit time averaging, performed at runtime. The calculation of f is thus analogous to dynamic procedure for determination of the Smagorinsky constant, but with the test filter replaced by the averaging.

For model tests in the original paper [15] a combination of Spalart-Allmaras RANS model with dynamic Smagorinsky model was utilized. The simulations of the channel flow for a range of Re_τ were performed and showed very good agreement for the velocity profiles and Reynolds stresses. Model predictions were superior to LES models and different modifications of DES (see 2.3.3). Later the approach was applied to naval hydrodynamics applications and also showed encouraging results [14].

2.3.2 LeMoS hybrid model (LH)

One of the interfacing hybrid URANS/LES approaches was proposed by Kornev et al. [70, 71]. This hybrid method follows the concept of unified soft-interface modeling. The anisotropic hybrid turbulent stress tensor is represented using eddy-viscosity assumption:

$$\tau_{ij}^h = 2 \nu_h \bar{S}_{ij}$$

with $\bar{S}_{ij} = \frac{1}{2}(\frac{\partial \bar{u}_i}{\partial x_j} + \frac{\partial \bar{u}_j}{\partial x_i})$ being a strain-rate tensor.

Computational domain is dynamically decomposed into RANS and LES regions based on the ratio $h = h(\mathbf{x}, t) = L(\mathbf{x}, t)/\Delta(\mathbf{x})$ between the integral length scale L and the characteristic cell size $\Delta = \sqrt{0.5(\Delta_{max}^2 + V^{2/3})}$. The difference between the RANS and LES regions is the way how ν_h field is calculated. The hybrid viscosity is represented as a weighted sum of kinematic turbulent viscosity and subgrid scale viscosity:

$$\nu_h = f \nu_t + (1 - f) \nu_{sgs}. \quad (2.98)$$

The blending function $f = f(\mathbf{x}, t)$ reads:

$$f = \begin{cases} 0, & h > h_2 \\ 1, & h < h_1 \\ \gamma(h), & h_1 \leq h \leq h_2 \end{cases} \quad (2.99)$$

$$\gamma(h) = \frac{1}{2} + \frac{1}{\pi} \arctan \left(40 \frac{h_1 - h}{(h_2 - h_1)^2} + 10 \frac{h_2 + h_1}{h_2 - h_1} \right),$$

where h_1 and h_2 are the parameters of the blending function. If a cell has $h > h_2$, it is supposed that the cell size lies in the inertial range, thus satisfying the LES constraint and the model uses the subgrid scale viscosity, modeled using Lilly's modification of Germano dynamic model [85]:

$$\nu_{sgs} = (C_s \Delta)^2 \bar{S} \quad (2.100)$$

Cells, having $h < h_1$ are considered too large for resolving the local energy-containing vortices, and for them the turbulent kinematic viscosity ν_t is calculated using Menter's $k - \omega$ SST model [99], equations for k, ω are solved in the background. Parameters h_1 and h_2 were chosen as 0.95 and 1.05 respectively. To estimate the integral length scale L , the Prandtl-Kolmogorov formula [127] without a correction factor is used. Recalling, that $\omega = \frac{\epsilon}{k \beta^*}$, one obtains:

$$L = \frac{k^{3/2}}{\epsilon} = \frac{\sqrt{k}}{\beta^* \omega}, \quad (2.101)$$

where $\beta^* = 0.09$. This way L is represented in terms of turbulent quantities, used in underlying $k - \omega$ SST model. Hybrid viscosity, obtained in the described manner is also used for the calculation of the production and diffusion terms in k and ω equations.

The approach presented above was implemented in OpenFOAM[®] CFD package and successfully validated for naval hydrodynamics applications [71, 2]. Due to good results of model validation, this will be one of the approaches, applied in the presented study.

2.3.3 DES family methods

One of the first attempts to hybridize RANS and LES was done by Spalart et al. [140]. He proposed to modify the underlying transport equation of the Spalart-Allmaras RANS turbulence model [139]:

$$\frac{\partial \tilde{\nu}}{\partial t} + \bar{u}_j \frac{\partial \tilde{\nu}}{\partial x_j} = c_{b1} \tilde{S} \tilde{\nu} + \frac{1}{\sigma_{\tilde{\nu}}} \left[\frac{\partial}{\partial x_j} ((\nu + \tilde{\nu}_t) \frac{\partial \tilde{\nu}}{\partial x_j}) + c_{b2} \frac{\partial \tilde{\nu}^2}{\partial x_j} \right] - c_{w1} f_w \left(\frac{\tilde{\nu}}{y} \right)^2, \quad (2.102)$$

depending on the mesh resolution. A rule for determining the kinematic turbulent viscosity is $\nu_t = \tilde{\nu} f_{\nu 1}(y^+)$. The complete description of the closure can be found in [139]. The last term on the right hand side of (2.102) represents the destruction of $\tilde{\nu}$ and contains the wall distance y_w . Spalart replaced y_w by \tilde{y}_w , given by the formula:

$$\tilde{y}_w = \min(y_w, C_{DES} \Delta), \quad (2.103)$$

where $C_{DES} = 0.65$ and Δ is the characteristic size of a computational cell. In the original version $\Delta = \Delta_{max} \equiv \max(\Delta_x, \Delta_y, \Delta_z)$ [140]¹. The performed modification increases the destruction term in (2.102) in regions, where $C_{DES} \Delta < y_w$ and this way reduces the eddy-viscosity, so that the model turns into a one-equation SGS model. This, however, does not mean that the eddy-viscosity will have a jump between the regions $C_{DES} \Delta > y_w$ and $C_{DES} \Delta < y_w$, since only the destruction term is changed, providing a smooth transition of hybrid viscosity.

If one assumes, that turbulence is in equilibrium (i.e. production equals dissipation), one can obtain:

$$c_{b1} \tilde{S} \tilde{\nu} = c_{w1} f_w \left(\frac{\tilde{\nu}}{y_w} \right)^2. \quad (2.104)$$

After some algebra and substitution of \tilde{y}_w one can obtain:

$$\tilde{\nu} = \frac{c_{b1}}{c_{w1} f_w} \tilde{y}_w^2 \tilde{S}, \quad (2.105)$$

which represents a Smagorinsky-like algebraic model in LES mode:

$$\tilde{\nu} = \left(\sqrt{\frac{c_{b1}}{c_{w1} f_w}} C_{DES} \Delta \right)^2 \tilde{S}, \quad (2.106)$$

The coefficient C_{DES} was found as a result of calibration of the derived one-equation SGS model for the decay of homogeneous isotropic turbulence. The criterion was the proper reproduction of a decay and absence of high-end spectrum build-up [140].

The acronym DES stands for ‘‘Detached-Eddy Simulation’’. The detached eddies, which shed from the wall in the separation region are this way opposed to the attached eddies, populating the boundary layers. The intention of the model is to resolve the former and to model the latter.

The same idea of making the length scale of a RANS turbulence model dependent on the grid resolution was used by Travin et al. [149, 147] for converting the $k - \omega$ SST model into DES (hereafter SST-DES). In the formulation of the Menter’s model the turbulence length scale is given by:

$$l_{k-\omega} = \frac{\sqrt{k}}{\beta^* \omega} \quad (2.107)$$

Analogous to SA-DES formulation, the modified length scale is found as:

$$\tilde{l} = \min(l_{k-\omega}, C_{DES} \Delta). \quad (2.108)$$

Now, in order to include this change into the model, the dissipative term in (2.53) was reformu-

¹Hexahedral cells were assumed to be used

lated:

$$\mathcal{D}_k = \beta^* k \omega \rightarrow \tilde{\mathcal{D}}_k = k^{3/2} / \tilde{l} \quad (2.109)$$

This time C_{DES} cannot be constant, since, as previously described, the SST model consists of two branches: $k - \epsilon$ and $k - \omega$ and for each of them the appropriate coefficient should be chosen. By the same means as for SA-DES, the coefficients $C_{DES}^{k-\omega}$ and $C_{DES}^{k-\epsilon}$ were determined which equal 0.78 and 0.61 respectively [147]. Blending of the C_{DES} coefficients is done identically to SST model constants:

$$C_{DES} = (1 - F_1)C_{DES}^{k-\epsilon} + F_1C_{DES}^{k-\omega} \quad (2.110)$$

In the following only the versions of DES models, based on $k - \omega$ SST model will be described in details (i.e. SST-DDES, SST-IDDES), since these have a wider range of applicability compared to SA ones (SA model was originally created for airfoils). In addition SST-based formulation has a considerable advantage that the transition from RANS to LES regions does not only depend on the distance to the wall and the mesh resolution, *but also on the solution*. Therefore, the RANS/LES interface may have a complex geometry and may be unsteady. According to the classification [37], SA-DES is an interfacing RANS/LES model with a hard interface, whereas SST-DES has a soft interface.

In order to ensure, that DES is applied as intended, one has to generate the computational grid in such a way, that the wall-parallel spacing $\Delta_{||}$ is larger than the boundary layer thickness δ [142].

Known issues of DES approach

The proposed method was initially applied for flows with massive separation [135, 147, 49], for which a noticeable improvement over URANS solution was observed. However the extensive application of DES revealed a number of problems associated with the model formulation [143, 107, 100]. In this section the issues which are common for both of the above described DES variants will be listed (e.g. the issue of near-wall damping in SA-DES is here ignored).

- **Grey area** As it has already been mentioned, the DES model should turn into URANS in the attached boundary layer and into LES far from the walls and in the separated flow. The switch of the destruction term between the regions is sharp, but this does not mean, that the model is able to instantly undergo the transition from statistically averaged smooth solution in the boundary layer to a developed LES downstream. The transition from RANS to a developed LES without any artificial forcing thus relies on inner flow instabilities and is completely case-dependent. Usually DES performs well in situations with strong flow instabilities (e.g. flows over bluff bodies). In other cases, where the separation is weak and the natural generation of resolved turbulence is not sufficient, the application of DES needs attention [100]. In this case also the numerical schemes applied for the discretization of convection term may play a significant role for the simulation results [147].
- **Modeled Stress Depletion (MSD) and Grid Induced Separation (GIS)** As previously described, in DES it is not desired, that LES enters the attached boundary layer. However, the only way to control LES propagation in the direction of the wall is the proper mesh generation strategy [142]. Therefore, if due to some reasons the wall-parallel grid spacing $\Delta_{||}$ becomes smaller than the boundary layer thickness, the switch to LES mode can occur in the vicinity of the wall, leading to reduction of eddy-viscosity which in turn decreases the modeled stresses. This would not be a problem if the decrease of modeled stresses would be compensated by the resolved turbulence. Unfortunately, the development of resolved turbulence in the boundary layer cannot happen naturally in the framework of DES until LES enters the buffer layer [143]. Therefore, the total stresses decrease, leading to reduction of skin friction. This phenomenon was called “modeled stress depletion”. If

a boundary layer is subject to adverse pressure gradient, MSD can result in a premature separation because of the lack of turbulent mixing [143]. The grid sensitivity is thus a serious deficiency of the DES method.

- **Log-Layer Mismatch (LLM)** This issue is related to application of DES in Wall-Modelled LES (WMLES) scenario. The WMLES approach can be shortly described as follows. In order to decrease the required wall-parallel grid resolution for LES [107, 100], the RANS model is applied in the vicinity of the wall and LES in the remainder of the flow. The RANS/LES interface in this case lies in the boundary layer, which is untypical for original DES. However, Nikitin et al.[107] tried to apply DES in its original formulation in a somewhat unnatural way. The calculation of the channel flow at various Reynolds numbers was conducted using a set of different computational codes. The results indicated, that DES works quite correctly in this case, sustaining the LES content. However, the time-averaged velocity profiles had inadequate shape, showing two logarithmic layers: the modeled one and the resolved one, which did not match. Hence the term log-layer mismatch. Because of the shift of the resolved logarithmic region the error in skin-friction coefficient reached 25% in some cases. Thus, it was shown, that DES is not applicable for WMLES “as is”.

The drawbacks listed above stimulated the development of further modifications of the approach which will be discussed in the next sections.

As one can see, all the listed issues are related to the behavior of the model at the interface between RANS and LES regions. One has to mention, that the other hybrid methods also possess the same shortcomings [143]. Later in Section 2.3.5 it will be shown that all these problems stem from a fundamental theoretical inconsistency of unified hybrid methods and are caused by a lack of momentum transport through the interface.

Delayed Detached-Eddy Simulation (DDES)

One of the problems which has been revealed after extensive application of DES was that the method predicted stronger separations, than RANS, when the mesh was refined (GIS). In their paper Spalart et al. [143] introduced a term “ambiguous grid spacing”, which refers to a grid, which does not satisfy the constraint $\Delta_{||} > \delta$ and at the same time is not fine enough to develop LES content. On such grid the above described MSD may occur and can cause nonphysical separations and reduction of skin friction.

In order to make the model results less dependent on the computational mesh a number of modifications of DES method was proposed. Menter and Kuntz [98] slightly reformulated the dissipative term in k -equation, compared to Strelets’ version:

$$\tilde{\mathcal{D}}_k = \beta^* k \omega \cdot F_{DES}, \text{ where } F_{DES} = \max\left(\frac{l_{k-\omega}}{C_{DES}\Delta}, 1\right) \quad (2.111)$$

This way the DES-limiter is formulated as a multiplier of the dissipative term. Afterwards, the first argument of $\max()$ was multiplied by $1 - F_2$ ¹, giving:

$$F_{DES} = \max\left(\frac{l_{k-\omega}}{C_{DES}\Delta}(1 - F_2), 1\right) \quad (2.112)$$

Since F_2 is tuned to detect the boundary layer, where it is 1, in this region of the flow the first argument becomes small, which guarantees, that RANS branch will be used, regardless of the cell size:

$$F_{DES} = 1 \implies \tilde{\mathcal{D}}_k = \beta^* k \omega. \quad (2.113)$$

¹See section 2.2.9

The function, which is used for modification of the length scale is called “shielding function” because it preserves the boundary layer from LES propagation into it. This modification was tested for NACA4412 airfoil and yielded the separation behavior much closer to RANS, even though still not perfect. Since then new modifications of this method were created by Menter. The so-called Stress-Blended Eddy Simulation (SBES) and Shielded Detached-Eddy Simulation (SDES) use an improved shielding function. Unfortunately, the formula of the latter has not been published till now [95].

Another attempt to combat MSD was done by Spalart et al. [143]. The model in question was SA-DES. Since the usage of F_1 or F_2 for SA-DES model is not possible, a more general formulation was proposed, which depends only on the wall distance, velocity gradient and effective viscosity. The function \tilde{y}_w was changed as follows:

$$\tilde{y}_w \equiv y_w - f_d \max(0, y_w - C_{DES}\Delta), \quad (2.114)$$

where

$$f_d \equiv 1 - \tanh([8r_d]^3), \text{ with } r_d \equiv \frac{\nu_t + \nu}{\kappa^2 y^2 \sqrt{\nabla \mathbf{u} : \nabla \mathbf{u}}} \quad (2.115)$$

The function f_d is designed analogous to $1 - F_2$ used by Menter and Kuntz: it is 0 in the boundary layer and 1 in the remainder of the flow. Tests of the new model formulation, named Delayed Detached-Eddy Simulation (DDES), for a range of flows (boundary layer, circular cylinder, airfoils) showed favorable results. The LES content was not suppressed by the shielding function, whereas the skin friction reduction due to MSD as well as grid-induced separation almost vanished. On the other hand the LLM problem was not solved [143]. Additionally, the model enhancements resulted into dependence of the result on the initial conditions, since \tilde{y} for SA-DDES has become dependent on the IC.

The latest modifications of DDES were proposed in [48], where the coefficients for the shielding function were adapted to the SST-DDES model and in [101], where modifications for speedup of RANS/LES transition were proposed.

Improved Delayed Detached-Eddy Simulation (IDDES)

Previously it was described that the application of raw DES in WMLES mode did not yield satisfactory results [107], but showed a potential for further development. At the same time the idea of application of DES as a wall model for LES in order to avoid the wall-parallel grid size restrictions was very attractive. Shur et al. [134] proposed the next version of DES, which preserves the DDES features and at the same allows for WMLES, this way combining the two simulation strategies in one model.

New formulation, Improved Delayed Detached-Eddy Simulation (IDDES) consists of a number of improvements over DDES:

1. Instead of using $\Delta = \Delta_{max}$ as in DES and DDES, it was proposed to utilize a more sophisticated expression:

$$\Delta_{IDDES} = \min(\max\{C_w y_w, C_w \Delta_{max}, \Delta_{wn}\}, \Delta_{max}), \quad (2.116)$$

where $C_w = 0.15$, y_w - wall distance, Δ_{wn} - grid spacing in wall-normal direction. This formula yields a linear variation of the subgrid length-scale in the vicinity of the wall and becomes Δ_{max} off the wall. Shur showed that this choice is superior to either of the previously used subgrid length-scale definitions for LES (Δ_{max} , $\Delta = V^{1/3}$), with regard to wall-bounded flows.

2. For the cases, when the inflow conditions of the simulation impose the turbulent content, the WMLES branch is introduced. For this scenario the following hybrid length scale is

used:

$$l_{WMLES} = f_B(1 + f_e)l_{RANS} + (1 - f_B)l_{LES}, \quad (2.117)$$

where f_B and f_e are the empirical functions. The function f_B is defined as:

$$f_B = \min(2 \exp[-9\alpha^2], 1), \text{ where } \alpha = 0.25 - y_w/\Delta_{max}. \quad (2.118)$$

It controls the model switching from RANS to LES mode, depending on the mesh parameters.

The so-called elevating function f_e is aimed at suppression of LLM by “intensification” of the RANS component near the RANS/LES interface in order to prevent the reduction of the modeled stresses. It is given by the following formulas ¹ :

$$f_e = \max(f_{e1} - 1, 0)\Psi f_{e2}, \quad (2.119)$$

with

$$f_{e1} = \begin{cases} 2 \exp(-11.09\alpha^2), & \alpha \geq 0 \\ 2 \exp(-9.0\alpha^2), & \alpha < 0 \end{cases} \quad (2.120)$$

and

$$f_{e2} = 1.0 - \max(f_t, f_l). \quad (2.121)$$

The f_t, f_l , in turn, read:

$$f_t = \tanh[(c_t^2 r_{dt})^3], f_l = \tanh[(c_l^2 r_{dl})^{10}], \quad (2.122)$$

where r_{dt}, r_{dl} are the turbulent and laminar parts of r_d

$$r_{dt} = \frac{\nu_t}{\kappa^2 y^2 \sqrt{\nabla \mathbf{u} : \nabla \mathbf{u}}} \quad (2.123)$$

$$r_{dl} = \frac{\nu}{\kappa^2 y^2 \sqrt{\nabla \mathbf{u} : \nabla \mathbf{u}}}. \quad (2.124)$$

The coefficients c_l, c_t are 5.0 and 1.87 for the SST version and 3.55 and 1.63 for the SA version.

3. Finally, the WMLES and DDES branches are combined by means of blending of their length-scales with each other in order to provide an automatic choice of the appropriate simulation strategy. For this, first, the DDES hybrid length-scale is modified:

$$\tilde{l}_{DDES} = \tilde{f}_d l_{RANS} + (1 - \tilde{f}_d) l_{LES}. \quad (2.125)$$

Here \tilde{f}_d is:

$$\tilde{f}_d = \max(1 - f_{dt}, f_B), \text{ where } f_{dt} = 1 - \tanh([8r_{dt}]^3). \quad (2.126)$$

With this new definition, the hybrid length-scale, including both WMLES and DDES may be constructed as:

$$l_{hyb} = \tilde{f}_d(1 + f_e)l_{RANS} + (1 - \tilde{f}_d)l_{LES}. \quad (2.127)$$

This expression is generalized for both SA and SST versions: l_{RANS} is y for SA version and $l_{k-\omega}$ for SST version and $l_{LES} = C_{DES}\Delta$. Here $\Delta = \Delta_{IDDES}$.

The proposed model was thoroughly tested for multiple flows. The channel flow simulations were conducted for the range of $Re_\tau = 395 - 18000$ on the grids which had a very large streamwise and spanwise spacing in wall units ($\Delta x^+, \Delta z^+$). The only modification for the meshes in the described range of Re_τ was the refinement in wall-normal direction so as to keep $y^+ < 1$. Simulation results indicated, that the problem of LLM was completely removed by the new modification of DES.

¹ Ψ function is needed only for SA version of IDDES. For SST version $\Psi = 1$.

At the same time the unsteady flow features (such as streaks) were successfully captured and sustained. The total stresses, produced by the model were shown to be independent of the variation of the streamwise grid spacing in acceptable range.

The test for a hydrofoil with the separation at the trailing edge was performed for $Re = 2.2 \cdot 10^6$, based on the chord length. The grids employed for the simulation corresponded to WMLES. A good agreement with the experimental data for the mean velocity profiles, including the separation zone, and a fair agreement for the Reynolds stresses was obtained. In order to force IDDES to switch to WMLES mode, the turbulent content from a turbulent flat plate simulation was imposed at the inlet.

Summarizing one can say that the main objectives, which triggered the model development were attained: namely the WMLES functionality was successfully added and combined with DDES.

Later Gritskevich [48] proposed a recalibrated version of IDDES based on $k-\omega$ SST model. After the recalibration of the shielding function f_d the model was validated for a number of flows. The tests have shown that the shielding of the boundary layer was considerably improved compared to the previous version [134] without the damping of resolved turbulence. This version of the model was employed in the current study and therefore a complete description of the SST-IDDES model will be given below

Assuming the constant density flow, the governing equations of SST-IDDES model can be written as follows:

$$\frac{\partial k}{\partial t} + \bar{u}_j \frac{\partial k}{\partial x_j} = \frac{\partial}{\partial x_j} \left[(\nu + \sigma_k \nu_t) \frac{\partial k}{\partial x_j} \right] + \tilde{\mathcal{P}}_k - k^{3/2} / l_{IDDES} \quad (2.128)$$

$$\frac{\partial \omega}{\partial t} + \bar{u}_j \frac{\partial \omega}{\partial x_j} = \frac{\partial}{\partial x_j} \left[(\nu + \sigma_\omega \nu_t) \frac{\partial \omega}{\partial x_j} \right] + 2(1 - F_1) \sigma_\omega \frac{1}{\omega} \frac{\partial k}{\partial x_j} \frac{\partial \omega}{\partial x_j} + \frac{\gamma}{\nu_t} \tilde{\mathcal{P}}_k - \beta \omega^2 \quad (2.129)$$

$$\nu_t = \frac{a_1 k}{\max(a_1 \omega, F_2 \bar{S})} \quad (2.130)$$

Definitions of $F_1, CD_{k\omega}, F_2$ correspond to those given previously in section 2.2.9. The limited production term $\tilde{\mathcal{P}}_k$ reads:

$$\tilde{\mathcal{P}}_k = \min(\nu_t \bar{S}^2, 10 \beta^* k \omega) \quad (2.131)$$

The hybrid length scale l_{IDDES} is given by the following expression:

$$l_{IDDES} = \tilde{f}_d (1 + f_e) l_{RANS} + (1 - \tilde{f}_d) l_{LES}, \text{with} \quad (2.132)$$

$$l_{LES} = C_{DES} \Delta \quad (2.133)$$

$$l_{RANS} = \frac{k^{1/2}}{\beta^* \omega} \quad (2.134)$$

$$C_{DES} = C_{DES1} F_1 + C_{DES2} (1 - F_1) \quad (2.135)$$

The subgrid length-scale is calculated as:

$$\Delta = \min\{C_w \max[y, \Delta_{max}], \Delta_{max}\} \quad (2.136)$$

As previously, \tilde{f}_d reads:

$$\tilde{f}_d = \max(1 - f_{dt}, f_B), \quad (2.137)$$

whereas the function f_{dt} is modified:

$$f_{dt} = 1 - \tanh([C_{dt1} r_{dt}]^{C_{dt2}}), \text{ where} \quad (2.138)$$

$$r_{dt} = \frac{\nu_t}{\kappa^2 y^2 \sqrt{0.5(\bar{S}^2 + \bar{\Omega}^2)}}. \quad (2.139)$$

The formulas for $f_B, \alpha, f_e, f_{e1}, f_{e2}, f_t, f_l$ remain unchanged. The expression for r_{dl} mimics (2.139):

$$r_{dl} = \frac{\nu}{\kappa^2 y^2 \sqrt{0.5(\bar{S}^2 + \bar{\Omega}^2)}}, \quad (2.140)$$

where $\bar{S}, \bar{\Omega}$ are the magnitudes of the strain rate and vorticity tensors respectively, calculated from the resulting “hybrid” velocity field. The model constants are:

$$\begin{aligned} \beta^* &= 0.09, \quad \kappa = 0.41, \quad a_1 = 0.31, \quad C_{DES1} = 0.78, \\ C_{DES2} &= 0.61, \quad C_{dt1} = 20, \quad C_{dt2} = 3, \quad C_l = 5.0, \quad C_t = 1.87. \end{aligned} \quad (2.141)$$

This version of SST-IDDES model was implemented in OpenFOAM library in the framework of the presented research. Results of validation of the model will be reported in Chapter 4.

2.3.4 Partially Averaged Navier-Stokes Equations (PANS)

This approach cannot be strictly speaking related to hybrid RANS/LES methods, because, in contrast to LES, the stresses in the model do not explicitly depend on the grid spacing. From this point of view, PANS should be understood as an improvement to RANS approach. However, in contrast to RANS, it allows to define, which portion of turbulent kinetic energy and dissipation rate should be resolved in the simulation.

The idea of Girimaji [44] is similar to that of FSM, described above. In order to bridge the gap between RANS and DNS it is proposed to damp the underlying RANS model. Prior to the simulation two parameters: f_k, f_ϵ should be defined, which determine the unresolved-to-total ratios of turbulent kinetic energy and dissipation rate respectively:

$$f_k = \frac{k_u}{k}, \quad f_\epsilon = \frac{\epsilon_u}{\epsilon}, \quad (2.142)$$

where k_u, ϵ_u are the modeled parts of TKE and dissipation rate. Apparently, $0 \leq f_k \leq f_\epsilon \leq 1$. Girimaji used the relations (2.142) to derive the transport equations for k_u, ϵ_u [43] from the $k-\epsilon$ model:

$$\frac{\partial k_u}{\partial t} + \bar{u}_j \frac{\partial k_u}{\partial x_j} = \frac{\partial}{\partial x_j} \left[\left(\nu + \frac{\nu_u}{\sigma_{ku}} \right) \frac{\partial k_u}{\partial x_j} \right] + \mathcal{P}_{ku} - \epsilon_s \quad (2.143)$$

$$\frac{\partial \epsilon_u}{\partial t} + \bar{u}_j \frac{\partial \epsilon_u}{\partial x_j} = \frac{\partial}{\partial x_j} \left[\left(\nu + \frac{\nu_u}{\sigma_{\epsilon u}} \right) \frac{\partial \epsilon_u}{\partial x_j} \right] + C_{\epsilon 1} \frac{\epsilon_u}{k_u} \mathcal{P}_{ku} - C_{\epsilon 2}^* \frac{\epsilon_u^2}{k_u} \quad (2.144)$$

$$\nu_u = C_\mu \frac{k_u^2}{\epsilon_u} \quad (2.145)$$

Due to averaging invariance, the form of the equations is identical to that of $k-\epsilon$ RANS model. Thus, all the changes, related to replacement of k, ϵ by k_u, ϵ_u are incorporated into the model constants:

$$\begin{aligned} \sigma_{ku} &= \sigma_k \frac{f_k^2}{f_\epsilon} \\ \sigma_{\epsilon u} &= \sigma_\epsilon \frac{f_k^2}{f_\epsilon}; \quad C_{\epsilon 2}^* = C_{\epsilon 1} + \frac{f_k}{f_\epsilon} (C_{\epsilon 2} - C_{\epsilon 1}) \end{aligned} \quad (2.146)$$

Next, a rule for determining f_k is proposed. The lowest local value of f_k , which can be employed on a given grid can be found as:

$$f_k(\mathbf{x}, t) = \frac{1}{\sqrt{C_\mu}} \left(\frac{\Delta}{L} \right)^{2/3} \approx 3 \left(\frac{\Delta}{L} \right)^{2/3}, \quad (2.147)$$

where $L = \frac{k^{3/2}}{\epsilon}$ and Δ is a characteristic cell size. Instead of using the field of f_k , Girimaji [44] proposes to find $\min(f_k)$ and use this value for the whole computational domain. The value of

f_ϵ should equal 1, unless one wants to resolve the vortices in the dissipative range.

In the original papers [44, 43] the computational results were, unfortunately inconclusive. However, in the later publications [8, 73] very good agreement of model predictions with experiments for industrial flows over bluff bodies is demonstrated. One has to mention, that in those studies a different RANS model is used and f_k is computed locally on each time step.

Using the damping functions for $k - \epsilon$ model, Ma et al. [90] developed a low-Re variant of original PANS. Model tests for the flow over periodic hills at different Reynolds numbers showed the velocity profiles very close to the wall-resolved LES. At the same time, it seems that for attached boundary layers the approach is problematic, since it could not reproduce the correct velocity profile. The origin of the problem is likely to be the same as in DES, namely the lack of resolved turbulence, which should compensate the decrease in modeled stresses.

Concluding, one can say, that the approach is very promising for simulations of flows over bluff bodies. Since in PANS, as opposed to URANS, one can control the portion of the resolved TKE, results can be considerably improved [8]. However, the model performance for attached boundary layers should be carefully analyzed.

2.3.5 Hybrid-Filtered Navier-Stokes (HFNS)

All the previously described hybrid approaches are based on the assumption, that in order to blend the statistically and spatially averaged solutions it is sufficient to appropriately change the value of the viscosity. On the one hand, there is no theoretical proof, that this assumption is generally valid. On the other hand, the fact that most unified hybrid approaches suffer from similar problems (gray area, MSD, LLM) indicates, that they might have some kind of inconsistency.

Instead of blending the RANS and LES momentum equations by viscosity, Germano [40] derived so-called hybrid-filtered Navier-Stokes equations, by using the blended filter H , which combines the RANS averaging operator E with LES filtering operator F . Introducing a blending function $\psi(\mathbf{x}) \in [0, 1]$, which is 1 in LES zone and 0 in RANS zone, one can write the hybrid filter in the following way¹:

$$H = \psi F + (1 - \psi)E \quad (2.148)$$

It is assumed that the filtering operator commutes with spatial derivative ($\langle \frac{\partial \phi}{\partial x_i} \rangle_F = \frac{\partial \langle \phi \rangle_F}{\partial x_i}$) and that the averaging of the hybrid-filtered field recovers the average of original field ($\langle \langle \phi \rangle_H \rangle_E = \langle \phi \rangle_E$). The hybrid filter turns out to be non-commutative with the spatial derivative:

$$\left\langle \frac{\partial \phi}{\partial x_i} \right\rangle_H = \frac{\partial \langle \phi \rangle_H}{\partial x_i} - \frac{\partial \psi}{\partial x_i} (\langle \phi \rangle_F - \langle \phi \rangle_E). \quad (2.149)$$

Based on the above definitions, the following relation between the filtered, averaged and hybrid-filtered fields can be found:

$$\langle \phi \rangle_F = \frac{1 - \psi}{\psi} (\langle \phi \rangle_H - \langle \phi \rangle_E) + \langle \phi \rangle_H \quad (2.150)$$

Application of the hybrid filter to the continuity equation (2.6) yielded:

$$\frac{\partial \langle u_j \rangle_H}{\partial x_j} = \frac{\partial \psi}{\partial x_j} (\langle u_j \rangle_F - \langle u_j \rangle_E), \quad (2.151)$$

indicating, that the velocity field $\langle u_j \rangle_H$ is not solenoidal. The hybrid-filtered Navier-Stokes equations were consequently obtained by application of H to (2.16)² (see Eqs. (2.152), (2.153), (2.154)). Components of G_{ij} are called Germano stresses [117].

¹In this section the designations $\langle \cdot \rangle_E$, $\langle \cdot \rangle_F$, $\langle \cdot \rangle_H$ should be understood as averaging, filtering and hybrid-filtering respectively.

²The force vector f is here assumed to be 0

One can see that the additional terms appeared in the momentum equation as the result of the filtering, they stem from the non-commutativity of the derivative with the hybrid filter. The form of the momentum and continuity equation is now not identical neither with RANS nor with LES. New terms depend on the gradient of the blending function as well as on the filtered and averaged velocity fields.

$$\begin{aligned}
\frac{\partial \langle u_i \rangle_H}{\partial t} + \frac{\partial \langle u_i \rangle_H \langle u_i \rangle_H}{\partial x_j} &= -\frac{1}{\rho} \frac{\partial \langle p \rangle_H}{\partial x_i} + \nu \frac{\partial^2 \langle u_i \rangle_H}{\partial x_j^2} - \frac{\partial \tau_H(u_i, u_j)}{\partial x_j} \\
&+ \frac{\partial \psi}{\partial x_i} (\langle p \rangle_F - \langle p \rangle_E) + \frac{\partial \psi}{\partial x_j} (\langle u_i \rangle_F \langle u_i \rangle_F - \langle u_i \rangle_E \langle u_i \rangle_E) \\
&+ \frac{\partial \psi}{\partial x_j} (\tau_F(u_i, u_j) - \tau_E(u_i, u_j)) - 2\nu \frac{\partial \psi}{\partial x_j} \frac{\partial}{\partial x_j} (\langle u_i \rangle_F - \langle u_i \rangle_E) \\
&- \nu \frac{\partial^2 \psi}{\partial x_j^2} (\langle u_i \rangle_F - \langle u_i \rangle_E),
\end{aligned} \tag{2.152}$$

$$\tau_H(u_i, u_j) = \psi \tau_F(u_i, u_j) + (1 - \psi) \tau_E(u_i, u_j) + G_{ij} \tag{2.153}$$

$$G_{ij} = \psi(1 - \psi)(\langle u_i \rangle_F - \langle u_i \rangle_E)(\langle u_j \rangle_F - \langle u_j \rangle_E). \tag{2.154}$$

The hybrid methods, which are based on the blending of the viscosity between the RANS and LES region are therefore inconsistent, in that they neglect the additional terms in the transition region ($0 < \psi < 1$) both in the momentum and continuity equations. As it is described by Rajamani and Kim [117], these terms as well as Germano stresses are responsible for the momentum transport through the interface. Piomelli et al. [111] tried to solve the gray area problem by introduction of forcing at the RANS/LES interface and the outcome was promising. However, there was neither a theoretical justification for introduction of the forcing nor a solid basis for determining the forcing parameters. As opposed to this ad-hoc forcing, additional terms in (2.152) are theoretically derived and have a definitive meaning: they intensify the interaction between the RANS and LES regions.

Preliminary tests of this approach [117] for the channel flow at different Re_τ showed that the problem of LLM has completely vanished without the introduction of empirical functions, as in IDDES or forcing as it was done by Piomelli.

The main challenge in application of HFNS is to obtain the field $\langle u_i \rangle_F$ from $\langle u_i \rangle_E, \langle u_i \rangle_H$. Formula (2.150) was successfully used by Rajamani and Kim. However, in their work they mention, that operation of $\langle u_i \rangle_F$ recovery is ill-conditioned in some situations causes the divergence of numerical method. Rocha and Menon [126] tried to make the procedure more robust by avoiding the formula (2.150) and recovering $\langle u_i \rangle_F$ by addition of random perturbation into the $\langle u_i \rangle_H$ field.

Concluding, one can say, that the HFNS is a very interesting approach and has a high theoretical value. Compared to other hybrid approaches it possesses a very important feature - strict mathematical consistency. It seems that the problem of gray area has a theoretically strict remedy. However, at the moment it is far from being ready for industrial applications.

2.4 Generation of turbulent inflow conditions

As it is known, the presence of turbulent vortices is essential for successful DNS, LES and RANS/LES application because of the role they play in momentum transport. However, specification of the inlet flow velocity which would lead to development of realistic flow structures in the simulation domain is not straightforward. A constant in time velocity profile, which is common for RANS simulations is obviously not applicable in this case, since in this scenario the turbulence would develop far downstream from the inlet. Therefore it is desired to generate

the unsteady inflow conditions, which would reproduce the realistic turbulence statistics, corresponding to the flow in question. For the RANS/LES simulations the generation of the proper turbulent content may as well be required inside the computational domain.

In order to enrich the simulations with the turbulent eddies, a number of methods is proposed in literature. Three main approaches can be distinguished. The first one is called recycling. This approach consists in mapping of the velocity field to the upstream inlet plane on each iteration, which leads to natural development of turbulent fluctuations. Application of this technique is straightforward, when the turbulence is assumed to be homogeneous in the streamwise and spanwise directions. When this is not the case, additional rescaling of the mapped field should be performed [89]. This method is inapplicable for the cases with complex geometries, which makes it unpractical for industrial applications. In figure 2.3 one can see the

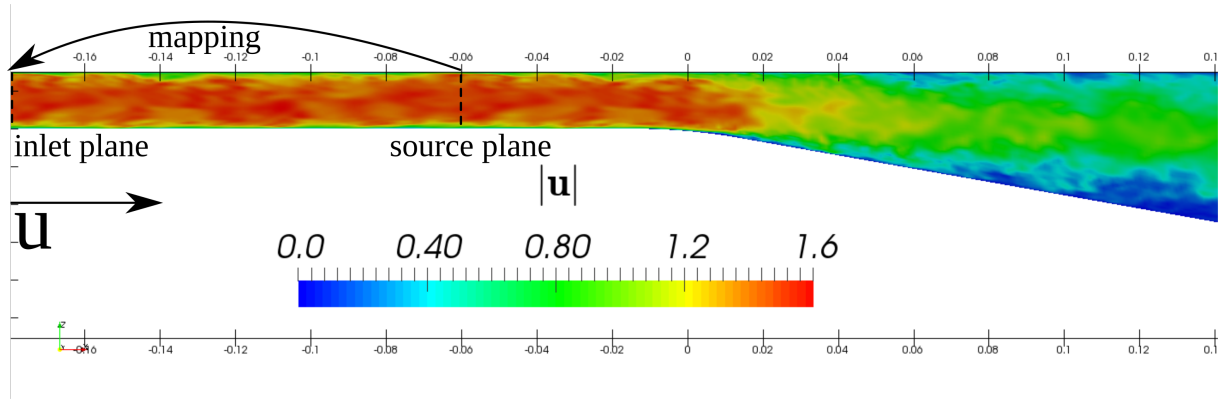


Figure 2.3: Schematic explanation of recycling approach for the case of plane asymmetric diffuser flow

example of application of recycling for the LES of the flow in a plane asymmetric diffuser. In order to generate the proper turbulent content in the diffuser throat the velocity field is mapped from the source plane to the inlet plane. If the constant velocity profile would have been set on the inlet, no turbulent content would develop in the channel in front of the diffuser, which would produce erroneous results.

The second approach relies on the auxiliary simulation. The turbulent fluctuations for the main simulation are mapped from another case, which is running in the background (see figure 2.4). For example, in [62] the velocity at the inlet is specified from the simulation of the developed channel flow. Usually, the most simple auxiliary case is chosen, which can still reproduce the statistics of the turbulence in the main flow. This technique can be applied in the situations with relatively complex geometry [129],[134]. In regard to the hybrid RANS/LES simulations, this approach can also be successfully applied to generation of the fluctuations at the interface [26]. The choice of the auxiliary flow, however, can be sometimes challenging, and therefore, at the moment the approach is not widely used in practice. One has to mention, that both of the above

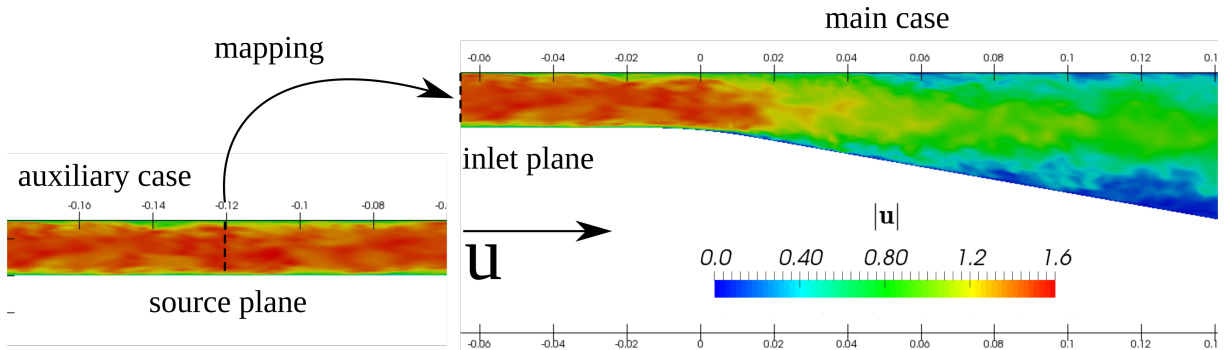


Figure 2.4: Schematic explanation of recycling approach for the case of plane asymmetric diffuser flow

mentioned concepts require a considerable amount of additional computational resources.

The most universal approach for enrichment of the flow with turbulent content is the generation of the artificial turbulent fluctuations - either at the inlet or directly in the domain (using the source terms in the momentum equation).

The variety of existing nowadays methods for turbulence synthesis can be split into two main groups: function-based and structure-based. The methods of the first group decompose the turbulent velocity field in the mean and fluctuating part and subsequently represent the latter as the sum of the sinusoidal modes with random parameters. The idea of such decomposition was originally proposed by Kraichnan [72], but was used for other purposes. Application of this idea for simulation of turbulent flows took place considerably later [81]. Further modifications of the method were developed by Smirnov [136] and most recently by Adamian [4]. The main problems of this class of methods is the impossibility of generating the divergence-free fluctuation field (which can further lead to nonphysical perturbations in the pressure field) and the difficulties in reproducing the proper length scales of generated structures near the wall. The latter drawback usually leads to rapid decay of synthesized turbulence and can cause a considerable drop of resolved turbulent stresses. In this case the realistic turbulence is obtained only farther downstream from the generator (if sustained at all). The distance between the generator plane and the streamwise coordinate, where the proper stress level is attained is called adaptation length. Adamian addressed this problem and achieved the adaptation length less than a channel height for channel flow simulations. Therefore, his modification can at the moment be considered as the best one from this family in terms of robustness (e.g. method of Smirnov fails in the vicinity of the wall), physical adequacy (e.g. it can account of anisotropy and inhomogeneity of turbulence) and ease of implementation. The problem of generation of non-solenoidal fluctuation field still remains unsolved in this family of methods.

Turbulence generators of the second group are based on the random generation of structures (e.g. vortons) in front of the inlet plane. While passing through the plane, these structures induce the fluctuation of the velocity field. This approach stems from the understanding of turbulent flow as a set of vortices. By construction such methods can take the characteristic size of structures into account and therefore can reproduce the correct integral length and autocorrelation functions, thus giving a more realistic fluctuation field than the function-based methods.

The first structure-based method was proposed by Kornev [66]. Later, in [67, 69] important theoretical results were obtained, establishing a connection between the the velocity distribution inside the generated structure and the second order statistics of the resulting fluctuation field. In [68] the method was made capable of generating the divergence-free velocity oscillations, but only for isotropic turbulence ($\overline{u_x'^2} = \overline{u_y'^2} = \overline{u_z'^2}$). Later versions of the method can reproduce the anisotropic turbulence without the violation of incompressibility constraint as well [74]. Different methods of this class were presented in [93], [57], [113].

Thus, the recently developed structure-based turbulence generators can handle anisotropic inhomogeneous turbulence without violating the incompressibility constraint, which makes them superior to function-based ones. However, the procedures of generation of the structures and mapping of the generated velocity fields to the computational mesh are not straightforward, which makes the implementation of such methods relatively complicated.

In this work the method of Adamian will be adopted [4, 5]. It was implemented in OpenFOAM® framework by Dr. Hannes Kröger as a boundary condition and rewritten by author in form of a momentum source, analogous to work of Gritskevich [47]. The function-based generator was chosen because of the ease of conversion of the implemented boundary condition to a form of a momentum source. In the next section the formulation of the generator will be presented.

2.4.1 Description of the synthetic turbulence generator

The generator which was used in the presented work represents a velocity field at the inlet plane as a sum of the mean and fluctuating part [4]:

$$\mathbf{u}(\mathbf{x}, t) = \bar{\mathbf{u}}(\mathbf{x}) + \mathbf{u}'(\mathbf{x}, t), \quad (2.155)$$

where $\bar{\mathbf{u}}(\mathbf{x})$ is taken from a preliminary RANS calculation. Therefore the task of generation of the turbulent velocity field reduces to estimation of $\mathbf{u}'(\mathbf{x}, t)$ on each time step from given turbulence parameters (Reynolds stresses, distribution of $(k, \epsilon, \text{etc.})$). The vector field of fluctuation is in turn found as a product

$$u'_i(\mathbf{x}, t) = a_{ij}(\mathbf{x}) v'_j(\mathbf{x}, t), \quad (2.156)$$

where $a_{ij}(\mathbf{x})$ is a matrix obtained by Cholesky decomposition of the Reynolds' stress tensor ($\tau_{ij}^t = a_{ij}a_{ji}$):

$$a_{ij} = \begin{pmatrix} \sqrt{\tau_{11}^t} & 0 & 0 \\ \tau_{21}^t/a_{11} & \sqrt{\tau_{22}^t - a_{21}^2} & 0 \\ \tau_{31}^t/a_{11} & (\tau_{32}^t - a_{21}a_{31})/a_{22} & \sqrt{\tau_{33}^t - a_{31}^2 - a_{32}^2} \end{pmatrix} \quad (2.157)$$

and $\mathbf{v}'(\mathbf{x}, t)$ is an auxiliary fluctuation field, obeying the conditions $\overline{v'_i} = 0$ and $\overline{v'_i v'_j} = \delta_{ij}$. The multiplication of $\mathbf{v}'(\mathbf{x}, t)$ by a_{ij} rescales the Reynolds' stresses of the field, so as to make these equal to the prescribed ones. The auxiliary fluctuation field is in turn represented by a sum of Fourier modes:

$$\mathbf{v}'(\mathbf{x}, t) = 2\sqrt{3/2} \sum_{n=1}^N \sqrt{q^n} \left[\boldsymbol{\sigma}^n \cos(\kappa^n \mathbf{d}^n \cdot \mathbf{x} + \phi^n + s^n \frac{t}{\tau}) \right] \quad (2.158)$$

Parameters in the formula above have the following meaning:

N - number of modes, which is determined during the generation process

q^n - normalized amplitude of the n -th mode, determined by local energy spectrum of turbulence

κ^n - magnitude of the wave number vector of the n -th mode $\boldsymbol{\kappa}^n$, which has a random direction and is determined by unit vector \mathbf{d}^n , uniformly distributed of the sphere $\boldsymbol{\kappa}^n = \kappa^n \mathbf{d}^n$

$\boldsymbol{\sigma}^n$ - unit vector, representing the direction of the velocity of the n -th mode and lying in the plane, orthogonal to \mathbf{d}^n ; direction of $\boldsymbol{\sigma}^n$ in that plane is defined by the angle, uniformly distributed over the range $[0, 2\pi)$

ϕ^n - the phase of the n -th mode; uniformly distributed over $[0, 2\pi]$ real number

s^n - dimensionless angular frequency of the n -th mode; random real number with Gaussian distribution, having the mean and the standard deviation equal 2π

τ - time scale of the considered problem

The normalized mode amplitudes

$$q^n = \frac{E(\kappa^n) \Delta \kappa^n}{\sum_{n=1}^N E(\kappa^n) \Delta \kappa^n}, \quad \sum_{n=1}^N q^n = 1 \quad (2.159)$$

are calculated using the modified dimensionless von Karman energy spectrum:

$$E(\kappa) = \frac{(\kappa/\kappa_e)^4}{[1 + 2.4(\kappa/\kappa_e)^2]^{17/6}} f_\eta f_{cut}. \quad (2.160)$$

The empirical functions f_η, f_{cut} read:

$$f_\eta = \exp\left(-\left[12\frac{\kappa}{\kappa_\eta}\right]^2\right), f_{cut} = \exp\left(-\left[\frac{4\max(\kappa - 0.9\kappa_{cut}, 0)}{\kappa_{cut}}\right]^3\right), \quad (2.161)$$

where $\kappa_\eta = \frac{2\pi}{l_\eta} = \frac{2\pi}{(\nu^3/\epsilon)^{1/4}}$ (ν - kinematic viscosity, ϵ - turbulence dissipation rate, obtained from RANS calculation, l_η is understood as a wavelength, corresponding to the wave number κ_η) and $\kappa_{cut} = \frac{2\pi}{l_{cut}}$. The parameter l_{cut} , representing the minimum wavelength, which can be resolved on the given computational mesh is estimated using the following empirical formula:

$$l_{cut} = 2 \min\{\max(\Delta_x, \Delta_z, 0.3\Delta_{\max}) + 0.1d_w, \Delta_{\max}\}, \quad (2.162)$$

in which $\Delta_x, \Delta_y, \Delta_z$ are the wall-parallel (x, z) and wall-normal (y) sizes of the cells¹, where the fluctuations are generated, d_w is the wall distance and $\Delta_{\max} = \max(\Delta_x, \Delta_y, \Delta_z)$. In the core of the flow l_{cut} is twice the mesh cell size. The empirical functions f_η, f_{cut} are designed to modify the spectrum near the wave numbers $\kappa_\eta, \kappa_{cut}$ [4]. The wave number κ_e , entering (2.160), corresponds to the maximum of the energy spectrum and therefore can be calculated using the length scale of the energy containing vortices l_e : $\kappa_e = \frac{2\pi}{l_e}$. The estimation of l_e is done using the following formula:

$$l_e = \min(2d_w, 3L), \quad (2.163)$$

in which L is the integral length scale of turbulence. The particular expression for L depends on the underlying RANS closure. Since in the present work the $k - \omega$ SST model is used, L is found from (2.101). The set of wave vectors $\boldsymbol{\kappa}^i$, used in the generator is the same for the whole region of generation. Their magnitudes are terms of the geometric progression:

$$\kappa^n = \kappa^{\min} \cdot (1 + \alpha)^{n-1}, n = 1 \div N, \quad (2.164)$$

where $\alpha \in [0.01, 0.05]$, $\kappa_{\min} = \beta\kappa_e^{\min}$, β is an empirical parameter chosen to be 0.5, κ_e^{\min} is the minimum wave number of energy-containing modes in the generation region, which is found as:

$$\kappa_e^{\min} = \frac{2\pi}{l_e^{\max}} = \max_{\mathbf{x}}\{l_e(\mathbf{x})\}. \quad (2.165)$$

The number of modes N is found as the largest integer number, for which k^N does not exceed $\kappa_{\max} = 1.5 \max_{\mathbf{x}}\{\kappa_{cut}(\mathbf{x})\}$. Finally, the time scale of the problem is estimated using the characteristic velocity U and the wavelength l_e^{\max} :

$$\tau = 2l_e^{\max}/U. \quad (2.166)$$

This definition of τ allows for generation of realistic vortical structures [4], elongated in the streamwise direction near the wall and almost isotropic in the core of the flow.

2.5 Free surface formulation

Flows around the conventional ships are two-phase (air/water) with interface between the phases being the free surface. Usually, when a ship moves at low Froude numbers ($Fn < 0.15$), the free surface is hardly deformed and therefore plays an insignificant role for the hydrodynamical effects. Under such conditions the free surface can be approximated as a symmetry plane. On the other hand, when the Froude number is considerably high, the deformation of the interface between two phases should be accounted for in order to get a realistic flow picture.

In some of the cases, which were studied in the present work the investigation of the influence of free-surface deformation on the flow was desirable. Due to this reason an interface capturing method, which was adopted in the study will be briefly described in this section.

¹It is assumed that the mesh in the turbulence generation region consists of hexahedral cells

There is a variety of methods, which allow for calculation of viscous free-surface ship flows. A good overview of existing approaches can be found in [158]. One can say, that the most popular of them, which is used in the majority of the commercial CFD codes is the Volume-of-Fluid (VOF) method, proposed by Hirt and Nichols [51]. Since the viscous free-surface solver, based on the VOF algorithm was available in OpenFOAM[®], it was adopted in the current study. Numerous successful applications of VOF method to free-surface ship flows were presented in literature [7, 122, 116, 30, 63, 102, 80] (incl. its OpenFOAM[®] implementation), which indicates that the method is suitable for the problem in question.

In the framework of the VOF method the so-called indicator function α is introduced to reflect the presence of the interface between the phases. The meaning of this function is the ratio of the volume occupied by water ¹ to the total volume of the considered cell:

$$\alpha = \frac{V_\alpha}{V_{cell}}. \quad (2.167)$$

Due to this reason α is also called volume fraction. Therefore, α should lie in the range $[0; 1]$, where $\alpha = 0$ corresponds to air phase and $\alpha = 1$ to water phase. The isosurface $\alpha = 0.5$ thus determines the free surface. The liquid properties, such as density and kinematic viscosity are found as the weighted averages of these of water and air:

$$\rho = \alpha\rho_w + (1 - \alpha)\rho_a \quad (2.168)$$

$$\nu = \alpha\nu_w + (1 - \alpha)\nu_a \quad (2.169)$$

The set of differential equations, which has to be solved in the framework of VOF consists of the momentum equation, continuity equation and the transport equation of the volume fraction [123] ²:

$$\frac{\partial \rho \bar{u}_i}{\partial t} + \frac{\partial (\rho \bar{u}_i \bar{u}_j)}{\partial x_j} = -\frac{\partial \bar{p}_d^*}{\partial x_i} + \frac{\partial}{\partial x_j} \left[\mu_{tot} \left(\frac{\partial \bar{u}_i}{\partial x_j} + \frac{\partial \bar{u}_j}{\partial x_i} \right) \right] - g_i x_i \frac{\partial \rho}{\partial x_i} \quad (2.170)$$

$$\frac{\partial \bar{u}_i}{\partial x_i} = 0 \quad (2.171)$$

$$\frac{\partial \alpha}{\partial t} + \frac{\partial \alpha u_j}{\partial x_j} + \frac{\partial}{\partial x_j} (\alpha(1 - \alpha)u_{rj}) = 0. \quad (2.172)$$

Here $\mu_{tot} = (\nu_t + \nu)\rho$ is the total dynamic viscosity, $\bar{p}_d^* = \bar{p}^* - \rho g_j x_j$ - dynamic pressure, \mathbf{g} - gravitational acceleration. The turbulent viscosity ν_t is calculated in the same manner as in a single-phase formulation. In cases, when LES or hybrid RANS/LES is conducted ν_t should be replaced by ν_{sgs} or ν_{hyb} accordingly. In the framework of the present work, the influence of the interface on the turbulence model is not modeled.

One can see, that the transport equation (2.172) contains an additional non-linear term $\frac{\partial}{\partial x_j} (\alpha(1 - \alpha)u_{rj})$, which is not present in a normal convection equation. This term is added for compression of the interface and is purely artificial. In authors opinion it is related to the numerical model and will be described in Section 3.3, along with the solution procedure for the system (2.170)-(2.172).

¹In general, VOF method can treat any two liquids, but in the problem under consideration, only water (phase 1) and air (phase 2) are dealt with

²For the ease of description the surface tension force is excluded from the model, since it plays next to no role for ship flows [54]

2.6 Dynamics of a ship with two degrees of freedom

For the prediction of squat one has to solve the equations of ship dynamics, coupled with the fluid dynamics. Generally speaking, if a ship is considered a rigid body, it has six degrees of freedom. Therefore in a most general formulation six motion equations should be solved [82]. However, for the estimation of dynamic sinkage(s) and trim angle(ψ) at straight course, only two degrees of freedom are usually taken into account. The coordinate system used in the model formulation is presented in Fig. 2.5. The origin of the inertial coordinate system $Oxyz$ is located

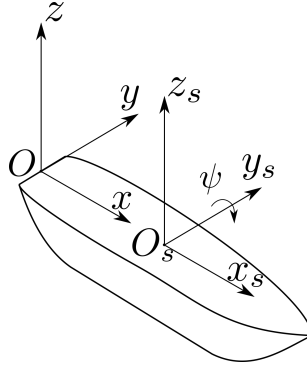


Figure 2.5: Ship coordinate system for squat computations

at the aft perpendicular at the level of the undisturbed free surface in the middle line plane. The origin of the ship-fixed coordinate system $O_s x_s y_s z_s$ is located at the center of gravity \mathbf{G} . Therefore $x_g = z_s \cos \psi + x_s \sin \psi + G_x$, $y_g = y_s$, $z_g = z_s + G_z + s$, where s is the ship sinkage.

In case of two degrees of freedom and the inversed motion ($V_{x_s} = V_{y_s} = 0$, $\omega_{x_s} = \omega_{z_s} = 0$) the following system describes the motion of the ship in the ship-fixed coordinate system with principle axes ($I_{xy} = I_{xz} = I_{yz}$, $S_x = S_y = S_z = 0$) [64]:

$$\begin{aligned} m \frac{dV_{z_s}}{dt} &= F_{z_s} - mg_{z_s} \\ I_{y_s y_s} \frac{d\omega_{y_s}}{dt} &= M_{y_s}. \end{aligned} \quad (2.173)$$

where m is the ship mass, $I_{y_s y_s}$ - inertial moment about y_s -axis, F_{z_s} , M_{y_s} are respectively the vertical force and the trimming moment acting on the ship, including hydrostatic, hydrodynamic as well as the fluid inertial forces, V_{z_s} - vertical ship speed in ship-fixed system, ω_{y_s} - ship's angular velocity vector about y_s axis.

The values of s and ψ can be obtained as:

$$\begin{aligned} s &= \int_0^t V_{z_s}(t) dt \\ \psi &= \int_0^t \omega_{y_s}(t) dt. \end{aligned} \quad (2.174)$$

The force F_{z_s} and moment M_{y_s} are found using the following formulas:

$$F_{z_s} = \int_{S_h} (R_{\psi}^T \mathcal{T} \cdot \mathbf{n}_s) \cdot \mathbf{k}_s dS \quad (2.175)$$

$$M_{y_s} = \int_{S_h} [\mathbf{r}_s \times (R_{\psi}^T \mathcal{T} \cdot \mathbf{n}_s)] \cdot \mathbf{j}_s dS, \quad (2.176)$$

with \mathcal{T} being the total stress tensor in the considered flow (in inertial system), R_{ψ} -

transformation matrix from the ship-fixed to the inertial system

$$R_\psi = \begin{pmatrix} \cos \psi & 0 & \sin \psi \\ 0 & 1 & 0 \\ -\sin \psi & 0 & \cos \psi \end{pmatrix}, \quad (2.177)$$

\mathbf{n}_s - unit normal to the ship hull surface in ship-fixed system, S_h - surface of the ship hull, \mathbf{r}_s - radius-vector of the point on the ship hull surface in the coordinate system $O_s x_s y_s z_s$, $\mathbf{j}_s, \mathbf{k}_s$ - unit vectors aligned with the y_s and z_s axes respectively.

The dynamics of the fluid during the squat computations will be modeled in conjunction with the presented above VOF formulation. In this case the components of \mathcal{T} can be expressed as:

$$\tau_{ij} = (\overline{p}_d^* + \rho g_z z) \delta_{ij} + 2\mu_{tot} S_{ij}. \quad (2.178)$$

Here the dynamic pressure field \overline{p}_d^* , density field ρ , tensor field S_{ij} and total dynamic viscosity μ_{tot} are found during the solution of the system (2.170)-(2.172). The fluid dynamics thus influences the ship motion on account of the stress tensor, whereas the ship dynamics influences the fluid on account of the motion of domain boundaries (ship hull).

This page intentionally left blank

Chapter 3

Numerical method

3.1 Finite volume method

In the framework of the presented research the Finite Volume Method (FVM) is used for the discretization of the underlying PDE. This method is nowadays one of the most widely applied discretization techniques in CFD, which is used in multiple computational codes: Fluent, StarCCM+, CFX, OpenFOAM to name but a few.

In this section the application of FVM to general convection-diffusion equation will be demonstrated. Since the computations in the present work were conducted using the FVM implemented in OpenFOAM, the description of the method will be adapted accordingly. [58, 159]. The FVM assumes that the computational domain is completely filled by non-overlapping

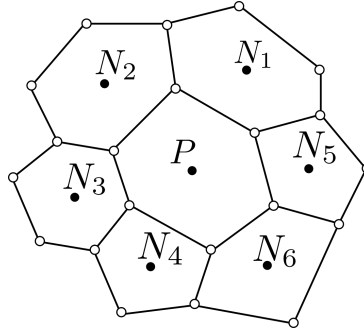


Figure 3.1: Sketch of a two-dimensional computational stencil in FVM

control volumes (CV). The unknown quantities in the framework of the cell-centered FVM, which is embodied in OpenFOAM, are stored in the geometric centers of control volumes \mathbf{x}_P . CV's share a number of flat faces with their neighbors. A typical structure of a finite volume mesh in two dimensions is sketched in Figure 3.3. OpenFOAM can operate with cells of arbitrary polyhedral shape.

Differential form of a convection-diffusion equation for the scalar field ϕ reads [153]:

$$\frac{\partial \rho \phi}{\partial t} + \nabla \cdot (\rho \mathbf{u} \phi) = \nabla \cdot (\rho \Gamma_\phi \nabla \phi) + S_\phi(\phi). \quad (3.1)$$

In order to be discretized using FVM this equation should be first converted into an integral form. In order to do so, (3.1) is integrated over the control volume and over the time step Δt , giving:

$$\int_t^{t+\Delta t} \int_{V_P} \frac{\partial \rho \phi}{\partial t} dV dt' + \int_t^{t+\Delta t} \int_{V_P} \nabla \cdot (\rho \mathbf{u} \phi) dV dt' = \int_t^{t+\Delta t} \int_{V_P} \nabla \cdot (\rho \Gamma_\phi \nabla \phi) dV dt' + \int_t^{t+\Delta t} \int_{V_P} S_\phi dV dt'. \quad (3.2)$$

The next step is the approximation of the volume integrals in (3.2) the ones containing no spatial differentiation operations are treated using the 2nd order accurate midpoint rule [153], [58], [109]:

$$\int_{V_P} \frac{\partial \rho \phi}{\partial t} dV \approx \left(\frac{\partial \rho \phi}{\partial t} \right)_P V_P \quad (3.3)$$

$$\int_{V_P} S_\phi(\phi) dV \approx (Su + Sp \phi_P) V_P, \quad (3.4)$$

with Su and Sp being the coefficients of the linearized representation of the source term; whereas the ones representing the convection and diffusion terms are first converted to surface integrals using the Gauss' theorem and then discretized. This procedure will be discussed in the following subsections.

3.1.1 Approximation of the convection term

Application of the Gauss' theorem to the integral of the convective term gives:

$$\int_{V_P} \nabla \cdot (\rho \mathbf{u} \phi) dV = \int_{S_P} \rho \phi \mathbf{u} \cdot \mathbf{n} dS. \quad (3.5)$$

The r.h.s of (3.5) is then represented as a sum of the integrals over the cell faces:

$$\int_{S_P} \rho \phi \mathbf{u} \cdot \mathbf{n} dS = \sum_{i=1}^N \int_{f_i} \rho \phi \mathbf{u} \cdot \mathbf{n} dS, \quad (3.6)$$

where N is the number of neighbors of the considered control volume and f_i stands for its i -th face. Application of midpoint rule to the terms in the sum yields:

$$\int_{f_i} \rho \phi \mathbf{u} \cdot \mathbf{n} dS \approx (\rho \mathbf{u} \cdot \mathbf{n})_{f_i} S_{f_i} \phi_{f_i}, \quad (3.7)$$

where the subscript $(\cdot)_{f_i}$ denotes the evaluation in the geometrical center of the i -th face and S_{f_i} - area of the i -th face. The coefficient in front of $\phi_f : F_{f_i} = (\rho \mathbf{u} \cdot \mathbf{n})_{f_i} S_{f_i}$ is called mass flux and is assumed to be known during the discretization process of (3.1). As it has been mentioned, in the framework of cell-centered FVM the field values are stored in the centers of control volumes, which means, that in order to obtain the values in the face center some kind of interpolation should be used. The value of the unknown ϕ on the face should be now represented in terms of cell center values.

Linear interpolation The most intuitive approach for doing this is to apply the linear interpolation between the cell values:

$$\phi_{f_i}^L = w \phi_P + (1 - w) \phi_N, \quad (3.8)$$

where the weight w is reads (see Figure 3.2):

$$w = \frac{|f_i N_i|}{|P N_i|}. \quad (3.9)$$

The formula (3.8) has a nominal second order of accuracy on uniform meshes [36], which is considered sufficient for industrial CFD. At the same time for Peclet numbers ¹ higher than 2 linear interpolation may lead to a nonphysical solution, because of the violation of the boundedness criterion [153, 109]. Therefore, in practice, pure linear interpolation for convective term is rarely used.

Upwind interpolation The so-called upwind interpolation uses the following formula for representation of the face value:

$$\phi_{f_i}^U = \begin{cases} \phi_P, & F \geq 0 \\ \phi_{N_i}, & F < 0 \end{cases} \quad (3.10)$$

¹Peclet number Pe is the ratio of convective flux to diffusive flux

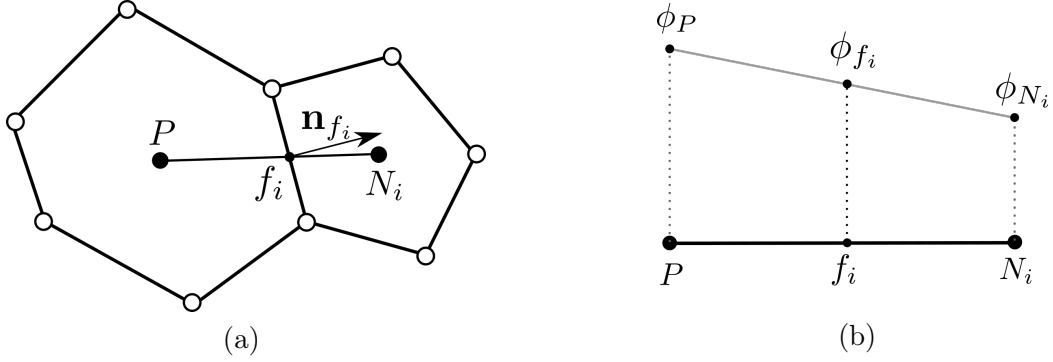


Figure 3.2: Face interpolation: (a) - central and neighbor cells and a face, on which the value in terms of ϕ_P and ϕ_{N_i} should be obtained, (b) - sketch of linear interpolation. P - center of the cell, for which the equation is discretized. N_i - center of one of the neighboring cells. The vectors $\overline{f_i N_i}$ and $\overline{P N_i}$ are used for the calculation of the weight w

One can see, that on the contrary to linear interpolation, it is dependent on the flow direction. This discretization technique is unconditionally bounded. However, this advantage is attained on account of the excessive numerical diffusion, since the scheme is only first order accurate.

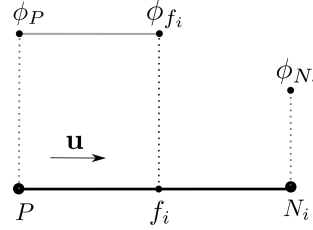


Figure 3.3: Upwind face interpolation: a piecewise-constant interpolation from the cell center, from which the flow is incoming

Linear upwind interpolation It is also possible to obtain a second order upwind-biased interpolation by using the gradient of the unknown variable in the cell centers:

$$\phi_{f_i}^{LU} = \begin{cases} \phi_P + \overline{P f_i} \cdot (\nabla \phi)_P, & F \geq 0 \\ \phi_{N_i} + \overline{N_i f_i} \cdot (\nabla \phi)_{N_i}, & F < 0. \end{cases} \quad (3.11)$$

The terms, which appeared in the representation of the face values can be thought of as a correction to the upwind scheme, increasing the order of accuracy of the latter. In fact, in OpenFOAM® these terms are treated as explicit source terms (contribute to S_u , introduced earlier). This technique is called deferred correction [36, 153] and was introduced to force the resulting linear system to satisfy the boundedness criterion [153] despite the higher order interpolation.

Strelets' blended scheme Performing the DES simulations of flows with massive separations Strelets [147] observed, that the upwind biasing of differencing schemes used for the convective term had a negative influence on the quality of the results. The reason for this is that the level of numerical diffusion of upwind-biased schemes is higher compared to centered scheme for the the same mesh. At the same time it was mentioned, that in the RANS regions the pure centered differencing scheme usually leads to the loss of stability of the numerical solution. In order to avoid these problems a blended scheme was proposed, which combined the fourth order centered scheme with the fifth order upwind scheme, depending on the local flow parameters. In the framework of the presented research the blending of linear and linear upwind interpolations in the same manner will be used:

$$\phi_{f_i}^{SB} = (1 - \sigma)\phi_{f_i}^L + \sigma\phi_{f_i}^{LU}, \quad (3.12)$$

where σ is given by:

$$\sigma = \sigma_{\max} \tanh(A^{C_{H1}}). \quad (3.13)$$

The function A is defined as:

$$A = C_{H2} \max \{[(C_{DES}\Delta/l_{turb})/g - 0.5], 0\}, \quad (3.14)$$

where the length scale l_{turb} is found from:

$$l_{turb} = (\nu_t + \nu)/[C_\mu^{3/2}K]^{1/2} \quad (3.15)$$

with $K = \max\{[(S^2 + \Omega^2)/2]^{1/2}, 0.1\tau^{-1}\}$ and τ being the characteristic convective time. The function g is designed to enforce the use of upwind scheme in the disturbed irrotational flow regions ($\Omega \ll 1, S > 0$):

$$g = \tanh(B^4) \\ B = C_{H3}\Omega \max(S, \Omega) / \max[(S^2 + \Omega^2)/2, 10^{-20}]. \quad (3.16)$$

The constants, used in the formulas above have the following values: $\sigma_{\max} = 1, C_{H1} = 3.0, C_{H2} = 1.0, C_{H3} = 2.0$. In the presented research the blended interpolation is used in all hybrid RANS/LES calculations of ship flows. For canonical flows, where it was possible without the divergence of numerical solution, the linear interpolation was used.

Blending depending on the mesh quality Experience shows, that computational meshes for complex geometries may sometimes contain a number of cells of bad quality. (for definition of various cell quality parameters see [58]). Usually the number of “bad” cells is very small compared to the total cell number. However, application of higher order discretization techniques in these cells can be problematic and lead to strong numerical instabilities. In order to be able to conduct a computation on a mesh, containing “bad” cells, additional blending dependent on mesh quality was added, which guaranteed the application of upwind interpolation in problematic regions.

Using the interpolation techniques, described above, all the terms in (3.7) are represented as a linear combination of cell-centered values of ϕ .

3.1.2 Approximation of the diffusion term

In order to discretize the diffusion term the Gauss theorem is applied, as previously:

$$\int_{V_P} \nabla \cdot (\rho \Gamma_\phi \nabla \phi) dV = \int_{S_P} \rho \Gamma_\phi \nabla \phi \cdot \mathbf{n} dS. \quad (3.17)$$

Now it is possible to split the surface integral into the sum of integrals over the faces, obtaining:

$$\int_{S_P} \rho \Gamma_\phi \nabla \phi \cdot \mathbf{n} dS = \sum_{i=1}^N \int_{f_i} \rho \Gamma_\phi \nabla \phi \cdot \mathbf{n} dS \approx \sum_{i=1}^N (\rho \Gamma_\phi)_{f_i} S_{f_i} (\nabla \phi \cdot \mathbf{n})_{f_i} \quad (3.18)$$

The coefficients $(\rho \Gamma_\phi)_{f_i} S_{f_i}$ are assumed to be known, whereas the normal gradient of the un-

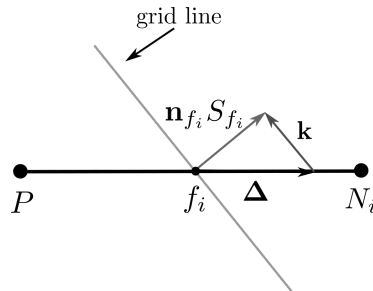


Figure 3.4: Sketch of the vectors, used for over-relaxed non-orthogonality correction approach

known ϕ at the face should be approximated, as previously, in terms of cell center values of ϕ . On the orthogonal mesh a simple central difference can be used for evaluating the normal derivative. On the contrary, for the mesh with considerable non-orthogonality application of CDS would lead to reduction of the accuracy to 1st order. Therefore, for general unstructured meshes a more sophisticated approaches for evaluation of the normal gradient are used. The overview of different approaches for discretization of $(\nabla\phi \cdot \mathbf{n})_{f_i}$ is given, for example, in [153, 58, 28]. In the present work the overrelaxed approach is used, consisting in application of the following formula:

$$(\nabla\phi \cdot \mathbf{n})_{f_i} S_{f_i} = \Delta \cdot (\nabla\phi)_{f_i} + \mathbf{k} \cdot (\nabla\phi)_{f_i}, \quad (3.19)$$

where Δ and \mathbf{k} are vectors such, that $\mathbf{n}_{f_i} S_{f_i} = \Delta + \mathbf{k}$ and $\Delta \parallel \overline{Pf_i}$. In the framework of the overrelaxed approach Δ is calculated as:

$$\Delta = \frac{\overline{Pf_i}}{\overline{Pf_i} \cdot \mathbf{n}_{f_i} S_{f_i}} S_{f_i}^2 = \frac{\overline{Pf_i}}{\overline{Pf_i} \cdot \mathbf{n}_{f_i}} S_{f_i} \quad (3.20)$$

Finally, after introduction of Δ and \mathbf{k} , the CDS is used for the first term in (3.21) (i.e. this term contributes to the matrix coefficients), whereas the second one is treated as the source term with $(\nabla\phi)_{f_i}$ being explicitly calculated from the given ϕ field:

$$(\nabla\phi \cdot \mathbf{n})_{f_i} S_{f_i} = \underbrace{|\Delta| \frac{\phi_{N_i} - \phi_P}{|\overline{Pf_i}|}}_{\text{implicit contribution}} + \underbrace{\mathbf{k} \cdot (\nabla\phi)_{f_i}}_{\text{explicit correction}}, \quad (3.21)$$

3.1.3 Temporal discretization

Using the formulas, given in the previous subsections, (3.2) can be now written as:

$$\begin{aligned} \int_t^{t+\Delta t} \left[\left(\frac{\partial \rho \phi}{\partial t} \right)_P V_P + \sum_{i=1}^N (\rho \mathbf{u} \cdot \mathbf{n})_{f_i} S_{f_i} \phi_{f_i} - \sum_{i=1}^N (\rho \Gamma_\phi)_{f_i} S_{f_i} (\nabla\phi \cdot \mathbf{n})_{f_i} \right] dt \\ = \int_t^{t+\Delta t} (Su + Sp\phi_P) V_P dt \end{aligned} \quad (3.22)$$

Using the forward differencing scheme for the approximation of the time derivative

$$\left(\frac{\partial \rho \phi}{\partial t} \right)_P = \frac{\rho_P^n \phi_P^n - \rho_P^o \phi_P^o}{\Delta t} \quad (3.23)$$

and time integration using midpoint rule

$$\int_t^{t+\Delta t} \phi(t) dt = \frac{1}{2} (\phi^o + \phi^n) \Delta t \quad (3.24)$$

and assuming that ρ, Γ_ϕ are constant in time one obtains [58]:

$$\begin{aligned} \frac{\rho_P \phi_P^n - \rho_P \phi_P^o}{\Delta t} + \frac{1}{2} \left(\left[\sum_{i=1}^N (\rho \mathbf{u} \cdot \mathbf{n})_{f_i} S_{f_i} \phi_{f_i} \right]^n + \left[\sum_{i=1}^N (\rho \mathbf{u} \cdot \mathbf{n})_{f_i} S_{f_i} \phi_{f_i} \right]^o \right) \\ - \frac{1}{2} \left(\left[\sum_{i=1}^N (\rho \Gamma_\phi)_{f_i} S_{f_i} (\nabla\phi \cdot \mathbf{n})_{f_i} \right]^n + \left[\sum_{i=1}^N (\rho \Gamma_\phi)_{f_i} S_{f_i} (\nabla\phi \cdot \mathbf{n})_{f_i} \right]^o \right) \\ = SuV_P + \frac{1}{2} (\phi_P^n + \phi_P^o) SpV_P \end{aligned} \quad (3.25)$$

The above linear algebraic equation after represents the discrete analog of the equation (3.1) for the case of Crank-Nicolson time-stepping scheme, which is second order accurate in time ¹. When (3.25) is written for each cell and the face values are represented by the values in the cell centers, one obtains a linear system [109]:

$$a_P \phi_P^n + \sum_{i=1}^N a_{N_i} \phi_{N_i}^n = b, \quad (3.26)$$

which has to be solved for ϕ_P^n , $\phi_{N_i}^n$ in order to obtain the values at the next (n) time step, starting from old one (o). Other time-stepping schemes are discussed in [58], including first order implicit Euler scheme and second order backward Euler scheme. In each case the resulting system of linear algebraic equations can be written as , whereby the coefficients a_P , a_{N_i} will be different.

The linear system, obtained from (3.1) using FVM has a sparse matrix and is solved using iterative methods, such as preconditioned bi-conjugate gradient (PBiCG) method or bi-conjugate gradient stabilized method (BiCGStab), which are both present in OpenFOAM[®]. The described above discretization procedure is used in OpenFOAM[®] for linearized momentum equation and for the transport equations of turbulence quantities.

It is straightforward to obtain a representation of the discretized Poisson equation from (3.22) by removing time integration as well as the terms, related to time derivative and convection. For this equation other methods for solving the linear system are used, such as preconditioned conjugate gradient (PCG) method [45] or geometric-algebraic multigrid method (GAMG) [153].

3.2 Solution algorithms for the incompressible Navier-Stokes equations

The presented above method of solving general convection-diffusion equation is unfortunately not sufficient for dealing with the system (2.6), (2.16). There are multiple reasons for this:

1. The convective term in (2.6) is non-linear with respect to velocity. On the contrary to (3.1), where ϕ is transported with the known velocity \mathbf{u} , in (2.16) the velocity is “being transported by itself” [58]. Discretisation procedure from Section 3.1.1 then yields:

$$\int_{V_P} \nabla \cdot (\rho \mathbf{u} \mathbf{u}) dV = \sum_{i=1}^N (\rho \mathbf{u} \cdot \mathbf{n})_{f_i} S_{f_i} \mathbf{u}_{f_i}, \quad (3.27)$$

where the discretization coefficients also depend on unknown \mathbf{u} . In order to overcome this difficulty, the velocity from the old time step is used for evaluation of the fluxes, leading to a Picard iteration [11]. Number of iterations, needed for the convergence of the velocity field depends on the time step size.

2. Continuity and momentum equations are coupled.
3. As it was previously mentioned in Section 2.1.6, the way of determining the pressure from (2.6), (2.16) is not straightforward. Direct application of presented above discretization procedures would result in an ill-conditioned system [11, 25].

The latter two issues are solved in this study by using a combination of PISO and SIMPLE algorithms for collocated grid arrangement. Both algorithms are based on derivation of pressure equation, which is used to find the correction for the velocity field in order to obtain conservative

¹The description of the discretization of the boundary conditions is omitted here. The reader is referred to [58, 123]

fluxes. The procedure of derivation of pressure equation on which the OpenFOAM® algorithms is based differs from that presented in the majority of books on CFD and therefore the formulation from [58] is briefly presented in the next sections.

3.2.1 Discrete pressure equation

The derivation of pressure equation starts from the semi-discretized momentum equation [58, 25]:

$$a_p \mathbf{u}_p = H(\mathbf{u}) - \nabla p, \quad (3.28)$$

where $H(\mathbf{u})$ reads:

$$H(\mathbf{u}) = - \sum_{i=1}^N a_{N_i} \mathbf{u}_{N_i} + \frac{\mathbf{u}^o}{\Delta t} \quad (3.29)$$

The discretized using FVM continuity equation has the following form:

$$\nabla \cdot \mathbf{u} = \sum_{i=1}^N \mathbf{u}_{f_i} \cdot \mathbf{n}_{f_i} S_{f_i} = 0 \quad (3.30)$$

From (3.28) \mathbf{u}_p can be formally expressed as:

$$\mathbf{u}_P = \frac{H(\mathbf{u})}{a_P} - \frac{1}{a_P} \nabla p. \quad (3.31)$$

The velocity on the faces, obtained by interpolation of the above formula, is then substituted into (3.30), which gives:

$$\nabla \cdot \left(\frac{1}{a_P} \nabla p \right) = \nabla \cdot \left(\frac{H(\mathbf{u})}{a_P} \right) \quad (3.32)$$

The discretization of Laplacian operator is done in the same way as for the diffusion term. The r.h.s is treated explicitly and is calculated as:

$$\nabla \cdot \left(\frac{H(\mathbf{u})}{a_P} \right) = \sum_{i=1}^N \left(\frac{H(\mathbf{u})}{a_P} \right)_{f_i} \cdot \mathbf{n}_{f_i} S_{f_i}. \quad (3.33)$$

Therefore the continuity equation in the original system is replaced by (3.32) and the set of discrete equations solved is:

$$a_P \mathbf{u}_P = H(\mathbf{u}) - \sum_{i=1}^N p_{f_i} \mathbf{n}_{f_i} S_{f_i} \quad (3.34)$$

$$\sum_{i=1}^N \left[\left(\frac{1}{a_P} \right)_{f_i} (\nabla p \cdot \mathbf{n})_{f_i} S_{f_i} \right] = \sum_{i=1}^N \left(\frac{H(\mathbf{u})}{a_P} \right)_{f_i} \cdot \mathbf{n}_{f_i} S_{f_i} \quad (3.35)$$

The fluxes F_{f_i} , which satisfy (3.30) by construction of the method are found as:

$$F_{f_i} = \mathbf{u}_{f_i} \mathbf{n}_{f_i} S_{f_i} = \left[\left(\frac{H(\mathbf{u})}{a_P} \right)_{f_i} - \left(\frac{1}{a_P} \right)_{f_i} (\nabla p)_{f_i} \right] \cdot \mathbf{n}_{f_i} S_{f_i}, \quad (3.36)$$

where p is the solution of (3.2.1). The coupling of equations (3.40), in the present study is done in segregated manner. The exact sequence of solution steps in SIMPLE, PISO and PIMPLE is different ¹ and will be discussed in following sections.

¹The solution procedures of OpenFOAM are considered

3.2.2 Pressure-velocity coupling algorithms

The SIMPLE algorithm

The SIMPLE¹ algorithm was proposed by Patankar [109] and was originally developed for steady-state problems. However, it can be successfully applied for transient problems as well. The method is designed for the cases where the solution can considerably change between the iterations (which is the cases for steady-state problems) which means, that the nonlinear effects are supposed to be of a higher importance than pressure-velocity coupling. Briefly formulated, steps of OpenFOAM SIMPLE method are²:

1. Solve implicitly under-relaxed equation (3.40) [153, 58, 109] with the pressure field taken from initial guess or previous iteration. Find $H(\mathbf{u})$, a_P in order to assemble (3.2.1)
2. Solve the equation (3.2.1) for p
3. Calculate the conservative fluxes using formula (3.36)
4. Under-relax the pressure field
5. Update the velocity field using formula (3.31)
6. Solve all other transport equations (e.g. k , ω)
7. Repeat the steps 1-6 till convergence

At convergence one obtains the velocity and pressure fields, satisfying the underlying equations.

The PISO algorithm

The PISO algorithm was developed by Issa [56] for unsteady flows. On the contrary to SIMPLE, for which it was assumed that the nonlinear effects play a major role, in PISO the time step is supposed to be small enough, for the non-linear effects to be negligible. Hence, the pressure-velocity coupling is more important. Solution procedure³ is the following:

1. Assemble and solve equation (3.40) [153, 58, 109] with the pressure field taken from initial guess or previous iteration. Find $H(\mathbf{u})$ in order to assemble (3.2.1)
2. Solve the equation (3.2.1) for p
3. Calculate the conservative fluxes using formula (3.36)
4. Correct the velocity field using formula (3.31)
5. Update the coefficients in (3.2.1) using the corrected velocity
6. Repeat steps 2-5 for prescribed number of iterations
7. Solve all other transport equations (e.g. k , ω)
8. Go to the next time step and start from step 1

The PIMPLE algorithm

The so-called PIMPLE method in OpenFOAM[®] is a combination of PISO and SIMPLE in the following manner. For each time step the user can specify a desired number of outer iterations n . On each outer iteration the above PISO procedure is used with a number of pressure correction steps m . There is also an option to under-relax the momentum equation and the pressure field, which makes the approach similar to SIMPLE. This algorithm allows for solving unsteady flows with relatively high Courant numbers. Values of Co up to 20 were attained by the author without the loss of stability.

¹Semi-Implicit Method for Pressure-Linked Equations

²See `simpleFoam` solver

³Corresponding to `pisoFoam` solver

3.3 Solution algorithm for the viscous incompressible free-surface flows

The system of equations of the VOF method differs from that dealt with in the previous sections of this chapter on account of the density gradient in the momentum equation and transport equation for indicator function. However, the solution procedure is very similar to the presented above with some modifications. The discretized momentum equation for each cell can in this case be written as:

$$a_P \mathbf{u}_P = H(\mathbf{u}) - \nabla p_d - \mathbf{g} \cdot \mathbf{x} \nabla \rho. \quad (3.37)$$

Then (3.28) \mathbf{u}_P is expressed as:

$$\mathbf{u}_P = \frac{H(\mathbf{u})}{a_P} - \frac{1}{a_P} \nabla p_d - \frac{1}{a_P} \mathbf{g} \cdot \mathbf{x} \nabla \rho, \quad (3.38)$$

giving the following pressure equation:

$$\nabla \cdot \left(\frac{1}{a_P} \nabla p_d \right) = \nabla \cdot \left(\frac{H(\mathbf{u})}{a_P} - \frac{1}{a_P} \mathbf{g} \cdot \mathbf{x} \nabla \rho \right) \quad (3.39)$$

the set of discrete equations solved is:

$$a_P \mathbf{u}_P = H(\mathbf{u}) - \sum_{i=1}^N (p_d)_{f_i} \mathbf{n}_{f_i} S_{f_i} - \mathbf{g} \cdot \mathbf{x}_P \sum_{i=1}^N \rho_{f_i} \mathbf{n}_{f_i} S_{f_i} \quad (3.40)$$

$$\sum_{i=1}^N \left[\left(\frac{1}{a_P} \right)_{f_i} (\nabla p_d \cdot \mathbf{n})_{f_i} S_{f_i} \right] = \sum_{i=1}^N \left[\left(\frac{H(\mathbf{u})}{a_P} \right)_{f_i} \cdot \mathbf{n}_{f_i} S_{f_i} \right] \quad (3.41)$$

$$- \sum_{i=1}^N \left[\left(\frac{1}{a_P} \right)_{f_i} (\mathbf{g} \cdot \mathbf{x})_{f_i} \rho_{f_i} \mathbf{n}_{f_i} S_{f_i} \right] \quad (3.42)$$

The fluxes F , which satisfy (3.30) by construction of the method are found as:

$$F_{f_i} = \mathbf{u}_{f_i} \mathbf{n}_{f_i} S_{f_i} = \left[\left(\frac{H(\mathbf{u})}{a_P} \right)_{f_i} - \left(\frac{1}{a_P} \right)_{f_i} (\nabla p_d)_{f_i} - \left(\frac{1}{a_P} \right)_{f_i} (\mathbf{g} \cdot \mathbf{x})_{f_i} \rho_{f_i} \right] \cdot \mathbf{n}_{f_i} S_{f_i} \quad (3.43)$$

where p_d is the solution of (3.42).

Additional attention should be paid to solution of volume fraction transport equation ¹. A challenge one faces here is the prevention of smearing of the indicator function due to the numerical diffusion. There are a few strategies, allowing to do so. One of them is the development of special interpolation techniques with compressive properties, such as CICSAM [152], HRIC [106], etc. Another opportunity is to use anti-diffusion for interface sharpening [137]. In OpenFOAM this problem is solved differently: an artificial compression term $\frac{\partial}{\partial x_j} (\alpha(1-\alpha)u_{rj})$ is added to the transport equation for volume fraction (see Eq. (2.172)). The compression flux, corresponding to this term reads:

$$F_{c,f_i} = C_\alpha \left| \frac{F_{f_i}}{S_{f_i}} \right| (\mathbf{n}^*)_{f_i}, \quad (3.44)$$

where $\mathbf{n}^*_{f_i}$ is the interface normal, interpolated from the cell center to the face and C_α is the coefficient, determining the compression intensity, which is usually taken unity. The normal is

¹The equation (2.172) contains the velocity \mathbf{u} , which is assumed to be divergence-free. However, the procedure of solution of Navier-Stokes equations provide only the fluxes F , which are conservative, not the velocity field. Therefore in all discretization procedures for eqn. (2.172) the fluxes are found from (3.43)

found as:

$$\mathbf{n}^* = \frac{\nabla \alpha}{|\nabla \alpha| + \epsilon}, \quad (3.45)$$

where ϵ is a small number, used for stabilizing the gradient calculation in regions, where α is constant.

In order to get a bounded solution without overshoots and undershoots semi-implicit MULES algorithm is used, based on the idea of flux-corrected transport method, proposed by Boris and Book [17]. The description of MULES can be found in [24]. Even though the modified transport equation for α is solved semi-implicitly, it is explicitly coupled with the momentum equation.

The solution algorithm of the VOF solvers in OpenFOAM has been changing over time. The latest detailed description of the numerical procedure can be found in [24]. Previous versions were described in [123], [12], [151].

3.3.1 Mesh deformation algorithm for shallow water

In order to predict ship squat using FVM one has to solve the VOF equations on the moving mesh, which would resolve the ship motion. In the present work the finite volume mesh

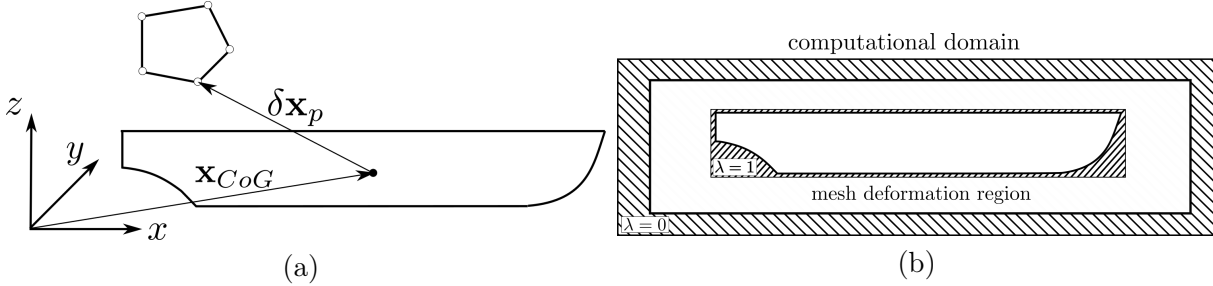


Figure 3.5: Mesh motion algorithm: (a) - sketch of the vectors used in formula (3.46), (b) - bounding boxes used for λ prescription in computational domain

is deformed in order to adapt it to the current ship position. Hence, the mesh points on the ship patch follow the ship motion as parts of the rigid body, points on the domain boundaries (except the ship) are fixed and the displacement of the rest of the points should be determined using some algorithm.

OpenFOAM provides multiple algorithms for determining the displacement of the mesh points based on solution of Laplace or pseudo-solid equations [59]. The built-in methods work fine for the cases, where the moving body is immersed in a large computational domain and is located far from the boundaries. However, this condition is not satisfied when a task of squat prediction is being solved. In this case the distance from the moving ship hull to the bottom is very small and built-in algorithms start losing stability.

In order to overcome this difficulty, a simple mesh motion algorithm was implemented by the author, using an explicit formula to determine the position of the mesh points \mathbf{x}_p at the timestep n :

$$\mathbf{x}_p^n = \mathbf{x}_p^0 + \lambda[(\mathbf{x}_{CoG}^n - \mathbf{x}_{CoG}^0) + R^n \cdot \delta \mathbf{x}_p], \quad (3.46)$$

where \mathbf{x}_p^0 is the initial (at time 0) coordinate of the point in global coordinate system, $\mathbf{x}_{CoG}^0, \mathbf{x}_{CoG}^n$ - coordinates of the center of gravity of the considered body at time 0 and n respectively, R^n - rotation matrix at the timestep n , dependent on yaw, pitch and roll angles, $\delta \mathbf{x}_p = \mathbf{x}_p^0 - \mathbf{x}_{CoG}^0$ is the initial radius vector of the point in the ship-fixed system and, finally, λ is a scalar field, determining, to which extent the point follows the rigid body motion. For $\lambda = 1$ a mesh point is moving as a part of rigid body, for $\lambda = 0$ the mesh point is fixed to its original position, in the region $\lambda \in (0, 1)$ the mesh is deformed (see Fig. 3.5). A sample of distribution of λ parameter

as well as results of mesh deformation for simple mesh are shown in Figure 3.6. Using this

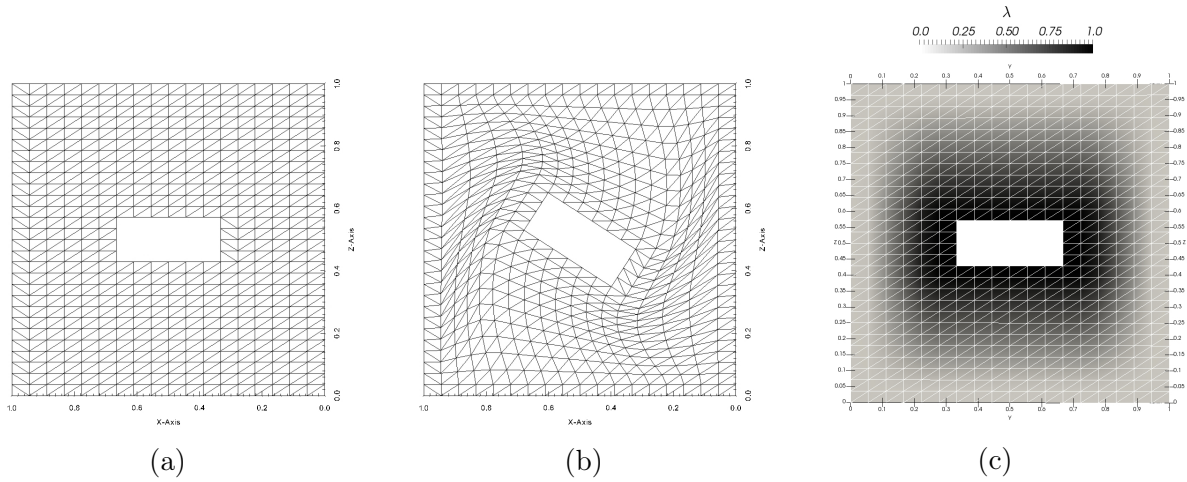


Figure 3.6: Example of application of presented algorithm: (a) - undeformed mesh, (b) - mesh with rotated body, (c) - distribution of λ . One can see that the cells in the vicinity of the body preserve their form

method it was possible to resolve the ship motion in shallow water for the dynamic under keel clearance as small as 5 mm for approximately nine meter long model, without creation of negative control volumes. Further reduction of the under keel clearance resulted in the breakdown of the computation because of the presence of cells with negative volume. Even though this method is not applicable for large body displacements, it possesses a number of attractive features: low computational cost and preservation of cell form in the bounding box around the moving body (see Fig. 3.6). The developed algorithm was initially implemented in OpenFOAM-2.1.x and later converted to OpenFOAM-2.3.x¹.

3.3.2 Details of trim and sinkage computation method

Quasi-steady VOF

Previously given description of VOF algorithm corresponds to a fully unsteady problem. This formulation has proven to be inefficient for squat prediction, since in this case a steady-state solution is sought and the time evolution of the unknown fields is not of interest. The same applies to the task of resistance prediction in calm water (if the flow is steady). For the latter problem a quasi-steady state solver `LTSInterFoam` is available in OpenFOAM, in which the Euler implicit time stepping scheme with spatially variable time step is used. The time step field is determined based on the local Courant number. This way the solution evolves with different speed in each cell. This approach clearly violates the conservation laws (before the convergence is attained), but allows to reach the steady-state solution much faster than the unsteady simulation. The adaptation of the `LTSInterFoam` for the squat prediction problems, i.e. inclusion mesh motion capabilities was performed by the author. The solver `LTSInterDyMFoam` was developed for OpenFOAM-2.3.x and validated for squat prediction in shallow water. The validation results will be presented in the next chapter.

Using quasi-steady state solver one can obtain the forces and moments acting on the ship underway. In a normal unsteady simulation one would need to substitute the calculated forces into the system (??) on each timestep and solve it numerically (using, for example, leapfrog method). The problem is, however, that in a quasi-steady calculation the timestep is different in each cell and therefore it is not clear, which of them should be used for integration of (??).

¹The analogs (so-called Slerp method) of the described algorithm appeared independently in official OpenFOAM distribution starting from OpenFOAM-2.3.x

To resolve this ambiguity, it was decided to use the time step size averaged over a bounding box around the ship hull, similar to that shown in Figure 3.5:

$$\Delta t = \sum_{box} \Delta t_P V_P / \sum_{box} V_P. \quad (3.47)$$

This value characterizes, how fast the flow in the near of the ship is evolving, and thus allows to adapt the time step for solution of ship motion equations to the quasi-steady simulation, in which the time step is locally determined.

Modification of 2DoF ship motion equations

In order to optimize the convergence rate of ship trim and sinkage additional damping terms are included into the equations (2.173), based on the analysis of the damped harmonic oscillator. For a vertical motion a linear hydrostatic spring is considered:

$$m \frac{dV_{z_s}}{dt} + D_s V_{z_s} + C_{hs} s = 0, \quad (3.48)$$

where D_s is the unknown damping coefficient and $C_{hs} = A_{wl} \rho g z$ is a hydrostatic spring coefficient. The optimal behavior of the oscillator from a point of view of squat prediction would be reaching a final value in a shortest period of time monotonically. This corresponds to the critical damping, which is achieved, when

$$\frac{D_s}{2m} = \sqrt{\frac{C_{hs}}{m}} \Rightarrow D_s = 2\sqrt{m C_{hs}} = 2\rho \sqrt{V_{z_s} A_{wl} g z}, \quad (3.49)$$

where V_s is ship displacement, A_{wl} - ship waterline area. Similar formulas can be derived for angular hydrostatic spring the damping coefficient for the trimming motion:

$$\frac{D_\psi}{2m} = \sqrt{\frac{C_{h\psi}}{I_{y_s y_s}}} \Rightarrow D_\psi = 2\sqrt{I_{y_s y_s} V_s g z \rho H}, \quad (3.50)$$

where H is the longitudinal metacentric height. The final form of the ship motion equations, used for squat prediction is

$$\begin{aligned} m \frac{dV_{z_s}}{dt} + D_s V_{z_s} &= F_{z_s} - m g_{z_s} \\ I_{y_s y_s} \frac{d\omega_y}{dt} + D_\psi \omega_y &= M_{y_s}, \end{aligned} \quad (3.51)$$

The values of trim angle and sinkage are obtained from (2.174).

Using the time step, defined by (3.47), the system (3.51) is solved using explicit Euler time stepping with F_{z_s} and M_{y_s} being calculated from (2.176), i.e. the coupling with the fluid motion equation is done in an explicit manner.

Part II.

Applications

Chapter 4

Validation

A number of computational methods was used in the presented work, ranging from quasi-steady state RANS to single-phase WMLES. Some of the methods had been already validated (such as LH) and did not generally need additional testing, whereas some of them (e.g. SSTIDDES model, squat prediction algorithm) required assessment of prediction accuracy. In the next sections the results of validation for the number of test cases are described.

4.1 Canonical flows

4.1.1 Channel flow

The channel flow test case was studied in order to check the OpenFOAM implementation (created by the author) of SSTIDDES model, and in particular its WMLES branch. The results for the velocity profile and the skin friction were analysed and compared with those from [48]. As a reference velocity profile the correlation of Reichardt [120, 134] was chosen.

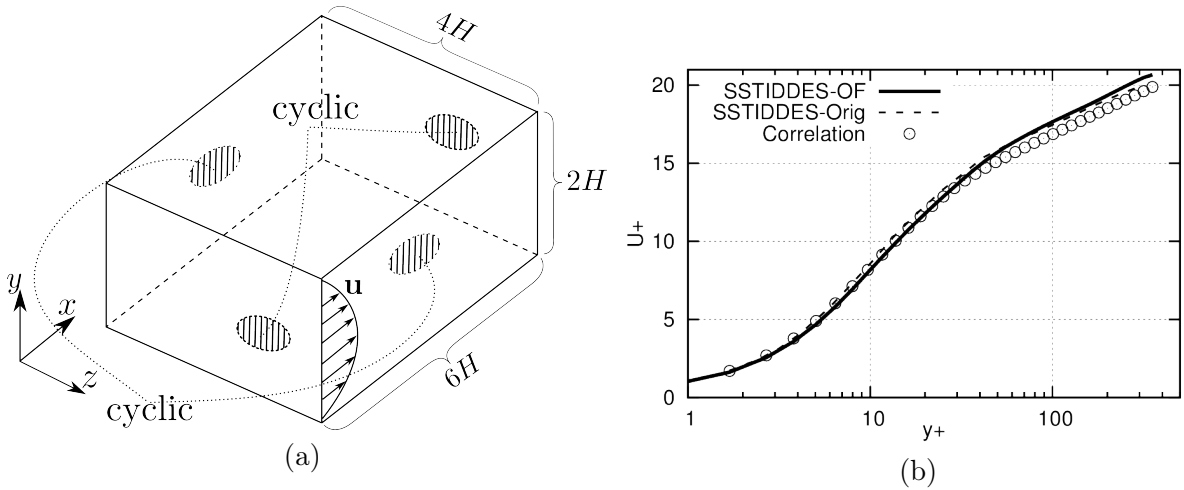


Figure 4.1: Channel flow test case: (a) - geometry of the case, (b) - comparison of the computed velocity profile with the correlation and the results of Gritskevich [48] (Orig) for $Re_\tau = 395$

Considered conditions

The following range of Reynolds numbers was considered: $Re_\tau = \frac{u_\tau H}{\nu} = 395, 2400, 18000$, which is consistent with that used in [48, 134]. In order to maintain the average fluid velocity u_m a pressure gradient was added to the flow in the form of a source term in momentum equation. The geometry of the computational case is shown in the Figure 4.1. In this formulation the average pressure gradient is the outcome of simulation and the averaged friction force can be calculated from it, using the relation $\frac{\partial p}{\partial x} = -4\rho u_\tau^2 H$. The fluid density can be taken unity.

Numerical setup

The velocity field was initialised from underresolved LES in order to get the turbulent content right from the start. Time step was chosen such, that for each cell $Co \leq 0.5$. The velocity profiles were averaged over dimensionless time $t_d = u_m t / H = 55$ and additionally averaged spatially in the spanwise direction. The domain size was $6H \times 4H \times 2H$. Structured

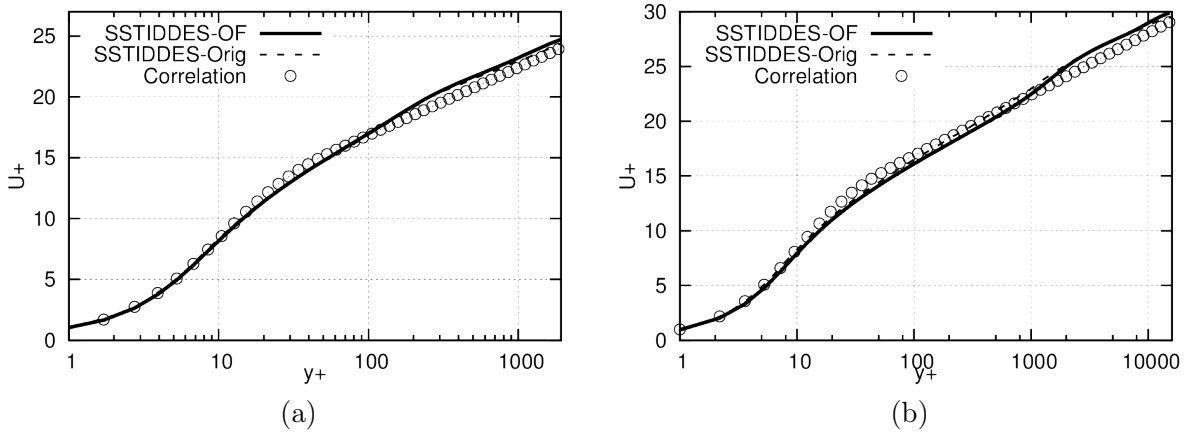


Figure 4.2: Comparison of the computed velocity profile (SSTIDDES-OF) with the correlation and the results of Gritskevich [48] (SSTIDDES-Orig) for: (a) $Re_\tau = 2400$ and (b) $Re_\tau = 18000$.

meshes with the parameter, corresponding to [48] were used. The streamwise and spanwise mesh spacings did not change from case to case and were $0.1H$ and $0.05H$ respectively. For the range of Reynolds numbers considered this gives the following spacings in wall units (x^+, z^+): (40, 20), (240, 120), (1800, 900). The size of the first wall-adjacent cell was adapted for each case, such that $\Delta y_1^+ < 1$ for all meshes with the wall-normal grading of 1.15. Thus, for the smallest Re_τ the resolution is sufficient for LES, but for other cases application of LES would lead to considerable errors. For all unknown quantities (\mathbf{u}, p, k, ω) the cyclic boundary conditions in spanwise and streamwise directions were imposed. The boundary conditions, imposed on the walls were: $\mathbf{u} = (0, 0, 0)$, $k = 1 \cdot 10^{-12}$, $\partial p / \partial n = 0$, [96]

$$\omega = 60\nu / [\beta_1(\Delta y_1^+)^2]. \quad (4.1)$$

For time stepping a three-layer backward Euler scheme was used. Convective term in momentum equation was discretised using a blended scheme with 1% of linear upwind interpolation and 99% of linear interpolation. Other convective terms (k, ω equations) were treated using TVD scheme with Sweby flux limiter. For diffusive terms Gauss scheme was used with over-relaxed approach for non-orthogonality treatment.

Results and discussion

In Figures 4.1b and 4.2 one can see, that the velocity profiles of the Gritskevich's implementation of SSTIDDES model and its OpenFOAM[®] version are in a very good agreement with each other and with the correlation. This indicates, that the developed code contains at least no serious errors. For the future additional benchmarking and comparison for other canonical flows (e.g. backward facing step) is planned. The scaling for the simulation was chosen such, that the exact value of $\tau_{wall} = \nu \left(\frac{\partial u_x}{\partial y} \right) \Big|_{y=\pm H}$ is 1. Its computed values were 0.97, 0.98, 0.95, for $Re_\tau = 395, 2400, 18000$ respectively, giving at most 5% discrepancy. These results show, that WMLES branch of IDDES is indeed capable of keeping the flow predictions at almost the same level of accuracy for a wide range of Reynolds numbers without the need for refinement in wall-parallel directions if $\Delta x/H$ is small. This considerably softens the constraint imposed on the mesh size, since only the wall-normal spacing should be adapted.

4.1.2 Asymmetric plane diffuser flow

The diffuser flow test case was computed in order to check the performance of the SSTIDDES model with the turbulence generator source for the prediction of the separation from a smooth surface. Since the geometry of the flow in the stern of a river cruiser is very similar to that in a diffuser, it was assumed a good test for the implemented model. The results of LH

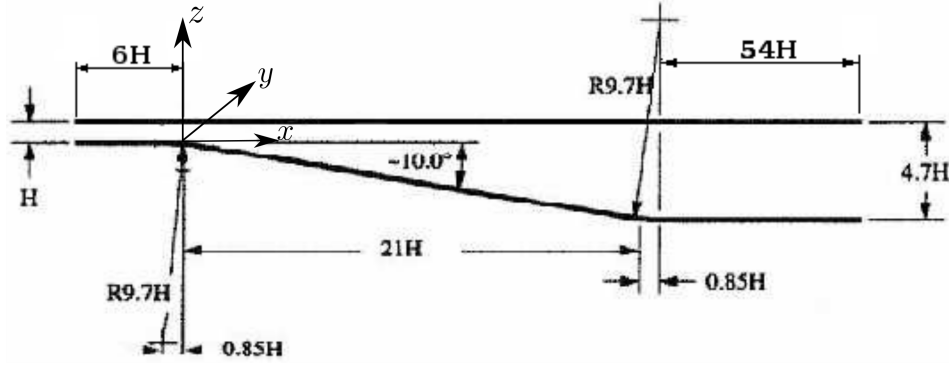


Figure 4.3: Geometry of the diffuser test case

model for the same flow are documented in [2], therefore the simulations for that model were not repeated.

Considered conditions

The geometry of the test case is shown in Figure 4.3. The flow was studied at $Re = 20000$, based on the channel height H and bulk velocity u_b : $Re = \frac{u_b H}{\nu}$. In the experimental setup of Buice and Eaton [18, 20] the channel height was equal to 0.015 m. For the calculations the kinematic viscosity was chosen to be $10^{-6} m^2 s^{-1}$, which corresponds to the bulk velocity of 1.33 m/s. The fluid is flowing in the positive x direction. It is assumed that the flow in the diffuser throat is a fully developed channel flow and that the width of the diffuser is large, so that the flow is statistically uniform in spanwise (y) direction. The width of the diffuser was chosen to be $4H$, on the left and right boundaries of the computational domain the cyclic boundary condition was imposed.

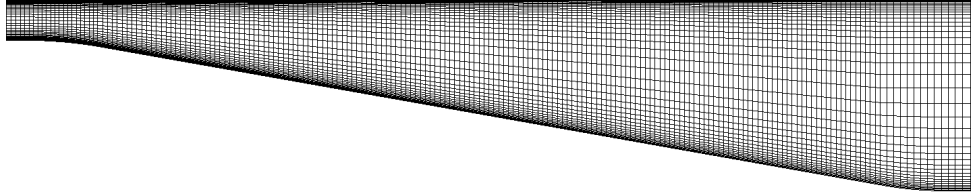


Figure 4.4: Fragment of the computational mesh (coarse)

Numerical setup

Three different computational approaches were used: dynamic Smagorinsky SGS model with recycling, SSTIDDES with recycling and SSTIDDES with the turbulence generator source applied. The recycling was applied in the diffuser throat. For doing so the throat was expanded to $12H$ in streamwise direction, from which the distance of $8H$ was used for recycling. In simulations with turbulence generator the synthetic fluctuations were added to the flow in a wall-normal layer of cells at the distance of $2H$ from inlet plane. The Reynolds stresses and the lengthscales were taken from preceding $k - \omega$ SST RANS solution.

Each of the approaches was used on three meshes with gradually decreased cell size in order to study the mesh influence on the solution. Mesh characteristics can be found in Table 4.1, whereas a sample of its structure is shown in Figure 4.4. For mesh generation `blockMesh` utility from OpenFOAM® toolbox was used. The dimensionless wall distance was less than 1 for all cases with wall-normal grading of 1.065. In order to save computational resources and to avoid reflection of numerical pressure waves from the outlet, cells were stretched towards the outlet.

The coarsest of the meshes is suitable neither for WMLES nor for LES, whereas, the resolution of the finest mesh is already close to that needed for LES [128]. These resolutions are chosen specially so as to see, how different approaches would behave given insufficiently fine

mesh. Since the well-resolved ship flow simulations at full scale are more an exception, than a rule, it is very important to get sure, that the model would not fail in these circumstances.

List of boundary conditions, imposed on the unknowns is presented in Table 4.2¹, whereas the sketch of the domain boundaries is shown in Figure 4.5. For all simulations `pimpleFoam`

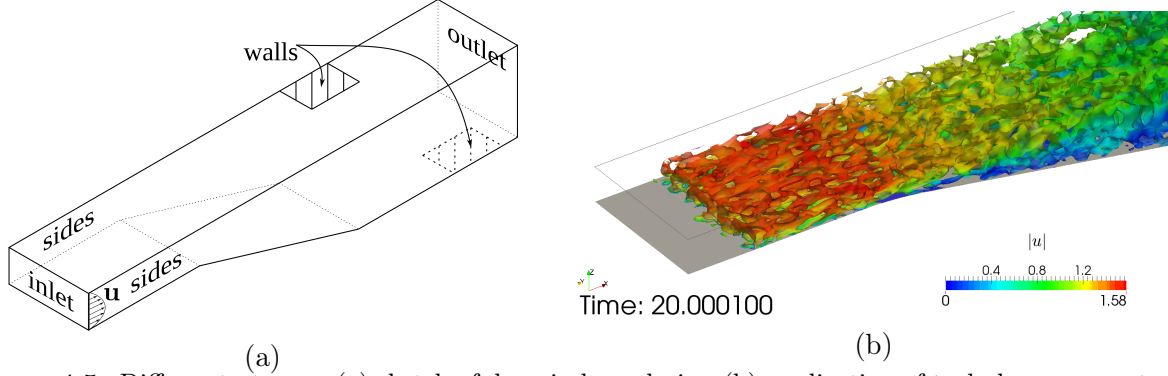


Figure 4.5: Diffuser test case: (a) sketch of domain boundaries, (b) application of turbulence generator

solver was used. The timestep was chosen such that for each cell $Co \leq 0.8$. The same schemes were used for the diffuser case as those described for the channel flow benchmark, except for the time stepping, for which Crank-Nicolson scheme was applied.

Simulations with recycling started from a constant velocity field, whereas turbulence generator cases used RANS solution as initial condition. In its turn the RANS solution was obtained using recycling in order to get a developed flow in the throat, so that the fields would not depend from their initial or inflow values. Total simulated model time was 25 s, from which 15 s were used for collection of statistical data. Taking the bulk velocity $u_b = 1.33$ m/s and diffuser geometry length of 81×0.015 m, one can find, that the fluid passed through the diffuser 23 times totally.

Table 4.1: Characteristics of the computational meshes

mesh	N_x	N_y	N_z	N_{tot}
coarse	274	40	45	493200
medium	387	60	70	1625400
fine	546	90	100	4914000

Table 4.2: Boundary conditions imposed on the unknowns

patch	\mathbf{u}	p	k	ω
inlet	r/rans	$\frac{\partial p}{\partial n} = 0$	r/rans	r/rans
outlet	$\frac{\partial \mathbf{u}}{\partial n} = 0$	$p = 0$	$\frac{\partial k}{\partial n} = 0$	$\frac{\partial \omega}{\partial n} = 0$
walls	$\mathbf{u} = 0$	$\frac{\partial p}{\partial n} = 0$	$k = 10^{-12}$	eq. (4.1)
sides	cyclic	cyclic	cyclic	cyclic

Results and discussion

Simulation results were analyzed for the mean axial velocity and resolved Reynolds stress $\langle u_x'^2 \rangle$ profiles and compared between different approaches and experimental data from [18, 20]. Comparison was done at different stations along the flow: $x = 6H, 14H, 27H, 34H, 40H, 47H, 53H$ and $60H$.

Combination of SSIDDES with recycling yielded almost a steady solution on coarse and medium meshes, because the model switched to RANS in the throat. Even when the velocity field was initialized from LES, after a few seconds of simulation all turbulent structures in the channel disappeared. Therefore, the level of resolved stresses was too low and according to the intention of IDDES, the model switched to RANS mode [134]. Experience of Nikitin et al. [107] showed, that turbulent content for channel flow simulation completely “dies out” in wall-modeled LES, when $\delta/h \geq 0.2$, where $h = H/2$. For the currently used meshes this condition was satisfied for all but the finest mesh, where $\delta/h \approx 0.17$. Therefore the absence of flow instabilities for coarse and medium grid does not contradict with the observations of other authors. For the

¹The value on the corresponding patch either is mapped from downstream on each iteration (which corresponds to recycling, r), or prescribed from preliminary RANS calculation, e.g. $k = k_{rans}$

finest mesh used the unsteadiness in the channel section was sustained and hence the model showed satisfactory results (see Figure 4.6). On the contrary to recycling, turbulence generator

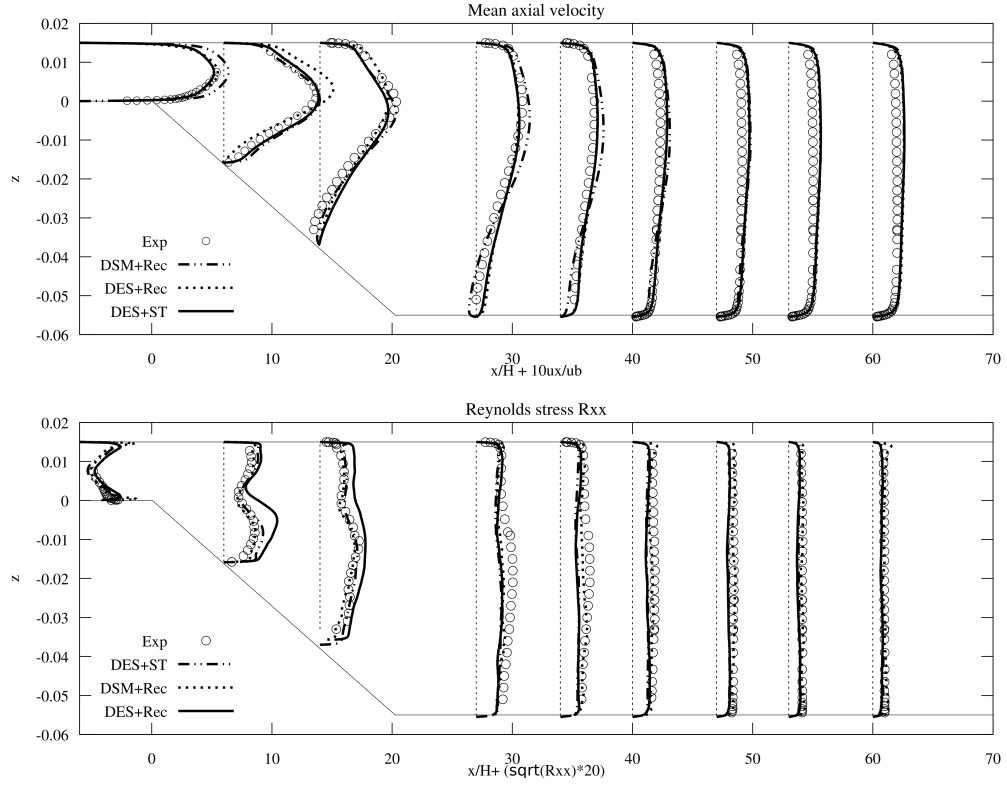


Figure 4.6: Comparison of velocity and Reynolds stress profiles along z -axis between different approaches on the fine mesh

(see Figure 4.8) produced the necessary unsteady content in the channel section on all meshes, for which reason the sampled profiles are in a good agreement with experimental data starting from the coarsest mesh used. Unfortunately, the mesh refinement did not bring any considerable improvement. The solution on the fine and medium meshes seems to be almost identical to that on the coarse mesh, except for $x/H = 6$. Although working correctly in the most of the flow, SSTIDDES predicts too weak separation and much smaller recirculation zone, than in experiment (see stations $x/H=14$ and 27), regardless of the mesh resolution or the enrichment strategy (recycling, synthetic turbulence). Results, delivered by LES are in some sections very poor on the coarse mesh. But when the cell size was reduced, a considerable improvement could be seen, The separation and the recirculation zone are predicted much more accurately, than by SSTIDDES already starting from the medium mesh. However, one has to keep in mind, that this performance of LES is due to moderate Re and therefore for ship flows the result is not expected to be that good. The friction coefficient on the upper wall predicted by LES was considerably lower than that predicted by SSTIDDES (see Figure 4.9).

One can draw a conclusion, that for the studied case SSTIDDES model showed satisfactory performance - mean velocity and Reynolds stress profiles were predicted accurately in most of the considered sections, even though the size of the separation region is clearly smaller than that observed in experiment. Good performance was attained, when the turbulent content in the channel was present. In order to achieve this, either an additional recycling section with fine mesh should be used in the throat or synthetic turbulence generator should be utilized. The fact, that the application of SSTIDDES with turbulence generator could deliver satisfactory results even on quite coarse meshes is very attractive for ship flow simulations. However, it is clear, that if the generator would be placed too far upstream, the unsteady content would be damped by the

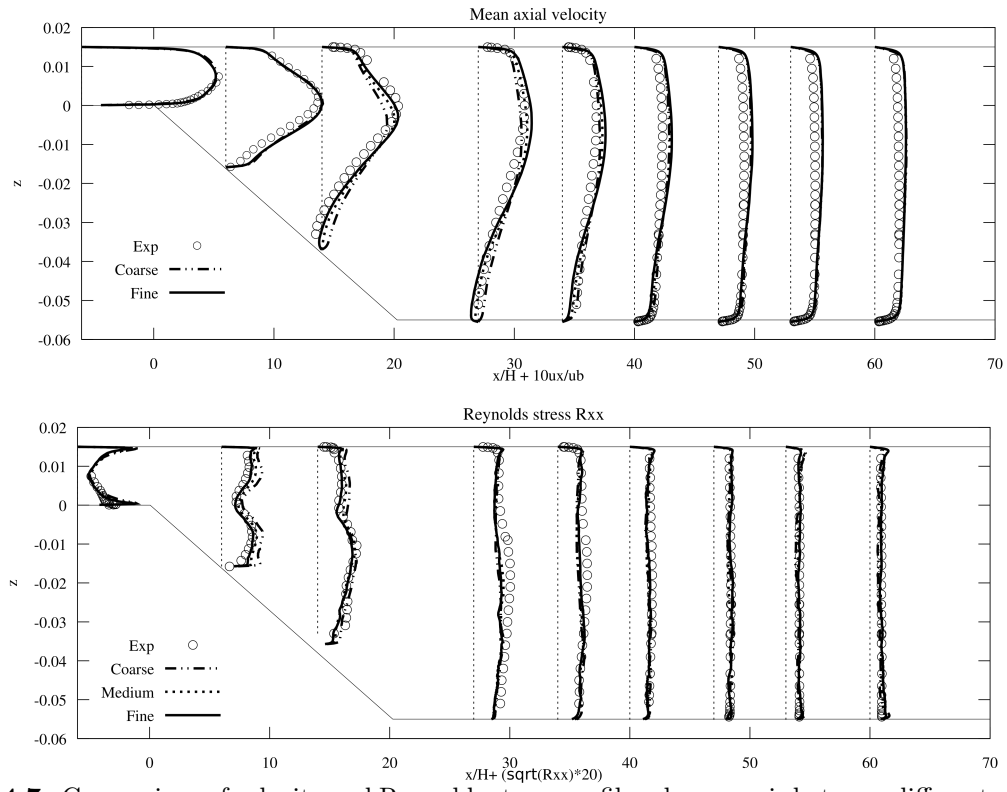


Figure 4.7: Comparison of velocity and Reynolds stress profiles along x-axis between different refinement levels for combination DSM + recycling

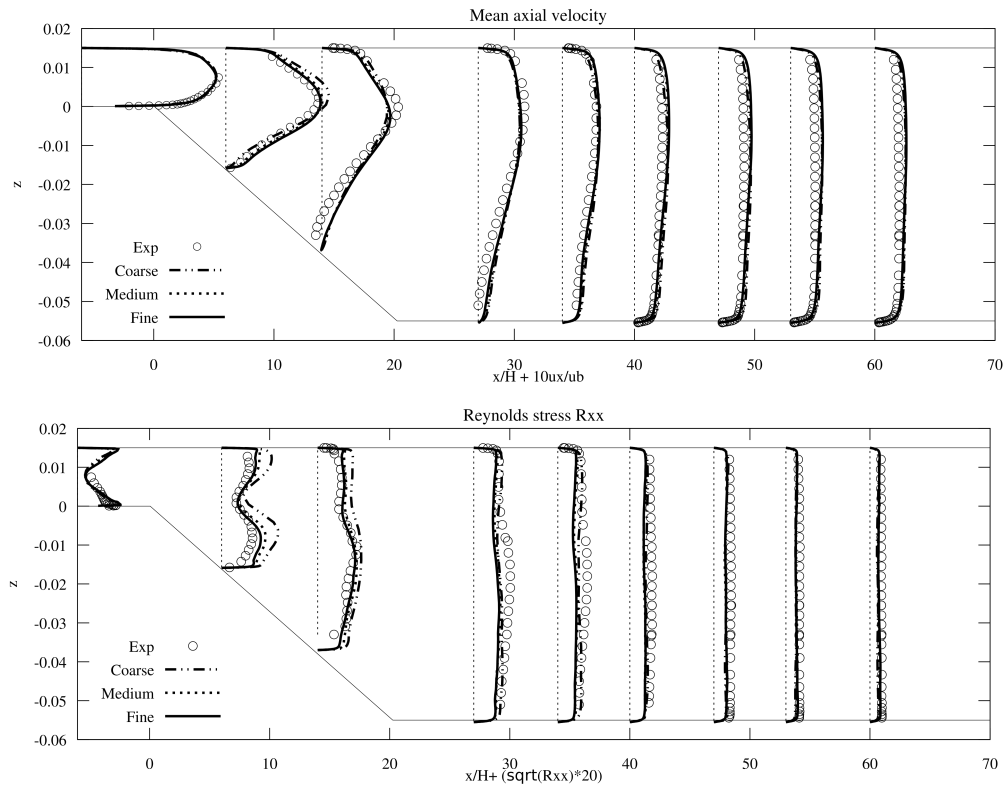


Figure 4.8: Comparison of velocity and Reynolds stress profiles along z-axis between different refinement levels for combination SSTIDDES + synthetic turbulence

numerical viscosity before reaching the section $x = 0$, which would cause the deterioration of the

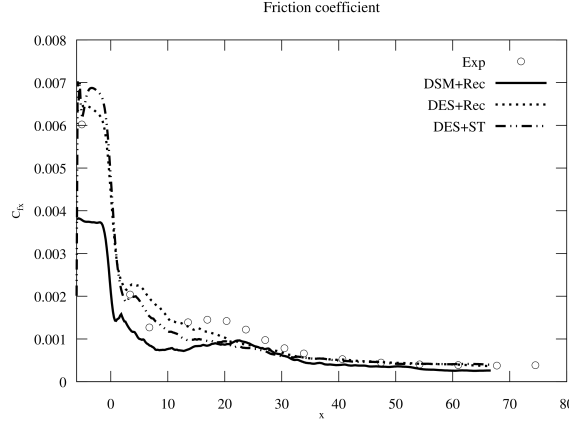


Figure 4.9: Plots of skin friction coefficient (upper wall) predicted by different approaches on the fine mesh

prediction accuracy.

The reason, why SSTIDDES suppresses the recirculation zone is not quite clear, but one of the possible reasons is the excessive subgrid scale diffusion. It was observed, that on the same meshes LES branch of SSTIDDES produced subrid viscosity approximately an order of magnitude larger than DSM. This could be the reason for smearing of the flow features.

4.2 Ship flows

4.2.1 Prediction of the wake of an inland ship in a restricted shallow channel

In the framework of the presented study the wake of an inland cruiser in shallow water is to be simulated at full scale, in which case the Reynolds number is of order 10^8 based on the ship length. Up to now the described validation cases were restricted to canonical flows at relatively low Reynolds numbers. However, it was also desired to test the performance of hybrid turbulence models (LH, SSTIDDES) for ship flows in realistic conditions. Since the wake measurements in full scale are next to impossible, only the model scale ones could be used for validation purposes. There is a lack of experimental data presented in literature on ship flows

Table 4.3: Conditions considered in the M1926 model simulations

B_c	[m]	9.8
U	[m/s]	1.24
h	[m]	0.5
T	[m]	0.25
h/T	[-]	2
Fn	[-]	0.12
Fn_h	[-]	0.56
Re	[-]	$1.36 \cdot 10^7$

under shallow water conditions. Thus the necessary data had to be searched for. Fortunately, the velocity field measurements in the ship wake were conducted at the Duisburg Development Centre for Ship Technology and Transport Systems (DST) in the framework of the AiF project WAKE [87]. DST performed tests for a model (M1926) of an inland ship in a shallow water towing tank. Stereo-PIV snapshots of the velocity in the ship wake for 9 model tests were kindly provided to the author.

The reference axial velocity distribution was obtained by averaging the snapshots of the velocity field over 9 experiments. During the experiment the model was free to sink and trim. The values of sinkage and trim angle were 0.02 m and 0.021° respectively.

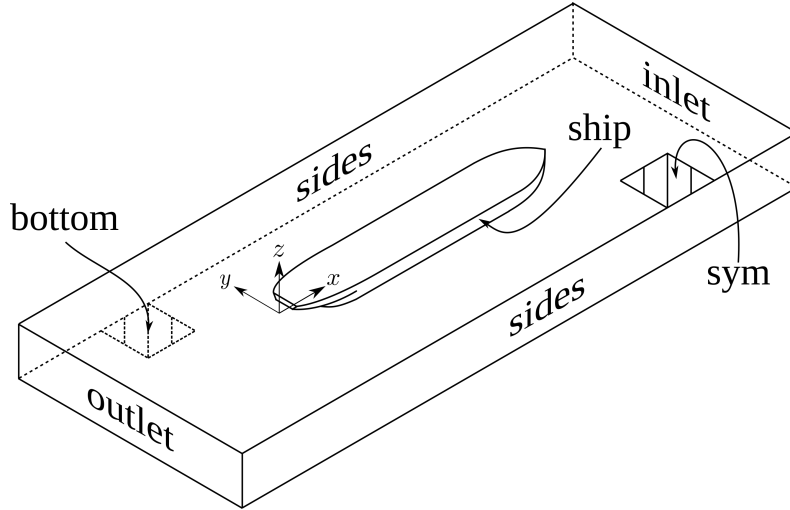


Figure 4.10: Sketch of computational domain boundaries for the single-phase simulation of the flow around M1926 model

Geometry and conditions

Parameters of the studied model were: $L_{oa} = 11$ m, $B = 1.14$ m, $T = 0.25$ m, $C_B = 0.877$. Bow and stern geometry can be seen in Figure 4.11. No propeller or any other appendages except the shaft were present in experiment. The velocity snapshots were taken in the vicinity of the propeller plane (see Figure 4.11). Considered conditions are presented in Table 4.3, where B_c is the breadth of the towing tank, U - model speed, h - water depth, T - ship draught, $Fn_h = \frac{U}{\sqrt{gh}}$ - depth Froude number.

Program of computations

First of all trim and sinkage as well as ship resistance were calculated and compared to experimental data using `LTSInterDyMFoam` solver with $k-\omega$ SST model for turbulence modeling. Since the agreement with experimental data was very good already for the coarsest mesh, no further computations with free surface were conducted. After that, ship geometry was shifted and

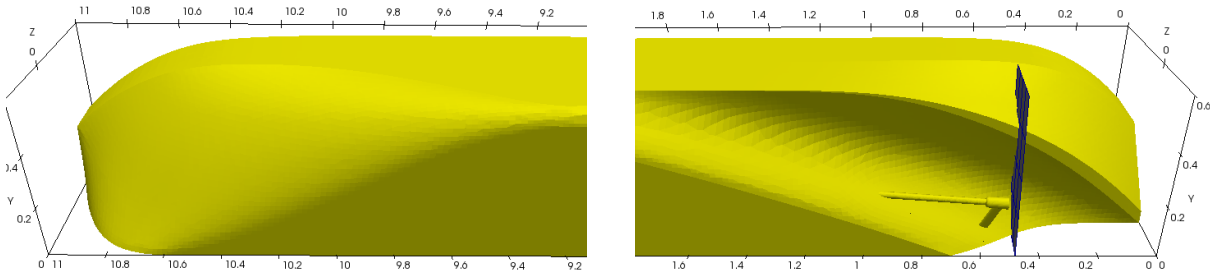


Figure 4.11: Bow and stern geometry of M1926 model. The plane where the velocity field was measured is shown at $x = 0.48$ at the stern.

rotated in accordance with the experimental values of trim and sinkage and only the fluid region was meshed, whereas the free surface was replaced by symmetry plane. Further computations were conducted in single phase formulation. It was possible to do so without considerable loss of accuracy since the free surface deformation was quite small ($Fn = 0.12$) and under these conditions it could not noticeably affect the ship wake. Computations were done on three meshes with gradually increased resolution. Three simulation strategies were used: RANS $k-\omega$ SST, SSTIDDES with turbulence forcing and LH model without forcing. It was not possible to use LH model with synthetic turbulence generator because of the problems with stability, which resulted into the divergence of the solution.

Numerical setup

The sketch of domain boundaries is shown in Figure 4.10. In order to avoid the influence of inlet and outlet truncation boundaries on the solution the length of the computational domain was made equal to $6L_{oa}$ with distance to inlet patch being $2L_{oa}$ and to the outlet patch - $3L_{oa}$.

The boundary conditions are summarised in Table 4.4. The inflow values k_∞, ω_∞ were computed using the formulas given in the OpenFOAM user guide:

$$k_\infty = (UI)^{3/2}, \omega_\infty = \frac{\sqrt{k}}{0.09l}, \quad (4.2)$$

where I is the turbulence intensity, usually chosen to be 2% and l is the characteristic length scale, which is taken equal 1% of the ship length. This gives $k_\infty = 2.80 \cdot 10^{-4} \text{m}^2 \text{s}^{-2}$, $\omega_\infty = 0.19 \text{s}^{-1}$. The inflow velocity $\mathbf{u} = (-U \ 0 \ 0)^T$. Finite volume meshes were created using StarCCM+[®] trimmer

Table 4.4: Boundary conditions imposed on the unknowns for M1926 validation case

Patch \ Variable	$\mathbf{u}, [\text{ms}^{-1}]$	$p, [\text{m}^2 \text{s}^{-2}]$	$k, [\text{m}^2 \text{s}^{-2}]$	$\omega, [\text{s}^{-1}]$
inlet	$\mathbf{u} = \mathbf{u}_\infty$	$\frac{\partial p}{\partial n} = 0$	$k = k_\infty$	$\omega = \omega_\infty$
outlet	$\frac{\partial \mathbf{u}}{\partial n} = 0$	$p = 0$	$\frac{\partial k}{\partial n} = 0$	$\frac{\partial \omega}{\partial n} = 0$
ship	$\mathbf{u} = 0$	$\frac{\partial p}{\partial n} = 0$	$k = 10^{-12}$	eq. (4.1)
sides	slip	$\frac{\partial p}{\partial n} = 0$	$\frac{\partial k}{\partial n} = 0$	$\frac{\partial \omega}{\partial n} = 0$
bottom	$\mathbf{u} = \mathbf{u}_\infty$	$\frac{\partial p}{\partial n} = 0$	WF	WF
sym	symmetry	symmetry	symmetry	symmetry

mesher. Three meshes were built for the case: coarse, medium and fine, containing 4.3M, 9.0M, 20M cells. Mesh refinement was done by decreasing the base cell size by $\sqrt{2}$. For each of the meshes $\Delta y_w^+ < 1.0$. Wall-normal grading of cells in the boundary layer mesh was 1.15. Stern region of the model was immersed into a refinement box with isotropic hexahedral cells with edge lengths of 0.016 m, 0.011 m and 0.008 m, in order to guarantee, that no sharp jumps in cell sizes would be present.

The turbulence generator was placed at a distance of $2(h - T) = 0.5$ m upstream from the end of the cylindrical part of the hull, so that the synthetic turbulence could “adapt” itself to the flow before reaching the stern region, see Figure 4.12. For the time stepping Crank-Nicolson

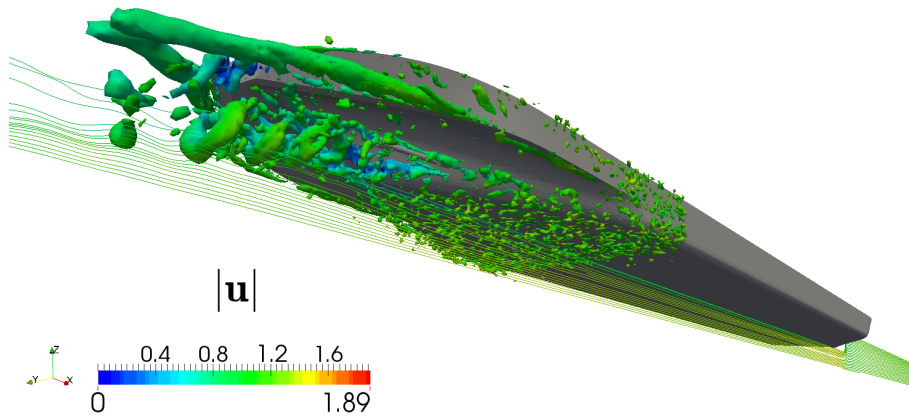


Figure 4.12: Vortical structures ($\lambda_2 = -20$) in the stern of M1926 predicted using SSTIDDES + synthetic turbulence generator. One can see, where the turbulent structures are added to the flow.

scheme was used. For the convective term in momentum equation a blended scheme of Strelets was applied with additional blending, dependent on the cell quality (see Chapter 3). Convection terms in auxiliary equations (k, ω) as well as diffusion terms were discretised in the same manner as in previously described validation cases. The timestep was chosen such that for each cell

$Co \leq 0.8$.

Results and discussion

The nominal wake ¹ $w = 1 + \langle u_x \rangle / U$ was calculated from the measured velocity field (see Figure 4.13a) and compared to the computed results in form of 2D contour plots (see Figure 4.13b,c and d, Figure 4.14b,c and d, Figure 4.16b,c and d) and 1D plots: along the line $x = 0.48$, $z = -0.23$ and along the circle in the propeller plane at $r/R = 0.7$ (see Figure 4.15). In order to get idea about performance of pure RANS for this case, also the results of the steady-state solver `simpleFoam` with $k - \omega$ SST model are presented.

Analysis of the Figures 4.13, 4.14 and 4.16 allows to conclude that the RANS $k - \omega$ SST model is suitable for the considered flow in terms of prediction of the wake. The reason for this is that the stern is very well streamlined and strong separations are absent. However, the anchor-like form of the wake near the middle-line plane is smeared, so that the inclination angle does not correspond to that observed in experiment. This problem becomes less pronounced on the fine mesh.

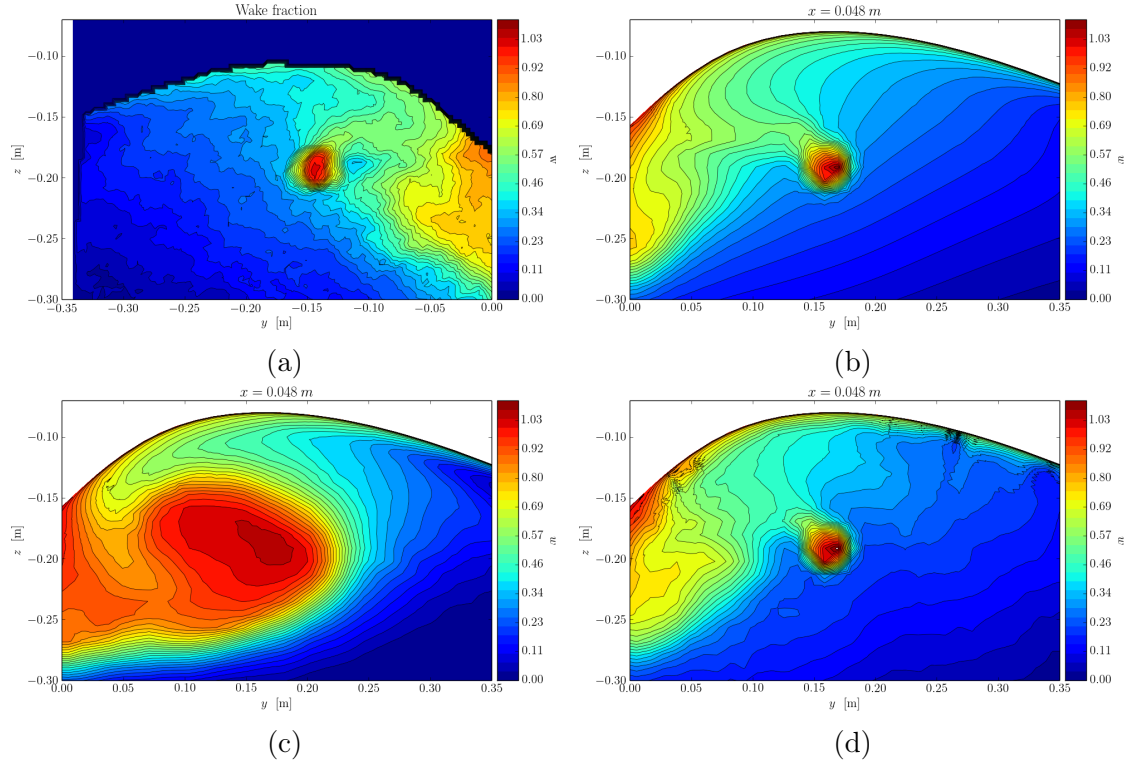


Figure 4.13: Comparison of the wake obtained on the coarse grid using different methods: (a) - experiment, (b) - RANS, (c) - LH, (d) - SSTIDDES

The peak of the wake in the propeller plane at $\phi \approx 270^\circ$, is not captured at all and the mesh refinement seems to play next to no role here (see Figures 4.15e and f). The solution converges already on the medium mesh with only slight variations between the medium and fine meshes near the middle line plane. Despite the satisfactory results of RANS for the mean velocity field, one has to keep in mind, that the considerably unsteady flow cannot be computed correctly by (U)RANS and therefore cannot be used for the prediction of unsteady propeller loadings [2].

Results for the mean velocity field, obtained using SSTIDDES appear to be of nearly the same quality as those delivered by RANS $k - \omega$ SST and even better in some regions (see, for example Figure 4.15a, $y \in [0, 0.1]$). Moreover, the peak at $\phi \approx 270^\circ$ was successfully captured on

¹The original formula for the wake is $w = 1 - avg u_x / U$, but since the longitudinal component of inflow velocity is negative, the sign in front of $\langle u_x \rangle / U$ should be changed

the coarse mesh. Unfortunately, on finer meshes it was smeared again. The anchor-like form of the wake is successfully reproduced and the inclination angle is visually close to experimentally observed one. The surprising result is that the solution on the coarse mesh is the best one, shown by SSTIDDES, whereas the solution on medium and fine grids slightly deteriorates. This may be a sign, that the shielding functions of SSTIDDES, being purely empiric, behave themselves inappropriately, when the mesh is refined and should be recalibrated. This issue requires further analysis. Despite of the problem, that the model did not tend to converge to experimental data, it still converged and showed no considerable variations between the medium and fine meshes.

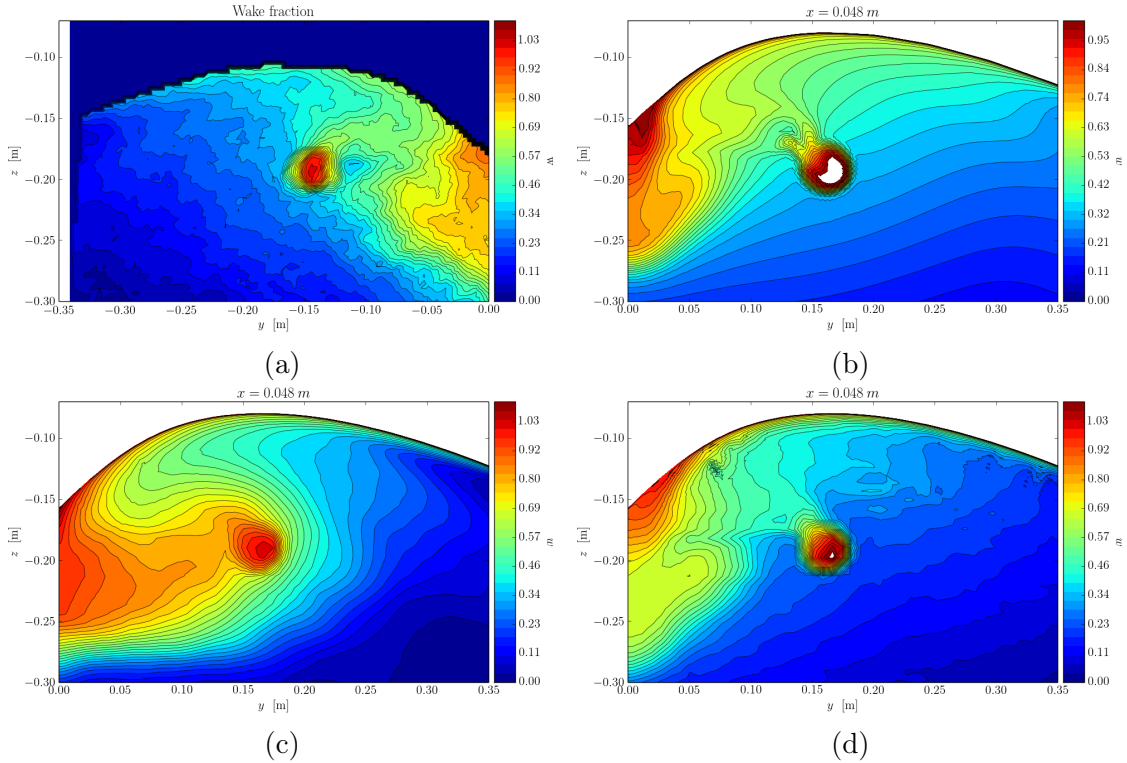


Figure 4.14: Comparison of the wake obtained on the medium grid using different methods: (a) - experiment, (b) - RANS, (c) - LH, (d) - SSTIDDES

On all meshes the LH model showed very strong separations at the stern and as a result predicted too high wake in the region $y \in [0, 0.22]$. This can be seen in Figures 4.13c, 4.14c, 4.16c, 4.13c and d, where the values of w are obviously overpredicted. As it is known, the DES-like models without shielding can function properly only when the constraint $\Delta x/\delta \geq 1$ is satisfied [143], which means, that the mesh spacing in wall-parallel direction should be equal to or larger than the boundary layer thickness. The meshes, which were used in the current study, do not satisfy this constraint because of their generation strategy. As previously mentioned the cell sizes in the stern region were quite small and approximately an order of magnitude smaller than the boundary layer thickness. Because the constraint was violated, application of LH model, which uses no shielding and has no control of resolved-to-modeled stress ratio, seems to have resulted in MSD. This mechanism is assumed to be the reason for observed separations (i.e. GIS occurred). One has to mention, that the accuracy of LH results would be improved if synthetic turbulent fluctuations would be introduced ¹ or the mesh would be designed differently (see, for example, [2]). However, the sensitivity of the model to the mesh used is of course a noticable drawback, which should be eliminated.

Here it should be emphasized that the interpretation of the grid sensitivity study for hybrid simulation is more complicated than for URANS because the turbulence model is directly influ-

¹Unfortunately, due to stability reasons described above, this could not be done.

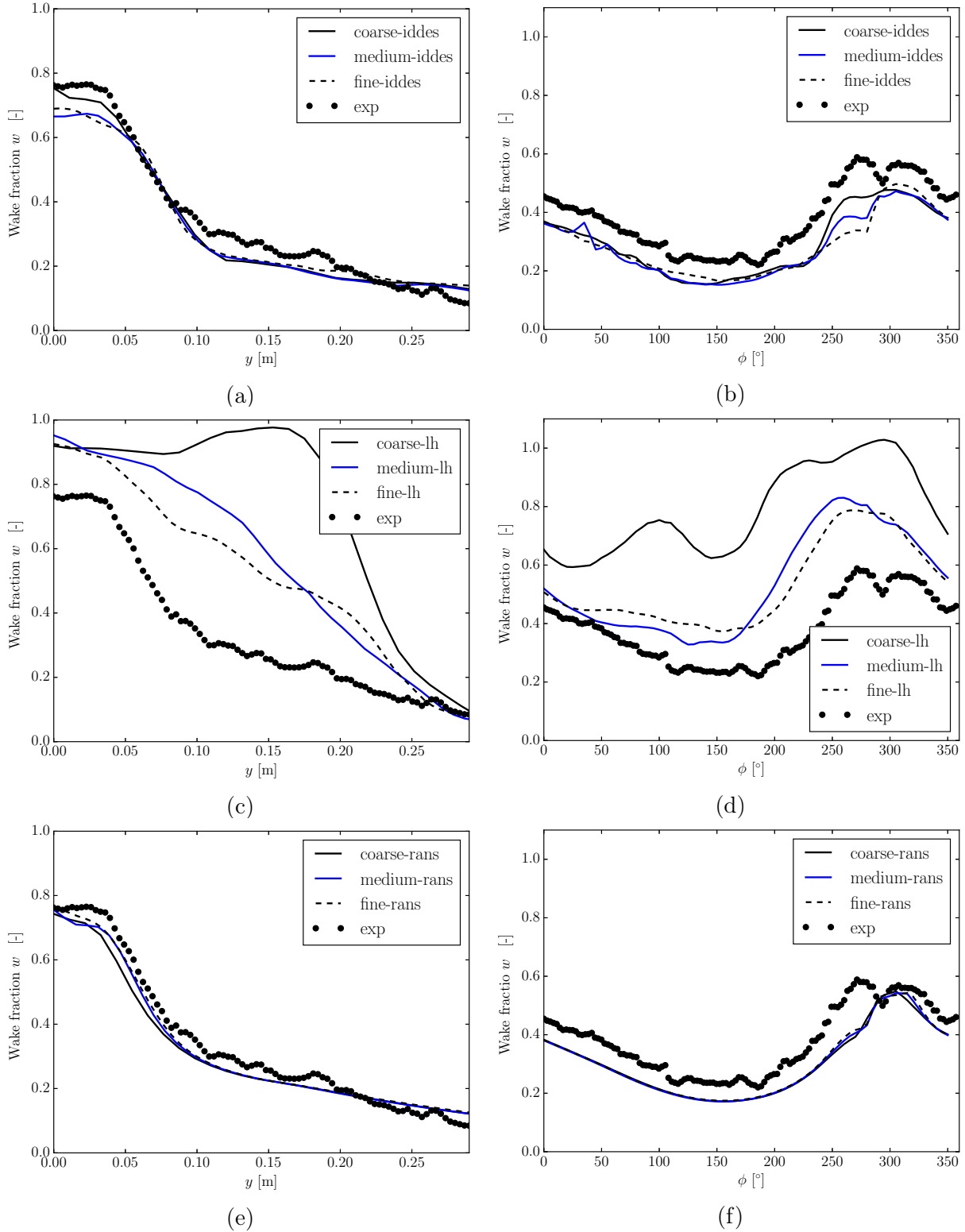


Figure 4.15: Comparison of the solutions obtained on different grids, sampled on the line $x = 0.48$ m, $z = -0.23$ m (left) and on the circle corresponding to $r/R = 0.7$ in the propeller plane (right)

enced by grid resolution. The main purpose of the grid study is to estimate the discretization error. In URANS the grid refinement reduces the discretization errors of underlying equations. In hybrid methods the refinement also increases the region, where LES is used and reduces the subgrid stresses. Therefore, it is impossible to distinguish the discretization error and model error in V&V procedure for hybrid methods.

Improvement of LH model An attempt was made to improve the model robustness and accuracy by introduction of shielding, which would force the RANS/LES interface of LH model to move farther from the wall and reduce the MSD¹. Since the criterion of the RANS/LES switch in LH model is the ratio of integral lengthscale L to cell size Δ it was decided to modify the lengthscale L in the following way:

$$\tilde{L} = L f_d, \quad (4.3)$$

where

$$f_d \equiv 1 - \tanh([8r_d]^3), \text{ with } r_d \equiv \frac{\nu_t + \nu}{\kappa^2 y^2 \sqrt{0.5(S^2 + \Omega^2)}}. \quad (4.4)$$

After that the modified lengthscale \tilde{L} is used for determination of RANS/LES interface (see Section 2.3.2) instead of L . In the boundary layer the function f_d tends to zero and reduces the integral lengthscale to zero near the wall, so that the ratio \tilde{L}/Δ is kept small in the vicinity of the body. The model therefore switches to RANS near the wall, regardless of the mesh resolution. In the following the modified version of LH model will be referred to as Shielded LeMoS Hybrid (SLH).

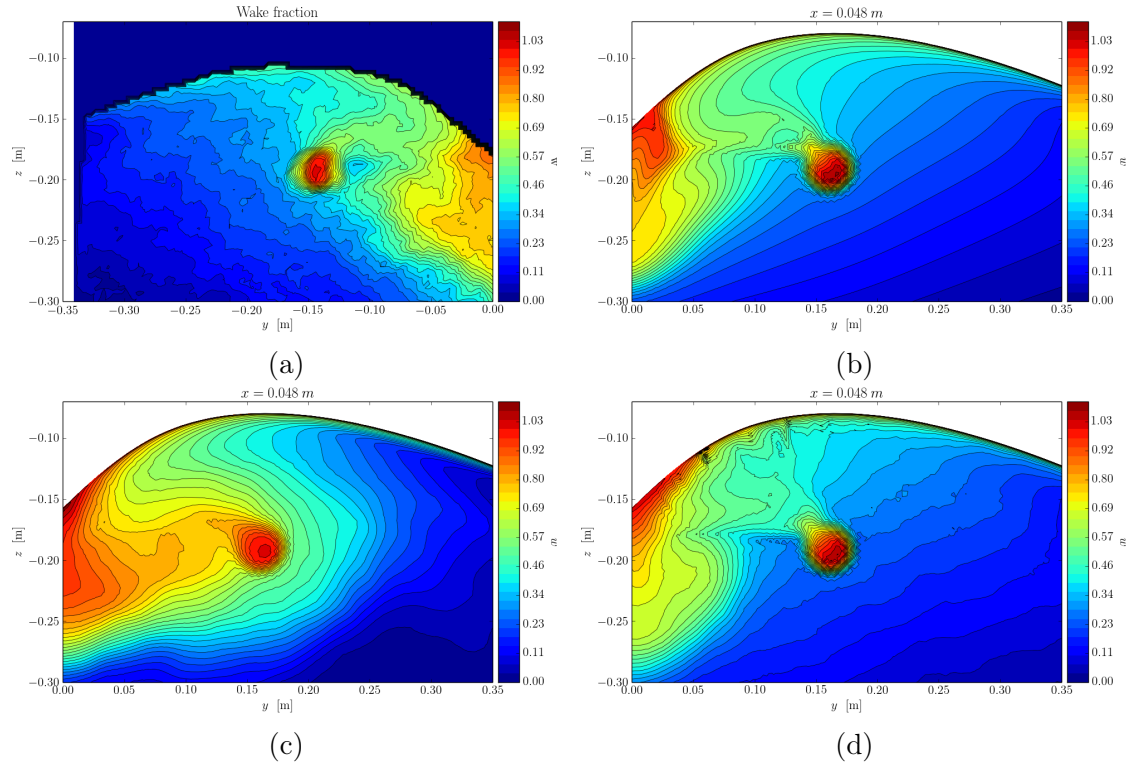


Figure 4.16: Comparison of the wake obtained on the fine grid using different methods: (a) - experiment, (b) - RANS, (c) - LH, (d) - SSTIDDES

SLH was tested on the coarse, medium and fine meshes and compared to the original LH (see Figures 4.17, 4.18). One can notice, that the application of shielding considerably improves the predictions, produced by the model. The inadequately strong separations predicted by LH were suppressed when SLH was used, which led to better agreement with experimental data on all of the analysed curves. Even though the values of wake are still not ideal (see Fig. 4.18a and b), the improvement due to the shielding can be clearly seen. The new model predicts the wake at $r/R = 0.7$ better, than RANS and SSTIDDES. A very interesting result is that on a sufficiently fine mesh SLH and SSTIDDES deliver almost identical results both for the wake fraction and for

¹This modification is analogous to conversion of DES to DDES

the standard deviation of longitudinal velocity. One can conclude, that the proposed modification of the model is superior to the old one in terms of robustness and accuracy. Therefore it can be recommended for use on ambiguous grids ($\Delta x/\delta < 1$ ¹).

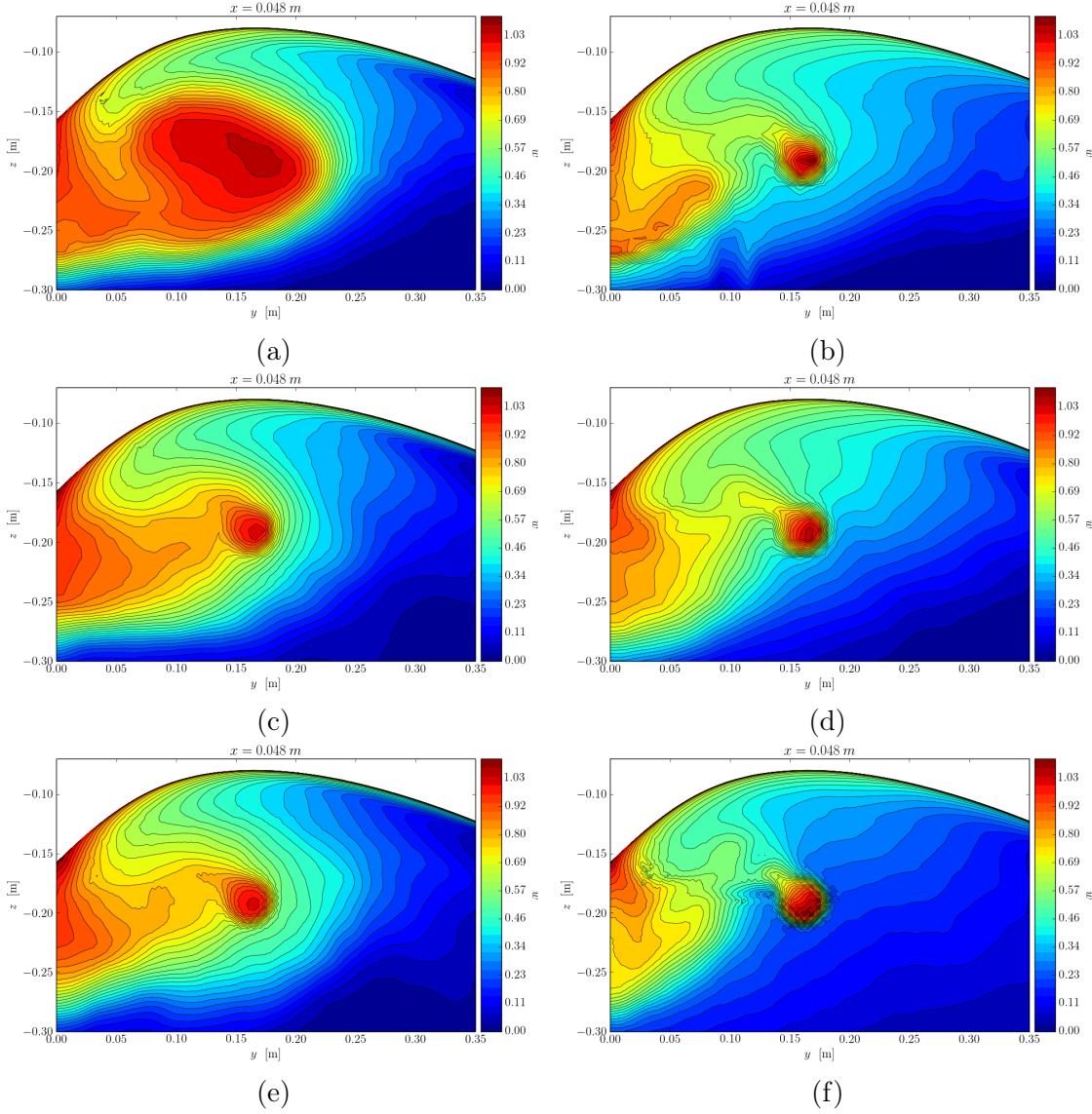


Figure 4.17: Comparison of the wake obtained using SLH (right) and original LH (left) formulation on different grids: (a),(b) - coarse mesh, (c),(d) - medium mesh (e),(f) - fine mesh

As long as hybrid models in the framework of this study are to be used for analysis of velocity fluctuations in the wake and unsteady thrust oscillations, also the relative standard deviation of longitudinal velocity

$$\sigma_u = \frac{1}{|\mathbf{u}_\infty|} \sqrt{\frac{1}{n-1} \sum_{i=0}^n (u_{x,i} - \langle u_x \rangle)^2} \quad (4.5)$$

in the number of points along the line $x = 0.48$ m, $z = -0.25$ m, $y \in [0, 0.4]$ m was analysed and compared between different models and mesh resolutions, even though the experimental data was not available.

From Figure 4.19 following conclusions can be drawn. It can be clearly seen, that the level of velocity fluctuations in the wake, predicted by LH without shielding is much higher

¹Definition of ambiguous grid was introduced by Spalart et al. [143]

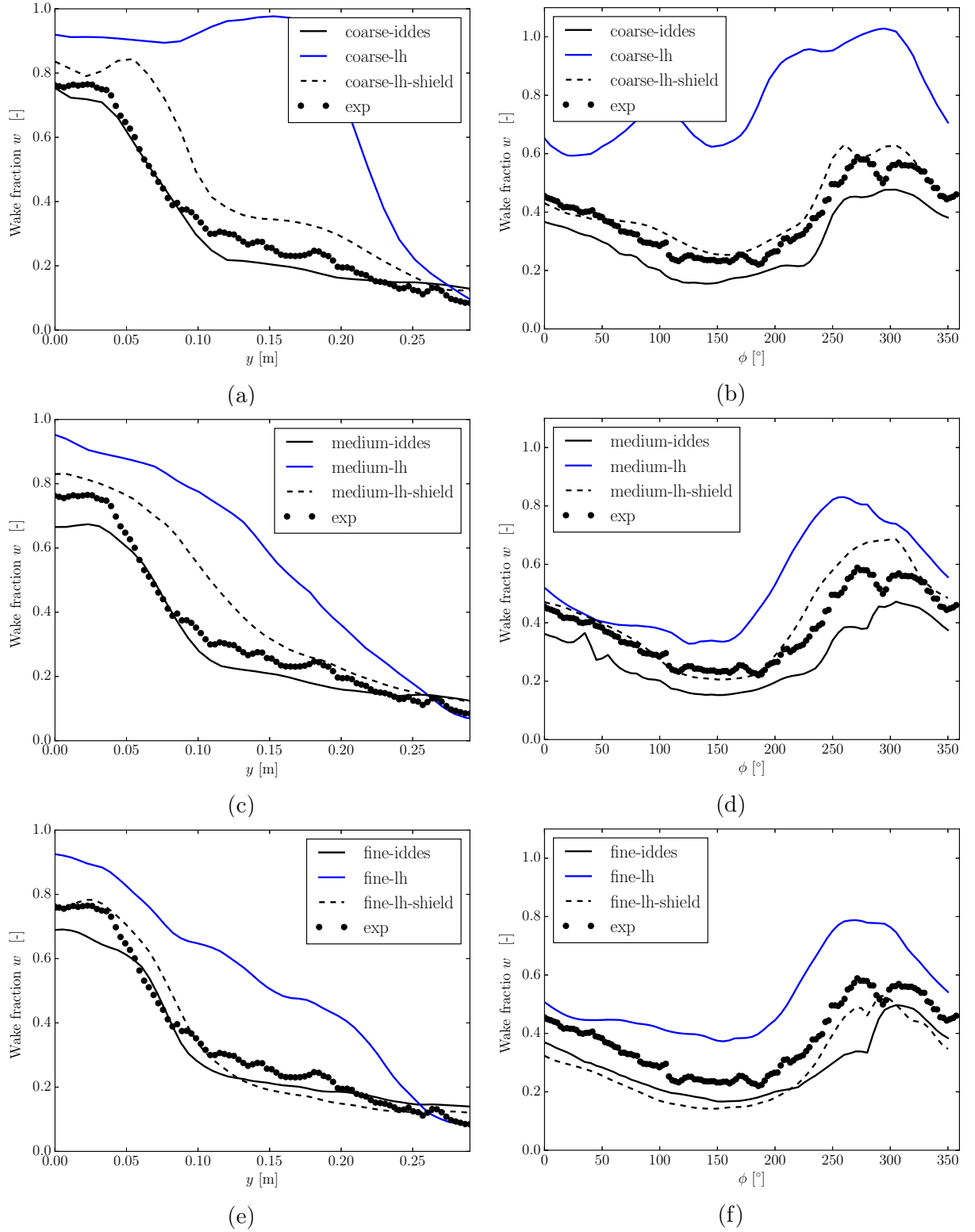


Figure 4.18: Comparison of the solutions obtained using LH, SLH and SSTIDDES on different meshes. Wake was sampled on the line $x = 0.48$ m, $z = -0.23$ m (left) and on the circle corresponding to $r/R = 0.7$ in the propeller plane (right)

in all points than that observed in SSTIDDES computations. The largest difference can be seen at $y = 0.08$ m, $y = 0.16$ m and $y = 0.24$ m where LH model (on the fine mesh) shows standard deviation of 19.5%, 25.2% and 12.4% of the ship speed, whereas the values, predicted by SSTIDDES are: 13%, 5% and 5%. The severe velocity fluctuations, shown by LH can be

related to the nonphysical separations, detected during the analysis of the wake. Therefore, it can be concluded, that LH model in case when MSD occurs tends to overpredict the velocity fluctuation intensity. Therefore, when using original LH one has to get sure, that no MSD was present in the computations. Application of the shielding results in noticeable reduction of σ_u almost in all considered points, except for $y = 0.08$. After the modification the predicted values of σ_u at $y = 0, 0.24, 0.32, 0.4$ m have become comparable to those shown by SSTIDDES. The dependence of the standard deviation on the cell size for SSTIDDES model is shown in Figure 4.19b. Obviously, there is a high uncertainty at the points $y = 0$ m and $y = 0.08$ m, whereas farther from the middle-line plane the variations are very low. The convergence can be judged on only pointwise: at some points monotonic convergence can be recognized, at some oscillatory convergence, whereas, for example at $y = 0$ m, $y = 0.16$ m the solution formally tends to diverge (variation of solution between the coarse and medium mesh is smaller than that between the medium and fine).

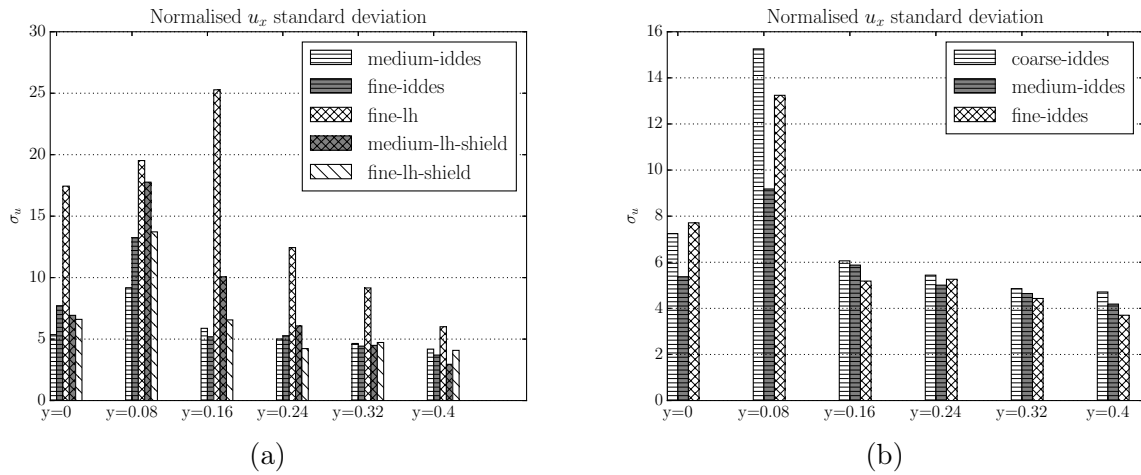


Figure 4.19: Standard deviation of velocity field at six points along the line $x = 0.48$ m, $z = -0.25$ m

4.2.2 Prediction of squat effect in a restricted shallow channel

Numerical prediction of squat effect is one of the important steps of the present study. Since in shallow water the dynamic trim and sinkage can be much higher, than in deep water, they can considerably change the underkeel clearance and on this account influence the wake. Therefore, in order to create a complete model of the processes, taking place in the stern, one has to take into account the dynamic trim and sinkage.

The algorithm, used for squat computations was described in Chapter 3. Two cases were used so far by the author for validation of the solver `LTSInterDyMFoam`. Results of the first one for a Post-Panamax container ship model PPM46 were presented at the Numerical Towing Tank Symposium 2013 [132]. The second validation study was done in the framework of a collaboration between the Federal Waterways Engineering and Research Institute (Bundesanstalt für Wasserbau (BAW)) and the University of Rostock [131]. Results of the latter research will be described in the following.

Geometry and conditions

A 1:40 scale model PPM55 of a Post-Panamax container ship was used for the simulations. The parameters of the model are presented in Table 4.5. In this research the bare hull without propeller or rudder was investigated, even though in the experiment the model was self-propelled. Influence of the propeller suction force on the flow was modeled using actuator disk method, namely its modification proposed by Hoekstra [52].

Main model dimensions were the following: waterline length $L_{wl} = 8.89$ m, ship breadth

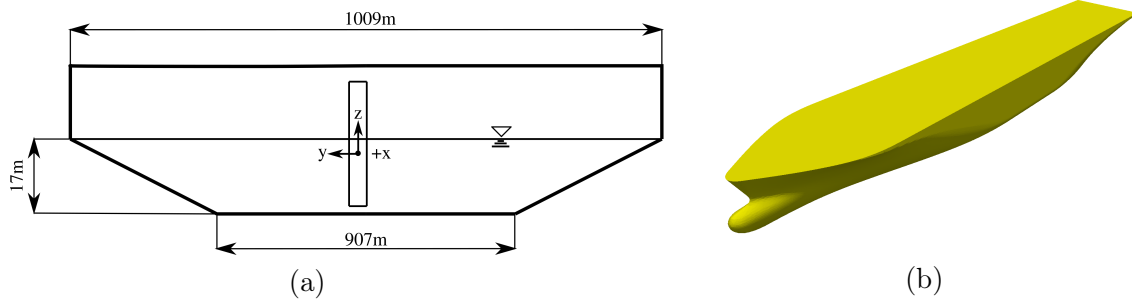


Figure 4.20: (a) - full scale channel section, (b) - PPM55 model geometry

$B = 1.375$ m, ship draft $T = 0.4$ m. A symmetric channel with the flat bottom and the bank slope 1:3 was considered, which corresponds to the geometry, used by the BAW for the experimental investigations of squat (see Figure 4.20a). The channel depth h was equal to 0.425m which corresponds to $h/T=1.06$ (see Table 4.5). The ship was assumed to move in the centre of the channel. The considered range of ship speeds and corresponding Froude and Reynolds numbers is listed in Table 4.5. This range corresponds to the experiments, undertaken at BAW. The time-averaged measured values of squat at the bow and at the stern were provided to the author. Boundary conditions imposed on the unknowns: $p_d, \mathbf{u}, k, \omega, \alpha$ are summarised in Table 4.6.

Table 4.5: Conditions considered in validation of squat prediction

U	Fn	Fn_h	$Re \cdot 10^{-6}$
[m/s]	[-]	[-]	[-]
0.68	0.073	0.33	6.07
0.76	0.081	0.37	6.72
0.82	0.088	0.40	7.30
0.88	0.094	0.43	7.80
0.90	0.097	0.44	8.02

Table 4.6: Boundary conditions imposed on the unknowns in squat computations

Patch \ Variable	\mathbf{u}	p	k	ω
inlet	$\mathbf{u} = (-U \ 0 \ 0)^T$	$\frac{\partial p}{\partial n} = 0$	$k = 2.80 \cdot 10^{-4}$	$\omega = 0.19$
outlet	$\frac{\partial \mathbf{u}}{\partial n} = 0$	$p = 0$	$\frac{\partial k}{\partial n} = 0$	$\frac{\partial \omega}{\partial n} = 0$
ship	$\mathbf{u} = 0$	$\frac{\partial p}{\partial n} = 0$	WF	WF
sides	slip	slip	slip	slip
bottom	$\mathbf{u} = (-U \ 0 \ 0)^T$	$\frac{\partial p}{\partial n} = 0$	WF	WF

Numerical setup

Numerical solution was obtained using the quasi-steady state VOF-solver **LTSInterDyM-Foam**, described earlier. For the mesh deformation the algorithm, developed by the author was used (see Chapter 3). The solution procedure started with the fixed ship attitude and after the convergence of the wave system the model was allowed to sink and trim. For turbulence modeling $k-\omega$ SST model of Menter was used with the automatic wall functions [94]. Unstructured hexa-dominant computational grids were generated by StarCCM+® trimmer mesher with the average $\Delta y_1^+ = 40$. The middle-line plane was considered a symmetry plane and thus only a half of the ship flow was calculated. For a half a ship finite volume meshes with approximately 2M cells were produced. Computational cells near the ship hull had an isotropic cubic form with the edge length of 0.01 m at the bow and at the stern and 0.02 m in the cylindrical part of the hull. Cells, located at the free surface were refined down to 0.005 m in vertical direction. At the inlet and

the outlet of the domain the control volumes were stretched in streamwise direction. Domain length was equal to $5 L_{wl}$: $2L_{wl}$ in front of the model and $2L_{wl}$ after, the dimensions were chosen according to preceding experience [132]).

Discretisation of convection terms was done using linear upwind interpolation. Diffusion terms were approximated using Gauss scheme with linear interpolation and explicit correction of face non-orthogonality. For time-stepping the Euler implicit scheme was employed.

Boundary conditions for the unknowns were almost the same, as in the previous validation case (see Table 4.6), except that the wall functions were also applied to ship patch and that the inclined parts of the banks were treated as the part of the bottom ($\mathbf{u} = (-U, 0, 0)^T$). For the volume fraction α Dirichlet boundary condition was imposed at the inlet ($\alpha = 1 - H(z)^1$), whereas on all other boundaries $\frac{\partial \alpha}{\partial n} = 0$.

The thrust, produced by the actuator disk was adapted to ship resistance in runtime.

Results and discussion

In Table 4.7 one can see the comparison of the predicted and measured values of squat at aft and fore perpendiculars, as well as the absolute discrepancy. It can be noticed, that the agreement with experimental data is very good, namely, the absolute value of discrepancy has not exceeded 1 mm, which corresponds to 4 cm at full scale. For a container ship with the draught $T = 16$ m this can be considered an accurate prediction (max error of 0.25% of T). The values of relative discrepancy have not exceeded 9.5%.

Table 4.7: Comparison of the experimental values of squat at fore and aft perpendiculars with computed ones

U [m/s]	Exp		OpenFOAM		Discrepancy	
	s_{AP} [m]	s_{FP} [m]	s_{AP} [m]	s_{FP} [m]	Δs_{AP} [m]	Δs_{FP} [m]
0.68	0.0100	0.0060	0.0091	0.0061	-0.0001	0.0009
0.76	0.0135	0.0070	0.0128	0.0067	0.0003	0.0007
0.82	0.0155	0.0088	0.0145	0.0084	0.0003	0.0010
0.88	0.0183	0.0105	0.0178	0.0095	0.0010	0.0005
0.90	0.0198	0.0115	0.0188	0.0111	0.0004	0.0010

A graphical representation of the validation data, presented in table above can be seen in Figure 4.21.

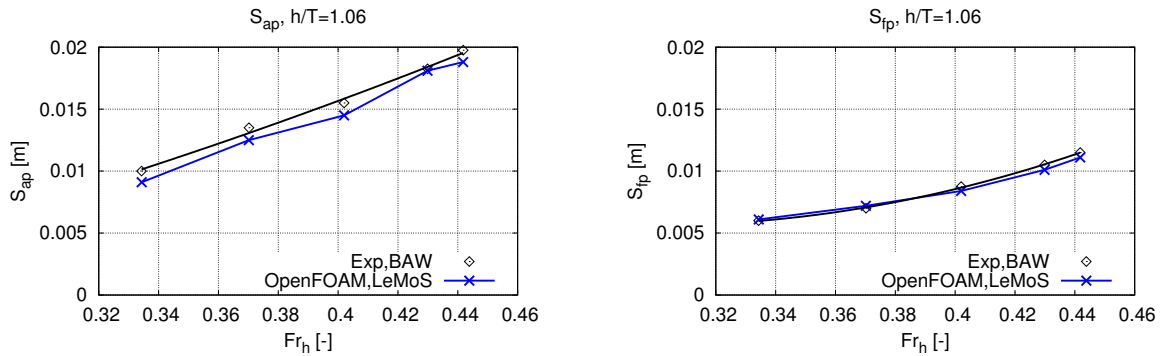


Figure 4.21: Plots of the measured and computed values of squat at aft (left) and fore (right) perpendiculars

¹Here $H(z)$ is the Heaviside function

Chapter 5

Nominal wake analysis

This chapter describes the numerical analysis of the unsteady effects in the wake of an inland cruise ship in shallow water with the use of hybrid turbulence modeling methods. Since it was assumed, that some kind of wake unsteadiness leads to amplification of vibration, the standard deviation and spectrum of longitudinal velocity in the propeller plane are analyzed at and compared between different regimes. The non-uniformity of the wake was also analyzed. Influence of the following factors on the intensity of velocity oscillations is studied:

- depth-by-draft ratio h/T
- depth Froude number Fn_h
- squat
- drift angle β

At this stage of the research the ship propulsors were not taken into account.

5.1 Geometry of the studied hull form

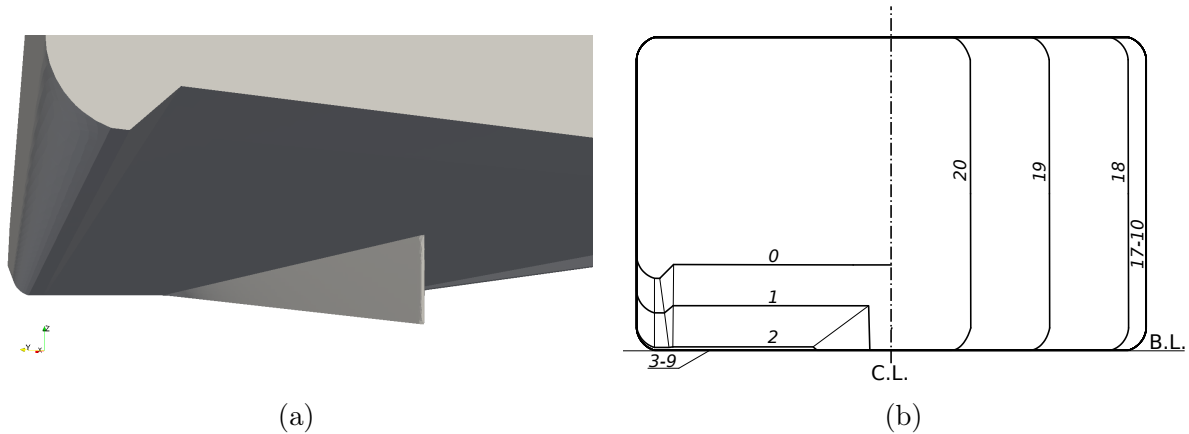


Figure 5.1: Generic hull form: (a) - the view of the stern geometry , (b) - body plan

A real CAD geometry of the river cruiser under consideration was not available. Due to this reason the generic hull form was used, which had the same dimensions ($L_{wl} = 135$ m, $B=12$ m, $T=2$ m) and similar form. The only exception was the form of the bow, which was simplified and replaced by the wedge. The body plan and the 3D stern geometry are shown in Figures 5.1a,b and 5.2. The block coefficient of the studied hull form was $C_B = 0.9$.

Since the phenomena to be studied (e.g. boundary layer separation) are dependent on Re and are hardly scalable, it was decided to conduct all the simulations at full scale.



Figure 5.2: Top, side and front views over the generic hull form

5.2 Choice of simulation conditions

Unfortunately, there was a lack of information on the regimes, at which the vibration occurs and therefore the choice of conditions for the simulations was made based on reasoning, which will be described in the following.

According to the data, provided by the shipyard, the operating speed of the vessel is 6 m/s. The unsteady effects in the stern were expected to be related to the influence of the depth restriction on the viscous wake. The range of h/T had to be chosen such, that this influence would be present. This was done after the analysis of the shallow water influence diagram, presented in the book of Basin et al. [9]. The diagram shown in Figure 5.3 generalizes the series of model tests and allows to roughly estimate the conditions, under which particular effects of depth restriction appear. From Figure 5.3 one can deduce, that the influence of bottom on the viscous wake

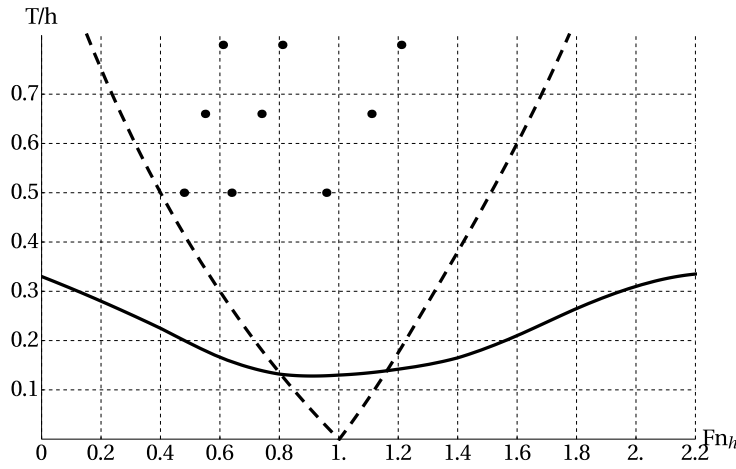


Figure 5.3: Shallow water influence diagram (taken from [9]). In the region above the dashed line the effects on the wavemaking wake and wave resistance are present. The region above the solid line corresponds to the influence on the viscous wake and frictional resistance. The points show the regimes, considered in the presented work

starts to be noticeable for $h/T < 3.0$. It was decided to choose $h/T \leq 2.0$ since at these depths the studied phenomena would be even more pronounced. This reasoning led to the following choice of h/T range: 1.25, 1.5, 2.0, giving the depths $h = 2.5, 3.0, 4.0$ m. The comparison of the solutions at different h/T would allow to draw conclusions on the dependency of the vibration on the fairway depth.

The operating speed of 6 m/s at $h/T = 1.25, 1.5, 2.0$ the Fn_h range 0.96 - 1.21. Such high Fn_h are not typical for the river cruisers, because the latter don't have enough power to overcome the typically high wave resistance, arising at near-critical regimes $Fn_h \approx 1$. However, these regimes were still taken into consideration, because, from the point of view of the author the scenario, when the cruiser suddenly enters a shallow region at full speed may be realistic and should also be analyzed.

Lower speeds were analyzed too, namely 4 m/s and 3 m/s. They correspond to the Fn_h range of 0.64-0.81 and 0.48-0.61 respectively. According to the computed values of resistance and ship propulsive characteristics at these regimes, the considered ship has enough power to maintain these speeds for the chosen h/T range. Therefore such conditions can be regarded as normal¹. All the regimes, which were dealt with in the present work are shown by black circles in Figure 5.3.

¹As opposed to the critical depth Froude number, which represent a rather extreme situation

Another parameter which was expected to have considerable influence on wake unsteadiness was the drift angle. The increase of the drift angle likely leads to the flow separation from the skeg on the downwind side. The vortices, generated at the skeg might interact with the propeller and on this account lead to force and moments oscillations. Unfortunately, there were not enough data to estimate realistic drift angles and therefore the values $\beta = 0^\circ, 10^\circ$ were chosen at will.

5.3 Description of the program of computations

The series of computations of the flow around a generic hull form, conducted in the framework of the presented research can be split into two groups: preliminary and final.

Preliminary study was conducted at the start of the research activities in order to get a first insight into the processes, taking place in the stern region. For this purposes the LH model was employed, because the results of the validation of the model for the number of flows were very promising [71, 70]. However, the experimental data, which could be used for testing of the model for shallow water ship flows was not available. Therefore the quantitative agreement was not the aim for these computations - only the qualitative analysis. In the preliminary computations the influence of depth restriction and wavemaking on the wake unsteadiness was studied. Also the influence of squat was taken into consideration.

As soon as the validation data for M1926 model became available it turned out that the LH model might overpredict the intensity of the velocity fluctuations in the wake because of the stronger separations¹. Nevertheless, since the full scale ship usually has weaker separations, than the model, it was decided to check this hypothesis also for the generic hull form. For this purpose SSTIDDES and LH computations of a flow around a generic hull were performed. The mesh resolution was also varied so as to see its potential influence on the solution. During the comparison of the two models it was ascertained, that for the full scale ship flow LH still tends to predict noticeably higher wake and Reynolds stresses than SSTIDDES and RANS. Thus LH showed the same problematic behavior as for the M1926 model (see Chapter 4). Due to this fact the author came to the conclusion, that SSTIDDES model is superior to LH for the particular mesh generation strategy, used in the research. Therefore, it was decided to conduct the final series of computations using SSTIDDES model.

Detailed description of the mentioned research activities will be given in the following sections.

5.4 Preliminary computations using LH model

Table 5.1: Summary of the computed preliminary cases. FS - free surface

Parameter \ Case label	1PH61	1PH62	2PH61	2PH62	2PH41	2PH42
Fn_h [-]	1.21	1.1	1.21	1.1	0.81	0.74
h/T [-]	1.25	1.5	1.25	1.5	1.25	1.5
U [ms ⁻¹]	6	6	6	6	4	4
FS	no	no	yes	yes	yes	yes

5.4.1 Single-phase simulations setup

At this stage of the study the ship motion with the speed of $U = 6$ m/s at straight course was considered at two different depth-by-draft ratios: $h/T = 1.25, 1.5$. These conditions yield $Fn_h = 1.21, 1.1$, $Re = 8.1 \cdot 10^8$. Even though at such high Fn_h ship's wavemaking is very intense

¹The explanations for the observed model behavior were given in 4

and it can significantly influence the viscous wake of the ship, in the single-phase simulations the free surface was modeled by a symmetry plane. This was also done in the work of Raven [118], who studied the influence of shallow water on the frictional resistance. The dimensions of computational domain were $L_D = 9L_{wl}$, $H_D = 2.5\text{m}$, 3.0m , $B_D = 2L_{wl}$.

For the simulations the unstructured hex-dominant meshes, produced by Star-CCM+[®] trimmer mesher were used. The approximate number of cells was 4M, the stern region was filled with isotropic uniform hexahedral cells ($0.06 \times 0.06 \times 0.06 \text{ m}^3$).

For full-scale simulations it is quite cumbersome to use low Reynolds meshes ($\Delta y_1^+ < 1$) therefore the wall functions were applied with $\Delta y_1^+ \approx 70$. Boundary conditions, imposed on the unknowns at the inlet, outlet, bottom, ship and river bank patches are summarized in Table 5.2, where ω_∞, k_∞ were found using the same formulas as for M1926 validation case. (see [96, 94] for details).

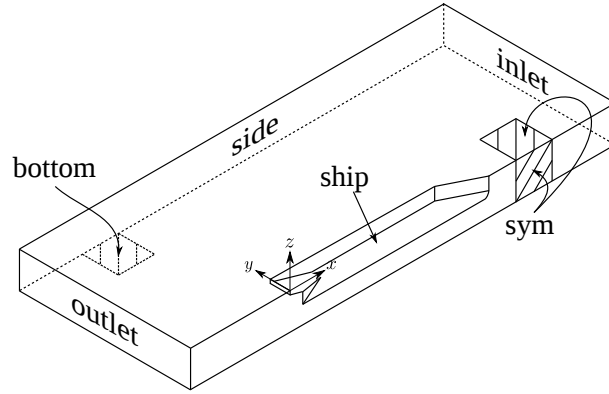


Figure 5.4: Sketch of the computational domain for single-phase simulations. Motion at straight course

Boundary, corresponding to the middle line plane was treated as symmetry plane (see Figure 5.4). Application of the symmetry conditions for scale-resolving simulations is strictly speaking erroneous. However, in the considered case the left and right parts of the stern flow, where the generation of flow instabilities is expected are separated with the skeg and therefore are not actively interacting with each other at straight course. Therefore, it is believed that the use of the symmetry plane condition for the middle-line plane will introduce only minor errors. Summary of the boundary conditions is presented in Table 5.2.

The simulation procedure was the following: first the RANS solution was obtained using `simpleFoam` solver with $k - \omega$ SST model, then it was used as an initial condition for URANS (10 s) with the same closure and after that the computation with LH was conducted for 40 s using `pimpleFoam` solver.

Table 5.2: Boundary conditions for the single-phase simulations

Variable \ Patch	ship	inlet	outlet	bottom	side	sym
$p \text{ [m}^2\text{s}^{-2}\text{]}$	$\frac{\partial p}{\partial n} = 0$	$\frac{\partial p}{\partial n} = 0$	$p = 0$	$\frac{\partial p}{\partial n} = 0$	$\frac{\partial p}{\partial n} = 0$	symmetry
$\mathbf{u} \text{ [ms}^{-1}\text{]}$	$\mathbf{u} = 0$	$\mathbf{u} = \mathbf{u}_\infty$	$\frac{\partial \mathbf{u}}{\partial n} = 0$	$\mathbf{u} = \mathbf{u}_\infty$	$\mathbf{u} = \mathbf{u}_\infty$	symmetry
$k \text{ [m}^2\text{s}^{-2}\text{]}$	$\frac{\partial k}{\partial n} = 0$	$k = k_\infty$	$\frac{\partial k}{\partial n} = 0$	$\frac{\partial k}{\partial n} = 0$	$\frac{\partial k}{\partial n} = 0$	symmetry
$\omega \text{ [s}^{-1}\text{]}$	WF	$\omega = \omega_\infty$	$\frac{\partial \omega}{\partial n} = 0$	WF	WF	symmetry

5.4.2 Two-phase simulations setup

Computations with the free surface were conducted with all the same geometry and conditions as for single-phase, except for the enlargement of the computational domain with the air region and additional consideration of speed 4 m/s. Extension of the computational domain led

to the increase of the number of computational cells to 6M.

The boundary conditions for p_d , \mathbf{u} , k , ω were the same as those previously used in validation study of squat prediction (see Chapter 4). The middle line plane was again considered a symmetry plane.

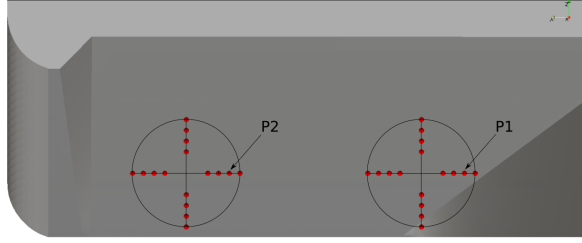


Figure 5.5: Points in the propeller plane, at which the velocity fluctuations were recorded. Fluctuations in P1 (3.065 1.23 -1.375) and P2 (3.065 3.53 -1.375) were used for comparative analysis in preliminary computations

5.4.3 Results and discussion

Single-phase

Analysis of the resolved kinetic energy First of all, in order to make sure, that the mesh resolution was sufficient to resolve the turbulent motions in the wake, the ratio of resolved to modeled turbulence kinetic energy was analysed (k_{res}, k_{mod} respectively). As it is known, reliable results using scale resolving simulations can be obtained if $k_{res}/k_{mod} > 80\%$. For LH model these quantities can be calculated as follows:

$$k_{mod} = fk + (1 - f)k_{sgs} \quad (5.1)$$

$$k_{res} = \frac{1}{2} \langle u'_i u'_i \rangle \quad (5.2)$$

$$k = k_{res} + k_{mod}, \quad (5.3)$$

where f is the blending function of LH model. The averaging in the formula (5.2) was done during the simulation (over 20 s), k is the TKE from the hybrid model, k_{sgs} was estimated using the formula proposed by Mason and Callen [92]:

$$k_{sgs} = \frac{(C_s \delta)^2 |S|^2}{0.3} \quad (5.4)$$

Figure 5.6 shows the distribution of the analyzed ratio in the propeller plane for $h/T = 1.25$. One can see, that at quite coarse resolution, used in the simulations, the amount of resolved kinetic energy in the area of interest is already higher than 80%. For $h/T = 1.5$ the similar result was obtained.

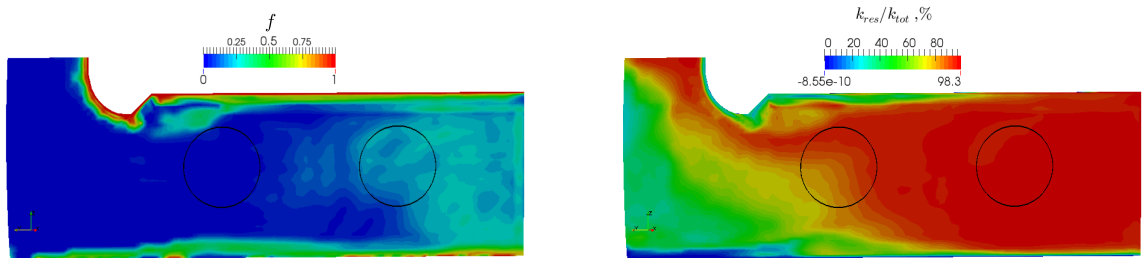


Figure 5.6: Average f (left) and k_{res}/k_{tot} (right) in the propeller plane. Propeller disks are shown with black circles

Vortical structures in the wake

In the Figure 5.7 the vortical structures identified in the wake using λ_2 criterion [60] are shown. One can easily see the difference between URANS and hybrid solutions. Both methods predict two stationary vortexes: at the skeg and the bilge. However, the scale resolving approach additionally shows flow instability, spreading downstream behind the skeg. Comparing different h/T ratios one can notice, that the amount of the eddies depends on the fairway depth. Obviously the region filled with unsteady vortexes becomes wider at lower depths. This can be easily explained by the fact, that the adverse pressure gradient grows, when h/T ratio decreases.

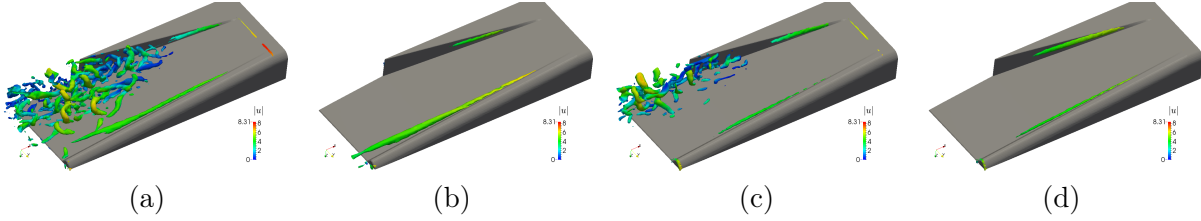


Figure 5.7: Comparison of the vortical structures ($\lambda_2 = -15$) predicted by URANS and hybrid model in a single phase formulation: (a) - 1PH61, hybrid, (b) - 1PH61, URANS, (c) - 1PH62, hybrid, (d) - 1PH62, URANS. View to the stern area from below ship

Axial velocity oscillations

Figures 5.9a-d show the time history of velocity fluctuations at the points P1 and P2 (see Figure 5.5), corresponding to $r/R = 0.7$ in the first (near the skeg) and second (near the bilge) propeller disks. The time interval $[0;10]$ s corresponds to URANS solution. One can see that in both cases URANS method shows almost a steady velocity field. The fluctuations are negligibly small. After switching to the hybrid model the wake soon becomes unstable. It can be seen, that in general the fluctuation amplitude is much larger for the first propeller. Influence of the

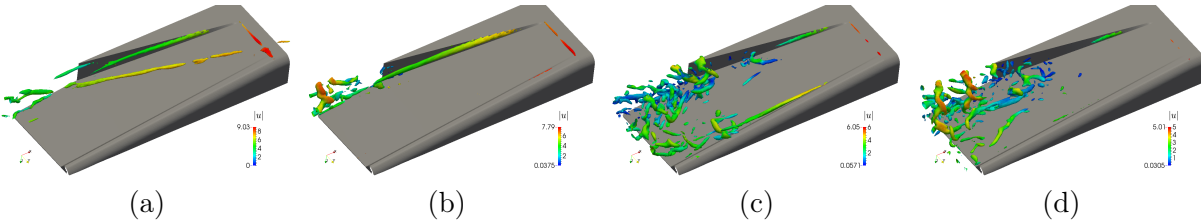


Figure 5.8: Comparison of the vortical structures ($\lambda_2 = -15$) obtained from two-phase simulations with the hybrid model for different regimes: (a) - 2PH61, (b) - 2PH62, (c) - 2PH41, (d) - 2PH42. View of the stern area from below

water depth on the vortical structures is also reflected in Figure 5.9(a-d).

The relative standard deviation of the axial velocity (Eq. (4.5)) for both cases is shown in the Table 5.3. One can see, that the flow for $h/T=1.25$ is richer with eddies and consequently the standard deviation for this case is 5% higher, reaching 19%. Analysis of the power spectral density of the velocity fluctuations in the wake shows, that there are no dominant frequencies which could reveal the periodic processes. Inertial interval of the spectrum can be clearly seen and it obeys the law of $-5/3$ (see Figure 5.11).

Two-phase results

The analysis of the two-phase flow at the same super-critical depth Froude numbers (cases 2PH61, 2PH62) showed the sharp change in the flow behavior compared to single-phase. Namely, the fluctuations in the wake are almost vanished. The reason for this is the disappearance of the unsteady vortexes (Figure 5.8a, b), which led to the flow stabilization.

In order to understand the mechanism, that led to the oscillation suppression one should

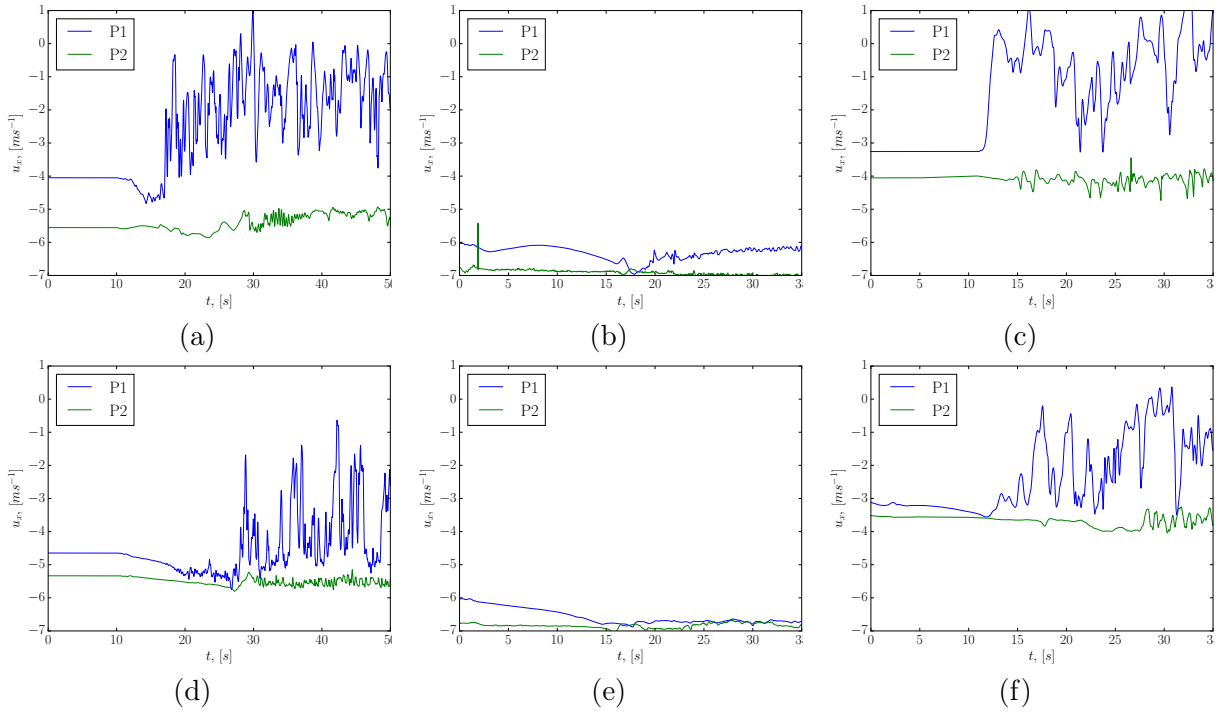


Figure 5.9: Time history of longitudinal velocity at two points in propeller disks. (a) - 1PH61, (b) - 2PH61, (c) - 2PH41, (d) - 1PH62, (e) - 2PH62, (f) - 2PH42

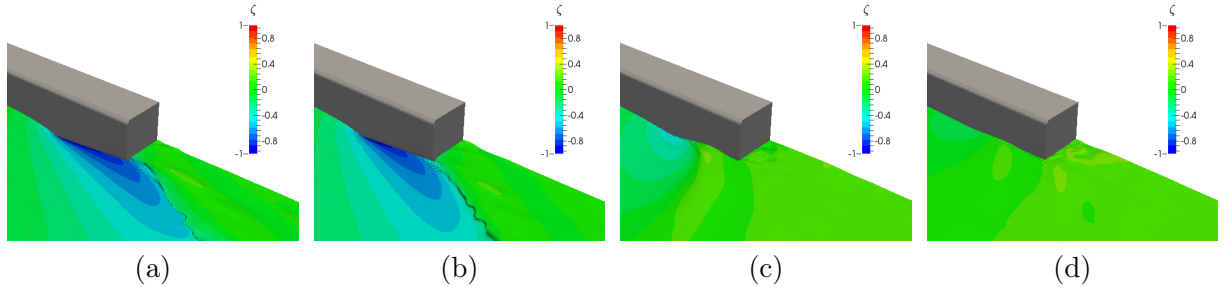


Figure 5.10: Stern wave pattern for different cases: (a) - 2PH61, (b) - 2PH62, (c) - 2PH41, (d) - 2PH42

look at the wave pattern in the stern (see Figure 5.10). As mentioned previously the flow in the stern area is similar to that in a diffuser. However strong free surface deformation, observed in near-critical regime, causes in this case the change of flow geometry. The phenomenon can be explained using the sketch presented in Figure 5.12.

There are two main reasons for the observed effect. First, the fluid motion follows the free surface contour, resulting in the appearance of negative vertical velocities in the area in front and behind the ship bottom edge. Second, the “diffuser” opening angle gets smaller. Due to this effect and water level depression the positive pressure gradient along the hull in the stern decreases. Due to these reasons the reduction of both separation and formation of strong vortices is observed. To check that the captured phenomenon is caused by free surface deformation, the computations with subcritical depth Froude number $Fn_h < 1$ were conducted, at the speed of 4ms^{-1} (cases 2PH41, 2PH42). The pictures of the stern wave patterns and the comparison of the corresponding unsteady vortical structures for different free surface cases are presented in Figure 5.8. The decrease of Fn_h expectedly diminished the stern wave (see Fig. 5.10), making the flow geometry closer to that in a single-phase simulation. Because of this the separation near the skeg appeared again and thus the flow behavior is very similar to that in cases 1PH61, 1PH62. As can be seen in Table 5.3, σ_u is higher (25%) for $U=4$ m/s than for $U=6$ m/s. However, the fluctuation amplitude is lower for lower speeds.

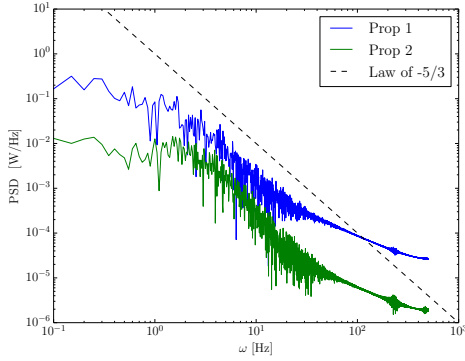


Figure 5.11: Power spectral density of the velocity fluctuations in the propeller disks at different h/T ratios, 1PH61

Case \ Point	Point	
	P1	P2
1PH61	0.19	0.02
1PH62	0.14	0.03
2PH61	0.04	0.01
2PH62	0.01	0.01
2PH41	0.25	0.04
2PH42	0.25	0.05

Table 5.3: Standard deviation of the longitudinal velocity for different cases at points P1 and P2 (in percent of u_x)

These results confirm, that the wavemaking directly influences the wake unsteadiness and therefore, the viscous wake under the studied conditions depends on the depth Froude number. To authors knowledge the effect of suppression of the flow unsteadiness at $Fn_h \approx 1$ has not been discussed in literature so far.

It should be mentioned, that even though in the critical regime the separation disappears and cannot influence the loadings on the first propeller, the observed change of the water level causes the aeration of the second propeller and may lead to another problems.

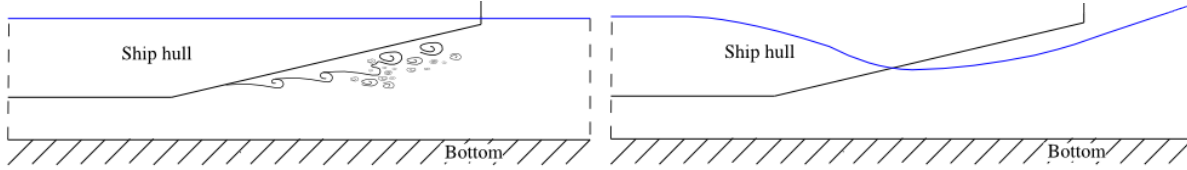


Figure 5.12: Schematic explanation of the free surface influence on the wake unsteadiness, revealed in the preliminary study: left - flow geometry in single-phase simulation, right - the case of critical Fn_h , stern wave causes the change of flow geometry

5.5 Preliminary computations using LH model with account for squat effect

In the previous section the computations were conducted without the dynamic trim and sinkage being taken into account. However, in a real situation the ship will always have some dynamic trim and sinkage, which can also influence the observed wake unsteadiness. Therefore, in some way ship squat should be also accounted for. The most realistic way would be to conduct the time-resolved 2DoF ship motion simulation, coupled with the flow simulation. However, this would be a very complicated computation.

Table 5.4: Summary of the computed cases with squat

Case label \ Parameter	2PH61S	2PH62S	2PH41S	2PH42S
Fn_h [-]	1.21	1.1	0.81	0.74
h/T [-]	1.25	1.5	1.25	1.5
U , [ms ⁻¹]	6	6	4	4

For now, it was decided to use simpler approach, namely, to predict ship squat using LTSInterDyMFoam and then conduct the further simulation with the predicted ship position.

Clearly, in this case the influence of unsteady trim and sinkage oscillations on the wake is neglected. However, as experience shows (see [131]), the fluctuations of ship attitude due to the wake unsteadiness are quite small, even in model scale. Therefore the chosen approach is considered sufficient for capturing the most important flow physics.

From the four cases listed above in Table 5.4, only for three of them it was possible to get the converged ship position, since in the case 2PH61S the ship grounded due to strong squat. The values of trim and sinkage for the rest of the cases are shown in Table 5.5.

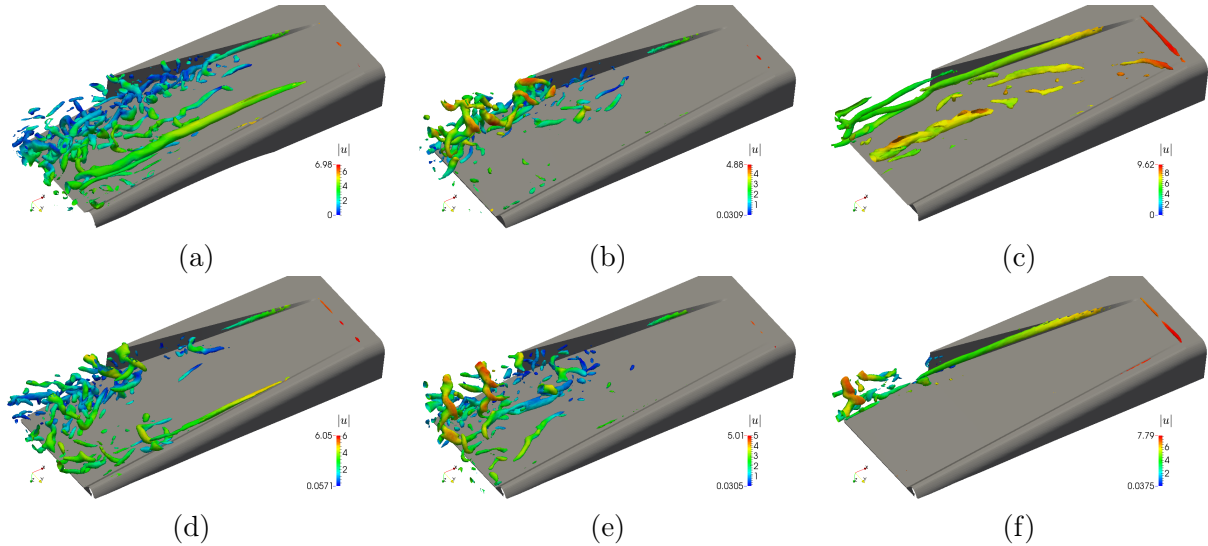


Figure 5.13: Comparison of the vortical structures ($\lambda_2 = -15$) predicted by LH model in a two-phase simulation with squat (upper row) and without squat (lower row): (a) - 2PH41S, (b) - 2PH42S, (c) - 2PH62S, (d) - 2PH41, (e) - 2PH42, (f) - 2PH62

From the snapshots of the vortical structures, presented in Figure 5.13 and the values in Table 5.5 the following conclusions can be drawn.

For the supercritical case the further reduction of the underkeel clearance due to sinkage and trim led only to a slight increase of the fluctuation intensity. The standard deviation in the disk of the first propeller rose to 7%, whereas on the second propeller it remained the same as in 2PH62. One can see, that the cause of this are the strong steady vortical structures, appeared near the skeg (see Figure 5.13c and compare to 5.13f).

In the case 2PH41S, where the ship was trimmed bow up and sunk by approximately 0.2 m the intensity of the fluctuations seem to have reduced at P1 and at the same time increased at P2. Thus, the flow instability has spread further to the bilge. On the contrary, for the case 2PH42S, where the vessel was trimmed bow down values of the standard deviation did not change noticeable. The reason for this is that the reduction of clearance in the stern due to sinkage was compensated by trimming bow down, so that the resulting height of the “diffuser throat” did not change.

Therefore, one can conclude, that the effect of squat on the unsteadiness is determined by the resulting change of the gap size between the ship and the bottom at the stern. Increase of the gap size leads to the diminishment of the adverse pressure gradient and vice versa. This is completely analogous to the dependence on the waterway depth. Since there is already a range of h/T studied, it was decided to avoid the study of squat influence in further computations.

Table 5.5: Values of trim angle, sinkage and standard deviation of longitudinal velocity for the considered cases

Case \ Quantity	$\sigma_{u,P1}$ [-]	$\sigma_{u,P2}$ [-]	ψ [rad]	s [m]
2PH61S	-	-	-	-
2PH62S	0.07	0.01	-0.0075	0.21
2PH41S	0.14	0.10	-0.0009	0.19
2PH42S	0.23	0.04	0.0025	0.18

5.6 Conclusions of the preliminary study

From the preliminary computations, which were described in the previous sections of this chapter one could already draw some important conclusions:

1. As could be seen, the URANS computations predicted almost steady velocity fields in the cases, where the LH model showed considerable flow instationarity. Therefore, it was once again proven that URANS may be inapplicable for the problems with significant inner flow instabilities.
2. Strong unsteady fluctuations of the velocity field in the propeller disc were observed under some motion conditions. In most cases the oscillations in the propeller disc near the skeg were much stronger than those near the bilge. This difference is related to the presence of boundary layer separations in the vicinity of the skeg and the strong skeg vortex.
3. The wave pattern of a vessel in near-critical regime ($Fn_h \approx 1$) can play a significant role for the instationarity of the viscous wake. The deformation of the free surface can change the flow geometry in the stern and on this account suppress the velocity oscillations.
4. Squat influence on the unsteadiness of the velocity field in the stern is determined by the resulting change of the size of the gap between the fairway bottom and the ship hull in the stern region.

5.7 Grid convergence study

The previous two sections described the preliminary computations, aimed at the qualitative analysis of the wake of a river cruiser. As long as no experimental data were available for the velocity or Reynolds stress distribution in the flow, the best way to control the quality of the results obtained was the assessment of the agreement with another models and the investigation of mesh convergence. Therefore, it was decided to conduct such a study and compare the performance of LH and SSTIDDES models on the meshes with gradually decreased cell size. Testing of SLH model was not possible at the moment, because the modification was developed after the mesh convergence study was completed. As previously, the SSTIDDES model was used with the turbulence generator, whereas LH - without the generator because of the stability reasons.

5.7.1 Conditions

As it has been previously shown, very complicated processes take place in the stern at critical regime, namely, the interaction of the viscous and the wave wakes. These phenomena, involving the influence of free surface on the turbulence generation should be studied further. However, since the considered regime is an exception for river cruisers, a simpler case with moderate Fn_h was chosen for the grid convergence assessment. The selected speed of vessel U was 3 m/s, which at $h/T = 1.25$ yields the depth Froude number $Fn_h = 0.6$ and $Re = 4 \cdot 10^8$.

Already at 4 m/s at $h/T=1.25$ one can see (Figure 5.10), that the stern wave is quite small and therefore should not have that high influence on separation effects, as at $Fn_h \approx 1$. This means, that for lower speed this influence would be even weaker and can be neglected. Due to this reason and in order to efficiently use the computational resources this task was solved in single-phase formulation with the free surface replaced by a symmetry plane. In this case one could avoid meshing of the air domain and the air/water interface and place more computational nodes in the wake region.

The computed values of trim angle and sinkage for the considered regime were 0.2° and 0.12 m respectively. Under these circumstances (trimming bow down), the gap size remains unchanged and therefore the squat influence is negligible (see the case 2PH42S).

The geometry of the ship was exactly the same as in preliminary research. The computational domain was limited to the water region. Boundary conditions were therefore the same as for the M1926 case (see Chapter 4), except that the wall functions were applied for the ship patch and that the middle line plane was treated as symmetry plane

5.7.2 Numerical setup

The number of computational cells in the coarse, medium and fine meshes was 3M, 6M and 11M respectively. As for M1926 case the stern region was filled with isotropic cubic cells with edge length of 0.078 m, 0.056 m, 0.039 m respectively. Mesh refinement was done by decreasing the base size of the mesh by $\sqrt{2}$. The average dimensionless wall distance of the first node of the mesh was $\Delta y_1^+ \approx 70$. Additionally, in order to check the sensitivity of the models on the wall treatment, a medium mesh with $\Delta y_1^+ \leq 1$ was generated. This is needed, because the wall functions which were applied for the most of the cases may not work correctly in the separation regions.

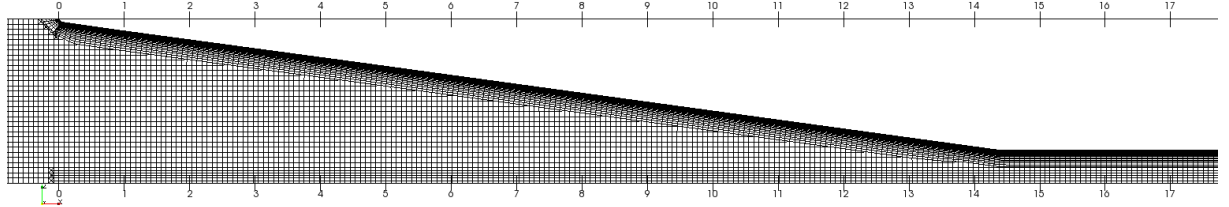


Figure 5.14: Y-Slice of the mesh structure at the stern (coarse mesh)

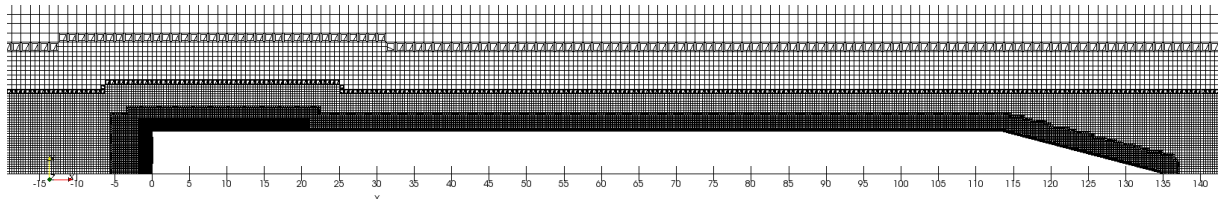


Figure 5.15: Top view of the mesh structure (coarse mesh)

The numerical schemes, used for discretization of the underlying PDE were the same as those used for M1926. Since the validation results for that case were satisfactory, it was decided to avoid introduction of any changes to these settings.

As previously, the solution was obtained in two steps. First, the RANS solution with $k - \omega$ SST model was sought for, which was then used as initial condition for hybrid simulations (SSTIDDES, LH). The statistics for the turbulence generator were taken from the RANS solution.

The algorithm of introduction of velocity fluctuations was the same as for diffuser flow and M1926 case. A layer of cells in the plane, normal to the flow direction was selected upstream of stern. Here, the distance L_g from the ship bottom edge was chosen similarly to the diffuser

flow, namely $5(h - T)$, where h is the fairway depth. The sensitivity of the results to the distance L_g was not studied because of the huge computational effort, which would be necessary. Unfortunately, since the mesh in the considered case was quite coarse, it may happen, that the placement of the generator farther from the stern would lead to suppression of the generated vortices before these reach the diffuser geometry.

5.7.3 Analysis of the results

Solutions were compared in the following form:

1. Distribution of the averaged longitudinal velocity \bar{u}_x along the line $x=3.065$ m, $z=-1.375$ m, $y \in [0, 4.5]$ m in the propeller plane, passing through the rotation axes of the front propellers
2. Total (modeled + resolved) turbulence kinetic energy along the same line
3. Relative standard deviation of the velocity field σ_u in four points, lying at the distance $r = 0.7R$ from the propeller axes (see Figure 5.17).

Additionally, for the finest mesh the analysis of the resolved to total turbulence kinetic energy was done along three lines, lying in propeller plane $x=3.065$ m, $z=-0.875$ m, -1.375 m, -1.875 m, $y \in [0, 4.5]$ m (see Figure 5.17).

Comments on the grid convergence analysis

Judgement on the convergence properties was not straightforward. Unfortunately, none of the models showed convergence in classical sense. This means that the variation of the solution between the coarse and medium meshes was in some regions lower than between the medium and fine ones. At the same time, in RANS and SSTIDDES results one can see that the curves for different meshes are lying very close to each other and the variation of the solution is very small. Moreover the comparison of the solution between the coarse and fine meshes shows ¹, that the decrease of cell size by half in each direction did not yield any significant change of analyzed parameters in the most regions of the flow. Therefore, it was decided to draw conclusions on the convergence based on the variation between the coarse and fine meshes. The smaller the variation was, the better convergence the model was considered to have.

Convergence analysis

The best convergence for the mean velocity profile was shown by SSTIDDES model. In Figure 5.16 one can notice, that the solutions on all three meshes are almost identical in the region $y \in [1; 4.5]$ m. Closer to the skeg, where the vortex is situated, one can see a slight solution variation. Formally, in some regions the solution diverges, but in fact the variations are negligible. Similar conclusions can be drawn about the prediction of the total turbulence kinetic energy: almost the same level of total TKE is predicted on all meshes for $y > 1.5$ m. The solutions on the coarse and fine meshes are again very close to each other. Keeping in mind that the cell size was halved in each direction from coarse to fine mesh, one can conclude, that for some reasons the medium mesh is an outlier, predicting a peak of k_{tot} at $y \approx 0.3$ m. This peak agrees with the RANS solution (see Figure 5.16h), showing that the reason, why the model produced different solution on the medium mesh is that it switched to RANS for $y < 1$ m, even though the cells were smaller, than in coarse mesh.

Variations of σ_u in the propeller plane are quite small with the maximum difference between the coarse and fine meshes of 2% (see Figure 5.16c)

Variation of the cell size for RANS $k - \omega$ SST model yielded only small variations in \bar{u}_x profile as well (see Figure 5.16g), and, as for previous model, the largest differences were observed

¹For RANS and SSTIDDES

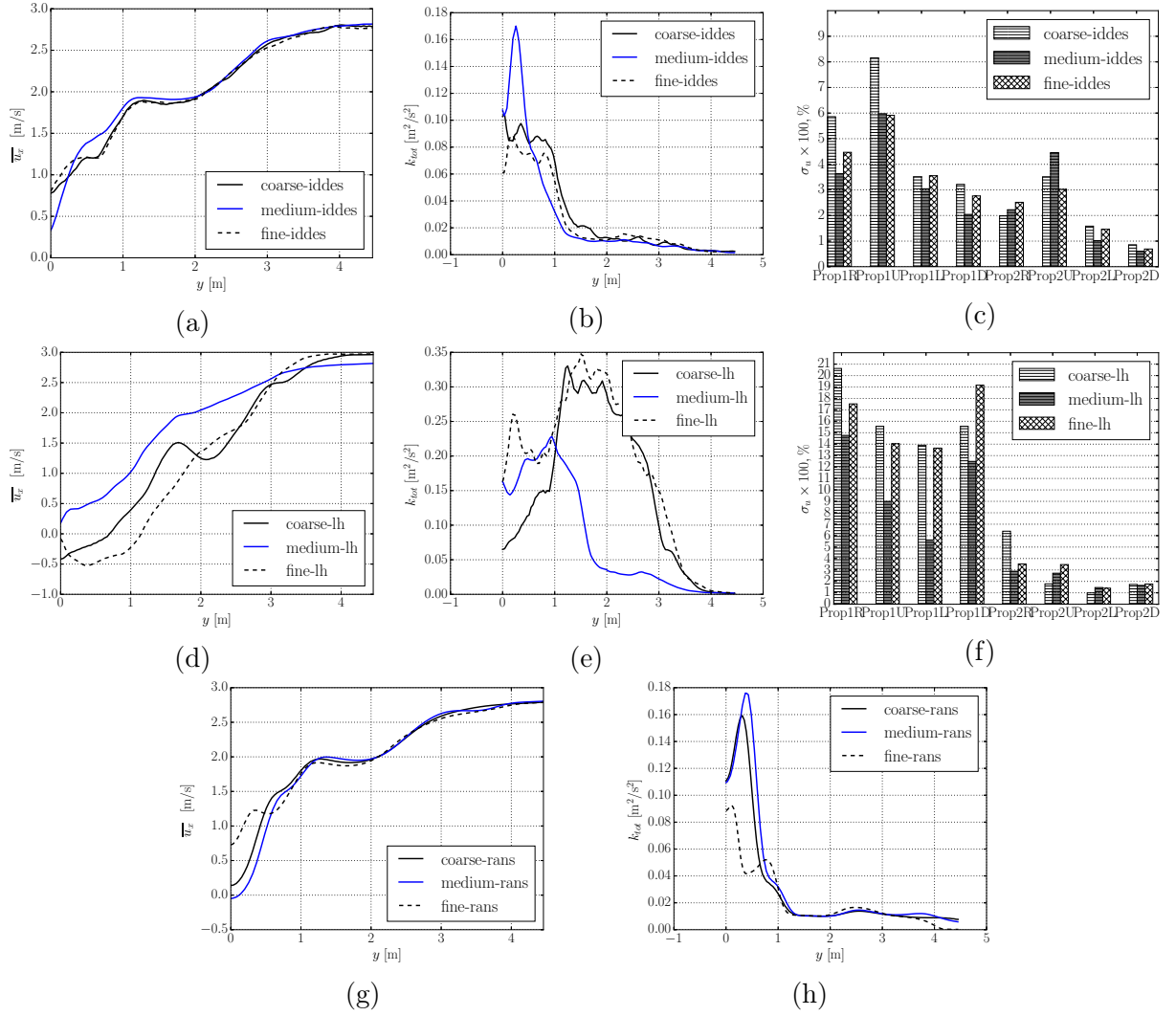


Figure 5.16: Comparison of $\langle u_x \rangle$, k_{tot} profiles between the different meshes for SSTIDDES, LH and RANS $k - \omega$ SST models along the line $x = 3.065, z = -1.375$ (a,b,d,e,g,h) ; convergence of the relative standard deviation in the propeller plane (c,f)

in the region $y < 1$ m. The changes in k_{tot} for $y < 1$ m are quite high (up to 0.1), but farther from the skeg the solutions are again almost identical.

Analysis of the results of the LH model revealed relatively high sensitivity of the solution on the mesh. The mean longitudinal velocity profiles and TKE oscillate much stronger between the meshes than for other models. However, the curves for fine and coarse meshes are (as for other models) quite close to each other and at the same time distinct from the medium mesh solution. The quantity σ_u in the propeller plane undergoes the same variations as k_{tot} , namely the difference between the fine and coarse mesh is limited to 2.5%, and between the coarse and medium - almost 10%. Therefore, arguably, there was some problem with the medium mesh, which influenced the solutions obtained using all models.

Comparison of $\overline{u_x}, k_{tot}, \sigma_u$ between the models on the fine mesh (see Figure 5.18) allows to conclude, that RANS and SSTIDDES models converged to almost the same result on the fine mesh, even though the latter solution is essentially unsteady and contains coherent turbulent vortices. The LH model showed completely different values for all quantities. The fact, that the model predicts velocity field, which is significantly distinct from RANS and other SRS approach causes suspicion. Here one should recall the results of the M1926 validation case, where the similar model behavior was observed. In that case the remedy was to use the new shielded modification (SLH), which yielded a much better agreement with experimental data. Most

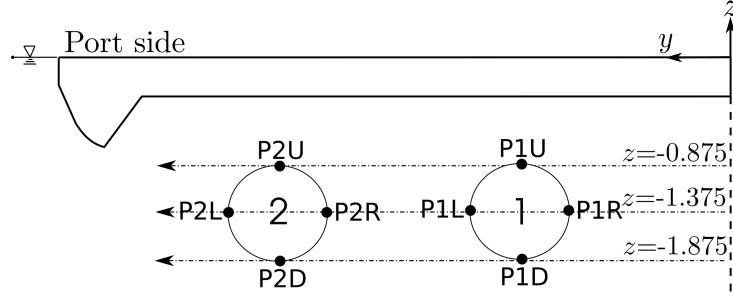


Figure 5.17: Sampling lines for comparison of solutions and probe points for collection of u_x statistic (P1U, P1R, P1L, P1D, P2U, P2R, P2L, P2D)

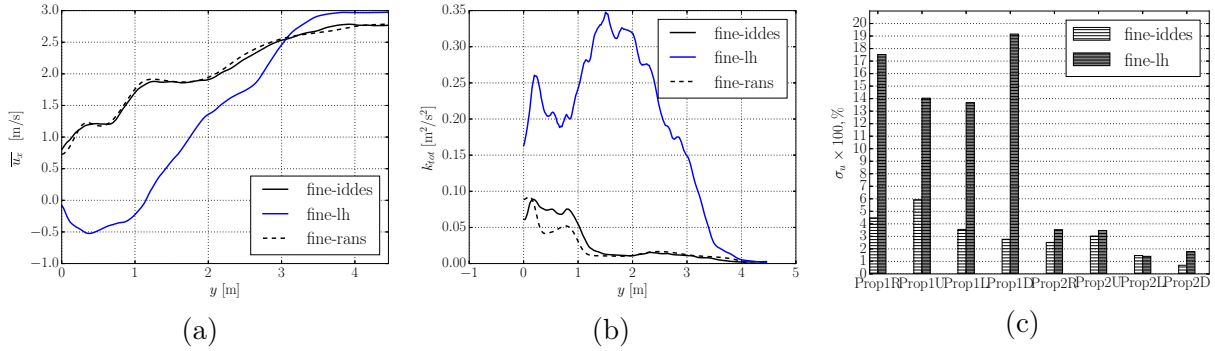


Figure 5.18: Comparison of the solutions produced by different models on the fine mesh

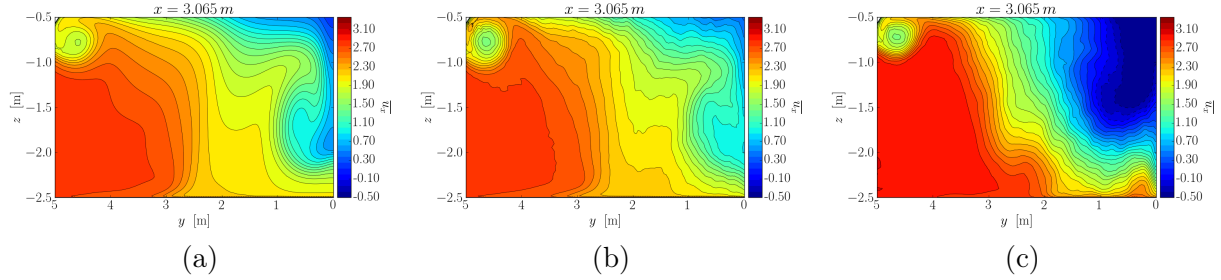


Figure 5.19: Contour plots of the time-averaged longitudinal velocity field $\langle u_x \rangle$ in the propeller plane, predicted by RANS (a), SSTIDDES (b), and LH (c) on the fine mesh

likely, the shielding would improve the LH predictions for generic hull form as well.

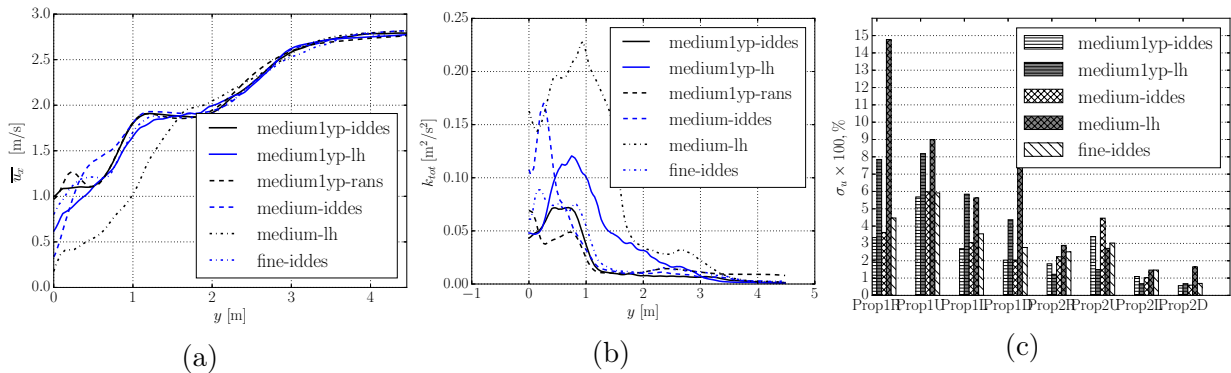


Figure 5.20: Sampling lines for comparison of solutions and probe points for collections of u_x statistic (1U, 1R, 1L, 1D), (2U, 2R, 2L, 2D)

Sensitivity to the wall treatment

As it is known, application of wall functions for the flows with adverse pressure gradients may lead to considerable deterioration of the results [161]. The flow in the stern of the considered generic hull is subjected to the positive pressure gradient and therefore it should be checked, whether the use of combination of high Reynolds mesh ($y^+ \approx 70$) with wall functions has any negative influence on the results. In order to analyze the sensitivity of the solution to the wall treatment, additional computations on a low Reynolds ($y^+ \leq 1$) medium mesh were conducted using LH, SSTIDDES and RANS. Comparison of the results can be seen in Figure 5.20. From these plots one can draw a number of very important conclusions:

- Flow picture, predicted by LH completely changed when the integration to the wall was used. The velocity field obtained on low Reynolds mesh almost reproduces those obtained using SSTIDDES and RANS (see Figure 5.21) and contains no strong separations. As for the TKE, its level has significantly decreased and became much closer to other models. Thus LH model seems to be very sensitive to the wall treatment. A following explanation can be given to the observed effect. The model has no shielding and therefore cannot prevent LES from entering the boundary layer. In this situation the model can produce accurate results only if the resolved turbulence is generated in some way. However, the buffer layer, where the most turbulence is produced is not resolved when $y^+ > 10$ and therefore the physical mechanism for generation of turbulent content in the boundary layer is absent when a high Reynolds mesh is used.

This leads to reduction of the wall-normal momentum transport and results in strong separations. On the other hand, when the buffer layer is resolved, there is a turbulent content generated, so that the resolved stresses prevent the nonphysical separation. This explanation, however is not exhaustive, because for M1926 validation case all meshes had $y^+ \approx 1$ and therefore the buffer layer was resolved. As could be seen the model predictions without shielding were nevertheless unsatisfactory.

- SSTIDDES seems to be almost insensitive to the wall treatment. Even though the solution on low Reynolds medium mesh changed compared to high Reynolds medium mesh, the resulting predictions agree very well with the solution on the fine and coarse meshes. Therefore, it seems, that the mesh rebuilding with different parameters simply solved the problem, which previously made the high Re medium mesh an outlier. This insensitivity is most likely the consequence of using the turbulence generator, which to some extent substitutes the natural mechanism of generation of turbulent structures discussed above ¹. However, the absence of the natural mechanism may lead to a situation where the generated turbulence would not be sustained and would decay. Even though for the current study it obviously made no difference, this issue has to be kept in mind.
- Obviously, neither RANS nor SSTIDDES showed any qualitative difference between the high Re and low Re solutions. Based on this fact, it was decided, that application of wall functions for the case of interest does not introduce any noticeable errors. Since no experimental data were available for comparison, the quantitative agreement could not be judged on anyway.

Analysis of the resolved TKE

Analysis of the ratio of the resolved to total TKE is one the ways to prove the reliability of the obtained flow predictions. If the ratio k_{res}/k_{tot} exceeds 80%, this generally means, that the bulk of turbulence energy, contained in large anisotropic vortices is resolved. Since the rest of

¹The accuracy of the results in this case is clearly dependent on the quality of generated turbulence

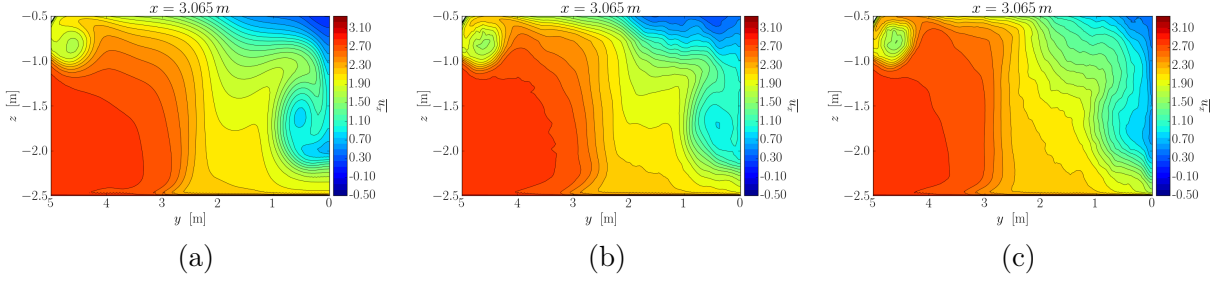


Figure 5.21: Contour plots of the longitudinal velocity field in the propeller plane, predicted by RANS (a), SSTIDDES (b), and LH (c) on the medium mesh with $y^+ \leq 1$

the structures are close to isotropic, their modeling accuracy is much higher, that for large-scale structures.

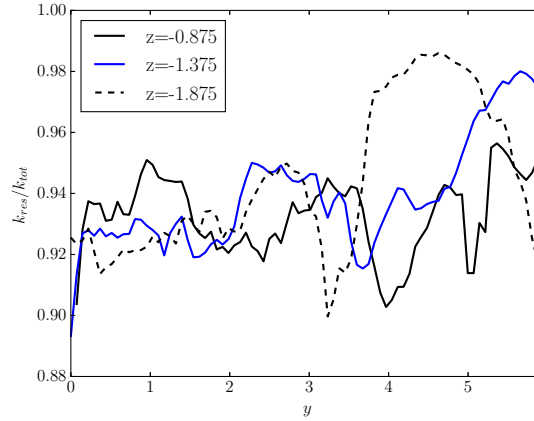


Figure 5.22: Profiles of k_{res}/k_{tot} ratio along three lines in propeller plane

In the presented case the ratio was analyzed along three lines in the propeller plane (see Figure 5.22). One can see, that on the fine mesh more than 90% of the TKE is resolved, indicating, that the mesh resolution was sufficient for a scale-resolving simulation.

5.7.4 Conclusions on the grid convergence study

Summarizing the collected information about the convergence of different models on different grids, one can conclude, that, being properly applied, all models yielded nearly the same predictions of the mean velocity field. At the same time the results for longitudinal velocity fluctuations in the propeller plane were quite different between the LH and SSTIDDES models.

SSTIDDES showed arguably the best performance, in that the variations of the solution between the meshes were much smaller, than even for RANS. Intensities of the velocity fluctuations observed on coarse and fine meshes are very close to each other and to low Reynolds medium mesh.

LH model without shielding showed behavior analogous to that in M1926 validation case. The levels of the TKE, observed in all cases were much higher, than for RANS and SSTIDDES. Application of low Re mesh improved the result for both the mean velocity field and the total TKE. However, the agreement with other models for the TKE level is still not very good.

For SSTIDDES and RANS the variations of the mean velocity field and TKE between the meshes were observed only in the region near the skeg vortex. The intensity of fluctuations of the velocity field seems to be the most sensitive parameter, but agrees well between the coarse and fine meshes, showing the variation of maximum 2.5% for σ_u . Reduction of the cell size by two times did not cause any qualitative change of the solution. However, it was decided to use the fine resolution for further study, since the computational resources, needed for the simulations were affordable.

5.8 Final computations of the nominal wake

The final computations of the nominal wake of the generic hull in shallow water were performed using SSTIDDES model. It was chosen because of its performance for M1926 validation case and robustness to mesh resolution. For the enrichment of the flow with unsteady content the turbulence generator of Adamian was used [4]. In order to evaluate the influence of depth on the velocity fluctuations and on the wake in the propeller disks, range of h/T ratios was studied. Both the wake instationarity and non-uniformity may contribute to force and moment oscillations and therefore both of these characteristics were assessed. Motion at straight course as well as with the drift angle $\beta = 10^\circ$ were considered.

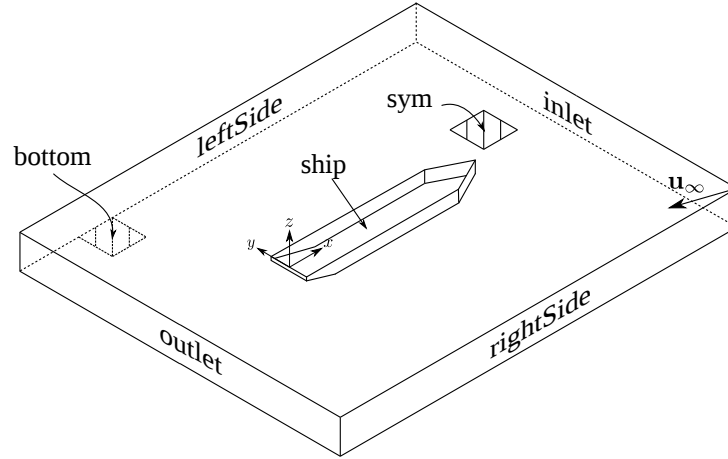


Figure 5.23: Sketch of the computational domain for the computations with the drift angle

5.8.1 Conditions and setup

Motion at straight course

For the final computations with the bare hull the same ship speed was chosen as that in the convergence study, i.e. $U = 3\text{m/s}$. The range of depth-by-draft ratios was $h/T = 1.25, 1.5, 2.0$. Mesh structure for computations at $\beta = 0^\circ$ replicated the one from the grid convergence study. Therefore for further information on the mesh parameters reader is referred to section 5.7. Meshes for $h/T = 1.5, 2.0$ were generated by extruding the bottom patch of the mesh for $h/T = 1.25$ downwards, so that the node distribution near the ship was completely identical between all depths. Only the mesh in the extruded region was different. This was done in order to avoid the influence of the changes in mesh structure on the studied effects.

Table 5.6: List of the considered conditions with corresponding labels

Parameter \ Case label	FB1-0	FB2-0	FB3-0	FB1-10	FB2-10	FB3-10
U [m/s]	3	3	3	3	3	3
h/T [-]	1.25	1.5	2	1.25	1.5	2
β [°]	0	0	0	10	10	10
Fn [-]	0.08	0.08	0.08	0.08	0.08	0.08
Re [-]	4.05E+08	<–	<–	<–	<–	<–
Fn_h [-]	0.61	0.55	0.48	0.61	0.55	0.48

Numerical settings, boundary conditions and inflow generator parameters were identical to those previously used in the mesh convergence study. Probe locations for velocity fluctuations were also placed at the same points, as before (see Figure 5.17).

The computations were conducted (with and w/o drift angle) for 60 s of the model time.

The first ten seconds were removed from the statistical samples in order to avoid the influence of transition effects ¹ on the results.

Motion with the drift angle

Table 5.7: Boundary conditions for nominal wake computations with the drift angle

Variable \ Patch	ship	inlet	outlet	bottom	side	sym
$p, [\text{m}^2\text{s}^{-2}]$	$\frac{\partial p}{\partial n} = 0$	$\frac{\partial p}{\partial n} = 0$	$p = 0$	$\frac{\partial p}{\partial n} = 0$	$\frac{\partial p}{\partial n} = 0$	symmetry
$\mathbf{u}, [\text{ms}^{-1}]$	$\mathbf{u} = 0$	$\mathbf{u} = \mathbf{u}_\infty$	$\frac{\partial \mathbf{u}}{\partial n} = 0$	$\mathbf{u} = \mathbf{u}_\infty$	$\mathbf{u} = \mathbf{u}_\infty$	symmetry
$k, [\text{m}^2\text{s}^{-2}]$	$\frac{\partial k}{\partial n} = 0$	$k = k_\infty$	$\frac{\partial k}{\partial n} = 0$	$\frac{\partial k}{\partial n} = 0$	$\frac{\partial k}{\partial n} = 0$	symmetry
$\omega, [\text{s}^{-1}]$	WF	$\omega = \omega_\infty$	$\frac{\partial \omega}{\partial n} = 0$	WF	WF	symmetry

For the computations with the drift angle it was no more possible to use symmetry plane assumption for the middle line plane. Therefore meshes for the whole ship were generated by mirroring of the corresponding meshes for straight course. Total number of computational cells of approximately 20-22M, depending on the depth. Therefore in this case the geometry of the computational domain as well as the boundary conditions were changed. The sketch of the domain with the names of its boundaries is shown in Figure 5.23. In this configuration the patches inlet and rightSide were treated as inflow boundaries, whereas outlet and leftSide - as outflow boundaries. The summary of boundary conditions used can be found in Table 5.7. Boundary conditions, imposed on the inlet and rightSide boundaries were the same. For outlet and leftSide boundaries the situation was similar, except for pressure, for which the BC on the leftSide patch was $\frac{\partial p}{\partial n} = 0$.

The complete list of the considered cases for the computations of the nominal wake is presented in Table 5.6.

5.8.2 Analysis of the results. Straight course

Analyzed were the wake in the propeller plane and the velocity fluctuations at eight points in the first and second propeller disks. Additionally, in order to better understand the physics of the flow the streamlines of the mean velocity field and contour plots of resolved Reynolds stresses $\langle u_x'^2 \rangle$ were generated.

The collected velocity statistics at the probe points were compared between the cases in the form of standard deviations σ_u (see Table 5.9) and the plots of empirical distribution functions (EDF) of longitudinal velocity fluctuation, built from the velocity samples ².

Influence of the fairway depth on the wake As one can conclude from Figures 5.24,5.25 the wake in the first propeller disk is much higher than in the second one. The non-uniformity of the velocity field for second propeller is quite low and seems to be almost independent of the depth in the considered range. On the contrary, the wake in the propeller disk near the skeg rapidly grows and becomes more irregular as the depth decreases.

Influence of the fairway depth on the flow instationarity ($\beta = 0^\circ$) From the values of σ_u presented in Table 5.9 one can draw a number of important conclusions. First of all, one can see, that the dependence of the wake instationarity on the depth is not the same for all points. For example, in the point P1R next to the skeg the fluctuation intensity clearly increases, when h/T decreases, whereas at the points P2L and P2D there is a reverse trend. At all other points the values of standard deviation do not show any clear dependency on the depth. Therefore it

¹RANS to RANS-LES transition

²EDF is a discontinuous piecewise constant function and should be normally plotted in this form. However, in order to compare multiple EDFs it was very useful to convert the piecewise constant representation to piecewise linear. All the EDF plots will be presented in this form

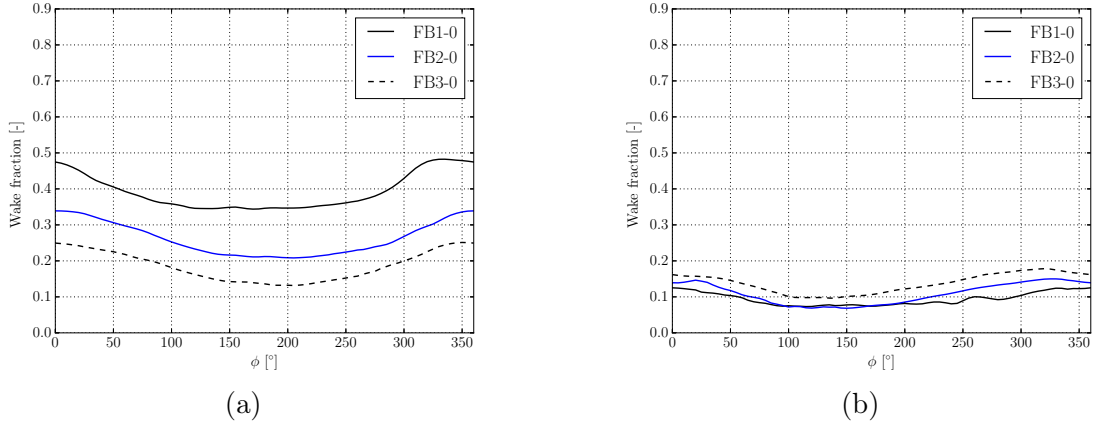


Figure 5.24: Nominal wake w in the propeller plane at $r/R=0.7$ for first (a) and second (b) propeller disks

is not possible to draw some general conclusions on the fluctuations intensity - such deductions should be done in combination with the description of local flow picture.

For the point P1R the intensity of the fluctuations grows due to the increase of the skeg vortex size, when the depth is reduced (see Figure 5.25). The points P1U, P1D and P1L are obviously not influenced by this vortex and therefore σ_u is likely to be determined only by the turbulent structures generated in the ship's boundary layer and then transported downstream. In the contour plots of the resolved Reynolds stresses ($\langle u_x'^2 \rangle$) (see Figure 5.25) one can see, that the distribution of $\langle u_x'^2 \rangle$ on the left from, above and below the first propeller disk is almost the same for all considered depths. The situation in the points P2U and P2R is similar.

On the left from and below the second propeller (points P2L and P2D) the fluctuations are intensified when the depth is increased. The reason for this is the change in flow direction at the stern at low h/T . Under these conditions the fluid flow at the stern is directed under the ship to the middle line plane (see the streamlines in Figure 5.30). Therefore, the turbulent fluid from under the ship and from the sides of the hull is not transported directly to the second propeller disk and is instead flowing into the space between the propeller disks. Therefore at $h/T = 1.25$ the second propeller works in a flow with a much lower level of turbulent fluctuations (see Figure 5.25). When the depth increases the y-component of the flow velocity in the stern reduces, so the turbulence from under the hull is advected directly into the second propeller disk. As a result σ_u at P2L, P2D at $h/T = 2.0$ reaches nearly the same level as in all other points (except for P1U). At the point P1U the observed velocity fluctuations were the most intense and at the same time independent of the depth.

Plots of empirical distribution function for three points: P1U, P1R and P2L are shown in Figure 5.26. These points are selected as examples of three different trends: P1U - the EDF is insensitive to the depth variation (curves are similar to those for P1D, P1L, P2U and P2R), P1R - the reduction of depth leads to the elongation of the EDF tails meaning that high peaks (up to 15%) become probable, P2L - increase of h/T causes considerable horizontal stretching of the EDF, indicating stronger instationarity of the velocity field (again with the peaks up to 15% for FB3-0). As one can see, the trend depends on the location of the points.

Probably the most important conclusion one can draw is that the reduction of the fairway depth leads to the situation, where the flow instationarity is concentrated near the first propeller disk, whereas the second propeller disk has much lower fluctuation intensity. Described above change in flow direction at the stern, increase of skeg vortex size and separation on the left from the skeg all are responsible for this phenomenon. Further depth reduction would make these effects even more pronounced and would lead to consequent increase of flow instationarity in the disc of the first propeller.

Table 5.8: Relative standard deviation of velocity σ_u in eight points in the propeller plane. For the point designations see Figure 5.17. The sketch of the probe points is added for the ease of understanding

	$\sigma_{u,P1R}$	$\sigma_{u,P1U}$	$\sigma_{u,P1L}$	$\sigma_{u,P1D}$	$\sigma_{u,P2R}$	$\sigma_{u,P2U}$	$\sigma_{u,P2L}$	$\sigma_{u,P2D}$
FB1-0	0.045	0.056	0.040	0.031	0.024	0.036	0.013	0.010
FB2-0	0.042	0.062	0.044	0.033	0.037	0.044	0.024	0.018
FB3-0	0.035	0.055	0.040	0.033	0.037	0.039	0.038	0.027

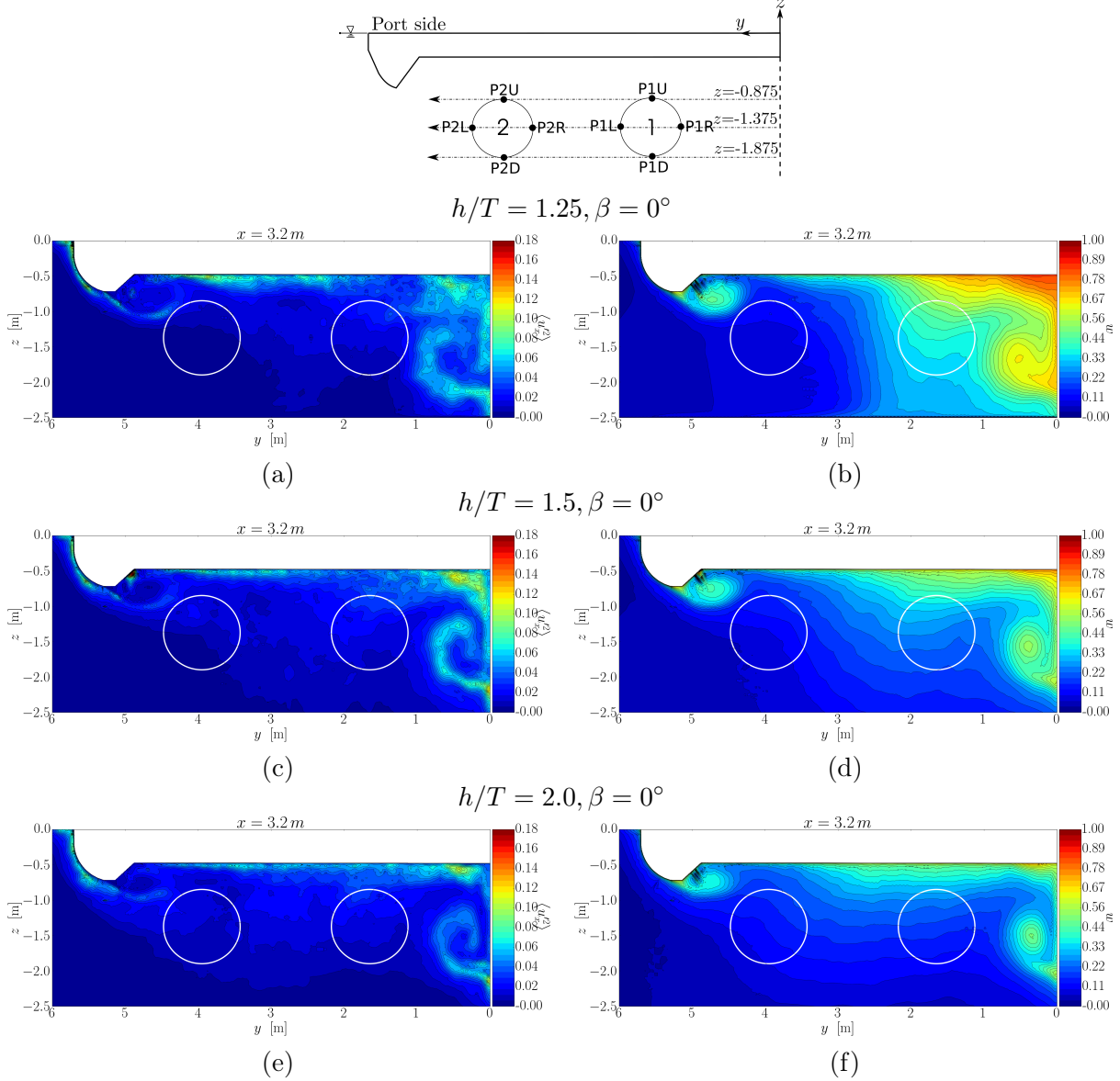


Figure 5.25: Plots of the resolved Reynolds stresses $\langle u_x'^2 \rangle$ (left) and wake (right). Figures correspond to the following cases: a, b - FB1-0; c, d - FB2-0; e, f - FB3-0

5.8.3 Analysis of the results. Drift angle $\beta = 10^\circ$

The same analysis was performed for the motion with the drift angle as previously for the straight course. Even though in this case, the propeller disks on the starboard side were also studied, it turned out, that in these locations the flow is almost undisturbed compared to the port side: the wake and velocity fluctuations were very low. Therefore, only the results for the port side propeller disks will be presented.

Influence of the fairway depth on the wake For all of the considered depths the numerical simulations predicted significantly lower wake for the motion at $\beta = 10^\circ$ as compared to the

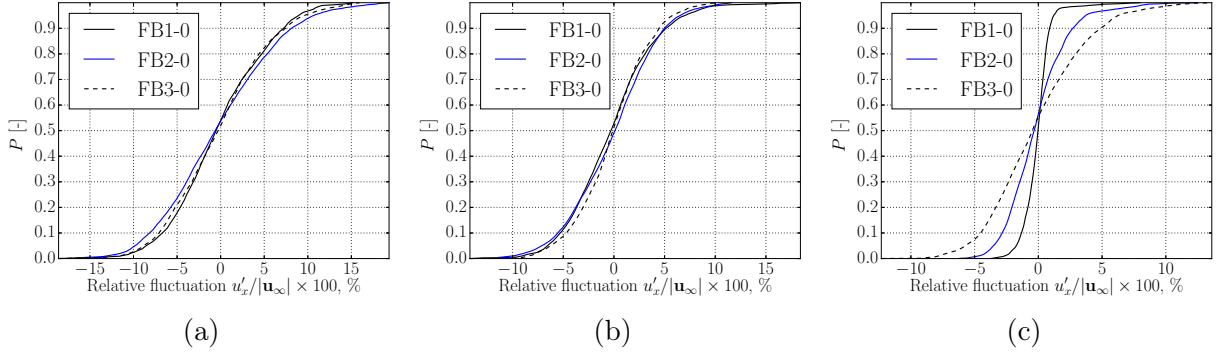


Figure 5.26: Comparison of empirical distribution functions of velocity fluctuations built at points (a) - P1U; (b) - P1R; (c) - P2L for different depths for $\beta = 0^\circ$

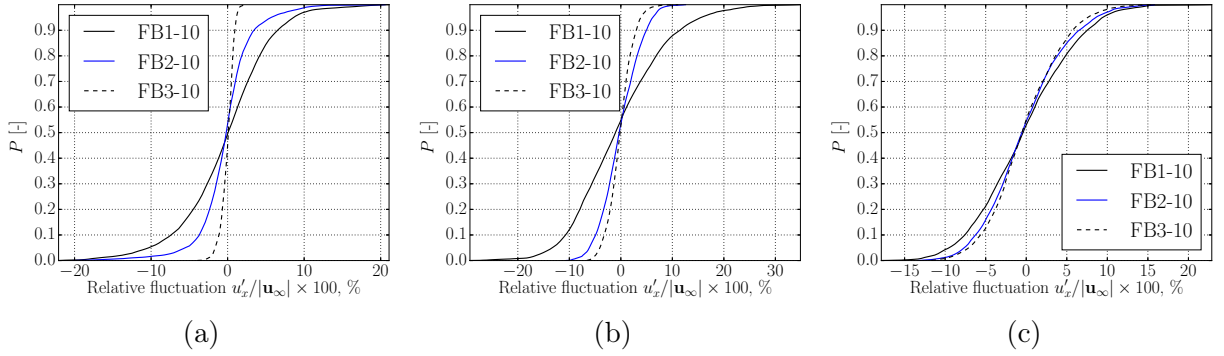


Figure 5.27: Comparison of empirical distribution functions of velocity fluctuations built at points (a) - P1U, (b) - P1R, (c) - P2L for different depths for $\beta = 10^\circ$

straight course (see Figure 5.28 and Figure 5.29b, d and f and compare to Figures 5.24 and 5.25). This can be explained as follows. When the fluid flows towards the ship at a drift angle ¹, it passes a much shorter distance under the ship, where the viscous forces act (see the streamlines in Figures 5.30b, d and f). Therefore, the fluid loses less energy than at straight course and enters the propeller disks at higher velocities than previously.

Even though the wake itself is low, its non-uniformity of the for $h/T = 1.25$ is much higher than that previously observed for the straight course. Obviously, the skeg vortex is responsible for this. When the depth decreases, this vortex grows much faster, than for the straight course. Its axis also shifts to the left and almost enters the first propeller disk at $h/T=1.25$. One can expect, that with the further depth reduction or increase of the drift angle this vortex will grow and shift farther to the left. This could potentially contribute to thrust fluctuation on account of both the non-uniformity and instationarity of the velocity field.

Influence of the fairway depth on the flow instationarity Motion with the drift angle also affects the wake instationarity. One can notice the following qualitative differences.

Firstly, the direction of the boundary layer growth is changed, so that the thickness of the turbulent region is dependent on y coordinate (see Figure 5.29).

Secondly, under these conditions the skeg has a “protective” effect. It keeps the part of turbulent fluid coming from under the hull from flowing directly into the first propeller disk. Instead of this the part of the fluid is sucked into the skeg vortex. In order to better understand the flow picture see Figures 5.30b, d and f.

Due to these two effects there is a region in the propeller plane, where the resolved Reynolds stress $\langle u_x'^2 \rangle$ is almost zero (and σ_u as well). The size of this undisturbed region strongly depends on h/T (see Fig. 5.29a, c and e). This situation is different from that documented for $\beta = 0^\circ$, where this region was present only at $h/T = 1.25$ and was situated on the left from the second

¹Inverse motion is considered

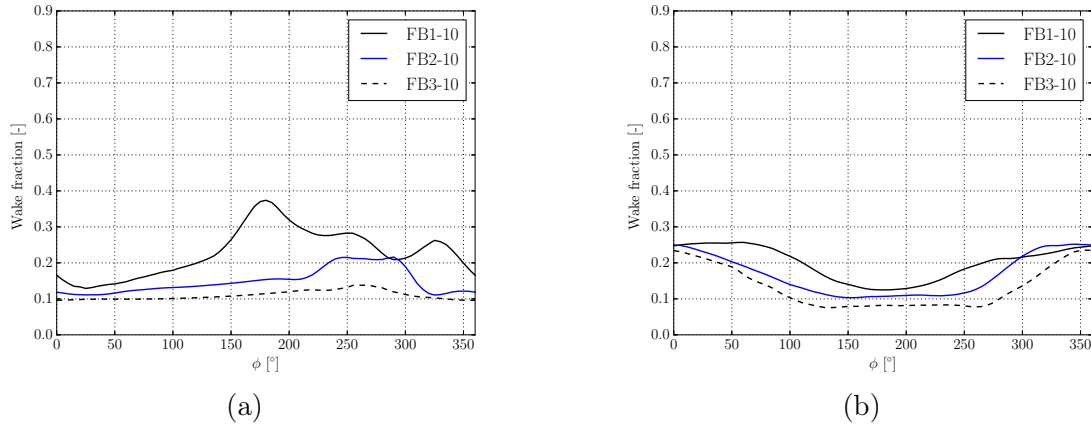


Figure 5.28: Nominal wake w in the propeller plane at $r/R=0.7$ for first (a) and second (b) propeller disks

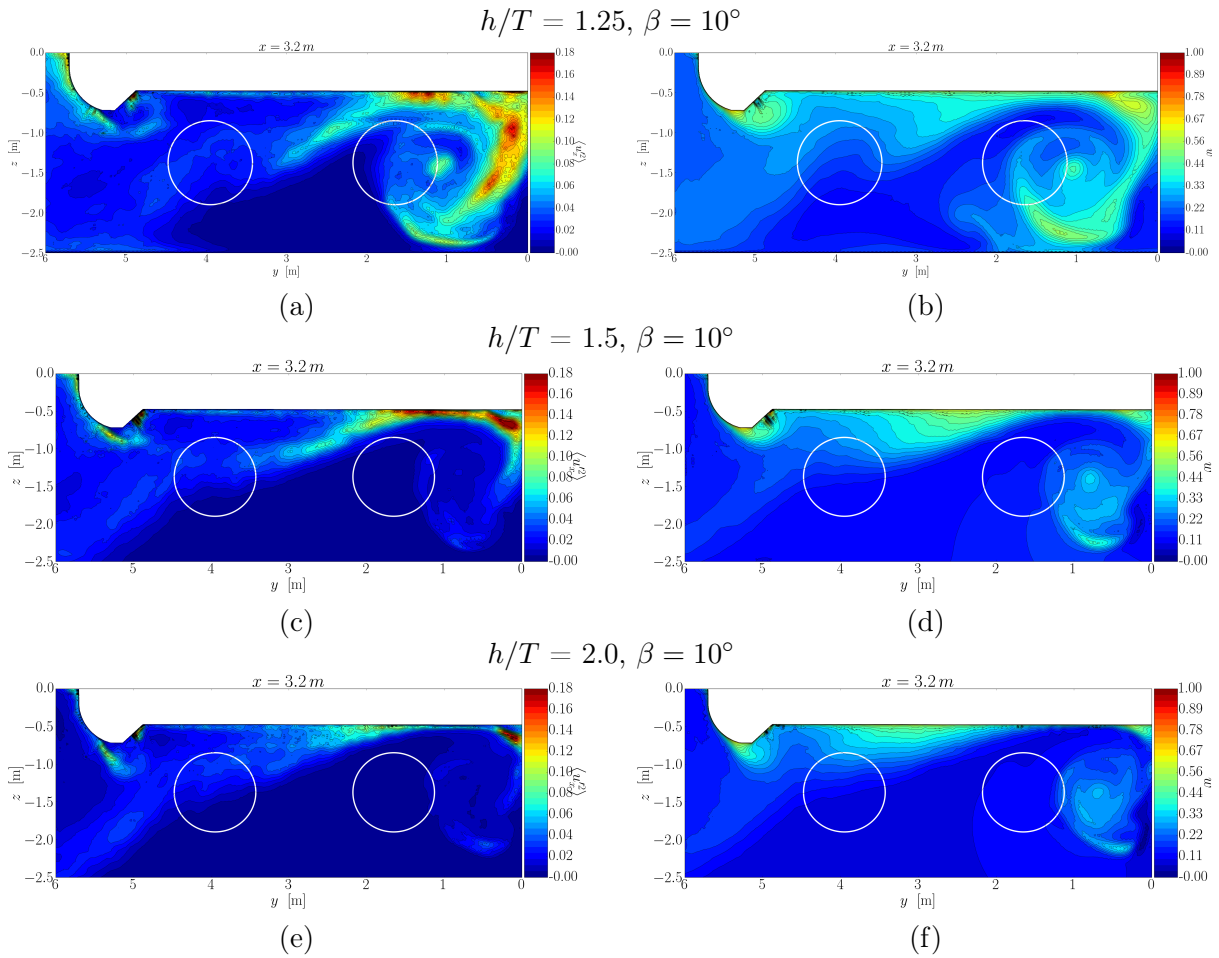


Figure 5.29: Plots of the resolved Reynolds stresses $\langle u_x'^2 \rangle$ (left) and wake (right). Figures correspond to the following cases: a, b - FB1-10; c, d - FB2-10; e, f - FB3-10

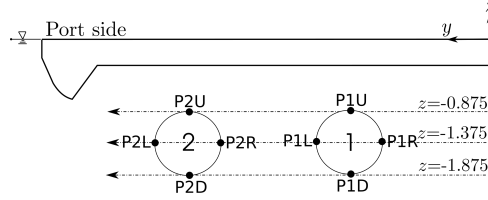
propeller.

In these circumstances the values of σ_u and the EDFs in some of the considered points show a much stronger sensitivity to h/T , that previously the straight course. This sensitivity is determined by whether or not the point is lying in the “undisturbed” region (which changes its form and size). Examples of such points are P1D, P1L and P2D. By $h/T \geq 1.5$ they are situated in that “calm” part of the wake and therefore σ_u in that points changes dramatically compared to $h/T = 1.25$ and becomes negligibly small.

Generally (except for point P2U) the values of σ_u in all points rapidly grow as the fairway depth decreases. This situation is distinct from that at straight course, where at lower $h/T = 1.25$ the flow instationarity was concentrated at the first propeller. The fastest growth of σ_u was documented for the points lying in the first propeller disk. For example at point P1R standard deviation at $h/T = 1.25$ is two times higher than that at $h/T = 1.5$ and reaches nine percent. Analyzing the EDF, one can see that at this point the velocity fluctuations can reach up to 25-27 percent of the inflow value (see Figure 5.27). From the EDF one can estimate, that the probability, that the absolute value of fluctuation will be higher than ten percent reaches 0.2 for P1R and 0.1 at P1U. Obviously, the reason for this is the presence of the large skeg vortex in that region. Rapidly increasing in size when fairway depth decreases it becomes a source of instationarity of the velocity field.

Table 5.9: Relative standard deviation of velocity σ_u in eight points in the propeller plane. For the point designations see Figure 5.17. The sketch of the probe points is added for the ease of understanding

	$\sigma_{u,P1R}$	$\sigma_{u,P1U}$	$\sigma_{u,P1L}$	$\sigma_{u,P1D}$	$\sigma_{u,P2R}$	$\sigma_{u,P2U}$	$\sigma_{u,P2L}$	$\sigma_{u,P2D}$
FB1-10	0.089	0.058	0.028	0.072	0.053	0.053	0.058	0.034
FB2-10	0.037	0.036	0.008	0.004	0.045	0.053	0.048	0.018
FB3-10	0.024	0.008	0.003	0.001	0.025	0.059	0.044	0.011



5.8.4 Concluding remarks for Chapter 5

In this chapter three series of computations of the nominal wake of a generic hull form of a river cruiser were presented: preliminary, related to grid convergence study and final.

The preliminary computations were aimed at gaining the initial insight into the flow picture in the stern of a river cruiser in shallow water. It was shown, that under these conditions the instationarity of the velocity field

- generally depends upon the size of the gap between the hull and the fairway bottom (influence of squat is determined by the change of under keel clearance in the stern)
- increases with the decreasing depth
- is nonuniform in the propeller plane, being stronger in the propeller disk near the skeg
- *depends on the wave pattern at critical regimes and is dramatically reduced under these conditions*

In order to assess the quality of the results in the preliminary study the grid convergence study was performed, in which the LH model, employed in preliminary study, was compared to SSTIDDES and RANS on a number of computational grids. The results of the study allowed to draw a conclusion, that LH model tends to overpredict the Reynolds stresses and the wake, when used with wall functions. At the same time, when the integration to the viscous sublayer was used, the LH model showed results much closer to other models. Because of LH's sensitivity to the mesh design it was decided to use SSTIDDES model for the final series of computations. Regardless of the flaws of LH model, which were revealed in the grid convergence study, it is assumed, that the model still captured the trends properly (dependence of wake instationarity on the depth and the wave pattern). Partly, this can be proven by the fact that similar trends were observed in final computations (even though different regime was analyzed).

The observed variations of the solution for the mean velocity field and total TKE between

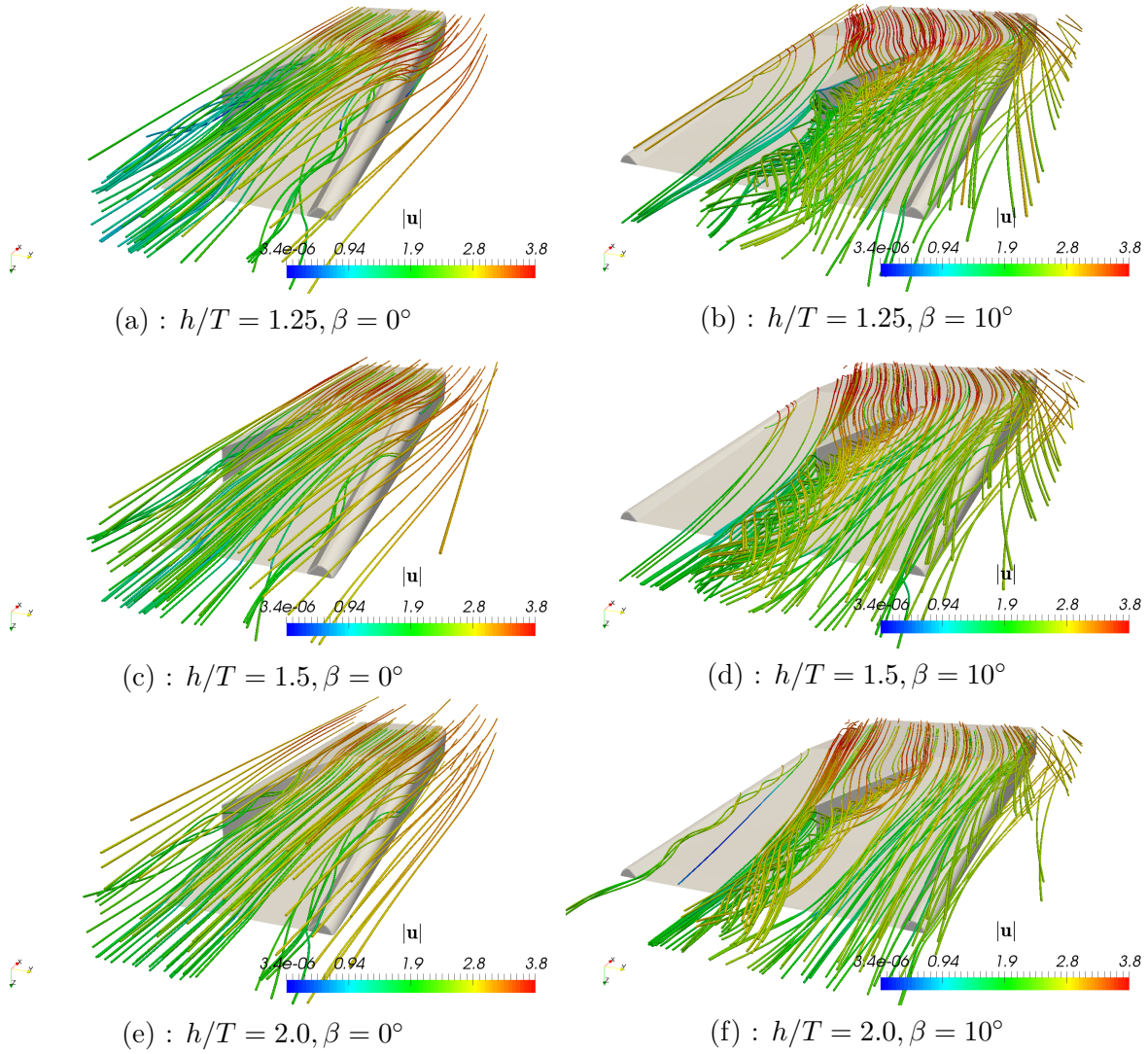


Figure 5.30: Streamlines built from the averaged velocity fields for the case with $\beta = 0^\circ$ (left) and with $\beta = 10^\circ$ (right). Figures a, c, e correspond to FB1-0, FB2-0, FB3-0, b, d, f - to FB1-10, FB2-10, FB3-10

the different meshes were quite small for SSTIDDES model. The decrease of the cell size by half in each direction as well as the switch from wall functions to integration to the wall did not cause any qualitative change in the solution and yielded only moderate quantitative change near the skeg. These facts in conjunction with previously performed validation studies and analysis of the ratio of resolved to total TKE indicate, that the predictions obtained in the final series of computations have the lowest uncertainty compared to other models and presumably correctly reflect the real flow picture. In order to draw stronger conclusions about the predictive capability of the used method further validation data is required.

The final series of computations was conducted for the ship motion in a range of depth Froude numbers at straight course and with the drift angle $\beta = 10^\circ$. The SSTIDDES model with the turbulence generator was used for flow simulation. From the obtained flow predictions the following general conclusions can be made:

1. When the ship moves at straight course the wake in the first propeller grows and becomes less uniform at lower depths, whereas in the second propeller the wake is insensitive to depth variation. Motion with the drift angle decreases the wake in both propeller disks, but increases its irregularity.
2. The distribution of σ_u is nonuniform in the propeller plane. At straight course its non-

uniformity increases for smaller depths. For example at $h/T = 1.25$ the most instationarity is concentrated in the near of the first propeller. The second propeller under these conditions is located in a “calm” region with much lower level of velocity fluctuations. At a drift angle, because of the presence of the skeg there is analogous undisturbed region in the center of the propeller plane. This region, however, decreases in size when depth is reduced.

3. For motion at $\beta = 10^\circ$ the instationarity of the velocity field shows overall strong dependence on h/T ratio. Fluctuations in almost all of the considered points increase. The most rapid growth was documented for the first propeller disk, where in some points σ_u at $h/T = 1.25$ increased by hundred or more percent compared to $h/T = 1.5$. Velocity fluctuation up to 25% were observed in the first propeller disk under these conditions.

One has to keep in mind, that even though being valuable, the described above flow picture is not completely realistic because of the absence of propeller suction forces, which can have considerable influence the flow. Moreover, it does not allow for estimating neither the fluctuations of forces and moments, arising on the propellers, nor the pressure pulses on the hull shell plating. The prediction of forces and moments on the propellers are the topic of the next chapter.

This page intentionally left blank

Chapter 6

Prediction of thrust oscillations on rotating propellers

In this chapter the results of hybrid RANS/LES computations of the flow around a generic hull form with working propellers are presented. The emphasis is placed on the analysis of the trust fluctuations, arising due to the wake nonuniformity and instationarity under shallow water conditions. This is an essential step for evaluation of possible sources of stern vibration. The pressure pulses, which can also contribute to the rise of stern vibration, observed on inland cruisers, will be analyzed as well.

6.1 Geometry and conditions

The conditions, considered in this series of computational cases correspond to final computations of the nominal wake in Chapter 5. The list of the conditions with the label for each case is presented in Table 6.1.

Table 6.1: List of considered conditions for the computations with rotating propellers

Parameter \ Case label	FP1-0	FP2-0	FP3-0	FP1-10	FP2-10	FP3-10
U [m/s]	3	3	3	3	3	3
h/T [-]	1.25	1.5	2	1.25	1.5	2
β [°]	0	0	0	10	10	10
Fn [-]	0.08	0.08	0.08	0.08	0.08	0.08
Re [-]	4.05E+08	<-	<-	<-	<-	<-
Fn_h [-]	0.61	0.55	0.48	0.61	0.55	0.48

The geometry and dimensions of the computational domain were left identical to the previously used ones. The only change was the incorporation of azimuth thrusters on the port size in the computational domain. Influence of the thrusters on the starboard side on the flow was modeled by actuator disks with prescribed thrust (see [52]). According to the data provided by

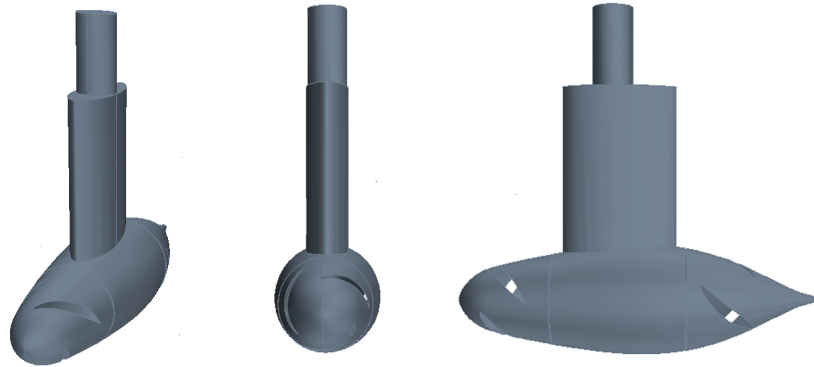


Figure 6.1: Geometry of the pods and shafting of the azimuth thrusters, designed by the author (propeller blades are not shown)

the shipyard, on each side of the river cruiser two rudderpropellers Schottel STP200 are installed. The exact geometry of the shafts and propellers was unfortunately not available. Therefore these

geometries were replicated with a considerable simplification (see Fig. 6.1). The geometry of propeller blades was also designed by the author (see Fig. 6.2). Radius of the front and rear propellers was equal to $R = 0.525$ m. Both propellers had the same sense of rotation - right and number of blades $Z = 3$. Maximum number of revolutions per second $n = 10s^{-1}$ was considered.

The resulting thrust produced by the propellers was estimated from the technical data for STP200 available in open access.

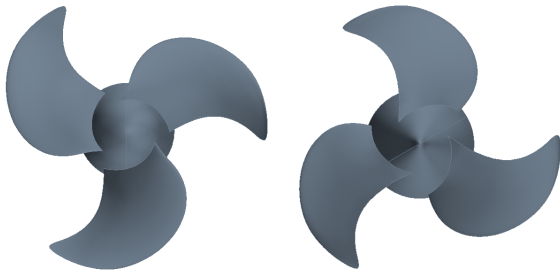


Figure 6.2: Geometry of the front (left) and rear (right) propellers, installed on the thrusters

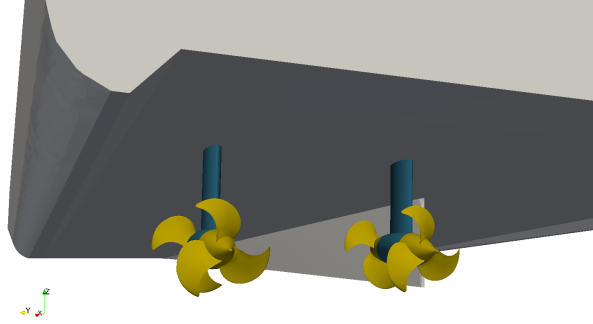


Figure 6.3: Generic hull form with thrusters on the port side

In simulations both with and without the drift angle the thrusters rotation axes were directed parallel to the middle line plane.

6.2 Numerical setup

Simulations were conducted using `pimpleDyMfoam` solver from OpenFOAM toolkit. This solver uses the PIMPLE method and allows for the motion of domain boundaries. Because of the SIMPLE-like subiterations on each time step the solver is able to cope with relatively high Courant numbers. The maximum Co attained by the author was 20, which was used in all simulations. For practical CFD computations of rotating propellers the time step is usually chosen such, that the propeller rotates by $\Delta\phi = 1 - 2^\circ$ per iteration (see, for example, [55]). In the current study $\Delta\phi$ was case-dependent and varied in the range 0.6-0.72. One has to mention, that even though on the propeller blade Co was approximately 20 (because of the high velocity and small cell size), in the remainder of the computational domain its value was smaller than 0.8 and therefore predictive capability of the hybrid turbulence model was not affected.

Propeller motion was resolved using rotating meshes. For each of the four propellers a cylindrical submesh was generated, which was added to the computational domain and merged with the supermesh. These submeshes, containing the propeller blades and a part of a hub were rotated with prescribed constant angular velocity $\boldsymbol{\omega} = (2\pi \cdot 10, 0, 0)$ rad/s. The boundary conditions for the unknowns on the propeller blades were the same as those used for the ship patch, except for the velocity, for which the Dirichlet BC $\mathbf{u} = \boldsymbol{\omega} \times \mathbf{r}_p = (0, -\omega_x z_p, \omega_x y_p)$ was imposed. Here \mathbf{r}_p is a radius-vector of a point on the propeller in local coordinate system. For the interpolation of the solutions between the main mesh and the submeshes Arbitrary Mesh Interface (AMI) was used, which embodies the conservative interpolation technique, proposed in [33].

Number of computational cells in the main mesh was in the range of 10-11M, depending on the fairway depth, whereas the rotating propeller submeshes contained approximately 0.5M cells each.

The same discretization schemes were used for simulations with thrusters as those for nominal wake predictions.

As in preceding computations, the initial conditions for SSTIDDES simulation and the

statistics for the turbulence generator were produced using RANS $k - \omega$ SST model. The unsteady computation was conducted for 30 s in each case, the last 20 s were used for collection of statistical data.

6.3 Results and discussion

The emphasis of the analysis was placed on the evaluation of total (front + rear propeller) thrust fluctuations and the pressure pulses on the hull surface. The probe points for pressure were located in the vicinity of the wall in the propeller planes above the rotation axes. Totally four points were considered: one above each propeller. In the following these points will be referred to as P1F (1st pod, front propeller), P1R (1st pod, rear propeller), P2F, P2F.

Assessment of thrust oscillations was done by evaluation of relative standard deviation of total thrust σ_T

$$\sigma_T = \frac{1}{\langle T \rangle} \sqrt{\frac{1}{n-1} \sum_{i=0}^n (T_i - \langle T \rangle)^2} \quad (6.1)$$

and the corresponding empirical distribution functions. Other components of forces on the propellers were not studied, because these were at least two orders of magnitude smaller than the longitudinal component (thrust) and their contribution was considered negligible. For the pressure pulses the analysis was performed in absolute values and was restricted to EDFs.

6.4 Motion at straight course

6.4.1 Thrust fluctuations

The statistical analysis of the thrust fluctuations for the motion at straight course is shown in Table 6.2. From the presented values of σ_T one can recognize a clear trend: the thrust fluctuations on the first pod (near the skeg) are intensified when the depth-to-draft ratio decreased, whereas for the second pod a reverse trend is observed. These tendencies agree quite well with the flow picture, observed in the computations of the nominal wake. Similar dependence was revealed there for σ_u : it increased on the first propeller and decreased on the second for smaller depths. For the first propeller disk also the wake nonuniformity has become higher at small depths, whereas for the second propeller disk it was nearly constant.

Table 6.2: Statistics of the total thrust oscillations on the first and second pods for the motion at straight course

Case	FP1-0		FP2-0		FP3-0	
Pod	1	2	1	2	1	2
$\langle T \rangle$ [N]	44280.76	45330.17	44226.65	44326.25	43505.36	43567.73
T'_{max} [N]	2559.62	2296.49	2323.19	2302.05	2196.04	2855.77
$T'_{max} / \langle T \rangle \times 100$ [%]	5.78	5.07	5.25	5.19	5.05	6.55
$\sigma_T \times 100$ [%]	2.44	2.07	2.26	2.42	2.20	2.86

Therefore, keeping in mind the results for the nominal wake, one can conclude, that the intensification of thrust oscillations on the first thruster in response to depth reduction is due to increase of both the nonuniformity and instationarity of the wake. Whereas for the second thruster only the latter effect played a role.

The strongest fluctuations were observed for the second thruster for $h/T=2.0$ with $\sigma_T = 2.86\%$ and peaks up to 6.5%. On the first pod the maximum of $\sigma_T = 2.44\%$ corresponded to $h/T=1.25$ with peaks up to 5.8%.

Plots of the EDFs of thrust are presented in Figure 6.4 and reflect the same trend as

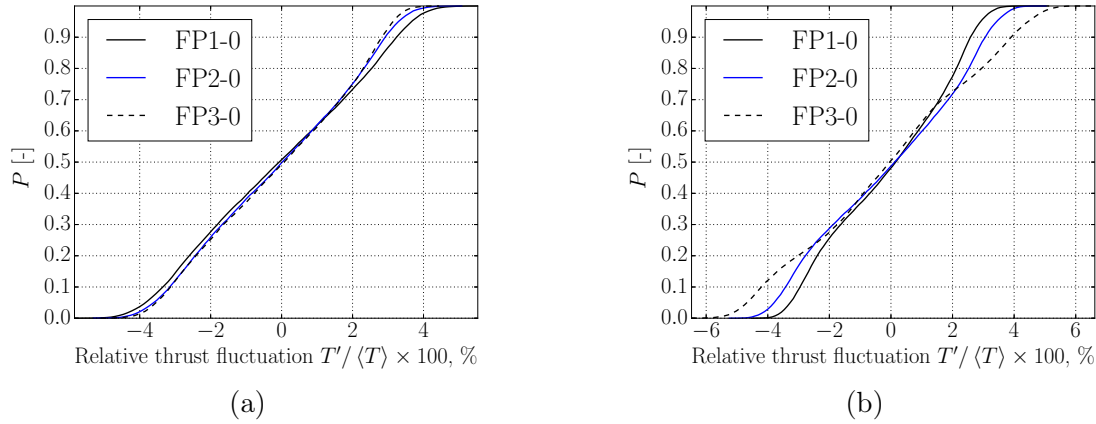


Figure 6.4: Comparison of empirical distribution functions of total (front + rear propeller) thrust fluctuations between different depths for $\beta = 0^\circ$: (a) - first thruster, (b) - second thruster

discussed above. Here one can see, that only the tails of the EDF are changed in response to depth variation, which means that the higher peaks become probable.

Analysis showed, that for all considered regimes the strongest thrust fluctuations corresponded to rear propellers. This can be explained by the fact that the rear propellers work in the slipstream of the front ones. Since the geometry of the pods and shafting was designed by the author and therefore is not flow-optimized, it might be, that for the real pods the fluctuations would be less intense.

The spectrum of the thrust fluctuations was analyzed separately for the rear and front propellers. Only the plots for the thruster near the skeg will be presented, since for the other one are qualitatively similar. In Figure 6.5 one can see, that for the front propeller the peaks of

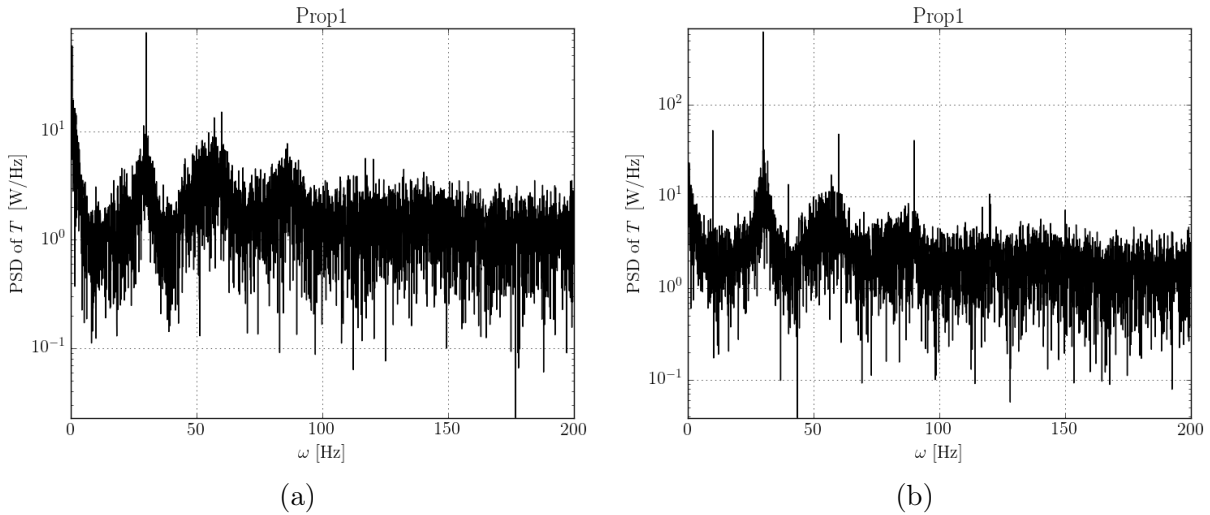


Figure 6.5: Power spectral density of the thrust fluctuations on the front (left) and rear (right) propellers of the thruster near the skeg at $h/T = 1.25$

the power spectral density correspond to the first and second blade-rate frequencies ($nZ, 2nZ$), but also contain a considerable low-frequency component ($\omega < 10\text{Hz}$). For the rear propeller the third, fourth and fifth ($3nZ, 4nZ, 5nZ$) can also be seen. Additionally, one can recognize two peaks of unknown origin at 10 and 40 Hz. For both propellers the spectrum is far from discrete. Similar results were obtained in [1].

6.4.2 Pressure pulses on the hull

According to the empirical distribution functions, built for pressure on the hull (see Figures 6.6,6.8) reduction of the fairway depth leads to increase of pressure pulses amplitude equally on

both pods. For example, at $h/T = 2.0$, all values of pressure peaks above the front propellers lie in the range from -4 to +2.5 kPa, whereas for $h/T = 1.25$ the range stretches from -7 to +7 kPa. Similar trend can be recognized for rear propellers. This equal rate of growth of the strength of pressure pulses indicates, that they are likely to be independent of both the instationarity and nonuniformity of the wake. At the same time the growth of amplitude is caused by the effect of the bottom proximity. Interesting result is that the negative fluctuations are more probable, than positive for the front propellers. For the rear propellers both signs are equally probable.

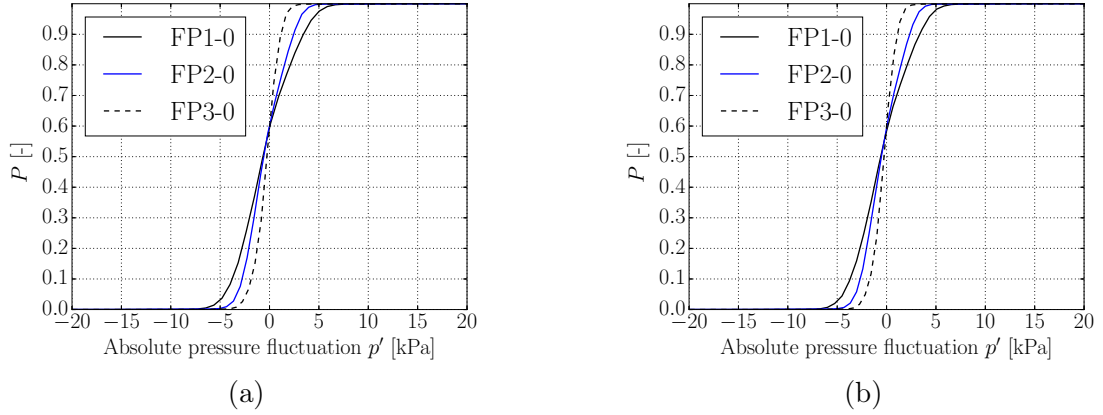


Figure 6.6: Comparison of empirical distribution functions of pressure pulses above front propellers between different depths for $\beta = 0^\circ$, (a) - first thruster, (b) - second thruster

6.4.3 Rough estimation of cavitation inception

In order to estimate the potential influence of cavitation on the vibration, a rough analysis of cavitation inception was conducted for the front propeller of near-skeg thruster. The vapor pressure p_v of water was taken 2000 kPa (which corresponds to 17°C). Zones on the propeller blade, where the total pressure was lower than the vapor pressure ($p < p_v$) were recognized for different h/T . The results are presented in Figure 6.7. Visually, the region, where cavitation may occur spreads in response to depth reduction. This may be explained by the fact, that the wake fraction is increasing with reduction of h/T (see Chapter 5) and as a result higher loads on propeller blades are created. These results confirm, that a more detailed assessment of cavitation

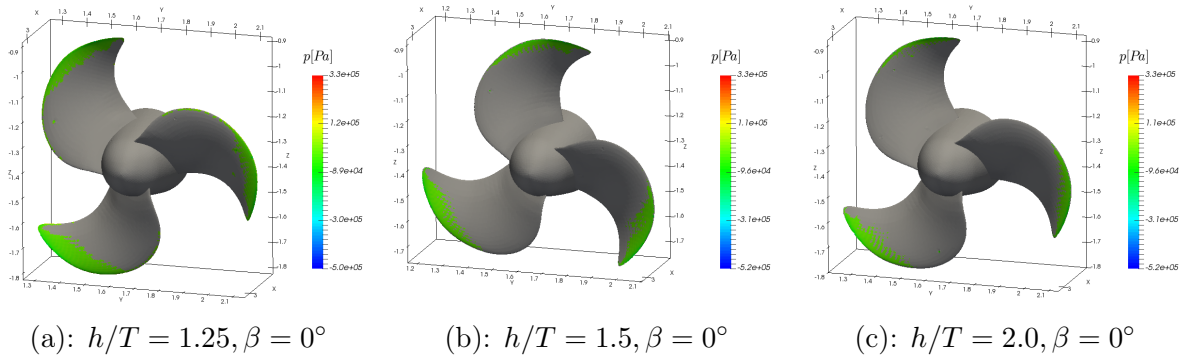


Figure 6.7: Comparison of the regions on the front propeller of the near-skeg thruster, where cavitation inception can occur

for the problem under consideration should be conducted in the future work.

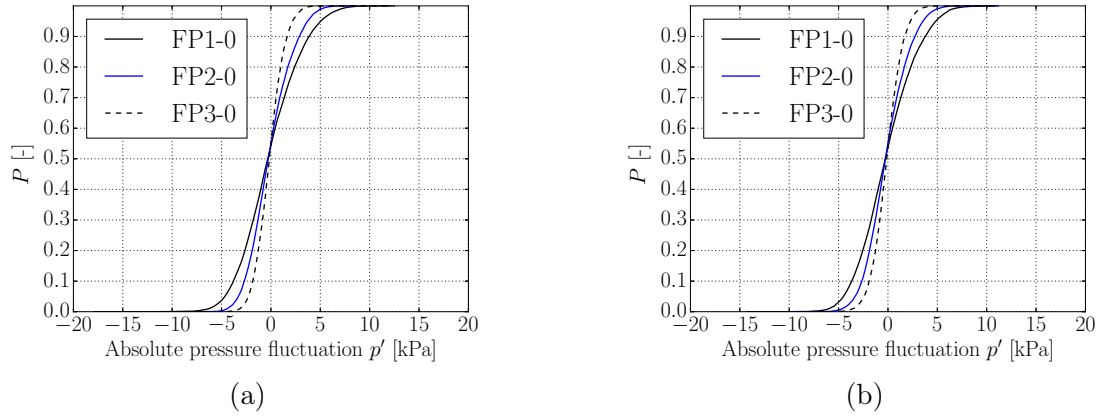


Figure 6.8: Comparison of empirical distribution functions of pressure pulses above rear propellers between different depths for $\beta = 0^\circ$, (a) - first thruster, (b) - second thruster

6.5 Motion with drift angle

6.5.1 Thrust fluctuations

Simulations of the nominal wake for ship motion at $\beta = 10^\circ$ showed, that at $h/T=1.25$ in the region near the skeg strong velocity fluctuations may occur, which are caused by the increase of the skeg vortex. At the same time in a number of points the fluctuation intensity was reduced compared to straight course because of the “protective” effect of the skeg.

Therefore it was expected, that computed thrust oscillations would noticeably increase at least for $h/T = 1.25$ for $\beta = 10^\circ$. However, the collected statistics indicate, that motion with a drift angle leads to considerable reduction of the standard deviation of thrust compared to straight course for the first thruster (see Figures 6.10 and 6.11). At the same time for the second thruster the fluctuation intensity only slightly changed, for $h/T = 1.25$ it did not change at all.

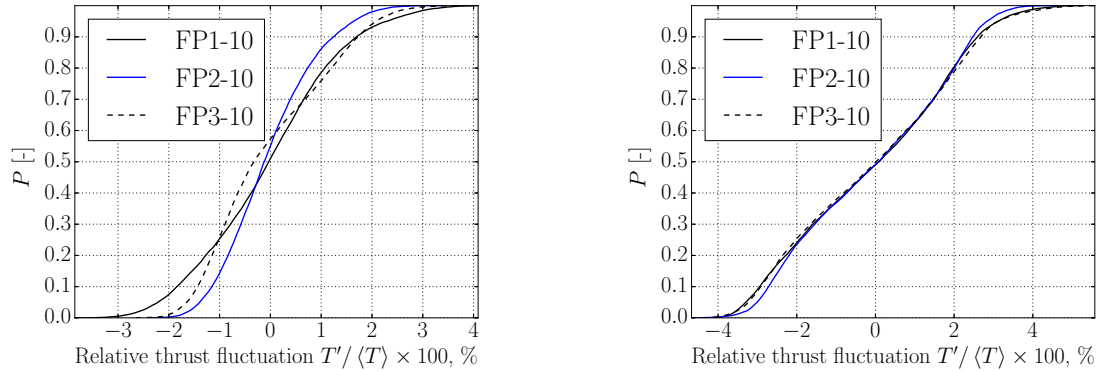


Figure 6.9: Comparison of empirical distribution functions of total (front + rear propeller) thrust fluctuations between different depths for $\beta = 10^\circ$: left - first thruster, right - second thruster

Table 6.3: Statistics of the total thrust oscillations on the first and second thruster for $\beta = 10^\circ$

Case	FP1-10		FP2-10		FP3-10	
Pod	1	2	1	2	1	2
$\langle T \rangle$ [N]	41669.85	42185.60	41180.08	41410.14	41244.05	41071.87
T'_{max} [N]	1687.33	2172.71	1372.51	1916.44	1561.29	2269.81
$T'_{max} / \langle T \rangle \times 100$ [%]	4.05	5.15	3.33	4.63	3.79	5.53
$\sigma_T \times 100$ [%]	1.34	2.08	0.90	1.96	1.20	2.12

The reason for the drop of the fluctuation intensity on the first thruster for h/T could be found out after the analysis of vortical structures in the wake (see Figure 6.19). One can notice,

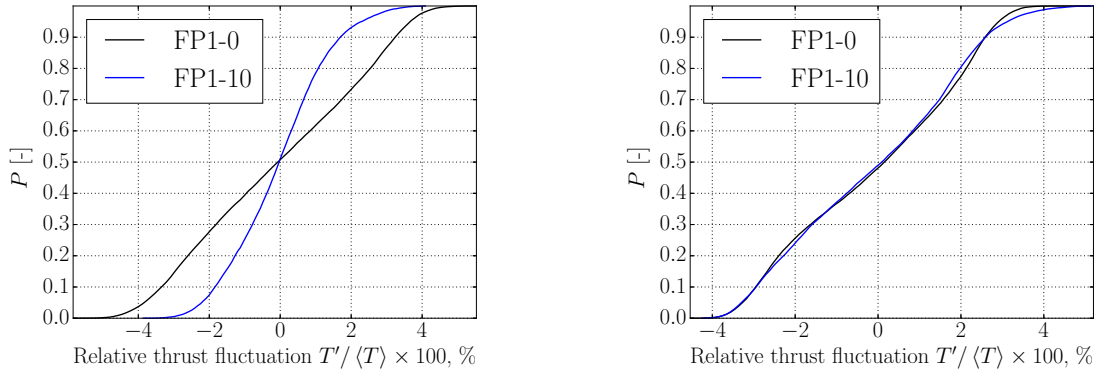


Figure 6.10: Comparison of empirical distribution functions of total (front + rear propeller) thrust fluctuations between $\beta = 0^\circ$ and $\beta = 10^\circ$ for $h/T=1.25$: left - first thruster, right - second thruster

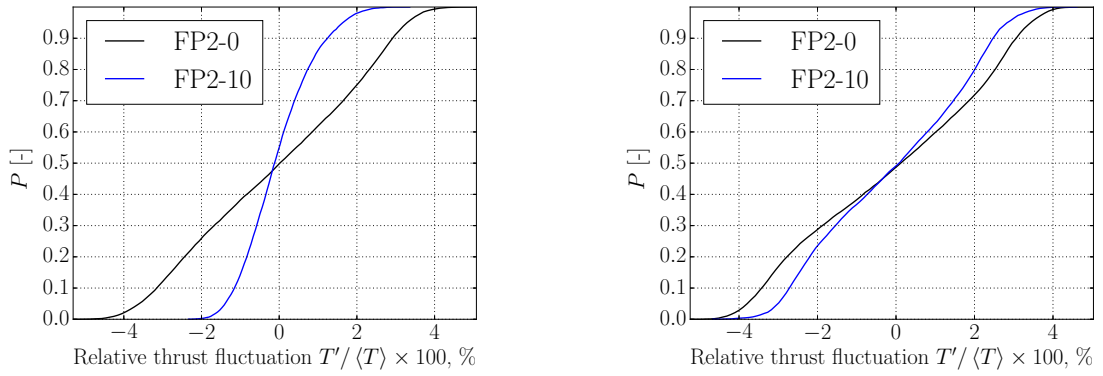


Figure 6.11: Comparison of empirical distribution functions of total (front + rear propeller) thrust fluctuations between $\beta = 0^\circ$ and $\beta = 10^\circ$ for $h/T=1.5$: left - first thruster, right - second thruster

that the skeg vortex, which was observed in the computations of the nominal wake is shifted towards the middle-line plane. This appears to be a result of the action the propeller suction force, which increased the longitudinal component of the velocity and by these means pushed the vortex aside from the propeller. As a consequence no unsteady structures enter the propeller plane. Comparison of the resolved Reynolds stresses $\langle u_x'^2 \rangle$ between cases FB1-10 and FP1-10

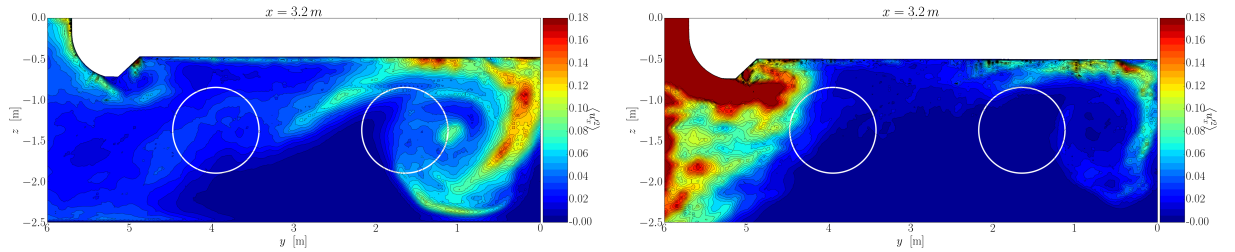


Figure 6.12: Resolved Reynolds stress $\langle u_x'^2 \rangle$ in the plane of the front propellers for $\beta = 10^\circ$; left - without propellers, right - with propellers

allows to conclude, that propeller suction force led to noticeable reduction of flow instationarity (see Figure 6.12). However, in this case the flow picture would be different if the thruster would be rotated parallel to the inflow velocity vector. Under these conditions the propeller might interact with the vortex, which can potentially influence the thrust oscillation. This scenario needs to be studied further.

Values of σ_T and thrust EDFs did not point to any clear dependency between the fairway depth and flow instationarity for motion with drift angle (see Table 6.3).

6.5.2 Pressure pulses on the hull

Pressure oscillations did not show a strong dependence on the fairway depth. Only the small changes in the EDFs could be observed (see Figures 6.13, 6.14). which point to the following trend. Decrease of depth diminishes the probability of negative fluctuations, but at the same time makes the negative peaks (< -5 kPa) more probable. As a result, the high peaks occur more often. For example at $h/T = 2.0$ the probability of peaks $|p'| > 5$ kPa is approximately 5%, whereas for $h/T = 1.25$ it increases up to 8%. This trend is observed in all considered points.

During the motion with the drift angle the amplitudes of pressure fluctuations on the hull were generally higher than those predicted at the same depths at straight course (see Figures 6.15, 6.16, 6.18). For all considered depths the recorded pressure values lay in the range approximately $[-8; 8]$ kPa.

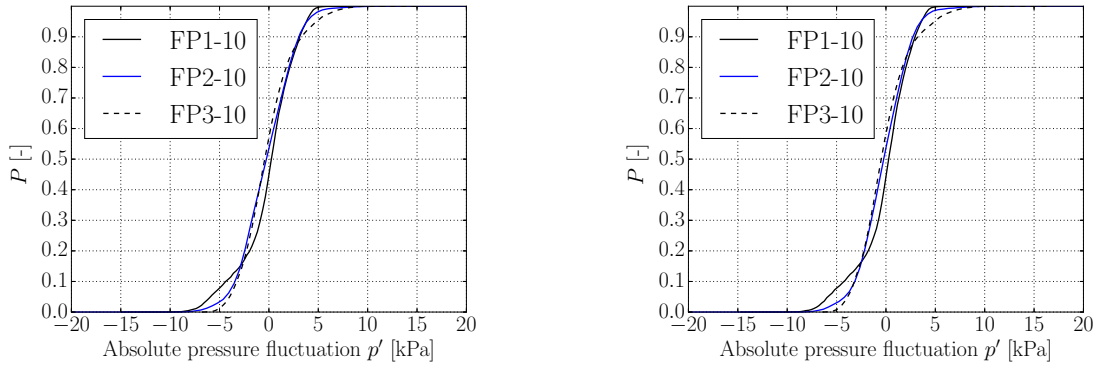


Figure 6.13: Comparison of empirical distribution functions of pressure pulses above front propellers between different depths for $\beta = 10^\circ$: left - first thruster, right - second thruster

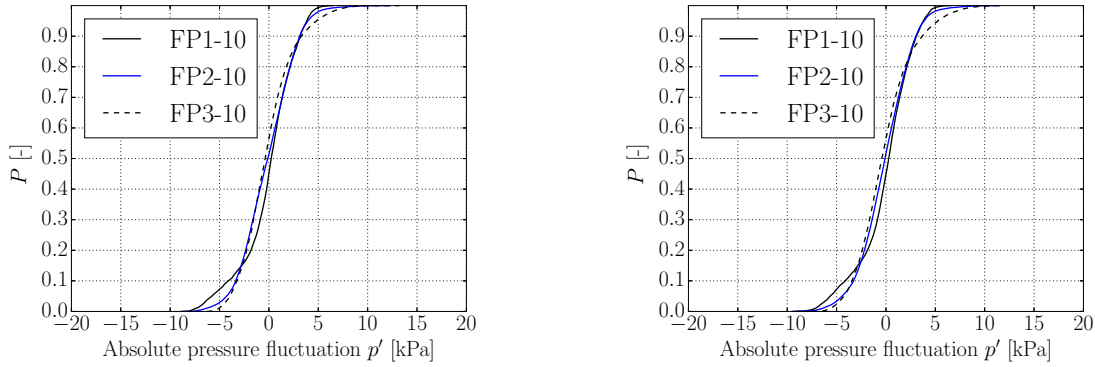


Figure 6.14: Comparison of empirical distribution functions of pressure pulses above rear propellers between different depths for $\beta = 10^\circ$: left - first thruster, right - second thruster

6.5.3 Rough estimation of cavitation inception

Compared to the case without the drift angle the results for $\beta = 10^\circ$ are considerably different. The dependence of the sizes of the cavitation inception regions on h/T ratio is still present, but additionally a very important qualitative change was observed. In Figure 6.7 the zones with $p < p_v$ were almost equally large on all blades, indicating that the periodic collapsing was unlikely to occur. For $\beta = 10^\circ$ the size of the regions changes between the blades. On some of them (in upper position) the zone with $p < p_v$ almost vanishes, whereas on the blades in lower position the regions of low pressure can occupy a half of the blade. This indicates, that the same effect, as described by Reed and Basset [119] may occur, namely, the sheet cavitation with periodic collapsing. Potentially, this effect may also contribute to vibration intensification. However, these results do not agree with the predictions, obtained previously for the wake fraction

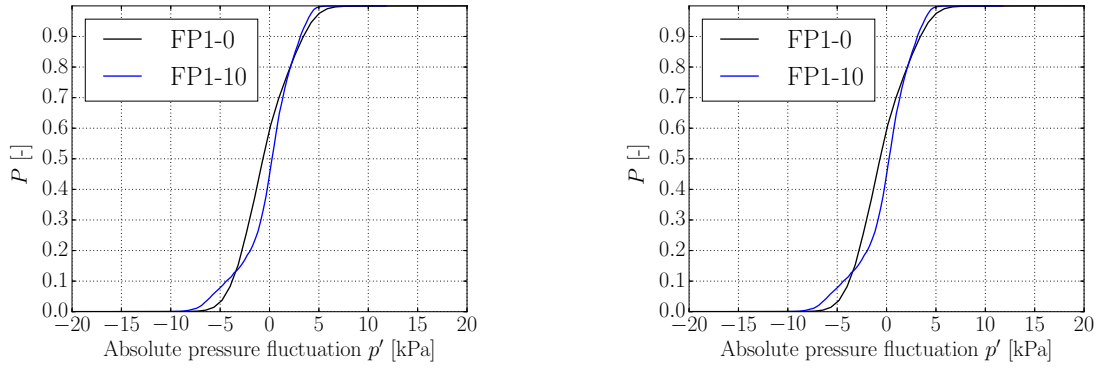


Figure 6.15: Comparison of empirical distribution functions of pressure pulses above front propellers between $\beta = 0^\circ$ and $\beta = 10^\circ$: left - first thruster, right - second thruster. $h/T=1.25$

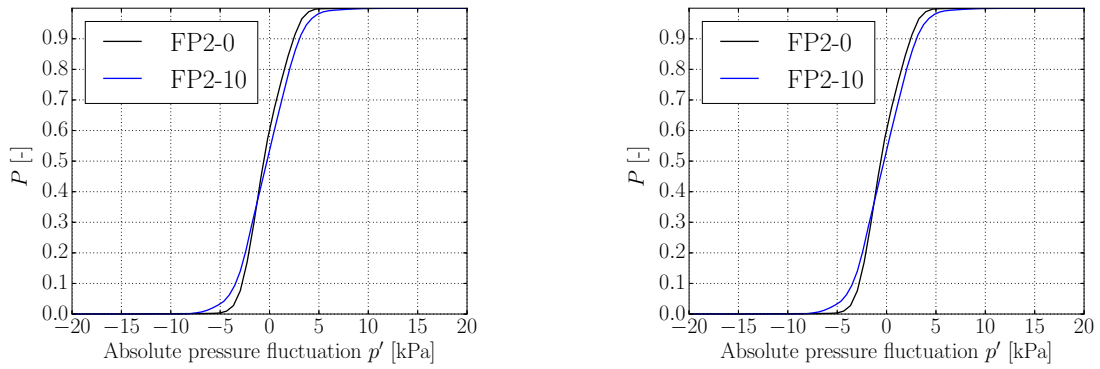


Figure 6.16: Comparison of empirical distribution functions of pressure pulses above front propellers between $\beta = 0^\circ$ and $\beta = 10^\circ$: left - first thruster, right - second thruster. $h/T=1.5$

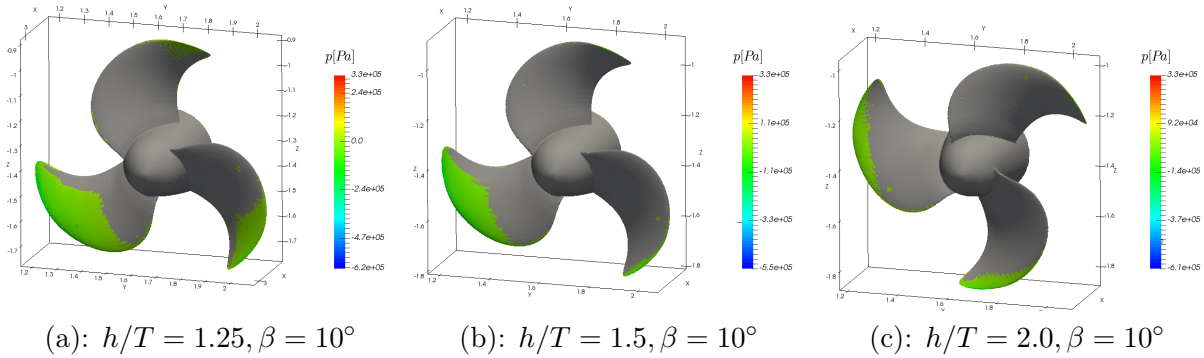


Figure 6.17: Comparison of the regions on the front propeller of the near-skeg thruster, where cavitation inception can occur

(see Chapter 5) and thrust oscillations. The wake fraction at $\beta = 10^\circ$ is reduced compared to straight course and the thrust oscillations are less intense too, pointing to the lower wake nonuniformity. Whereas the cavitation analysis indicated the increase of wake non-uniformity. The reason for this contradiction is not quite clear and should be studied further.

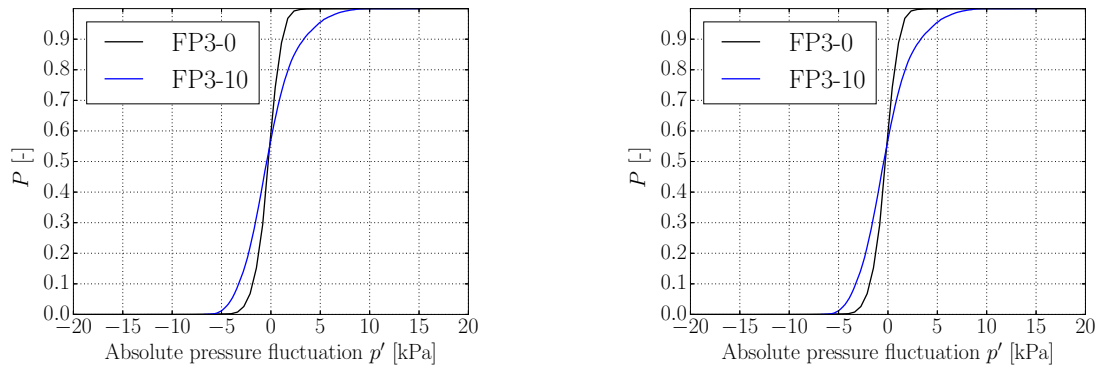
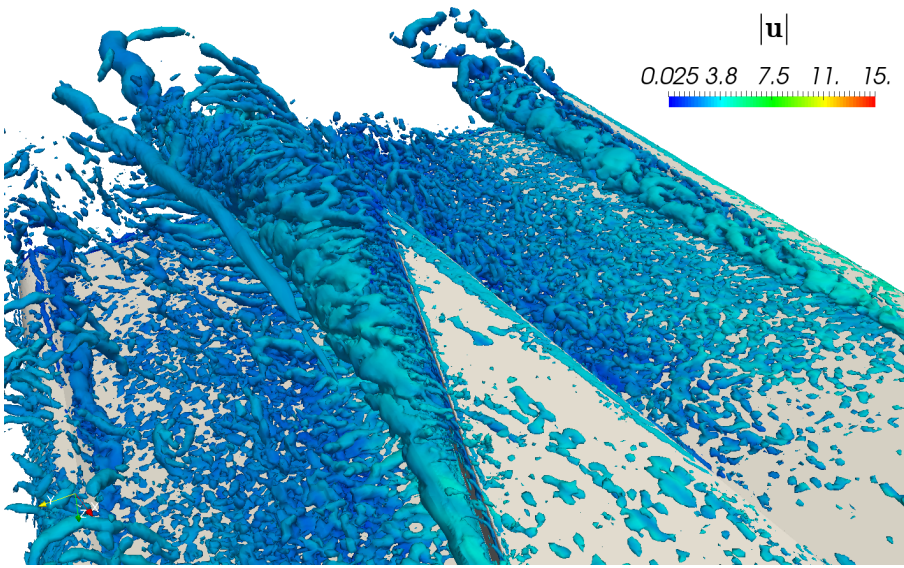
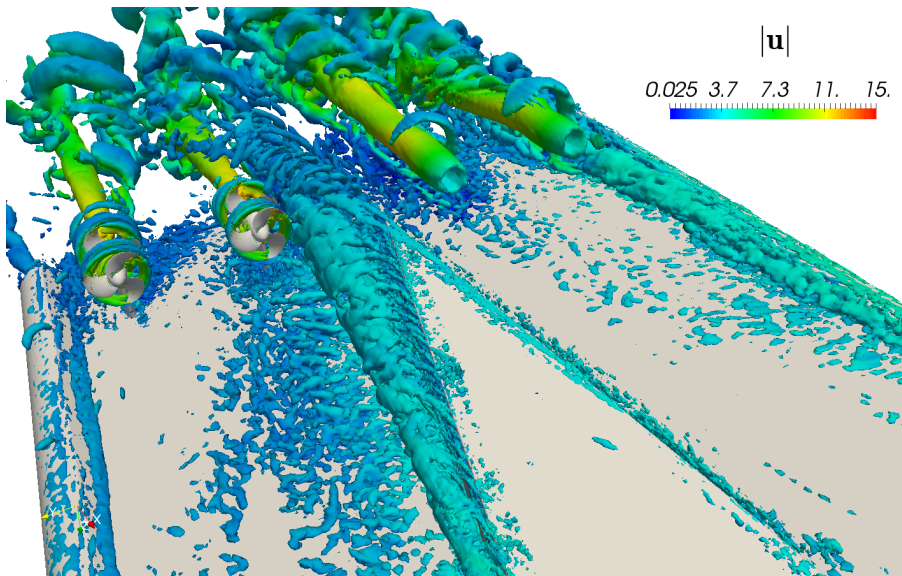


Figure 6.18: Comparison of empirical distribution functions of pressure pulses above front propellers between $\beta = 0^\circ$ and $\beta = 10^\circ$: left - first thruster, right - second thruster. $h/T=2.0$



(a)



(b)

Figure 6.19: Vortical structures in the wake of a river cruise ship during the motion with $\beta = 10^\circ$: (a) - without thrusters (b) - with thrusters, $h/T = 1.25$. Isosurfaces $\lambda_2 = -10$ [60]

Chapter 7

Conclusions and outlook

The aim of the presented study was the assessment of the influence of depth restriction on hydrodynamic sources of stern vibration, which arises on inland cruise vessels during the motion in shallow waterways. Solution of this task required application of novel turbulence modeling methods and therefore development and validation of corresponding models were also performed.

Main results of the research were presented in Chapters 4, 5, 6 and consist in:

1. Implementation of SSTIDDES model in conjunction with the volume source of turbulent fluctuations. Validation of implemented code for canonical flows.
2. Comparison of two hybrid RANS/LES approaches - SSTIDDES and LH for the prediction of the wake of a model of an inland ship.
3. Development of a shielded version of LH model, which considerably improved the accuracy of wake fraction predictions compared to the original version and made the predictions of the standard deviation of the longitudinal velocity closer to that of SSTIDDES.
4. Development of efficient quasi-steady state solver for squat prediction with a new mesh deformation algorithm specially adapted for shallow water. Validation for a squat prediction in shallow water.
5. Analysis of the nominal wake of a river cruiser using LeMoS hybrid model and assessment of influence of different parameters (depth Froude number, fairway depth) on the velocity fluctuations in propeller disks.
6. Assessment of the quality of the results by means of grid convergence study, comparison between different models and analysis of the resolved turbulence kinetic energy.
7. Determination of the dependence of wake fraction and velocity fluctuations in the nominal wake on the fairway depth and drift angle.
8. Calculation and analysis of thrust fluctuations and pressure pulses for the ship with rotating propellers. Investigation of the dependence of thrust oscillation on the depth-by-draft ratio and drift angle. Rough estimation of cavitation inception.

A summary of the main findings, stemming from the conducted research activities will be given below.

Validation of computational methods

Hybrid RANS/LES turbulence models

One of the main computational tools, used for the research were the hybrid RANS/LES turbulence models. Two models were utilized in the presented work: LeMoS hybrid model (LH), proposed by Kornev et al. [70] and a re-calibrated version of SSTIDDES model, proposed by Gritskevich et al. [48]. The former model was extensively tested for canonical flows and ship flows under deep water conditions in previous studies [3, 2] and therefore in this study it was tested only for shallow water conditions. The SSTIDDES model with a turbulence generator was implemented in OpenFOAM CFD toolkit by the author and therefore had to be validated. It

was tested for canonical flows (channel, diffuser) and showed good agreement with experimental data and the results of original implementation.

After that the performance of LH and SSTIDDES models was compared for the task of the prediction of the wake of an inland ship in shallow water at model scale. The SSTIDDES model showed good agreement with experimental data and results of RANS computations for the wake fraction. At the same time accuracy of LH model was considerably worse - it predicted the wake fraction significantly higher, than that experimentally observed. The resolved Reynolds stresses, computed using LH model were also much larger compared to SSTIDDES solution. This poor performance was attributed to the modeled stress depletion (see Section 2.3.3). MSD was partly due to the absence of shielding and partly due to the impossibility of application of turbulence generator which led to a lack of resolved turbulence. In order to improve the model robustness a shielded version of LH model (SLH) was developed and tested for the same case. The new version of the model turned out to be superior to the old one and in some regions of the flow even to the SSTIDDES. This performance was attained without the application of turbulence generator.

Quasi-steady state squat prediction

In order to be able to predict the dynamic trim and sinkage of a river cruiser a new version of OpenFOAM quasi-steady state VOF solver `LTSInterFoam` was developed. The new version - `LTSInterDyMFoam` allowed for resolution of the ship motion inside the computational domain. For mesh deformation a simple and efficient method developed by the author was employed. The solver was validated for the task of squat prediction for a model of a container ship moving in a shallow channel. Comparison of computational results with experimental data has shown very good agreement. This solver was later used for prediction of squat of the river cruiser in the preliminary study of nominal wake.

Analysis of the nominal wake under shallow water conditions

The fluctuations of forces and moments arising on the propellers and potentially leading to the vibration are dependent on the nonuniformity and instationarity of the wake. Therefore, a considerable part of the work was devoted to the analysis of the nominal wake of a generic hull form of a river cruise vessel. The conducted computations were aimed at understanding of the influence of different parameters, such as the depth-by-draft ratio, drift angle and depth Froude number on the wake fraction and velocity fluctuations. Three series of simulations were conducted: preliminary simulations, grid convergence study and final simulations.

Results of preliminary study

In the preliminary study LeMoS hybrid model was used to get a qualitative insight into the flow picture in the stern of a river cruiser navigating under shallow water conditions. Different motion regimes were studied in a doubled body (single-phase) and free-surface (two-phase) formulations. It was shown, that the velocity fluctuations in the disc of the first propeller (near the skeg) are generally much more intense at small depths than on the second one. Reduction of h/T led to increase of standard deviation of velocity field in the disk of the first propeller. This is attributed to the increase of adverse pressure gradient along the hull surface at the stern.

For the depth Froude numbers less than 0.85 no influence of the free surface on the wake instationarity was observed. However, at critical regimes ($Fn_h \approx 1$) the instationarity of the velocity field at the stern can be suppressed on account of free surface deformation, which changes of flow geometry and decreases the adverse pressure gradient. To author's knowledge this phenomenon, being an example of the influence of the wave wake on the viscous wake, has not been discussed in literature so far.

Squat influence on the wake unsteadiness was assessed as well. It was shown, that the determining criterion for this influence is the change of the gap size between the ship hull and the fairway bottom at the stern. In cases where the gap size decreased the instationarity of the velocity field spread to the bilge. At the same time, when the gap size remained approximately the same, no considerable change in statistics of velocity field was documented.

Even though in later computations it was shown, that the results of LH model don't agree well with solutions produced by another models, it is believed, that the observed trends were captured correctly, at least qualitatively.

Grid convergence study

Assessment of grid convergence and comparison of different methods was the only way to check the reliability of the model predictions at full scale. Based on the analysis of distributed parameters one could draw following conclusions. Grid convergence study revealed the sensitivity of LH model to the mesh resolution. It predicted stronger velocity fluctuations and higher wake fraction than that observed in SSTIDDES solutions. Very large variations of the considered parameters between the different mesh densities were documented for LH model. At the same time, SSTIDDES model showed much stabler behavior: the solutions did not change noticeably after the reduction of the cell size by two times. Thus, the same trend was observed as that for M1926 validation case. This led the author to conclusion that the original version of LH is not robust and therefore for final series of computations only the SSTIDDES model was used. The analysis of resolved-to-total TKE for SSTIDDES model showed that more that 80% of the TKE was resolved and therefore the results may be considered reliable.

Results of final computations

The final series of computations, conducted after the grid convergence and validation studies allowed to draw the more detailed conclusions on the dependency of the wake fraction parameters on the depth-by-draft ratio and the drift angle.

The change of depth-by-draft ratio influences the wake fraction and the flow instationarity differently for the two propeller disks analyzed and depends on the local flow physics.

The decrease of depth leads to intensification of velocity fluctuations in the propeller disk near the skeg and at the same time to suppression of oscillations on the second propeller. This situation is due to the appearance of an "undisturbed" region of the flow at lower depths (see Section 5.8.2). The wake fraction in the disk of the first propeller increased for smaller depths and at the same time remained almost unchanged for propeller disk near the bilge.

Motion with the drift angle $\beta = 10^\circ$ at $h/T = 1.5, 2.0$ decreased the wake fraction and the standard deviation of longitudinal velocity in the wake because of the "protective" effect of the skeg. The previously mentioned undisturbed region in this case was again present, but was located in the space between the two propeller disks - standard deviation of velocity in the points lying there was almost zero. At $h/T = 1.25$ this region is dramatically reduced in size because of the growth of the skeg vortex. In this situation the vortex entered the disk of the first propeller and caused very intense (amplitude up to 25% of the inflow value) fluctuations of longitudinal velocity.

Summary

Summarizing the conducted analysis, one can state, that both the instationarity and nonuniformity of the velocity field in the propeller plane can significantly increase with the diminishing of the depth-by-draft ratio. At the same time no strong separations were revealed in the stern, and therefore the unsteadiness seems to stem only from the skeg and bilge vortices and the turbulent fluctuations in the wake. However, whether or not the separations are present is dependent on the geometry of the stern and therefore the flow picture may vary for a particular

ship. The determining factor in this case would be the adverse pressure gradient.

Thrust fluctuations and pressure pulses on the ship hull in shallow water

Motion at straight course

In order to analyze the thrust and pressure fluctuations, simulations of a ship flow with four rotating propellers using SSTIDDES model were conducted. The exact geometry of the rudderpropellers was not available and was therefore replicated using available technical data.

Simulations at straight course showed the trend in the total thrust and pressure fluctuations, which agreed quite well with the previously obtained results for the nominal wake. Namely, the standard deviation of thrust fluctuations increased on the first thruster and decreased on the second one with diminishing h/T ratio. The strongest fluctuations for the first pod were observed at $h/T = 1.25$ with $\sigma_T = 2.44$ % and peaks up to 5.8%, whereas for the second pod the strongest fluctuations corresponded to $h/T = 2.0$ with $\sigma_T = 2.86$ % and peaks of up to 6.5%.

At the same time the pressure fluctuations on the hull surface above all propellers were monotonically intensified in response to depth reduction and reached the amplitude up to 7 kPa at $h/T = 1.25$.

Motion at $\beta = 10^\circ$

Motion with the drift angle considerably reduced the standard deviation of the thrust on the first propeller. At the same time the fluctuations on the second propeller were only slightly changed. These changes were attributed to the previously mentioned “protective” effect of the skeg in conjunction with the propeller suction forces. The latter factor led to reduction of resolved Reynolds stress in the propeller plane compared to bare hull computations. At $h/T = 1.25$, where the strongest velocity fluctuations were previously observed, the thrust fluctuations were not intensified. The reason for this is the influence of propeller suction force on the skeg vortex.

The amplitudes of pressure pulses at $\beta = 10^\circ$ were increased compared to the corresponding cases with $\beta = 0^\circ$ and reached up to 8 kPa.

Analysis of cavitation inception regions

A rough estimation of cavitation inception showed, that the cavitation may indeed occur under certain conditions. Zones with $p < p_v$ increased in size when depth was reduced for both $\beta = 0^\circ$ and $\beta = 10^\circ$. However, sizes of the inception regions were almost the same for all blades at straight course, whereas for motion with a drift angle the size of the low-pressure zone was strongly dependent on the position of the blade. This result shows, that the scenario for vibration intensification, described in [119, 164], may also be realistic for the considered conditions.

Conclusions on vibration intensification

The analysis of various hydrodynamic sources of vibration for shallow water conditions indicates, that all of them are affected by reduction of the fairway depth. The magnitudes of thrust oscillations and pressure pulses increase when h/T gets smaller. As it was shown the cavitation inception may also occur and may play a significant role as a source of vibration. Therefore it is to expect, that the vibration of the ship stern will be indeed intensified, when ship enters the restricted waters.

Outlook and future work

The further studies on the topic could be conducted in following directions:

1. **Application of the simulation methodology to the real hull form** In the framework of the presented study the exact geometries of the ship hull and thruster were not available. Even though the replicated geometries were visually close to the real ones, it is clear, that the form of the latter may be different. This may result into different levels of thrust and pressure fluctuations, than that documented in this work. However, the simulation methodology, employed in the study, can be readily applied for the analysis of real geometries.
2. **Structural analysis** Obviously, hydrodynamic analysis is not sufficient to evaluate the influence of the considered factors on the stern vibration. In order to be able to predict the rise of vibration, structural analysis should be conducted, which could use the data obtained in the presented study. However, such investigations cannot be undertaken without the sufficient description of the ship structure.
3. **Analysis of cavitation contribution** As it was mentioned in the introduction, pressure pulses on the ship hull may be dramatically intensified due to collapse of cavitation bubbles on the propeller blades. This effect can significantly contribute to the stern vibration excitation and should be also analyzed in further research. Rough analysis of the cavitation inception regions was conducted in the framework of the presented study and indicated that cavitation is likely to occur. In further studies the dynamics of the cavities and the corresponding pressure fluctuations on the hull should be studied in more details.
4. **Improvement of turbulence generators** Hybrid RANS/LES simulations require a mechanism for generation of turbulent content. In cases with strong separations the inner flow instabilities will play this role. But for flows around well-streamlined bodies application of RANS/LES methods without the synthetic turbulence generator would lead for shielded models to application of more RANS (and suppression of unsteadiness in the region of interest) and for unshielded - to MSD and GIS. Both scenarios may lead to erroneous solutions and are undesired. Therefore the quality of the generated turbulent fluctuations can play an important role in such computations and should be thoroughly controlled. This may be done by means of: comparison of different turbulence generators, investigation of the sensitivity of the results to the generator location and sources of statistics (e.g. EARSM instead of Boussinesq approximation).
5. **Improvement of hybrid models** The hybrid RANS/LES models can still be considered an active field of research. Multiple methods were proposed in past decades, but most of the methods seem to have similar flaws. The main problem of unified models is still the presence of the gray area, in which (as mentioned in Section 2.3.5) the lack of momentum transport between the RANS and LES regions is observed. Practically used remedies for particular issues (like MSD, GIS, LLM) were up to now all based on empiricism and may malfunction under certain conditions. On the other hand, theoretically backed HFNS turned out to be hardly applicable in practice. Therefore, further research and development in this area is needed.

This page intentionally left blank

Bibliography

- [1] N. Abbas. Determination of unsteady loadings on marine propellers using hybrid urans/les methods. PhD thesis. University of Rostock, 2016.
- [2] N. Abbas, N. Kornev, I. Shevchuk, and P. Anschau. CFD prediction of unsteady forces on marine propellers caused by the wake nonuniformity and nonstationarity. *Ocean engineering*:659–672, 2015. DOI: [10.1016/j.oceaneng.2015.06.007](https://doi.org/10.1016/j.oceaneng.2015.06.007).
- [3] N. Abbas, I. Shevchuk, and N. Kornev. Development and validation of a hybrid RANS-LES method for ship hydromechanics applications. In *Proceedings of 16th Numerical Towing Tank Symposium*. Duiburg-Müllheim, Germany, 2013.
- [4] D. Adamian and A. Travin. *Computational Fluid Dynamics 2010: Proceedings of the Sixth International Conference on Computational Fluid Dynamics, ICCFD6, St Petersburg, Russia, on July 12-16, 2010*. In: Alexander Kuzmin, editor. Springer Berlin Heidelberg, Berlin, Heidelberg, 2011. part An Efficient Generator of Synthetic Turbulence at RANS-LES Interface in Embedded LES of Wall-Bounded and Free Shear Flows, pages 739–744. DOI: [10.1007/978-3-642-17884-9_94](https://doi.org/10.1007/978-3-642-17884-9_94).
- [5] D. Y. Adamian and A. K. Travin. Assessment of an approach to generating inflow synthetic turbulence for large eddy simulations of complex turbulent flows. *Progress in flight physics*, 5:43–54, 2013.
- [6] I. Asmussen, W. Menzel, and H. Mumm. Ship Vibration. Germanisher Lloyd, 2001.
- [7] R. Azcueta. Computation of Turbulent Free Surface Flows Around Ships and Floating Bodies. PhD thesis. Technical University of Hamburg-Harburg, 2001.
- [8] B. Basara, Sinisa Krajnovic, Z. Pavlovic, and P. Ringqvist. Performance analysis of partially-averaged navier-stokes method for complex turbulent flows. In *6th AIAA Theoretical Fluid Mechanics Conference, Honolulu, 27 - 30 June 2011*.
- [9] A. Basin, I. Velednicky, and Lyahovicky. *Ship hydrodynamics in shallow water*. Leningrad, Sudostroenie, 1976.
- [10] G. K. Batchelor. *An Introduction to Fluid Dynamics*. Of *Cambridge Mathematical Library*. Cambridge University Press, 2000.
- [11] M. Benzi, G. H. Golub, and J. Liesen. Numerical solution of saddle point problems. *Acta numerica*, 14:1–137, May 2005. DOI: [10.1017/S0962492904000212](https://doi.org/10.1017/S0962492904000212).
- [12] E. Berberovic. Investigation of Free-surface Flow Associated with Drop Impact: Numerical Simulations and Theoretical Modeling. PhD thesis. TU Darmstadt, 2010.
- [13] L. C. Berselli, T. Iliescu, and W. J. Layton. *Mathematics of Large Eddy Simulation of Turbulent Flows*. Of *Scientific computation*. Springer, 1st edition, 2006.
- [14] S. Bhushan, M.F. Alam, and D.K. Walters. Evaluation of hybrid RANS/LES models for prediction of flow around surface combatant and Suboff geometries. *Computers & fluids*, 88:834–849, 2013. DOI: [10.1016/j.compfluid.2013.07.020](https://doi.org/10.1016/j.compfluid.2013.07.020).
- [15] S. Bhushan and D. K. Walters. A dynamic hybrid Reynolds-averaged Navier Stokes–Large eddy simulation modeling framework. *Physics of fluids*, 24(1), 015103, 2012. DOI: [10.1063/1.3676737](https://doi.org/10.1063/1.3676737).
- [16] S. Bhushan, T. Xing, and F. Stern. Vortical Structures and Instability Analysis for Athena Wetted Transom Flow with Full-Scale Validation. *Journal of fluids engineering*, 134(3):031201–031201, March 2012. 10.1115/1.4006173. DOI: [10.1115/1.4006173](https://doi.org/10.1115/1.4006173).

-
- [17] J. P. Boris and D. L. Book. Flux-Corrected Transport. *Journal of computational physics*, 135(2):172–186, 1997. DOI: [10.1006/jcph.1997.5700](https://doi.org/10.1006/jcph.1997.5700).
 - [18] C. U. Buice and J. K. Eaton. Experimental Investigation of Flow Through an Asymmetric Plane Diffuser. *Journal of fluids engineering*, 122(2):433–435, January 2000. 10.1115/1.483278. DOI: [10.1115/1.483278](https://doi.org/10.1115/1.483278).
 - [19] J. Carlton. *Marine Propellers and Propulsion*. Elsevier Science, 2012.
 - [20] Case 8.2: Flow through an asymmetric plane diffuser. http://www.ercoftac.org/fileadmin/user_upload/bigfiles/sig15/database/8.2/index.html.
 - [21] C. Cercignani. Chapter 1 - The Boltzmann Equation and Fluid Dynamics. In S. Friedlander and D. Serre, editors. Volume 1, in *Handbook of Mathematical Fluid Dynamics*, pages 1–69. North-Holland, 2002. DOI: [10.1016/S1874-5792\(02\)80003-9](https://doi.org/10.1016/S1874-5792(02)80003-9).
 - [22] X.-N. Chen. *Hydrodynamics of Wave-Making in Shallow Water*. Shaker, 1999.
 - [23] A. J. Chorin and J. E. Marsden. *A Mathematical Introduction to Fluid Mechanics*. Of *Texts in Applied Mathematics*. Springer New York, 2000.
 - [24] S.M. Damian. *An Extended Mixture Model for the Simultaneous Treatment of Short and Long Scale Interface*. Universidad Nacional del Litoral, Santa Fe, Argentina, 2013.
 - [25] M. Darwish, L. Mangani, and F. Moukalled. *The finite volume method in computational fluid dynamics : an advanced introduction with OpenFOAM® and Matlab®*. Of *Fluid mechanics and its applications volume 113*. Springer, 1st ed. 2015 edition, 2016.
 - [26] L. Davidson and M. Billson. Hybrid LES-RANS using synthesized turbulent fluctuations for forcing in the interface region. *International journal of heat and fluid flow*, 27(6):1028–1042, 2006. DOI: [10.1016/j.ijheatfluidflow.2006.02.025](https://doi.org/10.1016/j.ijheatfluidflow.2006.02.025).
 - [27] P. Davidson. *Turbulence: an introduction for scientists and engineers*. Oxford University Press, USA, 2015.
 - [28] I. Demirdžić. On the Discretization of the Diffusion Term in Finite-Volume Continuum Mechanics. *Numerical heat transfer part b fundamentals*, 68, 1, July 2015. DOI: [10.1080/10407790.2014.985992](https://doi.org/10.1080/10407790.2014.985992).
 - [29] K. Eeloot. Selection, Experimental Determination and Evaluation of a Mathematical Model for Ship Manoeuvring in Shallow Water. PhD thesis. University of Ghent, 2005.
 - [30] S. Enger, M. Peric, and R. Peric. Simulation of Flow Around KCS-Hull. In *Proceedings of the Workshop on CFD in Ship Hydrodynamics, Gothenburg, Sweden*, 2010.
 - [31] L. C. Evans. *Partial differential equations*. Of *Graduate Studies in Mathematics*. American Mathematical Society, 1998.
 - [32] C.-C. Fan, X. Xiao, J. R. Edwards, H. A. Hassan, and R. A. Baurle. Hybrid Large-Eddy / Reynolds-Averaged Navier-Stokes Simulation of Shock-Separated Flows. *Journal of spacecraft and rockets*, 41(6):897–906, 2004. doi: 10.2514/1.3735. DOI: [10.2514/1.3735](https://doi.org/10.2514/1.3735);[10.2514/1.3735](https://doi.org/10.2514/1.3735).
 - [33] R. E. Farrel and J. R. Maddison. Conservative interpolation between volume meshes by local Galerkin projection. *Comput. methods appl. mech. engrg.*, 200:89–100, 2011.
 - [34] H. F. Fasel, J. Seidel, and S. Wernz. A Methodology for Simulations of Complex Turbulent Flows. *Journal of fluids engineering*, 124(4):933–942, December 2002. 10.1115/1.1517569. DOI: [10.1115/1.1517569](https://doi.org/10.1115/1.1517569).
 - [35] C. L. Fefferman. Existence and Smoothness of the Navier-Stokes equation. Clay Mathematics Institute. Official Statement of the Problem. 2000.

- [36] J. H. Ferziger and M. Peric. *Computational methods for fluid dynamics*. Springer Science & Business Media, 2012.
- [37] J. Fröhlich and D. von Terzi. Hybrid LES/RANS Methods for the Simulation of Turbulent Flows. *Progress in aerospace sciences*, 44:349–377, 2008.
- [38] C. Fureby, S.L. Toxopeus, M. Johansson, M. Tormalm, and K. Petterson. A computational study of the flow around the {KVLCC2} model hull at straight ahead conditions and at drift. *Ocean engineering*, 118:1–16, 2016. DOI: [10.1016/j.oceaneng.2016.03.029](https://doi.org/10.1016/j.oceaneng.2016.03.029).
- [39] T. B. Gatski and C. G. Speziale. On explicit algebraic stress models for complex turbulent flows. *Journal of fluid mechanics*, 254:59–78, 1993. DOI: [10.1017/S0022112093002034](https://doi.org/10.1017/S0022112093002034).
- [40] M. Germano. Properties of the hybrid RANS/LES filter. *Theoretical and computational fluid dynamics*, 17(4):225–231, 2004. DOI: [10.1007/s00162-004-0116-6](https://doi.org/10.1007/s00162-004-0116-6).
- [41] M. Germano, U. Piomelli, P. Moin, and W. Cabot. A dynamic subgrid-scale eddy viscosity model. *Physics of fluids a*, 3(7):1760–1765, 1991. DOI: [10.1063/1.857955](https://doi.org/10.1063/1.857955).
- [42] S. Ghosal and P. Moin. The Basic Equations for the Large Eddy Simulation of Turbulent Flows in Complex Geometry. *Journal of computational physics*, 118(1):24–37, 1995. DOI: [10.1006/jcph.1995.1077](https://doi.org/10.1006/jcph.1995.1077).
- [43] S. Girimaji. Partially-Averaged Navier-Stokes Model for Turbulence: A Reynolds-Averaged Navier-Stokes to Direct Numerical Simulation Bridging Method. *Journal of applied mechanics*, 73(3):413–421, November 2005. 10.1115/1.2151207. DOI: [10.1115/1.2151207](https://doi.org/10.1115/1.2151207).
- [44] S. Girimaji and K. Abdol-Hamid. Partially Averaged Navier–Stokes Model for Turbulence: Implementation and Validation. *Aiaa paper*, 502, 2005.
- [45] G. H. Golub and C. F. Van Loan. *Matrix Computations*. Of Johns Hopkins Studies in the Mathematical Sciences. Johns Hopkins University Press, 1996.
- [46] A. von Graefe, B. O. el Moctar, V. Shigunov, H. Söding, and T. Zorn. Squat computations for containerships in restricted waterways. In *Proceedings of the 2nd International Conference on Manoeuvring in Shallow & Coastal Waters*, 2011.
- [47] M. Gritskevich. Simulation of wall-bounded turbulent flows using a zonal RANS / LES approach with a volume source of turbulent fluctuations. In russian. PhD thesis. Saint-Petersburg Polytechnic University, 2012.
- [48] M. Gritskevich, A. Garbaruk, J. Schütze, and F. Menter. Development of DDES and IDDES Formulations for the $k\text{-}\omega$ Shear Stress Transport Model. *Flow, turbulence and combustion*, 88(3):431–449, 2011. DOI: [10.1007/s10494-011-9378-4](https://doi.org/10.1007/s10494-011-9378-4).
- [49] Hedges, L. S., Travin, A. K., and Spalart, P. R. Detached-Eddy Simulations Over a Simplified Landing Gear. *Journal of fluids engineering*, 124(2):413–423, May 2002. 10.1115/1.1471532. DOI: [10.1115/1.1471532](https://doi.org/10.1115/1.1471532).
- [50] A. Hellsten and S. Wallin. Explicit algebraic Reynolds stress and non-linear eddy-viscosity models. *International journal of computational fluid dynamics*, 23(4):349–361, 2009. DOI: [10.1080/10618560902776828](https://doi.org/10.1080/10618560902776828).
- [51] C. W. Hirt and B. D. Nichols. Volume of fluid (VOF) method for the dynamics of free boundaries. *Journal of computational physics*, 39(1):201–225, 1981. DOI: [10.1016/0021-9991\(81\)90145-5](https://doi.org/10.1016/0021-9991(81)90145-5).
- [52] M. Hoekstra. A RANS-based analysis tool for ducted propeller systems in open water condition. *International shipbuilding progress*, 53(3), 2006.
- [53] J. P. Hooft. Manœuvring Large Ships in Shallow Water—I. *Journal of navigation*, 26:189–201, 02, April 1973. DOI: [10.1017/S037346330002405X](https://doi.org/10.1017/S037346330002405X).

-
- [54] J. Huang, P. M. Carrica, and F. Stern. Coupled ghost fluid/two-phase level set method for curvilinear body-fitted grids. *International journal for numerical methods in fluids*, 55(9):867–897, 2007. DOI: [10.1002/flid.1499](https://doi.org/10.1002/flid.1499).
 - [55] S. Ianniello, R. Muscari, and A. Di Mascio. Ship underwater noise assessment by the acoustic analogy. Part I: nonlinear analysis of a marine propeller in a uniform flow. *Journal of marine science and technology*, 18(4):547–570, 2013. DOI: [10.1007/s00773-013-0227-0](https://doi.org/10.1007/s00773-013-0227-0).
 - [56] R. I. Issa. Solution of the implicitly discretised fluid flow equations by operator-splitting. *Journal of computational physics*, 62(1):40–65, 1986. DOI: [10.1016/0021-9991\(86\)90099-9](https://doi.org/10.1016/0021-9991(86)90099-9).
 - [57] N. Jarrin, S. Benhamadouche, D. Laurence, and R. Prosser. A synthetic-eddy-method for generating inflow conditions for large-eddy simulations. *International journal of heat and fluid flow*, 27(4):585–593, 2006. Special Issue of The Fourth International Symposium on Turbulence and Shear Flow Phenomena - 2005. DOI: [10.1016/j.ijheatfluidflow.2006.02.006](https://doi.org/10.1016/j.ijheatfluidflow.2006.02.006).
 - [58] H. Jasak. Error Analysis and Estimation for the Finite Volume Method with Applications to Fluid Flows. PhD thesis. Imperial College of Science, Technology and Medicine, 1996.
 - [59] H. Jasak and Z. Tuković. Automatic Mesh Motion for the Unstructured Finite Volume Method. 2004.
 - [60] J. Jeong and F. Hussain. On the identification of a vortex. *Journal of fluid mechanics*, 285:69–94, 1995.
 - [61] T. Jiang. *Ship Waves in Shallow Water*. Of *Fortschr.-Ber., VDI Reihe 12. Nr. 466*. VDI Verlag, Germany, 2001.
 - [62] H.-J. Kaltenbach, M. Fatica, R. Mittal, T. S. Lund, and P. Moin. Study of flow in a planar asymmetric diffuser using large-eddy simulation. *Journal of fluid mechanics*, 390:151–185, 1999.
 - [63] S. E. Kim, B. J. Rhee, H. Shan, J. Gorski, E. J. Paterson, and K. Maki. A Scalable Multiphase RANSE Capability Based on Object-Oriented Programming and Its Applications to Ship Hydrodynamics. In *Proceedings of the Workshop on CFD in Ship Hydrodynamics, Gothenburg, Sweden*, 2010.
 - [64] N. Kornev. *Lectures on ship manoeuvrability*. bookboon.com, 2013.
 - [65] N. Kornev. *Propellertheorie*. Shaker, 2009.
 - [66] N. Kornev and E. Hassel. A new method for generation of artificial turbulent inflow data with prescribed statistic properties for LES and DNS simulations. *Schiffbauforschung / schriftenreihe für ingenieurwissenschaften*, 42(4), 2003.
 - [67] N. Kornev and E. Hassel. Method of random spots for generation of synthetic inhomogeneous turbulent fields with prescribed autocorrelation functions. *Communications in numerical methods in engineering*, 23(1):35–43, 2007. DOI: [10.1002/cnm.880](https://doi.org/10.1002/cnm.880).
 - [68] N. Kornev and E. Hassel. Synthesis of homogeneous anisotropic divergence-free turbulent fields with prescribed second-order statistics by vortex dipoles. *Physics of fluids*, 19(6), 068101, 2007. DOI: [10.1063/1.2738607](https://doi.org/10.1063/1.2738607).
 - [69] N. Kornev, H. Kröger, and E. Hassel. Synthesis of homogeneous anisotropic turbulent fields with prescribed second-order statistics by the random spots method. *Communications in numerical methods in engineering*, 24(10):875–877, 2008. DOI: [10.1002/cnm.1009](https://doi.org/10.1002/cnm.1009).

- [70] N. Kornev, A. Taranov, E. Shchukin, and L. Kleinsorge. Development of hybrid URANS-LES methods for flow simulation in the ship stern area. *Ocean engineering*, 38:1831–1838, 2011.
- [71] N. Kornev, A. Taranov, E. Shchukin, J. Springer, M. Palm, and Yu. Batrak. Development, application and validation of hybrid URANS-LES methods for flow simulation in the ship stern area. In *29th Symposium on Naval Hydrodynamics, Gothenburg, Sweden*, 2012.
- [72] R. H. Kraichnan. Diffusion by a Random Velocity Field. *Physics of fluids*, 13(1):22–31, 1970. DOI: [10.1063/1.1692799](https://doi.org/10.1063/1.1692799).
- [73] S. Krajnovic, G. Minelli, and B. Basara. Partially-averaged Navier–Stokes simulations of two bluff body flows. *Applied mathematics and computation*, 272:692–706, 2015.
- [74] H. Kröger and N. Kornev. Generation of anisotropic divergence free synthetic turbulence at inflow boundaries for LES and DNS using the Turbulent Spot Method. In *Proceedings of 8th International Symposium on Turbulence, Heat and Mass Transfer (THMT)*, 2015.
- [75] O. A. Ladyzhenskaya and R. A. Silverman. *Mathematical theory of viscous incompressible flow*. Of. Gordon & Breach Science Publishers Ltd, 2nd revised edition edition, 1969.
- [76] L. D. Landau and E. M. Lifshitz. *Fluid Mechanics: Landau and Lifshitz: Course of Theoretical Physics*. (Bd. 6). Elsevier Science, 2013.
- [77] L. Larsson, H.C. Raven, and J.R. Paulling. *Ship Resistance and Flow*. Of *Principles of naval architecture*. Society of Naval Architects and Marine Engineers, 2010.
- [78] B. E. Launder, G. J. Reece, and W. Rodi. Progress in the development of a Reynolds-stress turbulence closure. *Journal of fluid mechanics*, 68:537–566, 03, April 1975. DOI: [10.1017/S0022112075001814](https://doi.org/10.1017/S0022112075001814).
- [79] B. E. Launder and D. B. Spalding. The numerical computation of turbulent flows. *Computer methods in applied mechanics and engineering*, 3(2):269–289, 1974. DOI: [10.1016/0045-7825\(74\)90029-2](https://doi.org/10.1016/0045-7825(74)90029-2).
- [80] H. Lee and S.H. Rhee. A dynamic interface compression method for VOF simulations of high-speed planing watercraft. *Journal of mechanical science and technology*, 29(5):1849–1857, 2015. DOI: [10.1007/s12206-015-0405-6](https://doi.org/10.1007/s12206-015-0405-6).
- [81] S. Lee, S. Lele, and P. Moin. Simulation of spatially evolving turbulence and the applicability of Taylor’s hypothesis in compressible flow. *Physics of fluids a*, 4(7):1521–1530, 1992. DOI: [10.1063/1.858425](https://doi.org/10.1063/1.858425).
- [82] E. M. Lewandowski. *The dynamics of marine craft: maneuvering and seakeeping*. World Scientific Publishing Company, 1st edition, 2003.
- [83] D. K. Li, N. Berchiche, and C. E. Janson. Influence of Turbulence Models on the Prediction of Full-Scale Propeller Open Water Characteristics with RANS method. In *Proceedings of 26th Symposium on Naval Hydrodynamics, Rome, Italy*, 2006.
- [84] M. Liefvendahl and R. Bensow. Simulation-Based Analysis of Hull-Propeller Interaction for a Single-Screw Transport Ship. In *Proceedings of 30th Symposium on Naval Hydrodynamics*.
- [85] D. K. Lilly. A proposed modification of the Germano subgrid-scale closure method. *Physics of fluids a: fluid dynamics (1989-1993)*, 4(3):633–635, 1992. DOI: [10.1063/1.858280](https://doi.org/10.1063/1.858280).
- [86] D. K. Lilly. The representation of small-scale turbulence in numerical simulation experiments. In *Proceedings IBM Scientific Computation Symposium On Environmental Sciences*, 1967, pages 195–210.

-
- [87] S. List, K. Rüchner, and B. Friedhoff. WAKE. An veränderliche Wassertiefen angepasste Konzepte zur Energiesparung durch Vergleichmäßigung des Propellerzustroms. Bericht 2162. 2015.
 - [88] E. N. Lorenz. Deterministic nonperiodic flow. *J. atmos. sci.*, 20:130, 1963.
 - [89] T. Lund, X. Wu, and K. Squires. Generation of Turbulent Inflow Data for Spatially-Developing Boundary Layer Simulations. *J. comput. phys.*, 140(2):233–258, March 1998. DOI: [10.1006/jcph.1998.5882](https://doi.org/10.1006/jcph.1998.5882).
 - [90] J. M. Ma, S.-H. Peng, L. Davidson, and F. Wang. A Low Reynolds Number Partially-Averaged Navier-Stokes Model for Turbulence. *International journal of heat and fluid flow*, 32:652–669, 3, 2011.
 - [91] R. Manceau, J. R. Carlson, and T. B. Gatski. A rescaled elliptic relaxation approach: Neutralizing the effect on the log layer. *Physics of fluids*, 14(11):3868–3879, 2002. DOI: [10.1063/1.1511547](https://doi.org/10.1063/1.1511547).
 - [92] P. J. Mason and N. S. Callen. On the magnitude of the subgrid-scale eddy coefficient in large-eddy simulations of turbulent channel flow. *Journal of fluid mechanics*, 162:439–462, January 1986. DOI: [10.1017/S0022112086002112](https://doi.org/10.1017/S0022112086002112).
 - [93] F. Mathey. Aerodynamic noise simulation of the flow past an airfoil trailing-edge using a hybrid zonal RANS-LES. *Computers & fluids*, 37(7):836–843, 2008.
 - [94] F. Menter, J. C. Ferreira, T. Esch, and B. Konno. The SST turbulence model with improved wall treatment for heat transfer predictions in gas turbines. In *Proceedings of the international gas turbine congress*, 2003, pages 2–7.
 - [95] F. R. Menter. Best practice: Scale-Resolving Simulations in ANSYS CFD, version 2.00. *Ansys germany gmbh*.
 - [96] F. R. Menter. Two-equation eddy-viscosity turbulence models for engineering applications. *Aiaa journal*, 32(8):1598–1605, 1994.
 - [97] F. R. Menter. Zonal Two Equation Kappa-Omega Turbulence Models for Aerodynamic Flows. In. NASA Ames Research Center, 1993.
 - [98] F. R. Menter and M. Kuntz. *The Aerodynamics of Heavy Vehicles: Trucks, Buses, and Trains*. In. Rose McCallen, Fred Browand, and James Ross, editors. Springer Berlin Heidelberg, Berlin, Heidelberg, 2004. part Adaptation of Eddy-Viscosity Turbulence Models to Unsteady Separated Flow Behind Vehicles, pages 339–352. DOI: [10.1007/978-3-540-44419-0_30](https://doi.org/10.1007/978-3-540-44419-0_30).
 - [99] F. R. Menter, M. Kuntz, and R. Langtry. Ten Years of Industrial Experience with the SST Turbulence Model. In *Turbulence, Heat and Mass Transfer 4*. K. Hanjalic, Y. Nagano, and M. Tummers, editors. Begell House, Inc., 2003.
 - [100] C. Mockett. A comprehensive study of detached-eddy simulation. PhD thesis. TU Berlin, 2009. DOI: [10.14279/depositonce-2305](https://doi.org/10.14279/depositonce-2305).
 - [101] C. Mockett, M. Fuchs, A. Garbaruk, M. Shur, P. Spalart, M. Strelets, F. Thiele, and A. Travin. *Progress in Hybrid RANS-LES Modelling: Papers Contributed to the 5th Symposium on Hybrid RANS-LES Methods, 19-21 March 2014, College Station, A&M University, Texas, USA*. In. Sharath Girimaji, Werner Haase, Shia-Hui Peng, and Dieter Schwamborn, editors. Springer International Publishing, Cham, 2015. part Two Non-zonal Approaches to Accelerate RANS to LES Transition of Free Shear Layers in DES, pages 187–201. DOI: [10.1007/978-3-319-15141-0_15](https://doi.org/10.1007/978-3-319-15141-0_15).

- [102] B. O. el Moctar, J. Kaufmann, J. Ley, J. Oberhagemann, V. Shigunov, and T. Zorn. Prediction of Ship Resistance and Ship Motions Using RANSE. In *Proceedings of the Workshop on CFD in Ship Hydrodynamics, Gothenburg, Sweden*, 2010.
- [103] B. O. el Moctar, U. Lantermann, P. Mucha, J. Höpken, and T. E. Schellin. RANS-Based Simulated Ship Maneuvering Accounting for Hull-Propulsor-Engine Interaction. *Ship technology research*, 61(3):142–161, 2014. DOI: [10.1179/str.2014.61.3.003](https://doi.org/10.1179/str.2014.61.3.003).
- [104] P. Moin and J. Kim. Numerical investigation of turbulent channel flow. *Journal of fluid mechanics*, 118:341–377, May 1982. DOI: [10.1017/S0022112082001116](https://doi.org/10.1017/S0022112082001116).
- [105] A. S. Monin, A. M. Yaglom, and J. L. Lumley. *Statistical Fluid Mechanics: Mechanics of Turbulence*. (Bd. 1) of *Dover books on physics*. Dover Publications, 2007.
- [106] S. Muzaferija, M. Peric, P. Sames, and T. Schelin. A Two-Fluid Navier-Stokes Solver to Simulate Water Entry. In *Proceedings of Twenty-Second Symposium on Naval Hydrodynamics*, 1998.
- [107] N. V. Nikitin, F. Nicoud, B. Wasistho, K. D. Squires, and P. R. Spalart. An approach to wall modeling in large-eddy simulations. *Physics of fluids*, 12(7):1629–1632, 2000. DOI: [10.1063/1.870414](https://doi.org/10.1063/1.870414).
- [108] T. Nishikawa. Application of Fully Resolved Large Eddy Simulation to Japan Bulk Carrier with an Energy Saving Device. In *Proceedings of the Workshop on CFD in Ship Hydrodynamics*. Tokyo, 2015.
- [109] S. Patankar. *Numerical Heat Transfer and Fluid Flow*. Of *Series in computational methods in mechanics and thermal sciences*. Taylor & Francis, 1980.
- [110] S.-H. Peng. Hybrid RANS-LES modeling based on zero- and one-equation models for turbulent flow simulation. In *Proceedings of the 4th Int. Symp. Turb. And Shear Flow Phenomena*, 2005.
- [111] U. Piomelli, E. Balaras, H. Pasinato, K. D. Squires, and P. R. Spalart. The inner-outer layer interface in large-eddy simulations with wall-layer models. *International journal of heat and fluid flow*, 24(4):538–550, 2003. Selected Papers from the Fifth International Conference on Engineering Turbulence Modelling and Measurements. DOI: [10.1016/S0142-727X\(03\)00048-1](https://doi.org/10.1016/S0142-727X(03)00048-1).
- [112] R. H. Pletcher, J. C. Tannehill, and D. Anderson. *Computational Fluid Mechanics and Heat Transfer, Second Edition*. Of *Series in Computational and Physical Processes in Mechanics and Thermal Sciences*. Taylor & Francis, 1997.
- [113] R. Poletto, T. Craft, and A. Revell. A New Divergence Free Synthetic Eddy Method for the Reproduction of Inlet Flow Conditions for LES. *Flow, turbulence and combustion*, 91(3):519–539, 2013. DOI: [10.1007/s10494-013-9488-2](https://doi.org/10.1007/s10494-013-9488-2).
- [114] S. B. Pope. *Turbulent Flows*. Cambridge University Press, 2000.
- [115] L. Quartapelle. *Numerical solution of the incompressible Navier-Stokes equations*. Volume 113 of *International Series of Numerical Mathematics*. Birkhäuser, 2013.
- [116] P. Queutey and M. Visonneau. An interface capturing method for free-surface hydrodynamic flows. *Computers & fluids*, 36(9):1481–1510, 2007. DOI: [10.1016/j.compfluid.2006.11.007](https://doi.org/10.1016/j.compfluid.2006.11.007).
- [117] B. Rajamani and J. Kim. A Hybrid-Filter Approach to Turbulence Simulation. *Flow, turbulence and combustion*, 85(3):421–441, 2010. DOI: [10.1007/s10494-010-9254-7](https://doi.org/10.1007/s10494-010-9254-7).
- [118] H. C. Raven. A computational study of shallow-water effects on ship viscous resistance. In *Proceedings of 29th Symposium on Naval Hydrodynamics*. Gothenburg, Sweden, 2012.

-
- [119] F. E. Reed and N. L. Bassett. Further Studies of Propeller-Excited Vibration on Great Lakes Cargo Ships. *Sname transactions*, 97:375–396, 1989.
 - [120] H. Reichardt. Vollständige Darstellung der turbulenten Geschwindigkeitsverteilung in glatten Leitungen. *Zamm - journal of applied mathematics and mechanics / zeitschrift für angewandte mathematik und mechanik*, 31(7):208–219, 1951. DOI: [10.1002/zamm.19510310704](https://doi.org/10.1002/zamm.19510310704).
 - [121] D. Rempfer. On boundary conditions for incompressible Navier-Stokes problems. *Applied mechanics reviews*, 59(3):107–125, 2006.
 - [122] H. S. Rhee, B. P. Makarov, H. Krishinan, and V. Ivanov. Assessment of the volume of fluid method for free-surface wave flow. *Journal of marine science and technology*, 10(4):173–180, 2005. DOI: [10.1007/s00773-005-0205-2](https://doi.org/10.1007/s00773-005-0205-2).
 - [123] H. Rusche. Computational Fluid Dynamics of Dispersed Two-Phase Flows at High Phase Fractions. PhD thesis. Imperial College of Science, Technology and Medicine, 2002.
 - [124] P. Sagaut. *Large Eddy Simulation for Incompressible Flows: An Introduction (Scientific Computation)*. Of. Springer, 3rd edition, 2005.
 - [125] P. Sagaut, S. Deck, and M. Terracol. *Multiscale and Multiresolution Approaches in Turbulence: LES, DES and Hybrid RANS/LES Methods : Applications and Guidelines*. Imperial College Press, 2013.
 - [126] M. Sánchez-Rocha and S. Menon. An order-of-magnitude approximation for the hybrid terms in the compressible hybrid RANS/LES governing equations. *Journal of turbulence*, 12:N16, 2011. DOI: [10.1080/14685248.2011.560153](https://doi.org/10.1080/14685248.2011.560153).
 - [127] H. Schlichting. *Boundary layer theory*. Springer, 2000.
 - [128] J. U. Schlüter, X. Wu, and H. Pitsch. Large-eddy simulation of a separated plane diffuser. *Aiaa paper*, 672:2005, 2005.
 - [129] Schlüter J. U., Pitsch H., and Moin P. Large-Eddy Simulation Inflow Conditions for Coupling with Reynolds-Averaged Flow Solvers. *Aiaa journal*, 42(3):478–484, 2004. doi: 10.2514/1.3488. DOI: [10.2514/1.3488](https://doi.org/10.2514/1.3488); [10.2514/1.3488](https://doi.org/10.2514/1.3488).
 - [130] H. G. Schuster and W. Just. *Deterministic chaos: an introduction*. John Wiley & Sons, 2006.
 - [131] I. Shevchuk, C.-U. Böttner, and N. Kornev. Numerical analysis of the flow in the gap between the ship hull and the fairway bottom in extremely shallow water. In *Proceedings of the 4th international conference on ship manoeuvring in shallow and confined water*. Hamburg, 2016.
 - [132] I. Shevchuk and N. Kornev. Application of OpenFOAM to prediction of ship squat in restricted waterways. In *Proceedings of 16th Numerical Towing Tank Symposium*. Duiburg-Müllheim, Germany, 2013.
 - [133] Americal Bureau of Shipping. Guidance Notes on Ship Vibration. 2006.
 - [134] M. Shur, P. Spalart, M. Strelets, and A. Travin. A hybrid RANS-LES approach with delayed-DES and wall-modelled LES capabilities. *International journal of heat and fluid flow*, 29(6):1638–1649, 2008.
 - [135] M. Shur, P. R. Spalart, M. Strelets, and A. Travin. Detached-eddy simulation of an airfoil at high angle of attack. In W. Rodi and D. Laurence, editors, *Engineering Turbulence Modelling and Experiments 4*, pages 669–678. Elsevier Science Ltd, Oxford, 1999. DOI: [10.1016/B978-008043328-8/50064-3](https://doi.org/10.1016/B978-008043328-8/50064-3).

- [136] A. Smirnov, S. Shi, and I. Celik. Random Flow Generation Technique for Large Eddy Simulations and Particle-Dynamics Modeling. *Journal of fluids engineering*, 123(2):359–371, February 2001. DOI: [10.1115/1.1369598](#). DOI: [10.1115/1.1369598](#).
- [137] K. K. So, X. Y. Hu, and N. A. Adams. Anti-diffusion method for interface steepening in two-phase incompressible flow. *Journal of computational physics*, 230(13):5155–5177, 2011. DOI: [10.1016/j.jcp.2011.03.011](#).
- [138] T. Soomere. *Long Ship Waves in Shallow Water Bodies*. In. *Applied Wave Mathematics: Selected Topics in Solids, Fluids, and Mathematical Methods*. Ewald Quak and Tarmo Soomere, editors. Springer Berlin Heidelberg, Berlin, Heidelberg, 2009, pages 193–228. DOI: [10.1007/978-3-642-00585-5_12](#).
- [139] P. Spalart and S. Allmaras. *A one-equation turbulence model for aerodynamic flows*. In. In Aerospace Sciences Meetings. doi:10.2514/6.1992-439. American Institute of Aeronautics and Astronautics, January 1992. DOI: [10.2514/6.1992-439](#).
- [140] P. Spalart, W. Jou, M. Strelets, and S. Allmaras. Comments of feasibility of LES for wings, and on a hybrid RANS/LES approach. In *International Conference on DNS/LES, Aug. 4-8, 1997, Ruston, Louisiana*. 1997.
- [141] P. R. Spalart. Strategies for turbulence modelling and simulations. *International journal of heat and fluid flow*, 21(3):252–263, 2000. DOI: [10.1016/S0142-727X\(00\)00007-2](#).
- [142] P. R. Spalart. Young person’s guide to detached-eddy simulation grids. Technical report.
- [143] P. R. Spalart, S. Deck, M. L. Shur, K. D. Squires, M. Kh. Strelets, and A. Travin. A New Version of Detached-eddy Simulation, Resistant to Ambiguous Grid Densities. *Theoretical and computational fluid dynamics*, 20(3):181–195, 2006. DOI: [10.1007/s00162-006-0015-0](#).
- [144] C. G. Speziale. Analytical Methods for the Development of Reynolds-Stress Closures in Turbulence. *Annual review of fluid mechanics*, 23(1):107–157, 1991. DOI: [10.1146/annurev.fl.23.010191.000543](#).
- [145] C. G. Speziale, S. Sarkar, and T. B. Gatski. Modelling the pressure-strain correlation of turbulence: an invariant dynamical systems approach. *Journal of fluid mechanics*, 227:245–272, June 1991. DOI: [10.1017/S0022112091000101](#).
- [146] Speziale, C. Turbulence Modeling for Time-Dependent RANS and VLES: A Review. *Aiaa journal*, 36(2):173–184, 1998. doi: 10.2514/2.7499. DOI: [10.2514/2.7499](#).
- [147] M. Strelets. *Detached eddy simulation of massively separated flows*. In. In Aerospace Sciences Meetings. doi:10.2514/6.2001-879. American Institute of Aeronautics and Astronautics, January 2001.
- [148] D. A. Von Terzi, R. D. Sandberg, J. Sivasubramanian, and H. F. Fasel. High Accuracy DNS and LES of High Reynolds Number, Supersonic Base Flows and Passive Control of the Near Wake. In *2005 Users Group Conference (DOD-UGC’05)*, 2005, pages 119–127. DOI: [10.1109/DODUGC.2005.32](#).
- [149] A. K. Travin. Physical and Numerical Upgrades in the Detached-Eddy Simulation of Complex Turbulent Flows. In *Advances in LES of complex flows: proceedings of the Euromech Colloquium 412, Munich, Germany, October 2000*. F. Rainer and W. Rodi, editors. In Fluid Mechanics and Its Applications. Springer, 1st edition, 2002.
- [150] E. O. Tuck. Hydrodynamic Problems of Ships in Restricted Waters. *Annual review of fluid mechanics*, 10(1):33–46, 1978. DOI: [10.1146/annurev.fl.10.010178.000341](#).
- [151] O. Ubbink. Numerical prediction of two fluid systems with sharp interfaces. PhD thesis. Imperial College of Science, Technology and Medicine, 1997.

-
- [152] O. Ubbink and R. I. Issa. A Method for Capturing Sharp Fluid Interfaces on Arbitrary Meshes. *Journal of computational physics*, 153(1):26–50, 1999. DOI: [10.1006/jcph.1999.6276](https://doi.org/10.1006/jcph.1999.6276).
 - [153] H. Versteeg and W. Malalasekera. *An Introduction to Computational Fluid Dynamics: The Finite Volume Method (2nd Edition)*. Of. Prentice Hall, 2nd edition, 2007.
 - [154] M. I. Vishik and A. V. Fursikov. *Mathematical Problems of Statistical Hydromechanics. Of Mathematics and its Applications*. Springer Netherlands, 2012.
 - [155] Y. Voitkounski, editor. *Ship Theory Handbook, In 3 Volumes. Vol I. Hydromechanics, Resistance of Ship, Ship Propulsion Devices*. Leningrad, Sudostroenie, 1985.
 - [156] W. S. Vorus and J. R. Paulling. Society of Naval Architects and Marine Engineers, 2010.
 - [157] V. Voskoboinick, N. Kornev, and J. Turnow. Study of Near Wall Coherent Flow Structures on Dimpled Surfaces Using Unsteady Pressure Measurements. *Flow, turbulence and combustion*, 90(4):709–722, 2012. DOI: [10.1007/s10494-012-9433-9](https://doi.org/10.1007/s10494-012-9433-9).
 - [158] J. Wackers, B. Koren, H. C. Raven, A. van der Ploeg, A. R. Starke, G. B. Deng, P. Queutey, M. Visonneau, T. Hino, and K. Ohashi. Free-Surface Viscous Flow Solution Methods for Ship Hydrodynamics. *Archives of computational methods in engineering*, 18(1):1–41, 2011. DOI: [10.1007/s11831-011-9059-4](https://doi.org/10.1007/s11831-011-9059-4).
 - [159] H. G. Weller, G. Tabor, H. Jasak, and C. Fureby. A tensorial approach to computational continuum mechanics using object-oriented techniques. *Computers in physics*, 12(6):620–631, 1998. DOI: [10.1063/1.168744](https://doi.org/10.1063/1.168744).
 - [160] D. C. Wilcox. Reassessment of the scale-determining equation for advanced turbulence models. *Aiaa journal*, 26(11):1299–1310, 1988. doi: 10.2514/3.10041. DOI: [10.2514/3.10041](https://doi.org/10.2514/3.10041).
 - [161] D. C. Wilcox. *Turbulence modelling for CFD*. DCW Industries, La Cañada, 1993.
 - [162] T. Xing, S. Bhushan, and F. Stern. Vortical and turbulent structures for KVLCC2 at drift angle 0, 12, and 30 degrees. *Ocean engineering*, 55:23–43, 2012. DOI: [10.1016/j.oceaneng.2012.07.026](https://doi.org/10.1016/j.oceaneng.2012.07.026).
 - [163] E. Zeidler. *Applied functional analysis: applications to mathematical physics*. Of *Applied Mathematical Sciences*. Springer, springer edition, 1995.
 - [164] H. G. Zibell and E. Müller. Binnenschiffe für extrem flaches Wasser - Ergebnisse des VEBIS-Projektes. *Handbuch der Werften* 23, 1996.
 - [165] Z. Zong and K. Y. Lam. Hydrodynamic influence on ship-hull vibration close to water bottom. English. *Journal of engineering mathematics*, 37(4):363–374. DOI: [10.1023/A:1004601227471](https://doi.org/10.1023/A:1004601227471).

Selbstständigkeitserklärung

Hiermit versichere ich, die vorliegende Dissertation eigenständig und ausschließlich unter Verwendung der angegebenen Hilfsmittel, angefertigt zu haben. Alle öffentlichen Quellen sind als solche kenntlich gemacht. Die vorliegende Arbeit ist in dieser oder anderer Form zuvor nicht als Prüfungsarbeit zu Begutachtung vorgelegt worden.

Rostock,

Ivan Shevchuk